Electrical and Computer Engineering ETDs   Engineering ETDs

Fall 11-14-2016

Experimental Investigation of Plasma Dynamics in Jets and Bubbles Using a Compact Coaxial Plasma Gun in a Background Magnetized Plasma

Yue Zhang
University of New Mexico

Follow this and additional works at: https://digitalrepository.unm.edu/ece_etds

Part of the Electrical and Computer Engineering Commons, and the Plasma and Beam Physics Commons

Recommended Citation

Zhang, Yue. "Experimental Investigation of Plasma Dynamics in Jets and Bubbles Using a Compact Coaxial Plasma Gun in a Background Magnetized Plasma." (2016). https://digitalrepository.unm.edu/ece_etds/309

Yue Zhang

Candidate

Electrical and Computer Engineering

Department

This dissertation is approved, and it is acceptable in quality
and form for publication:

Approved by the Dissertation Committee:

Mark Gilmore, Chairperson

Edl Schamilogu

Scott Hsu

Ylva M Pihlstrom

EXPERIMENTAL INVESTIGATION OF PLASMA DYNAMICS IN JETS AND

BUBBLES USING A COMPACT COAXIAL PLASMA GUN IN A BACKGROUND

MAGNETIZED PLASMA

By

YUE ZHANG

B.S., Electrical Engineering, Xi'an Jiaotong University, 2003
M.S., Electrical Engineering, Xi'an Jiaotong University, 2006

DISSERTATION

Submitted in Partial Fulfillment of the
Requirements for the Degree of

Doctor of Philosophy
Engineering

The University of New Mexico
Albuquerque, New Mexico

December, 2016

Dedication

To my parents Zhiping Zhang and Fenghong Ji

Acknowledgements

I would like to my dissertation committee, Dr. Mark Gilmore, Dr. Edl Schamilogu, Dr. Scott Hsu, and Dr. Ylva M Pihlstrom for their valuable recommendations pertaining to this study and assistance in my professional development.

My deepest gratitude is to my advisor Dr. Mark Gilmore, for his guidance, input, support, and encouragement for the past ten years. He opened a new research window for me in plasma physics. He has my deepest respect.

I would also like to express my special thanks to Dr. Scott Hsu. His generous of experiment equipment support, deep understanding of plasma physics, and affluent experimental experiences in pulse power and plasma gun, kindled my research enthusiasm. Both the equipment support and the physics discussion with him turned out to be the key things to make this dissertation happen.

I am deeply grateful to Bei Zhao, who stays with me and supports me during the hardest time through my graduate studies, and to my parents for the most unselfish and consistent support to me. I am fortunate to have you all in my life.

I am especially grateful to all the past and present members of Dr. Mark Gilmore's Plasma and Fusion Science Lab for their help, support and friendship. They made my graduate school a fulfilling experience.

EXPERIMENTAL INVESTIGATION OF PLASMA DYNAMICS IN JETS AND BUBBLES USING A COMPACT COAXIAL PLASMA GUN IN A BACKGROUND MAGNETIZED PLASMA

By

Yue Zhang

B.S., Electrical Engineering, Xi'an Jiaotong University, 2003
M.S., Electrical Engineering, Xi'an Jiaotong University, 2006
Ph.D., Engineering, University of New Mexico, 2016

ABSTRACT

Numerous solar, space, and astrophysical observations of jet- and bubble-like plasma structures exhibit morphological similarities, suggesting that there may be common plasma physics at work in the formation and evolution processes of these structures at different system scales. The ideal magnetohydrodynamics (MHD) provide the necessary theoretical basis for employing laboratory experiments to investigate key physical processes in nonlinear astrophysical and solar systems, especially when magnetic fields are present.

A coaxial magnetized plasma gun has been designed, installed, tested and operated in the HelCat linear device at the University of New Mexico. The combination of various plasma structures generated by the coaxial gun and diverse main chamber conditions provides a wide range of controllable experimental conditions to simulate the underlying physic processes of different astronomical systems.

In Region I, a current-driven plasma jet is formed. The plasma column experiences the current-driven kink instability consistent with the Kruskal-Shafranov criterion. When a

perpendicular background magnetic field is applied, the jet column length increases with a longer life-time, and appears to show greater stability. Evidence suggests that magnetic tension, caused by the curvature of background magnetic field, leads to an axial sheared flow, which contribute to the stabilization. The calculated results are accordant with the stabilization criterion $\frac{d_{v_z}}{dr} > 0.1 k V_A$- reported by other research groups for similar magnetic geometrics.

In Region II, spheromak-like plasma formation is verified. Taylor relaxation process occurs simultaneously, converting toroidal flux into poloidal flux. At the same time, the spatial and temporal profiles of λ evolve. When the spheromak plasma propagates into the background magnetic field, the typical self-closed magnetic configuration does not hold any more. At the upper-side, the Rayleigh -Taylor instability has been observed. The theoretical analysis is present and the instability growth rate has been calculated.

Details of the experiment setup, diagnostics, experimental results and theoretical analysis for region I and II are discussed in this thesis work.

Contents

viii

ix

List of Figures

xviii

List of Tables

Chapter 1 Background and Introduction

Plasma is the fourth state of matter containing freely moving ions, electrons and possibly neutral atoms. These ions and electrons collide with other charged particles via coulomb interactions. Furthermore, the charged particles' movement creates an electrical current which induces a magnetic field. The coupling of electrical current and magnetic field exerts a Lorentz force on the plasma, leading to complex behavior of the plasma.

Plasma makes up 99% of all visible matter.[1] Plasma physics determines the dynamics of many astrophysical systems including stars, relativistic jets, interstellar media and solar physics phenomena, including solar coronal mass ejections, the solar wind, and solar flares. As a result, studying plasma physics is important to understand the fundamental behavior of the universe.

The three main characteristic parameters for a plasma are: 1) plasma density, n, measured in particles per cubic meter (m^{-3}); 2) magnetic flux density, B (for convenience this will herein be referred to as simply the magnetic field), measured in Telsa (T) or Gauss (G); 3) temperature, T, measured in electron-Volts (eV) with 1 eV = 11604.53 kelvin (K). The plasma generated in the **P**lasma **B**ubble **E**xpansion e**X**periment (PBEX) at the University of New Mexico (UNM) has a density of ~10^{20} m^{-3}. For comparison, the solar corona has a density of ~10^{15} m^{-3}, and the interstellar medium has a density of ~10^7 m^{-3}. The magnetic field of PBEX is ~ 500 – 2000 G. For reference, radio-faint galaxies like M31 and M33 have weak fields about 5 μG, while gas-rich galaxies with high star-formation rates, like M51 and M83, have 15 μG on average.[2] In the astrophysics, the strongest large-scale fields (50-100 μG) were found in starburst galaxies, such as M82, and in nuclear starburst regions, as in the center of NGC1097.[3] The temperature of the PBEX plasma is around 10 eV. Although it is hotter than

other similar experimental plasmas,[4, 5] it is still a modest plasma temperature, considering many space plasmas being $\sim 10 - 100$ eV. Figure 1.1 shows the scale range of various plasmas at different temperatures and densities.
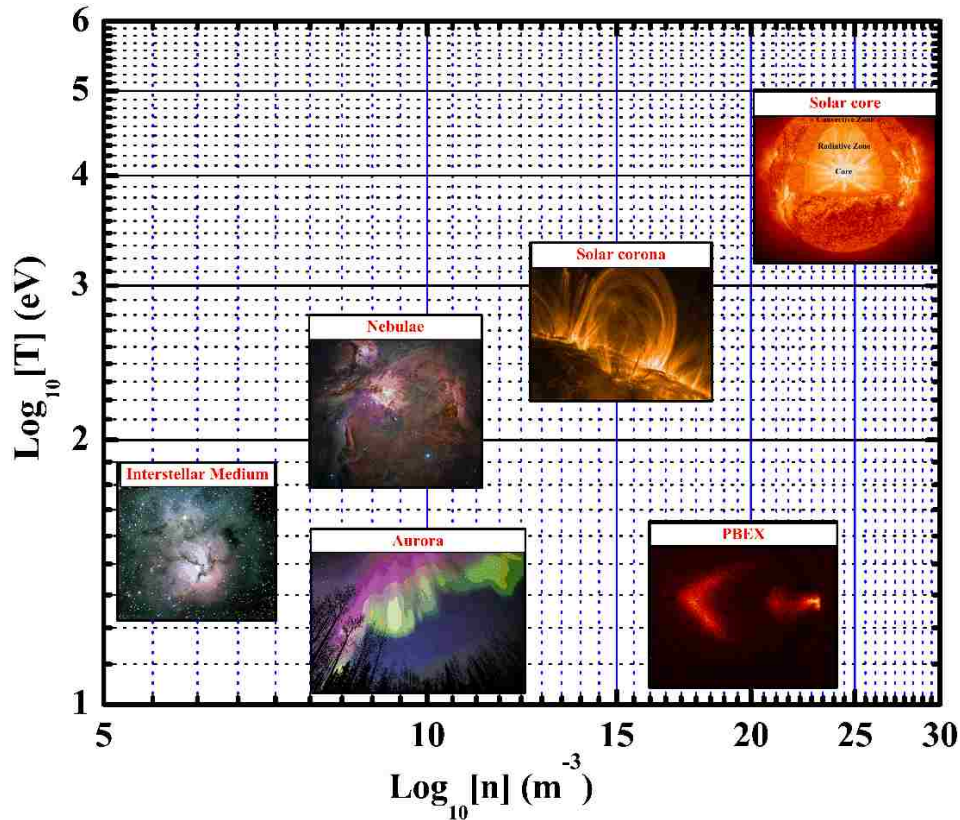
Figure 1.1. Multiple plasma sources in density-temperature space. Photo credits: Interstellar medium: https://imaginecosmos.com/galaxies/interstellar-medium/; Aurora: Image courtesy of Sebastian Saarloos; Nebulae: NASA/ESA/J.Hester; Solar corona: NASA-SOHO; Solar Core: SOHO (ESA&NASA).

1.1 Magnetohydrodynamic (MHD) theory

As discussed above, the charged particles in a plasma interact via electric and magnetic fields. As a result, the equations to describe plasma dynamics are very complicated. The three main theories, listed here from complex to simple, are as follows: the Vlasov theory which tracks a species' velocity distribution function in the space-velocity phase space subject to the charged particles' motion, possible collisions, and Lorentz force.[6] The two-fluid theory takes

moments of the distribution function in the Vlasov equations, separates ion and electron motion as two individual flows, and analyses these independent dynamic behaviors and interactions. MHD theory simplifies the two-fluid theory even further and treats the plasma as a single conductive fluid. Despite its simplicity, the magnetic flux "frozen-in" property, and the system dimension independence property (to be described shortly) make it a powerful, and valuable, tool to interpret many plasma phenomena. MHD theory will be the primary theory used for analysis in the following chapters. These MHD properties will discuss in detail in this section.

MHD theory combines elements of the Navier-Stokes equations which describe fluid dynamics, and Maxwell's equations which describe electromagnetism. The Eulerian form of the MHD equations in SI units are:

Continuity equation $\quad \frac{\partial \rho}{\partial t} + \nabla \cdot (\rho \vec{v}) = 0$ (1.1)

Equation of motion $\quad \rho \frac{d\vec{v}}{dt} = \rho \left(\frac{\partial \vec{v}}{\partial t} + \vec{v} \cdot \nabla \vec{v} \right) = \vec{J} \times \vec{B} - \nabla \overleftrightarrow{P}$ (1.2)

Ohm's law $\quad \vec{E} + \vec{v} \times \vec{B} = \eta \vec{J}$ (1.3)

Faraday's law $\quad \nabla \times \vec{E} = -\frac{\partial \vec{B}}{\partial t}$ (1.4)

Ampere's law $\quad \nabla \times \vec{B} = \mu_0 \vec{J}$ (1.5)

Energy equation $\quad \frac{P}{\rho^\gamma} = constant$ (1.6)

where ρ is the plasma mass density, $\vec{v}$ is the velocity vector (velocity of the center of mass of ions and electrons). $\overleftrightarrow{P}$ is the plasma pressure tensor. Typically, MHD theory reduces the tensor and uses only the scalar pressure P. $\vec{E}, \vec{B}$, and $\vec{J}$ are the electric field, the magnetic field, and the current density vectors, respectively. η is the plasma resistivity, and γ is the adiabatic index,

3

which is also called the heat capacity ratio and depends on gas species and the heating procession type. For a sufficiently collisional and fully stripped plasma, $\gamma = 5/3$.

The continuity equation, equation of motion, and energy equation described in MHD theory are very similar to those for neutral fluid hydrodynamics except that the equation of motion contains the Lorentz force term ($\vec{J} \times \vec{B}$). Ampere's law is in the same expression as in the Maxwell's equation for the non-relativistic case. A note that needs to be addressed is that although relativistic MHD equations are widely used for various astrophysical cases, such as an active galactic nucleus (AGN),[7] the non-relativistic MHD equations are employed here to analysis the plasma dynamics for PBEX at UNM since the plasma propagation velocity is much less than the speed of light.

Several criteria must be satisfied for a plasma to be well described using the MHD equations. Firstly, the plasma phenomenon needs to be non-relativistic (velocities are much less than the speed of light) as discussed above. Secondly, the characteristic lengths of the plasma dynamics are much longer than the Debye length $\lambda_D = \sqrt{\frac{\epsilon_0 K_B T}{n q^2}}$ (the distance over which a plasma acts as a charged particle), where n is the plasma particle number density, ϵ_0 is the vacuum permittivity, K_B is the Boltzmann constant, T is the plasma temperature and q is the particle charge. Thirdly, the characteristic time scale of the plasma dynamics is much longer than the ion and electron cyclotron periods $t_{e(i)} = \frac{2\pi m_{e(i)}}{eB}$ (the time it takes a charged particle to complete an orbit in a magnetic field). In another word, the motions of ions and electrons are well coupled, which leads to the result that the Hall term of the electron motion equation can be ignored for the given MHD Ohm's law. Lastly, plasma dynamics are much

slower than the particle collision rate which means the particle distribution is Maxwellian and the plasma can be treated as a single fluid.

1.1.1 Lorentz force: magnetic tension, magnetic pressure, and force-free state

Substituting Ampere's law (Eq. 1.5) into the Lorentz force, one easily obtains

$$\vec{J} \times \vec{B} = \frac{1}{\mu_0} \left(\nabla \times \vec{B}\right) \times \vec{B} = \frac{1}{\mu_0} \vec{B} \cdot \nabla \vec{B} - \nabla\left(\frac{B^2}{2\mu_0}\right) \tag{1.7}$$

Reforming $\vec{B} = B\widehat{B}$ where $\widehat{B}$ is a unit vector in the direction of $\vec{B}$, then $\nabla \vec{B}$ can be expressed as $\nabla \vec{B} = \nabla(B\widehat{B}) = (\nabla B)\widehat{B} + B(\nabla\widehat{B})$. Combining this $\nabla \vec{B}$ expression with the vector calculus identity $\nabla(\vec{A} \cdot \vec{D}) = (\vec{A} \cdot \nabla)\vec{D} + (\vec{D} \cdot \nabla)\vec{A} + \vec{A} \times (\nabla \times \vec{D}) + \vec{D} \times (\nabla \times \vec{A})$ to Eq. 1.7, it gets

$$\vec{J} \times \vec{B} = \frac{1}{\mu_0} \vec{B} \cdot \nabla \vec{B} - \nabla\left(\frac{B^2}{2\mu_0}\right) = -\nabla\left(\frac{B^2}{2\mu_0}\right) + \frac{B^2}{\mu_0} \widehat{B} \cdot \nabla\widehat{B} \tag{1.8}$$

The first term corresponds to the magnetic pressure, with $P_B = \frac{B^2}{2\mu_0}$. An important parameter of a plasma is the plasma beta, defined as the ratio of plasma thermal pressure to the magnetic pressure:

$$\beta = \frac{P}{P_B} = \frac{P}{B^2/2\mu_0} \tag{1.9}$$

The second term $\frac{B^2}{\mu_0} \widehat{B} \cdot \nabla\widehat{B}$ can be further decomposed into two terms:

$$\frac{B^2}{\mu_0} \widehat{B} \cdot \nabla\widehat{B} = \widehat{B}\widehat{B} \cdot \nabla\left(\frac{B^2}{2\mu_0}\right) - \frac{B^2}{\mu_0} \frac{\widehat{R}}{R_c} \tag{1.10}$$

where $\widehat{\boldsymbol{R}}$ is the unit vector pointing from the center of curvature to the magnetic field line and $\boldsymbol{R}_c$ is the radius of curvature of the field line. Figure 1.2 shows the configuration for any location on a curved magnetic field.
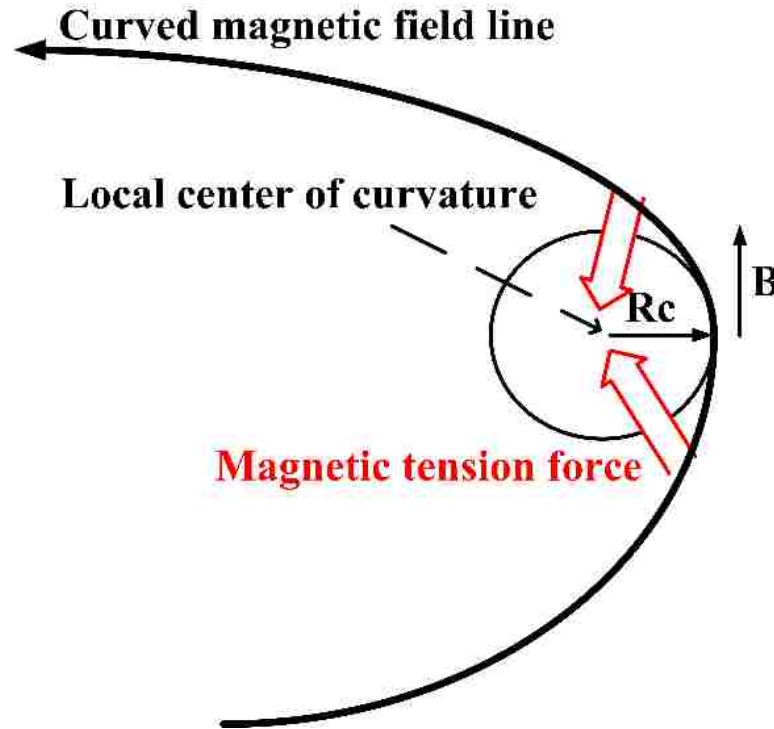
Figure 1.2. A local cylindrical coordinate system along with a curved magnetic field at any location with the magnetic tension force indicated. $\widehat{\boldsymbol{B}} = \widehat{\Phi}$.

The first term of Eq. 1.10 cancels out the magnetic pressure gradient term in Eq. 1.8 in the direction along the magnetic field lines. This implies that the magnetic pressure force is not isotropic and only the perpendicular components, $\nabla_{\perp}\left(\frac{B^2}{2\mu_0}\right)$, exert force on the plasma. The second term in Eq. 1.10 corresponds to the magnetic tension force which is directed towards the center of the field lines' curvature as indicated in Figure 1.2. Thus, the tension force acts to straighten out the field lines and push the plasma in the direction that will reduce the length of the field lines.

So the total magnetic force from Eq. 1.7 can be rewritten as:

$$\vec{J} \times \vec{B} = -\nabla_\perp \left(\frac{B^2}{2\mu_0} \right) - \frac{B^2}{\mu_0} \frac{\hat{R}}{R_c} \tag{1.11}$$

where the first term is the magnetic pressure in the direction perpendicular to the magnetic field, and the second term is the tension term which acts to straighten out the magnetic field curvature. These two terms are not necessarily perpendicular to each other.

A force-free state is a special plasma state where there is no net $\vec{J} \times \vec{B}$ force acting on the plasma. For this condition to be true, $\vec{J} \times \vec{B}$ needs to be zero. Combining this with Ampere's law (Eq. 1.5), it gives the force-free plasma equation:

$$\nabla \times \vec{B} = \alpha \vec{B} \tag{1.12}$$

where α is a spatially-depend scaler. An important note here is that Eq. 1.12 indicates that a force-free plasma state must have a three-dimensional (3D) configuration. The curl of a two-dimensional $\vec{B}$ produces perpendicular components which will be invalid for $\vec{J} \times \vec{B} = 0$. Details of the force-free state are discussed in Section 1.3.

1.1.2 Ideal MHD theory

Assuming thermal equilibrium, Fokker-Planck theory shows that for a fully ionized plasma, the resistivity is:[8]

$$\eta \ (\Omega \cdot m) = \frac{Z e^2 m_e^{1/2} \ln \Lambda}{3\pi^{3/2} \epsilon_0^2 (2k_B T_e)^{3/2}} \tag{1.13}$$

where Z is the ion charge state, m_e is the electron mass, ϵ_0 is the vacuum electrical permittivity, $\ln \Lambda$ is the Coulomb logarithm (usually assumed $\ln \Lambda \sim 10$), k_B is the Boltzmann constant, T_e is the plasma temperature in eV, and e is the electron charge.

This resistivity calculated from Eq. 1.13 is called Spitzer resistivity.[6] Note that the resistivity is independent of plasma density, but is $\propto T^{-3/2}$, which means that higher temperature plasmas have lower resistivity.

A useful practical form for the plasma resistivity calculation is:[9]

$$\eta\ (\Omega \cdot m) = 5.15{\times}10^{-5}\,\frac{Z\ln\Lambda}{\mathrm{T}_e^{3/2}} \tag{1.14}$$

For comparison, the resistivity of copper is $1.72 \times 10^{-8}\ \Omega \cdot m$, for aluminum, it is $2.65 \times 10^{-8}\ \Omega \cdot m$ and stainless steel is about $140 \times 10^{-8}\ \Omega \cdot m$.[10] For PBEX, the plasma has a temperature of 10 eV and a resistivity of $163{\times} 10^{-8}\ \Omega \cdot m$, which is fractionally more resistive than stainless steel.

Following the discussion above and taking $\eta = 0$ in Ohm's law (Eq.1.3), the MHD theory can be simplified to the ideal MHD theory where the plasma is treated as having zero resistivity. Then the ideal MHD Ohm's law can be written as:

$$\vec{E} + \vec{v}{\times}\vec{B} = 0 \tag{1.15}$$

1.1.2.1 Magnetic flux frozen-in condition

One of the most important characteristic properties of the ideal MHD theory is that the magnetic flux is "frozen" into the plasma's moving frame. This means that for the ideal MHD case, the moving plasma tends to drag the magnetic field lines along with it.

To see this, by substituting Ampere's law (Eq.1.5) and the ideal MHD Ohm's law (Eq. 1.15) into Faraday's law (Eq. 1.4), the ideal MHD induction equation can be derived as:

$$\frac{\partial \vec{B}}{\partial t} = \nabla{\times}\left(\vec{v}{\times}\vec{B}\right) \tag{1.16}$$

Consider a surface $\vec{S}(t)$ moving together with the plasma. The total magnetic flux through it is:

$$\psi(t) = \int_{\vec{S}(t)} \vec{B}(\vec{x},t) \cdot d_{\vec{S}} \tag{1.17}$$

where $d_{\vec{S}}$ is the elementary surface area vector perpendicular to the surface. The changing rate of the magnetic flux is:

$$\frac{d\psi(t)}{dt} = \lim_{\delta t \to 0} \left(\frac{\int_{\vec{S}(t+\delta t)} \vec{B}(\vec{x},t+\delta t) \cdot d_{\vec{S}} - \int_{\vec{S}(t)} \vec{B}(\vec{x},t) \cdot d_{\vec{S}}}{\delta t} \right)$$

$$= \lim_{\delta t \to 0} \left(\frac{\int_{\vec{S}(t+\delta t)} \left(\vec{B}(\vec{x},t) + \delta t \frac{\partial \vec{B}(\vec{x},t)}{\partial t} \right) \cdot d_{\vec{S}} - \int_{\vec{S}(t)} \vec{B}(\vec{x},t) \cdot d_{\vec{S}}}{\delta t} \right)$$

$$= \lim_{\delta t \to 0} \left(\frac{\int_{\vec{S}(t+\delta t)} \vec{B}(\vec{x},t) \cdot d_{\vec{S}} - \int_{\vec{S}(t)} \vec{B}(\vec{x},t) \cdot d_{\vec{S}}}{\delta t} \right) + \int_{\vec{S}(t)} \frac{\partial \vec{B}(\vec{x},t)}{\partial t} \cdot d_{\vec{S}} \tag{1.18}$$

Eq.1.18 indicates that the total change of magnetic flux can be decomposed into: 1) the integration of the surface area changing with the plasma movement (the first term), and 2) the magnetic field changing in time (the second term). Details are given in Kulsrud [11] that the first term can be written as:

$$\lim_{\delta t \to 0} \left(\frac{\int_{\vec{S}(t+\delta t)} \vec{B}(\vec{x},t) \cdot d_{\vec{S}} - \int_{\vec{S}(t)} \vec{B}(\vec{x},t) \cdot d_{\vec{S}}}{\delta t} \right) = -\int_{\vec{S}} \nabla \times \left(\vec{v} \times \vec{B} \right) \cdot d_{\vec{S}} \tag{1.19}$$

Substituting the equation Eq.1.17 and Eq. 1.19 back into Eq. 1.18, will produce:

$$\frac{d\psi(t)}{dt} = \int_{\vec{S}} \left(\frac{\partial \vec{B}(\vec{x},t)}{\partial t} - \nabla \times \left(\vec{v} \times \vec{B} \right) \right) \cdot d_{\vec{S}} = 0 \tag{1.20}$$

Therefore, the magnetic flux is constant in the frame of the plasma and the magnetic field lines are "frozen-in" the plasma. This property is employed to analyze spheromaks' toroidal and poloidal magnetic flux convection shown in detail in Chapter 3.

1.1.2.2 Ideal MHD scaling independence

Another important property of ideal MHD theory is that the MHD equations can be reduced to a dimensionless form to simplify and recover the physical systems' characteristic properties. Although the MHD equations (Eq. 1.1-Eq. 1.6) are all written with dimensional variables, they can be dimensionless based on the chosen units of length, mass, and time.

First, one can define three nominal quantities: the system length, l_0, for length scale, the plasma density, ρ_0, for mass scale, and the magnetic field, B_0, at some representative position. Then Alfvén speed ($v_A = \frac{B_0}{\sqrt{\mu_0 \rho_0}}$) and the pressure term ($P_0 = \frac{B_0^2}{\mu_0} = \rho_0 v_A^2$) can be determined. Finally, t_0, for time scale, is written as $t_0 \equiv \frac{l_0}{v_A}$.[12]

After normalizing to these nominal quantities, the reduced MHD equations are:[13]

$$\frac{\partial \tilde{\rho}}{\partial \tilde{t}} + \widetilde{\nabla} \cdot \left(\tilde{\rho} \widetilde{\boldsymbol{v}} \right) = 0 \tag{1.21}$$

$$\tilde{\rho} \left(\frac{\partial \widetilde{\boldsymbol{v}}}{\partial \tilde{t}} + \widetilde{\boldsymbol{v}} \cdot \widetilde{\nabla} \widetilde{\boldsymbol{v}} \right) = \left(\widetilde{\nabla} \times \widetilde{\boldsymbol{B}} \right) \times \widetilde{\boldsymbol{B}} - \widetilde{\nabla} \widetilde{P} \tag{1.22}$$

$$\frac{\partial \widetilde{\boldsymbol{B}}}{\partial \tilde{t}} = \widetilde{\nabla} \times \left(\widetilde{\boldsymbol{v}} \times \widetilde{\boldsymbol{B}} \right) + \frac{1}{S} \widetilde{\nabla}^2 \widetilde{\boldsymbol{B}} \tag{1.23}$$

where the tilde ($\sim$) indicates the normalized physical quantities or operations, and S is the Lundquist number, defined as $S \equiv \frac{v_A l_0}{\eta}$, where v_A is the Alfvén speed, l_0 is the system length, and η is the plasma resistivity. High Lundquist numbers indicate highly conducting plasmas, while low Lundquist numbers indicate more resistive plasmas. Laboratory plasma experiments typically have Lundquist numbers between $10^2 - 10^8$, while for most astrophysical and space plasma, the Lundquist number can be greater than 10^{20}.[14] The physical meaning for such large

Lundquist numbers is that the magnetic diffusion is negligible compared to the magnetic convection during plasma evolution. As a result, the last term of Eq. 1.23 can be dropped. Therefore Eq. 1.21 – Eq. 1.23 reduce to a set of ideal MHD equations which still depend on the normalized parameters but may be easily scaled to larger or smaller systems.

This dimension independence property of ideal MHD strongly suggests that a small scale plasma system, like laboratory plasma, may be a useful tool to study the dynamics of large scale plasma, i.e. astrophysical plasma, as long as the ideal MHD requirements are meet. A detailed example will be discussed in Section 1.3.

1.2 Magnetic helicity, Taylor relaxation and applications

As discussed in Section 1.1.1, a force-free configuration is a plasma state that satisfies $\vec{J} \times \vec{B} = 0$ which means $\vec{J}$ and $\vec{B}$ are parallel to each other. Eq. 1.12 can also be expressed as $\vec{J} = \alpha \vec{B}$ for a scale-depend α. A system's total magnetic energy W is defined as the integral of the magnetic energy density over the system volume V:

$$W = \int \frac{B^2}{2\mu_0} dV \tag{1.24}$$

Magnetic energy is conserved in an ideal force-free plasma system. This property is also used to analyze PBEX plasma performance.

1.2.1 Magnetic helicity and Taylor relaxation

Magnetic helicity, κ, is an important concept of an MHD plasma and is defined as:

$$\kappa = \int \vec{A} \cdot \vec{B} \, d_V \tag{1.22}$$

where $\vec{A}$ is the vector potential, $\vec{B}$ is the associated magnetic field defined as $\vec{B} = \nabla \times \vec{A}$, and the entire plasma volume V is the integration space.

Magnetic helicity, κ, is a topological measurement of number of linkages of magnetic flux tubes with each other and number of twists of magnetic field. It turns out to be a conserved quantity in ideal MHD theory as long as no magnetic field perpendicular to the surface, S, enclosing the volume, V.[15] It remains unchanged during any continuous deformation process of the system even though the geometry has been changed.

Taylor relaxation is a process where a plasma configuration self-organizes and decays into a minimum magnetic energy state ($W \rightarrow W_{min}$) while conserving the magnetic helicity. This is perhaps easy to predict, considering the "frozen-in" property, magnetic field lines must be converted along with the plasma movement; as a result, the topological relations between these lines must be preserved throughout the plasma evolution.

This consequent minimum energy state is the Taylor state which satisfies:[16]

$$\nabla \times \vec{B} = \lambda \vec{B} \tag{1.23}$$

where λ is a spatial constant.[17]

Comparing Eq. 1.12 and Eq. 1.23, it is seen that the Taylor state is a special state because not only is it a force-free state, but it is also the lowest energy state. λ is determined by system specific parameters. For a given system, the final Taylor state is governed by the system's magnetic energy, magnetic helicity, and boundary conditions.

1.2.2 Spheromaks

A spheromak is a toroidally shaped plasma whose configuration is similar to a cylindrically symmetric smoke ring, or a donut shape.[18] A spheromak arranges its internal current and associated magnetic field to satisfy Eq. 1.23, reaching the Taylor state which is force free and has the lowest energy. Taking advantage of the geometrical symmetry, it is

convenient in the practical analysis to decompose the global magnetic field into two components: a toroidal magnetic field (which is in the φ direction of a cylindrical coordinate) and a poloidal magnetic field which combines the r and z directions in a cylindrical coordinate.

1.2.3 Astrophysical jets and radio lobes as Taylor relaxed states

Jets, and their corresponding outflow, have been observed over a wide range of astrophysical systems spanning various length scales. For some young stellar objects (YSO), the length is usually less than a light year.[19, 20] On the other hand, in active galactic nuclei (AGN), jets span millions of light years in length as estimated from observations.[21]

Although the mechanisms that power, launch, and collimate the jet structures are still under debate, as well as the detailed magnetic geometry and interaction with the surrounding media, there is general agreement that astrophysical jets share some elements in common: a massive central body, an associated material disk surrounding it, and a nominally poloidal magnetic field.[22]

Various physical models ranging from MHD to pure hydrodynamics[23] have been employed to explain the jet formation. In the region far away from the source, the pure hydrodynamic theories may work well where the distance-decreased magnetic field is negligible in this region. But for the near-source region, most of the modern theories propose that the magnetic field plays an important role in the mechanism for jet formation and propagation.[24, 25] Furthermore several theories have proposed that jets are in the force-free state and the relaxation process may be responsible for the jet formation.[26, 27]

In active galaxies, minimum energy estimates based on the observed radio emission suggest that 10%, or more, of the total gravitational energy released by the collapse of a supermassive black hole is deposited into lobe-scale magnetic fields and relativistic particles.

The underlying physical process inside the lobe is proposed as a magnetic self-organization by driven relaxation.[28] Comparisons between the radio lobes and laboratory spheromak have been made to show some physical features in common.[29, 30]

1.3 Rayleigh-Taylor (RT) instability

The Rayleigh-Taylor (RT) instability is a well-known hydrodynamic instability, occurring at the interface between two fluids of different densities when the heavier fluid is pushing the lighter fluid.[31] A simple graph illustration of the Rayleigh-Taylor instability is given in Figure 1.3.
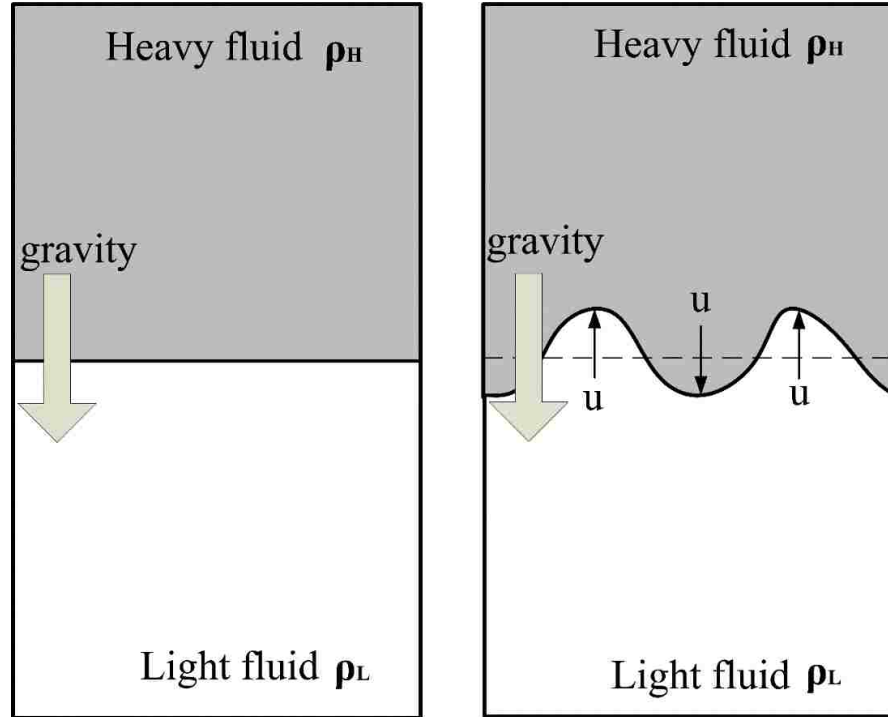
Figure 1.3. Sketch of RT instability.

The RT instability growth of a perturbation at the interface is exponential, and takes place at the rate $\exp(\gamma t)$ in which

$$\gamma \equiv \sqrt{Agk} \qquad (1.24)$$

where γ is the temporal growth rate, g is the acceleration, k is the spatial wavenumber of the perturbation on the interface, and A is the Atwood number, defined as $A \equiv \frac{\rho_H - \rho_L}{\rho_H + \rho_L}$ in which ρ_H is the density of heavier fluid and ρ_L is the density of lighter fluid.

From Eq. 1.24, it is easy to predict that the RT instability prefers small scale perturbations since the larger k gives faster growth rate as shown in Figure 1.3. Later in time, the RT instability develops to the well-known bubble and finger-like structures which further experience Kevin-Helmholtz (KH) instability.[31]

1.3.1 RT instability in a magnetized plasma

The RT instability in a magnetized plasma was first investigated by Kruskal and Schwarzschild in 1954.[32] At the interface between the plasma (the heavy fluid) and vacuum (the light fluid). In other word, the light fluid can be considered to be the vacuum magnetic field with the Atwood number set to 1.[33, 34] MHD theory shows that the growth rate of the two-dimensional (2D) magnetic Rayleigh-Taylor instability is[35, 36]

$$\gamma^2 = a\vec{k} - \frac{(\vec{k} \cdot \vec{B})^2}{\mu_0 \rho_{plasma}} \qquad (1.25)$$

where γ is the temporal growth rate, a is the acceleration, $\vec{B}$ is the unperturbed magnetic field vector, $\vec{k}$ is the perturbation wave-vector, and ρ_{plasma} is the plasma density.

Mathematical analysis of Eq. 1.25 shows that the term of $\vec{k} \cdot \vec{B}$ actually acts to reduce the growth rate. This means that for the case when $\vec{k}$ is not perpendicular to $\vec{B}$, the magnetic field tension force has a stabilizing effect. Furthermore, along the magnetic field ($\vec{k} \parallel \vec{B}$), any perturbations with $k > \mu_0 \rho_{plasma} a / B^2$ are completely suppressed which is consistent with

the magnetic field tension discussion in Section 1.1.1. On the other hand, for a perturbation with $\vec{k} \perp \vec{B}$, the RT instability has the fastest growth rate since $\vec{k} \cdot \vec{B} = 0$, and the magnetic RT instability is reduced to the hydrodynamic case. From a physical perspective, this RT instability property can be understood in this way: the fastest instability mode is the mode that does not deform the magnetic field, but keeps the original magnetic field geometry. This property ($\vec{k} \cdot \vec{B} = 0$) will be employed in Chapter 4 to interpret experimental data of PBEX project.

1.3.2 RT instability in astrophysical observations
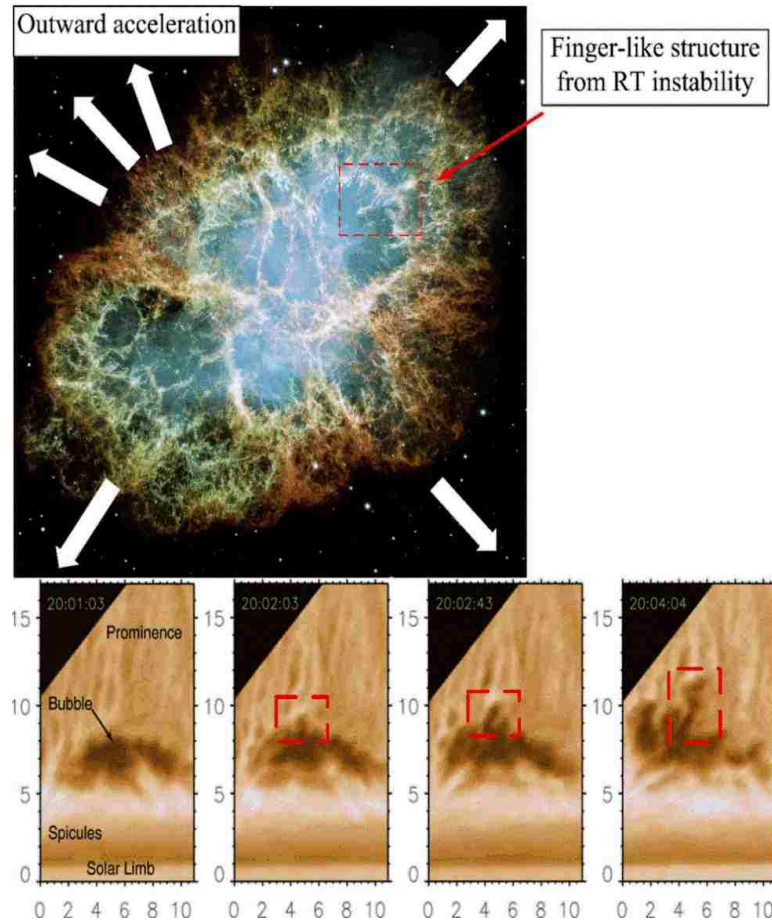
Figure 1.4. Top: The Crab Nebula shows the finger-like structures from RT instabilities as the material expands outwards. Images credit: NASA, ESA, J.Hester and A. Loll. Bottom: Observations showing the formation and temporal evolution of dark plumes in a quiescent prominence observed on 2007 August 8 20:01 UT observed in the Hα line. The axes are labeled in megameters. Images is taken from [37].

RT instability structure is observed in the Crab Nebula shown in Figure 1.4 Top. The expanding pulsar wind nebula powered by the Crab pulsar is sweeping up ejected material from the supernova explosion.[38] The RT instability has also recently been discovered in the solar corona, when a relatively dense solar prominence overlies a less dense plasma bubble,[39] as shown in Figure 1.4, Bottom. This latter case is a clear example of the MRT instability.[35, 37]

1.4 Laboratory astrophysics

Most astrophysical objects are usually remote and often static. It is difficult to make direct measurements from long range observations. The dimensionless nature of ideal MHD discussed in Section 1.1 suggests that the plasma dynamics on an astrophysics scale can be studied with laboratory experiments if the dynamical scaling constraints are properly applied.

1.4.1 Scaling constraints

To see how closely the dimensionless parameters of the PBEX scale to those of a much larger scale astrophysical system, a comparison is made between young stellar objects (YSO) jets and those jets launched in PBEX:[40]

$$l_a = c_1 l_p \quad \rho_a = c_2 \rho_p \quad P_a = c_3 P_p \tag{1.26}$$

$$\vec{B}_a = \sqrt{c_3}\,\vec{B}_p \quad \vec{v}_a = \sqrt{\frac{c_3}{c_2}}\,\vec{v}_p \quad t_a = c_1\sqrt{\frac{c_2}{c_3}}\,t_p \tag{1.27}$$

The plasma parameters of the YSO jets[41] and PBEX argon plasma are listed in Table 1.1. Employing Eq.1.26, it gives the following scaling constraints: $c_1 = \frac{l_{YSO}}{l_{PBEX}} = 6.67 \times 10^{15}$, $c_2 = \frac{\rho_{YSO}}{\rho_{PBEX}} = 3.02 \times 10^{-12}$, and $c_3 = \frac{P_{YSO}}{P_{PBEX}} = 6.25 \times 10^{-12}$.

The actual ratio of the YSO and PBEX magnetic field is $\frac{\vec{B}_{YSO}}{\vec{B}_{PBEX}} = 2.5\times10^{-6}$, equal to the requirement $\sqrt{c_3} = 2.5\times10^{-6}$ in Eq.1.27, and the actual ratio of velocity is $\frac{\vec{V}_{YSO}}{\vec{V}_{PBEX}} = 8.57$, which is in the same order of the required $\sqrt{\frac{c_3}{c_2}} = 1.44$. These scaling constrains are satisfied very well, indicating that astrophysical jet dynamics and laboratory jet evolution may have very similar morphology, kinetic behaviors, and magnetic structure since they follow the same equations and have similar scaling parameters.

Table 1.1. Plasma system parameters for YSO jet and PBEX jet.

Parameter	PBEX jet	YSO jet
l (m)	0.15	10^{15}
V (km/s)	35	300
T (eV)	10	0.7
ρ (kg/m³)	6.63×10^{-6}	2×10^{-17}
P (Pa)	1.6×10^{4}	10^{-9}
B (T)	0.2	5×10^{-7}

Substituting the calculated values of c_1, c_2, and c_3 into the third scaling relation in Eq.1.27, one gains $\frac{t_{YSO}}{t_{PBEX}} = c_1\sqrt{\frac{c_2}{c_3}} = 4.6\times10^{15}$ which indicates that plasma dynamics that occurs over the period of 10 μs in the laboratory plasma jet correspond to thousands of years of the YSO system evolution.

This analysis strongly supports that laboratory experiments could reproduce astrophysical processes during some segment of their time-evolution. Unlike astrophysical observations, the physical conditions of the laboratory can be measured and controlled with much greater confidence and more accurate. In addition, laboratory experiments can provide both local measurements of key physical quantities simultaneously at numerous places and global morphologies in comparison with the remote astrophysics observations. Such laboratory experiments add a new dimension to the process of interpreting observational data, relating them to the existing theories, and validating computer codes which are used to interpret and predict astrophysical phenomena.[42]

In 2012, American Astronomical Society (AAS) established a new division. The mission of the Division of Laboratory Astrophysics Division (LAD) is "to advance our understanding of the Universe through the promotion of fundamental theoretical and experimental research into the underlying processes that drive the Cosmos."[43] As a result, laboratory astrophysics have come to an important branch in the astrophysical research.

1.4.2 Plasma gun experiments

During the last 10-20 years, laboratory plasma astrophysics has developed from the state of a few distinct experiments to a broad area of research. Among all the experiments carried out, plasma guns have been employed as a powerful tool to study the physics process by producing dynamical astrophysical phenomena on a laboratory scale. The Caltech plasma gun experiment from Dr. Paul Bellan group,[44] and the Swarthmore College plasma gun experiment (the Swarthmore Spheromak eXperiment SSX) from Dr. Michael Brown group,[45] and the professor Sergey Lebedev's conical wire arrays experiment[46] at Imperial College are the main well-developed research groups for this research field.

For the Caltech Bellan group, a planar magnetized coaxial plasma gun is mounted at one end of a 1.48 m diameter, 1.58 m long cylindrical vacuum chamber.[29, 44, 47] The plasma gun has a 19.1 cm diameter disk-shape cathode and a co-planar annulus-shape anode with an inner diameter of 20.3 cm and an outer diameter of 51 cm. Diagnostic instruments used in Caltech plasma gun experiment include a high-speed visible-light IMACON 200 camera, a 30 – 60 eV band extreme ultra-violet (EUV) optical system,[48] a 12-channel spectroscopic system,[49] and a 20-channel three-dimension (3D) magnetic probe array. The sketch of the facility and the diagnostics system is shown in Figure 1.5.[41]
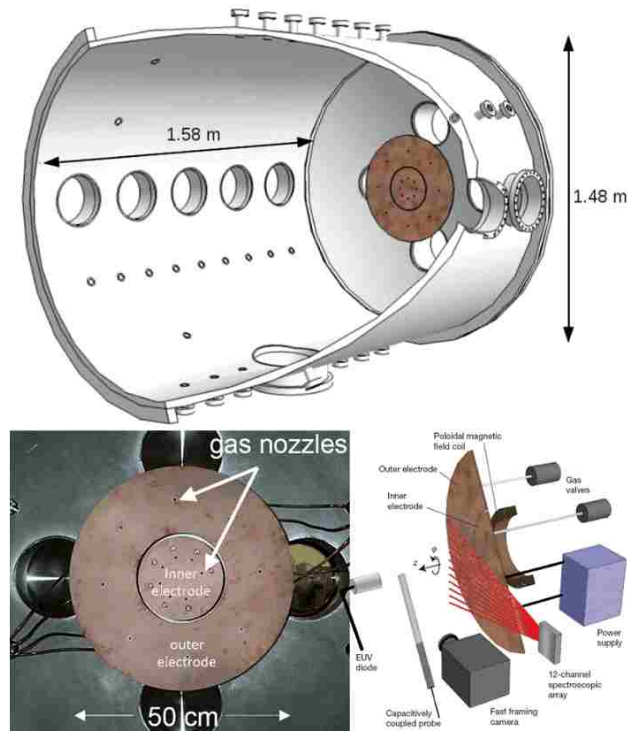
Figure 1.5. An overview of Caltech plasma gun facility and diagnostics systems. Excerpted from [39]

For the Swarthmore Brown group, two plasma guns are employed to launch spheromak plasma in the opposite direction into the flux conserver. Each plasma gun is powered by a capacitor which can store a 10 kV charge and release it with a 100 kA peak current to produce

about gigawatts of power. A pair of ignitrons acts as high-speed, high-voltage switches. A bundle of coaxial cables connects to the electrodes of the plasma gun. The sketch of the experiment setup is shown in Figure 1.6. Diagnostics employed in SSX includes: 3D magnetic probe array, ion Doppler spectrometer, Mach probe, 4-point Langmuir probe, vacuum ultra-violet (VUV) spectrometer, and soft x-ray detector (SXR).[50]
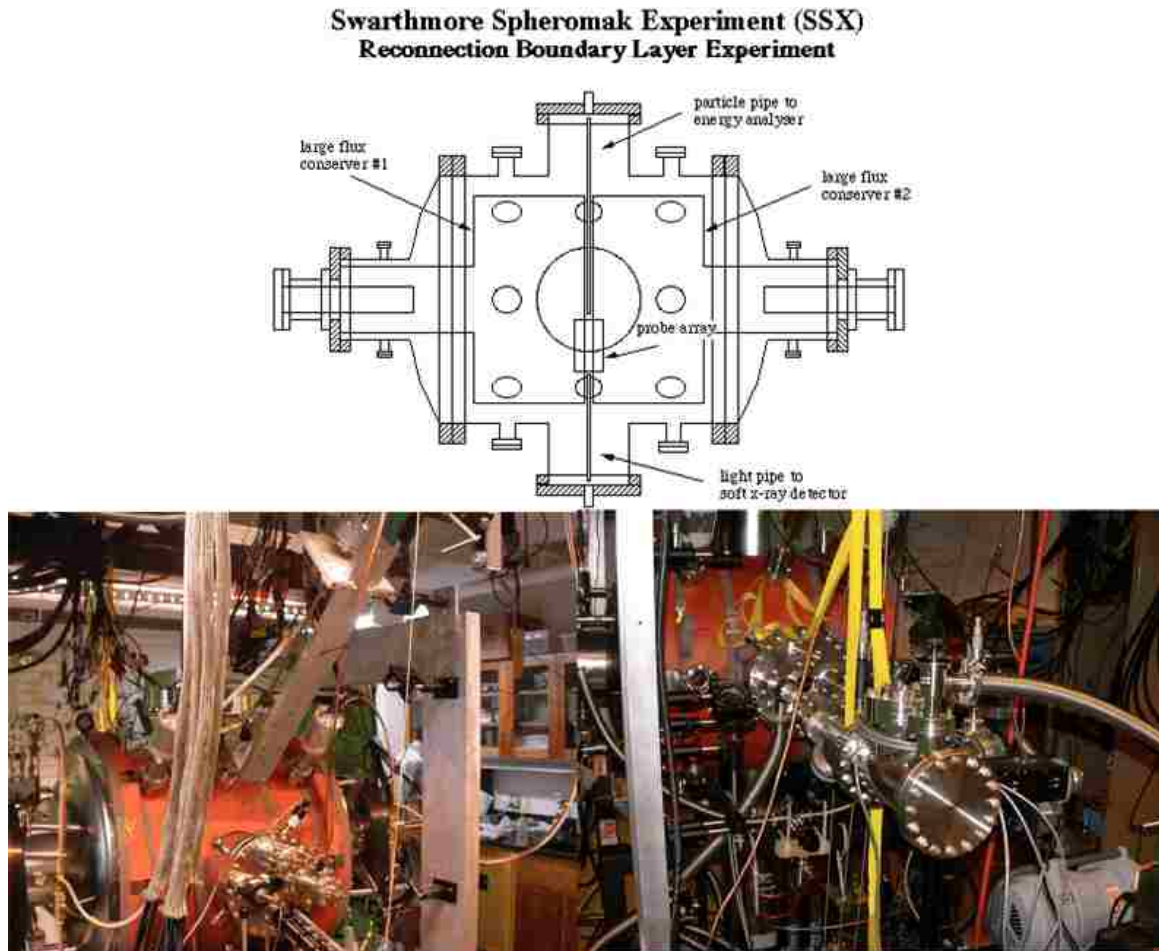
Figure 1.6. An overview of the Swarthmore Spheromak Experiment (SSX) facility. Excerpted from [50].

Multiple research projects have been carried out by these two groups to investigate Taylor relaxation process, various plasma instabilities, magnetic reconnection process, and magnetohydrodynamic turbulence on spheromaks and jets generated by plasma guns.[4, 44, 51]

Table 1.2. Plasma properties for Caltech experiment, PBEX, and SSX.

Parameter	Caltech jet	PBEX jet	SSX
l (m)	0.3	0.15	0.5
V (km/s)	15	35	25
T (eV)	1.5	10	20
n_e (m^{-3})	10^{22}	10^{20}	10^{19}
B (T)	0.20	0.30	0.15

At the University of New Mexico (UNM), a coaxial plasma gun has been installed on the linear plasma device, HelCat (Helicon-Cathode), for the PBEX project.[52] The following chapters will discuss the design, construction, diagnostics, and physical interpretation to the performance of the coaxial plasma gun in detail. While for the PBEX project, the coaxial gun builds upon the analysis techniques from these research groups above, it is both unique in its construction and its operation, launching plasma into a magnetized plasma/magnetic field. Some innovative research work has been done on the PBEX project which is discussed in Chapter 4. The basic parameters of the plasma generated from these three groups are listed in Table 1.2.

1.4.3 Plasma parameters in PBEX

A wide range of plasma parameters have been measured in PBEX using the following diagnostic tools: Langmuir probe, ion Doppler spectrometer, 3D magnetic probe array, electrostatic probe array, fast CCD camera etc. The plasma generated by the coaxial plasma gun of PBEX may be characterized the parameters listed in Table 1.3 and Table 1.4. Note that the ion charge state Z = 1 and the measured average velocity is 3.1 cm/μs.

Table 1.3. Plasma parameter in PBEX jet.

Description	Symbol	Value	Units
Magnetic field strength	B	500	Gauss
Density	n_e	10^{20}	m^{-3}
Temperature	T_e	10	eV
Characteristic length	l	25	cm
Electron gyro-radius	r_e	0.0213	cm
Ion gyro radius (Argon)	r_i	5.76	cm
Debye length	λ_D	2.34×10^{-6}	m
Electron gyro frequency	ω_{ce}	8.79×10^9	rad/sec
Ion gyro frequency	ω_{ci}	1.2×10^5	rad/sec
Electron plasma frequency	ω_{pe}	5.64×10^{11}	rad/sec
Ion plasma frequency	ω_{pi}	2.09×10^9	rad/sec
Electron-electron collision rate	v_{ee}	1.25×10^8	sec^{-1}
Ion-ion collision rate	v_{ii}	1.63×10^5	sec^{-1}
Electron thermal velocity	V_{Te}	132	cm/us
Ion thermal velocity	V_{Ti}	0.49	cm/us
Ion sound velocity	C_s	0.492	cm/us
Plasma skin depth	c/ω_{pe}	0.0531	cm
Ion inertial length	c/ω_{pi}	14.42	cm
Mach Number	M	6.3	
Alfven velocity	V_A	3.075	cm/us

Table 1.4. Plasma parameter in PBEX jet Continued

Description	Symbol	Value	Units
Magnetic Mach Number	M_M	≈ 1	
Beta	β	0.1612	
Magnetic Reynolds	R_M	200	

1.5 Overview of this thesis

In Chapter 1, some brief introduction to plasma physics, MHD theory, Taylor relaxation and Rayleigh-Taylor instability has been presented. A more detailed introduction regarding specific topics will be given in Chapter 3 and Chapter 4. Also in Chapter 1, the property of ideal MHD theory has been discussed to show that the ideal MHD equations can reduce to be a dimensionless form, which make it possible to simulate astrophysical phenomena in a laboratory experimental environment. Furthermore, as an example, the plasma parameters of jets generated in the PBEX project, and YSO jets have been validated using the scaling law. The results indicate that the similar physical process are occurring for both systems even the scale differences are dramatic.

In Chapter 2, a detailed description of the coaxial plasma gun design, construction and parameter validation will be presented. Also multiple diagnostics systems that are designed, calibrated, and tested will be described. Those diagnostic systems to be described include: Langmuir probe, multiple-tip electrostatic probe array, fast CCD camera, B-dot probe array, Pearson coil and high voltage probe. Chapter 2 also works as a well-documented reference for the prospective students of the PBEX project.

In Chapter 3, the key parameter λ, which governs the performance of plasma guns, will be discussed theoretically and calculated under different physical models. Then based on the images obtained from the fast CCD camera, plasma performances will be classified into four distinct regions as shown in Table 1.5. The practical λ value to distinguish these four regions will be determined. For the focus of this dissertation, the emphasis will be on Region I and Region II. For Region III, ion saturation current measurements will show the plasma combination which agrees with the images obtained. The merging plasma phenomena occur due to the underdamped ringing of the discharge current. Current construction of a crowbar circuit aims to eliminate this discharged current ringing and isolate the dynamics to a single ringing. Future work may look to investigate the interesting dynamics at play when these two plasmas reach one another.

Table 1.5. Plasma formation regions

Region	Plasma formation
I	jet formation
II	spheromaks-like formation
III	merging plasma
IV	stuffing plasma

Following the plasma gun performance classification, a detailed physics analysis will be carried out for the Region I case, in which plasma jet has been formed and launched into the vacuum. MHD theory analysis along with a snowplow model shows the arrow-shaped jet front head formation. Then the MHD Bernoulli equation will be discussed to show the relation between the jet propagation velocity and the poloidal current. In addition, the global helical

magnetic field structure will be determined from the magnetic field data, which is consistent with simulation results and theoretical predictions. Furthermore, as shown in the images, the plasma column undergoes the m=1 current-driven kink instability. The Kruskal-Shafranov criterion will be examined from both the magnetic field data and the images.

Chapter 3 will discuss the Region II case. The properties of Spheromaks which are formed and propagated into the main vacuum chamber will be characterized. A poloidal magnetic field vector plot clearly shows a closed poloidal magnetic field which indicates that a spheromak-like plasma has formed successfully with a closed magnetic flux surface. The vector plot will also show a clear X-point, which illustrates the magnetic reconnection process when the spheromak plasma detaches the gun muzzle. Additionally, the poloidal and toroidal magnetic field data from a single shot will be fitted into a Bessel function to show the spheromak formation. Simultaneously during the spheromak formation process, it will be shown that the Taylor relaxation process converts the initial dominant toroidal magnetic flux into poloidal flux with the total flux roughly conserved.

Furthermore, for the spheromak case, the spatial- and time-evolution of λ will be calculated from poloidal current density and toroidal magnetic flux. The calculated λ radial profile will show that λ is peaked near the magnetic axis and decreased monotonically away from the axis. The result of the λ time-evolution calculation, in the center region of the main chamber, shows the peak value is nearly a constant, indicating a force-free Taylor state achieved.

Overall, Chapter 3 will summarize the coaxial plasma gun performance, and characterize the magnetized plasma properties for both jet and spheromak propagating into the vacuum. The analysis results will be shown to be consistent with the results reported by other

research groups which validate the gun operation and performance as designed and theoretically predicted.

In Chapter 4, launching a plasma jet and spheromak into background magnetized plasma, or background magnetic field will be discussed in detail. First, the comparison of the image data and magnetic field data will show that there is no distinct difference between these cases. As a consequence, this chapter's discussion will focus on the case of launching plasma into background magnetic field. Second, for launching plasma jets into a background magnetic field, a more stabilized plasma column with longer jet length will be observed in the image. The kink instability growth rate will be reduced. The background magnetic field, which is perpendicular to the jet propagation direction, will be shown to play an important role to impact the evolution process of the plasma jet. Based on the "frozen-in" property of the ideal MHD theory, the background magnetic fields are dragged by the plasma jet movement. At the same time, the curved background magnetic field exerts a magnetic tension force on the plasma jet. As a result, a radially sheared flow, V_z, is formed. This result will be confirmed from two methods: 1) the snow plow model is modified by adding the magnetic tension force term. The simulation results will indicate axial sheared flow. 2) the radial profile of the jet's axial propagation velocity at different chamber locations will be measured and calculated, which also exhibits an axial shear flow. Similar axial sheared flow has been reported in a Z-pinch experiment.[53] This mechanism as a candidate for jet stabilization will be proposed. By linearizing the MHD equations along with the initial condition, a stability criterion will be found for m=1 kink instability: it can be stabilized by the axial plasma flow with linear shear $\frac{d_{v_z}}{dr} > 0.1 k V_A$, where k is the axial wave number and V_A is the Alfvén velocity. This mechanism is thought to be at work in the PBEX case: an axial sheared flow caused by the

27

tension force may be a candidate for the kink instability growth rate reduction. Finally, launching a spheromak into a background magnetic field will be investigated. The poloidal and toroidal magnetic field vector plots will show that immediately after the plasma leaves the gun port, the spheromak-like self-closed magnetic field configuration does not hold any more. Both poloidal and toroidal magnetic field point in single directions. Furthermore, based on the image data, a magnetic Rayleigh-Taylor (MRT) instability develops perpendicularly to the interface between the lateral side of the plasma leading edge and the background magnetic field. This instability occurs when the background magnetic field is dragged by the plasma movement. The MRT instability growth rate is measured from the images which is consistent with theoretical calculations.

Chapter 2 Coaxial Plasma Gun Experiment in HelCat

2.1 Introduction

A coaxial magnetized plasma gun was designed, installed, tested and operated in the HelCat (Helicon-Cathode) linear plasma device at the University of New Mexico. Currently the coaxial plasma gun is operating routinely for multiple plasma research projects related to astrophysics and solar physics.

The first coaxial plasma gun experiment was performed six decades ago by Alfvén, Lindberg, and Mitild,[54, 55] where interesting features of magnetic helicity and flux amplification were reported.[56] More recent experiments have been carried out to examine plasma gun behavior into a vacuum by a number of research groups.[4, 5, 47, 57] Outside of a limited amount of work, primarily aimed at tokamak refueling by plasma guns, little effort has been made to study the interaction physics of the plasma generated by coaxial guns with other plasma sources. The Plasma Bubble Expansion eXperiment (PBEX) project employs a compact magnetized coaxial plasma gun which generates and injects plasma into a low density, low temperature background plasma provided by HelCat to investigate the interaction physics.[52] The coaxial plasma gun is designed to be as geometrically simple as possible: a copper disk, employed as the inner electrode, is surrounded by a copper cylindrical annulus as the outer electrode, as shown in Figure 2.1. A solenoidal magnetic field coil, providing the bias flux (stuffing flux), is located outside of the cylindrical body. A large end-view window has been installed in HelCat to provide the additional advantage that the entire plasma evolution process can be observed topologically, as indicted in Figure 2.2. D. The various hardware components of the coaxial gun are described in detail in Section 2.2.
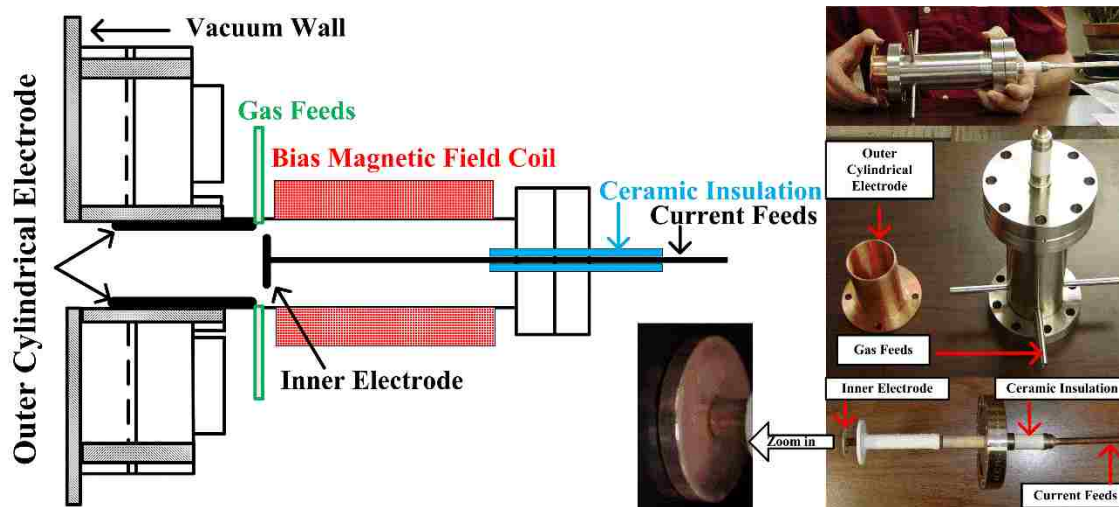
Figure 2.1. Side-view schematic of coaxial plasma gun, showing inner electrode, cylindrical outer electrode, gas feed lines, and discharge current feeds. The gun is mounted on one side of the vacuum chamber of HelCat.

2.2 Coaxial plasma gun apparatus

2.2.1 HelCat Linear Plasma Device

The HelCat Linear Plasma Device, shown in Figure 2.2, is an approximately 4 m long, 50 cm diameter cylindrical vacuum chamber in two 2-meter sections. Each section has multiple 10 inch conflat type ports, on one of which the coaxial plasma gun is mounted. The chamber has a large rectangular window (20 cm × 40 cm) at the end of the chamber (at the cathode location) that provides a good view of the entire cross-section of the chamber.[58] Vacuum is maintained at ~ 5×10^{-7} Torr (6.0×10^{-5} Pa) by two 1000 L/min turbo molecular pumps, one at the mid-chamber and the other at the end behind the cathode source, with independent valves and backing systems. A roughing pump system (p ~ 0.667 Pa) is installed for multiple probe diagnostic systems, along both sides of the linear vacuum chamber.

30
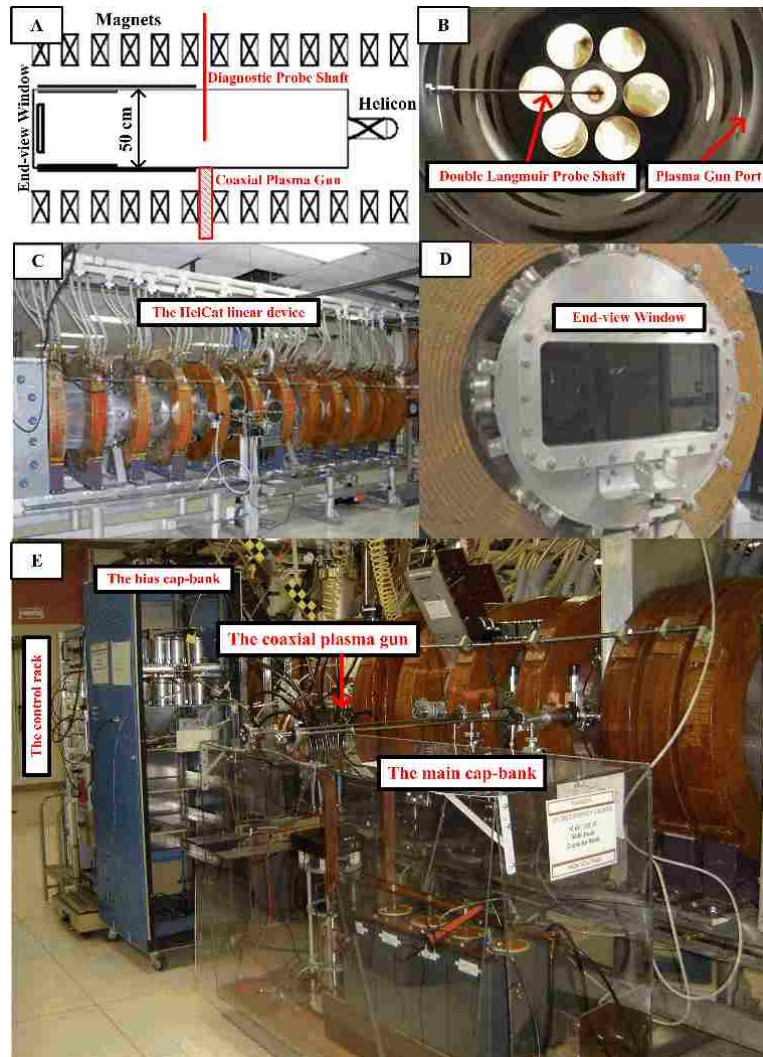
Figure 2.2. A: Schematic top-view of HelCat Linear Device with coaxial plasma gun and end-view window installed. B: A cross-section view of HelCat showing plasma gun port with a double Langmuir probe installed at the opposite port. C: Schematic side-view of HelCat Linear Device with water-cooled solenoidal magnetic coils.[59] D: End window (20 cm × 40 cm) with full view of chamber cross section. E: A picture of the PBEX setup: the coaxial gun, the pulse power systems, and the HelCat linear device.

Magnetic fields are produced by multiple solenoidal magnetic coils. There are thirteen coils in total which are water-cooled as shown in Figure 2.2, C. The currents flowing through these coils provides various background magnetic field conditions for the PBEX project. Magnetic field ripple is measured to be < 1% along the chamber axis and ~ 3% at the plasma edge near r = 20 cm.[59] For PBEX project, steady and flare magnetic fields of B = 200 Gauss

31

(G) and 500 G are produced in these experiments with DC currents of 46 A and 114 A respectively.
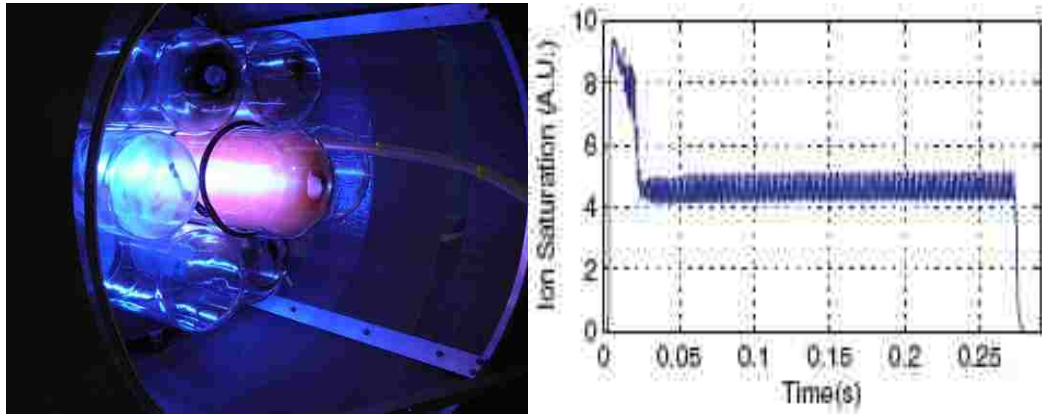
Figure 2.3. Left: Helicon plasma produced by a helical antenna, using Argon as working gas. Right: Typical ion saturation current, I_{sat}, versus time at B=220 G at r= 3 cm.

The "background" argon plasma is provided by helicon source for the PBEX project. For a helicon-sourced plasma, a helical antenna made of copper tube is installed outside of a Pyrex tube (40 cm long and 15 cm diameter), which is mounted to the source end of the vacuum chamber via a stainless steel end flange, indicated in the left of Figure 2.3. The helicon source can be operated in both steady state mode and pulse mode with up to 5kW power provided to the antenna network via a three-stage amplifier. For the PBEX project, the helicon source is usually operated in pulsed mode at a frequency of 10.0 MHz with pulse lengths around 200 milliseconds (ms). The typical helicon plasma time behavior is depicted in the right-side of Figure 2.3. Shown is the typical ion saturation current measurement from a double Langmuir probe located 3 cm from the center of the plasma, where the initial peak is due to high RF power at beginning for neutral gas break down. Considering the lifetime of the plasma generated by the coaxial plasma gun is around 40 microseconds (µs), the 200 ms discharge time is reasonably treated as "steady state".

Typical radial profiles of HelCat helicon Argon plasma density, *n*, are shown in Figure 2.4, with flared background magnetic fields of 200 G and 500 G respectively.[60]
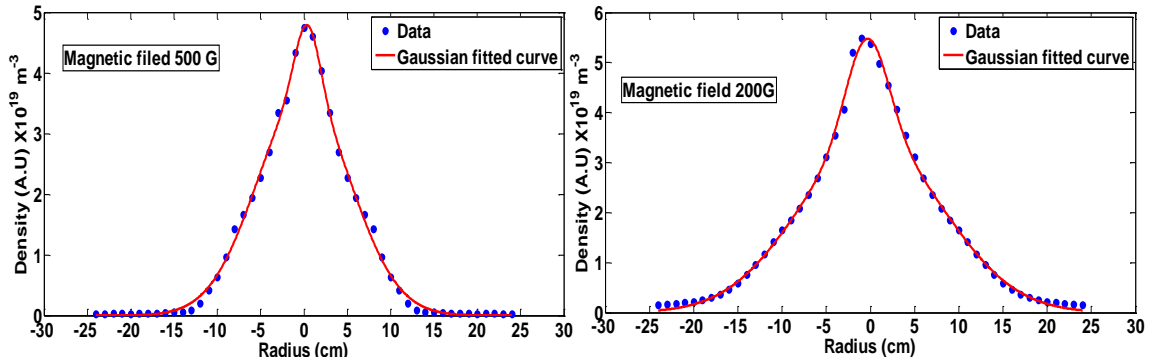
Figure 2.4. Radial profiles of plasma density, n, of Helicon argon plasma as the background plasma source. Left: magnetic field 500 Gauss; Right: magnetic field 200 Gauss.

2.2.2 Coaxial magnetized plasma gun

The compact magnetized coaxial plasma gun is mounted on one 10 inch conflat port where the location is shown in Figure 2.2, A. As indicated in Figure 2.1, the gun is cylindrical, 10 cm long, and 8.55 cm and 5.08 cm in outer and inner diameter respectively. The gun consists of (1) an inner copper tube (0.009 cm wall) with a 2.54 cm diameter copper disk electrode at the left-most end, (2) a cylindrical coaxial 5.08 cm diameter copper annular electrode, and (3) a magnetic field coil that physically covers the whole cylindrical body of the gun. The dimensional details are listed in Section 2.2.4, and shown in Figure 2.16.

A 1.27 cm wide annular vacuum gap separates the inner electrode copper disk and the outer electrode cylindrical copper tube. There are four, 0.64 cm diameter gas puff feed lines symmetrically located around the cylindrical body of the plasma gun to achieve a fast, and localized, gas fill in the gap between inner and outer electrodes. Details of the gas injection are given in Section 2.2.5.
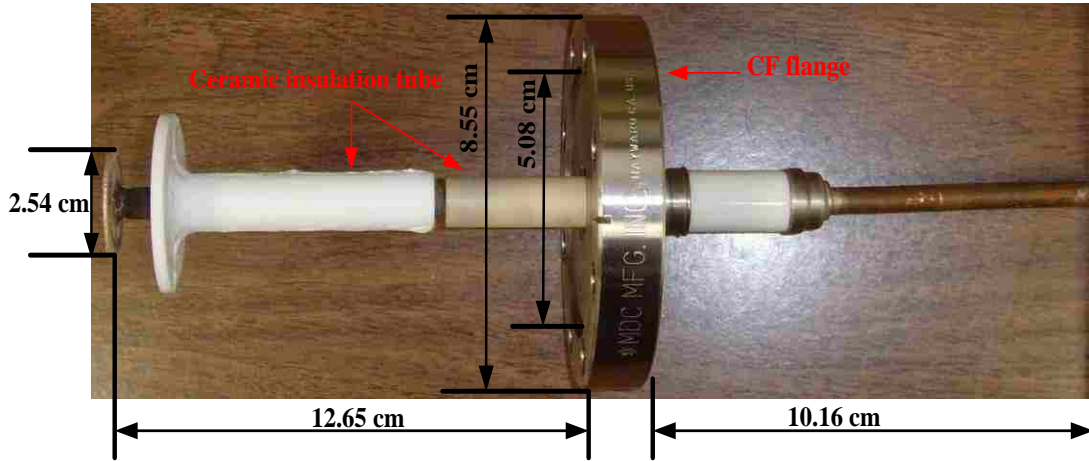
Figure 2.5. Coaxial plasma gun drawing with dimensions.

The feed-through is mounted on a 3-3/8" CF flange. As shown in Figure 2.5, the inner electrode extends 10.16 cm from the flange face on the air side, and 12.65 cm on the vacuum side. The insulator of the inner electrode is an alumina ceramic tube, holding up to 12 kV withstand voltage. The outer cylindrical electrode is mounted via stainless steel bolts directly to the vacuum chamber inner surface, electrically connected to the chamber ground. The inner electrode is connected to the main gun cap-bank via eight, parallel, double-layer, low inductance (0.51 µH/m) coaxial cables (Belden YK-198), which carry electrical power from the main capacitor bank to the gun electrodes with low line loss, as illustrated in Figure 2.6.
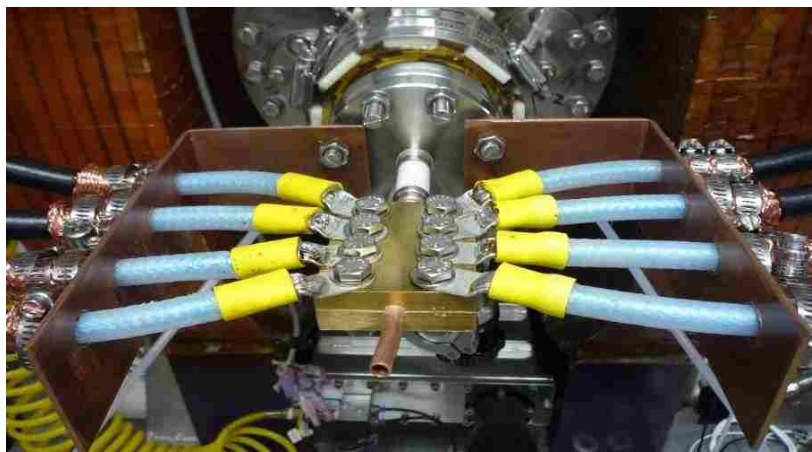
Figure 2.6. Eight double-layer coaxial cables connect the main cap-bank to the inner electrode.

34

2.2.3 Main cap-bank power system and characterization

2.2.3.1 Main cap-bank power system design, construction and schematics

The coaxial plasma gun is powered by an ignitron-switched 120 µF capacitor bank (cap-bank). The cap-bank consists of four capacitors (Aerovox/PXSOD53), each of which has a capacity of 30 µF/10 kV, giving total capacitance of 120 µF. The DC power supply (Glassman High Voltage Inc. /10YDC), provides up to 10 kV DC charge voltage with a negative polarity and 30 mA charge current, and is employed to charge the cap-bank via a current-limited resistor. The cap-bank can be operated from 4 kV up to 10 kV, providing a peak discharge current, I_{gun}, up to 100 kA.

The cap-bank power circuit schematic is shown in Figure 2.7, where SW1, SW2, and SW3 are relay switches. R is a 120 Ω resistor to limit the charging current during the charging process, and also functions as a dump resistor to discharge the remaining voltage on the cap-bank. The ignitron switch (Model No. GL-37207A) can handle a peak voltage of 25 kV, and a peak current of 300 kA.[61] A Pearson coil (5 mV/A sensitivity) is placed around the copper bar which connects the ignitron switch to the double-layer coaxial cables, and is used to measure the discharge current, I_{gun}. A high voltage probe (Model No. Tektronix P6015A with attenuation ratio 1000:1) is utilized to measure the real-time discharge voltage V_{gun}.

The cap-bank power system is operated as followings:

1) With SW1 and SW2 close and SW3 and the ignitron-switch open, the DC power supply begins charging the main cap-bank through the current-limiting resistor, R.

2) When the capacitor bank voltage reaches the required value, SW1 and SW2 open to isolate the DC power supply from the rest of the circuit for protection purposes. SW3 and the ignitron-switch remain open in step 2.

3) The ignitron-switch then is closed by the trigger control signal. The capacitor bank discharges through the gap between the electrodes of the coaxial plasma gun, ionizes the neutral gas into plasma, and closes the current loop.

4) After the discharge process is completed, no discharge current flows, and the ignitron-switch goes to open status. SW3 closes to dump the remaining voltage on the cap-bank through the resistor, R.
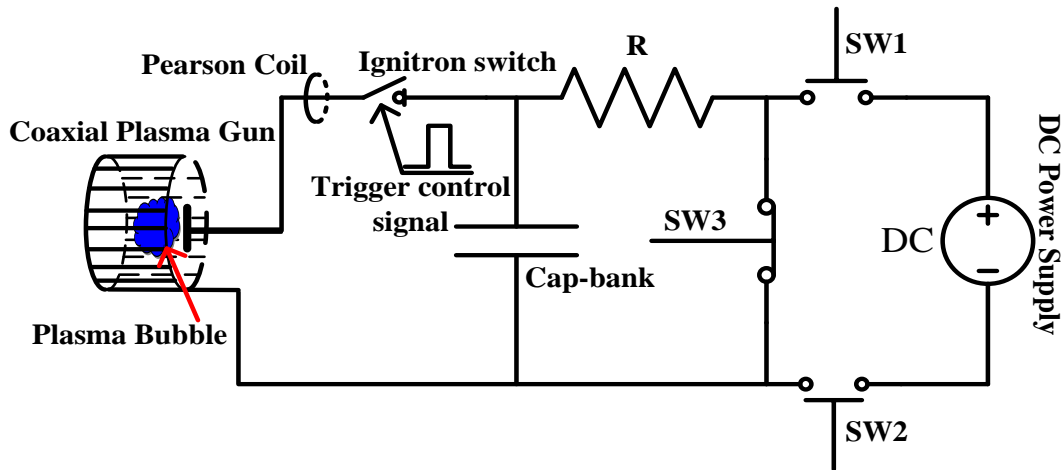
Figure 2.7. Main cap-bank circuit schematic.
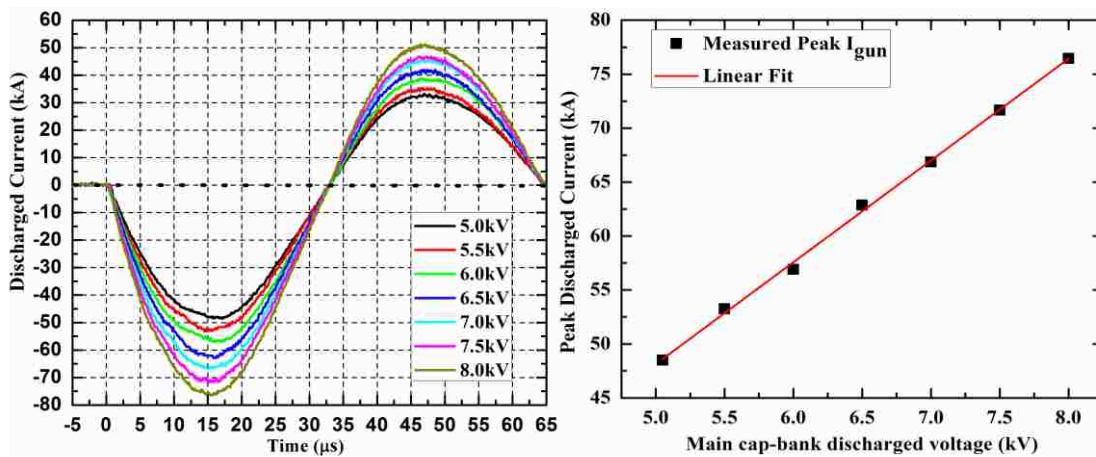
Figure 2.8. Left: Discharge current waveforms under different main cap-bank charging voltages; Right: Linear relationship between charging voltage and peak currents.

2.2.3.2 Main cap-bank discharge voltage and current characterization

The discharge current waveforms under different main cap-bank charge voltages have been investigated, and the results are plotted in Figure 2.8, right. The linear relationship between peak discharged current and charge voltage, Equation 2.1, has been characterized based on the experimental data, as shown in Figure 2.8, left.

$$I_{gun}(kA) = 9.43V_{gun}(kV) + 0.98 \qquad (2.1)$$

2.2.4 Solenoidal bias flux (stuffing flux) coil design and bias magnetic field characterization

2.2.4.1 Bias flux solenoidal coil design and construction

Figure 2.9. A: Picture of the cylindrical body of the plasma gun before adding the solenoidal bias coil; B: Partial side-view picture of the gun after bias coil installation; C: Top-view picture of the gun after the bias coil is installed.

The external bias flux coil covers the main cylindrical body of the plasma gun. The coil consists of 10 layers, 44 turns per layer (440 turns total), of 12 AWG insulated square magnet wire, and has an inductance of 6.25 mH and resistance of 0.5 Ω (measured by LCR meter, model HP 4263B).[52] The coil magnet wire has Polyester A/I Topcoat insulation, which is rated

for 200°C, and has a break-down voltage of 4 kV. A layer of fiberglass between the windings and the cylinder was also added during fabrication by the manufacturer as detailed in Figure 2.9.

2.2.4.2 Power system for bias flux coil

The pulsed, bias magnetic flux is generated by an electrical pulse through the solenoidal coil. A cap-bank array with a total of 60 mF is employed to produce the electrical pulse for the coil. The power system schematic for charging the cap-bank array is shown in Figure 2.10, where R1 is a 150 Ω current limiting resistor, R2 is a 250 Ω dump resistor, D1 and D2 are power electronic diodes, SW is the dump relay, and C is the bias flux cap-bank. A Silicon-Controlled Rectifier (SCR), activated by the trigger control signal, is employed as the main switch in the power system.
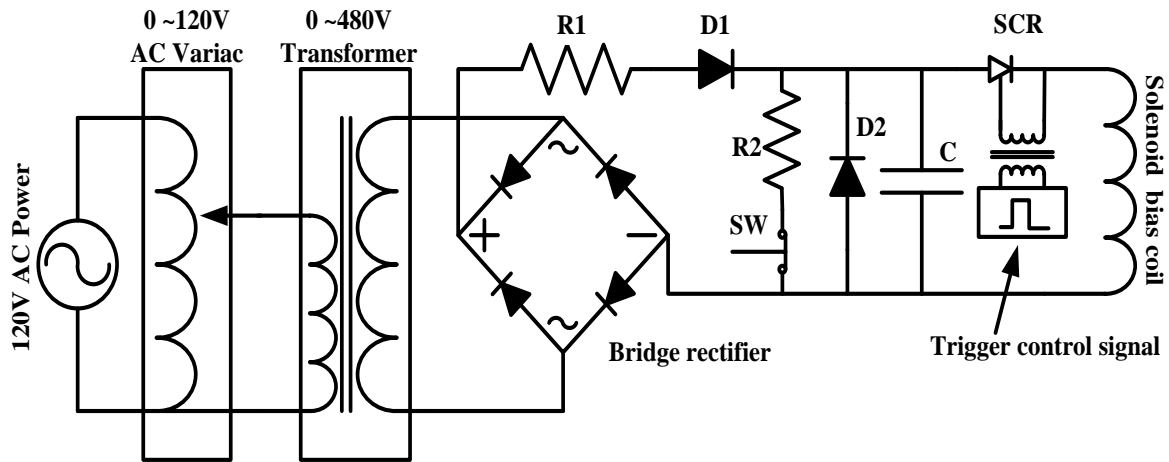
Figure 2.10. Circuit schematic of bias flux cap-bank power system.

The cap-bank array power system is operated as follows:

1) With SW and SCR open, AC power, via a bridge rectifier AC-DC converter, starts charging the cap-bank array through the current-limited resistor, R1, and power diode, D1.

38

2) When the cap-bank array voltage reaches the pre-set value, the SCR is closed by the trigger control signal. The cap-bank array discharges through the solenoidal bias coil to generate an electrical pulse, consequently inducing a pulsed bias magnetic flux.

3) After the discharge process is completed, and no discharge current flows, the SCR returns to open status. SW closes to dump the remaining voltage on the cap-bank array through the resistor, R2.

2.2.4.3 Solenoidal bias flux coil inductance calculation

The formula employed in this chapter to calculate the inductance of this multi-layer air core solenoidal coil is[62]:

$$L_{Bias-coil} \text{ (H)} = \frac{k_N \mu_0 \mu_r \pi N^2 D^2}{4l} \times 10^{-3} \qquad (2.2)$$

Where μ_0 is the permeability of free space $(4\pi \times 10^{-7} \ Hm^{-1})$; μ_r is the relative permeability $= 1$; N is the total number of turns $= 440$; D is the average winding radius $= 0.0675$ m; l is the coil length $= 0.1016$ m; and k_N is Nagaoka coefficient, which is 0.74 since the ratio D/L is 0.66 for this case.

Based on Eq.2.2, the calculated inductance $L_{Bias-coil}$ is 6.34 mH, which is very close to the measured value of 6.25 mH.

2.2.4.4 Pulsed discharge current calculation, simulation and measurement

Since the solenoidal coil inductance has been determined above, a simple RLC theoretical model is set up to calculate the pulsed current flowing through the solenoidal bias coil. The circuit model is shown in Figure 2.11, left.

When the switch closes at t=0, the following equations are used to determine the current and voltage in the circuit:

$$LC \frac{d^2 V_C}{dt^2} + RC \frac{dV_C}{dt} + V_C = 0 \tag{2.3}$$

$$I_L = -C \frac{dV_C}{dt} \tag{2.4}$$

where V_C is the initial voltage of capacitor bank and I_L is the discharge current through the solenoidal bias coil. Considering the components' value for this case, where C is 60 mF, R is 0.5 Ω, and L is 6.25 mH, a Matlab code is utilized to calculate waveforms of I_L under different voltages. The plots are shown in Figure 2.11, right.
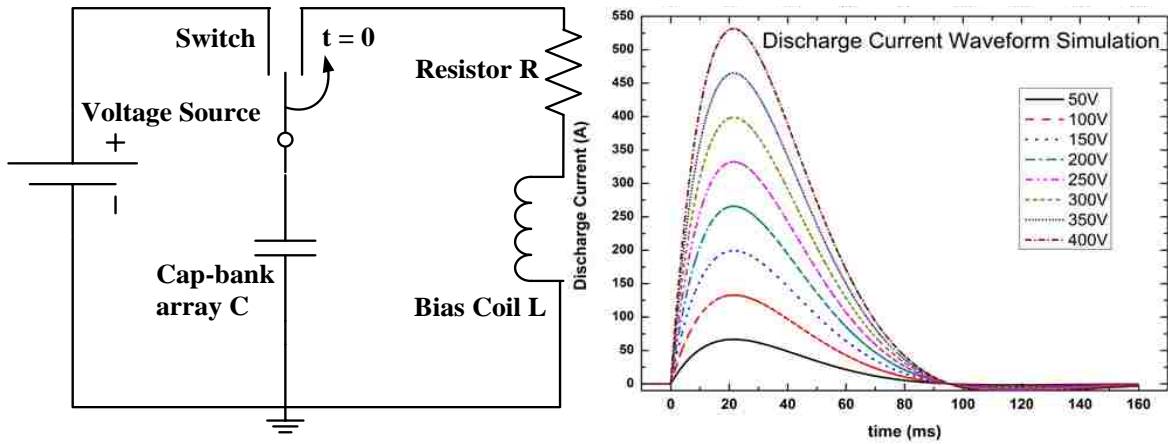
Figure 2.11. Left: RLC circuit model for discharge current calculation; Right: The calculated discharge current waveforms under different charge voltages.

Also, the circuit simulation software, TopSpice, was employed to model this circuit. The circuit schematic is shown in Figure 2.12, left, and the discharge current simulation results are shown for different voltages in Figure 2.12, right. Based on the theoretical calculation, TopSpice simulation, and experimental measurements discussed above, the comparisons of these three results are plotted in Figure 2.13, right, for the case where the discharge voltage is 400 V. By comparison, the peak experimental currents, which determine the mount of bias flux for the PBEX project, agrees well with the simulated values.

Employing a probe and oscilloscope, the cap-bank array discharge currents were measured under different charging voltages, and the results are shown in Figure 2.13, Left. From the results, it is clear that at time t = 22.9 ms, discharge current reaches the peak value. Details of the peak current values may be found in Table 2.1.
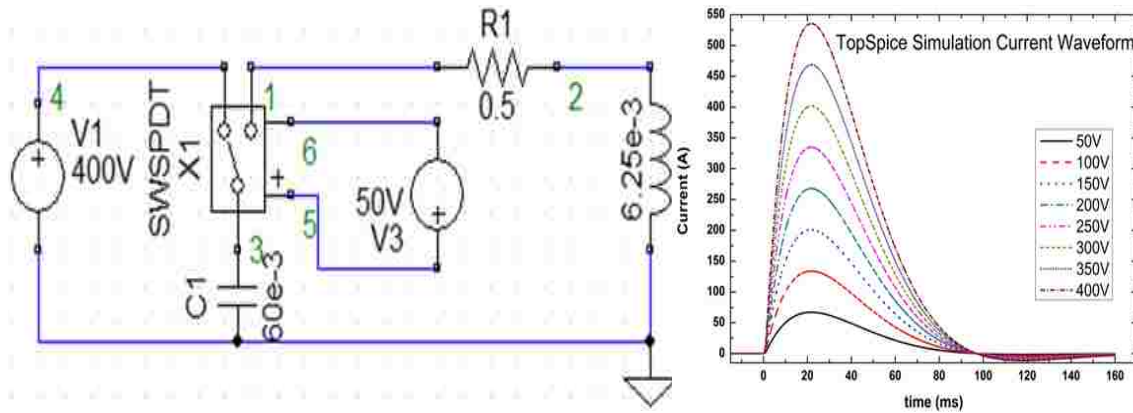
Figure 2.12. Left: TopSpice circuit schematic for simulation; Right: discharge current simulation results under different voltages.
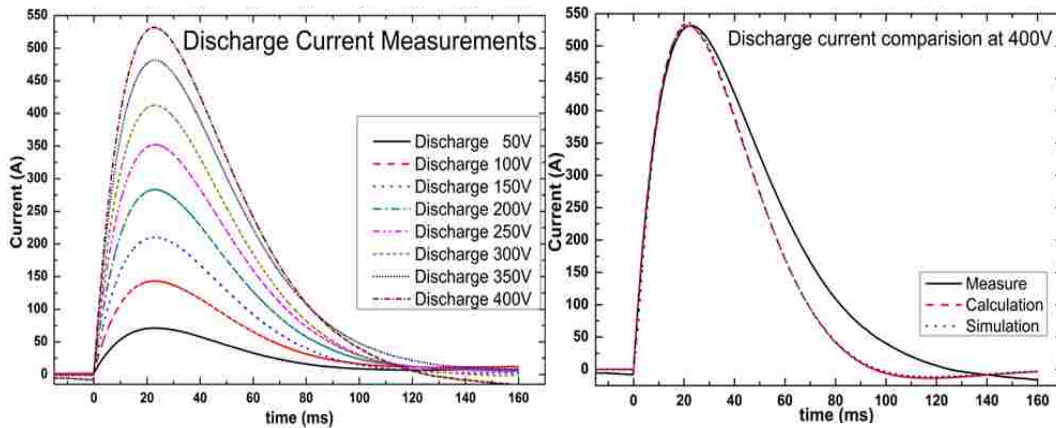
Figure 2.13. Left: discharge current measurements under different voltages; Right: the discharge current results comparison of calculation, simulation and measurement for the 400V charge voltage case.

2.2.4.5 Bias flux calculation, simulation and measurement

For the general case of a multi-layer solenoid, as per the specifications shown in Figure 2.14, the magnetic field along the axis is obtained based on Eq. 2.5:[63]

41

$$B_x = \frac{\mu_0 IN}{2L(R-r)}\left[\left(x+\frac{L}{2}\right)\ln\frac{\sqrt{R^2+\left(x+\frac{L}{2}\right)^2}+R}{\sqrt{r^2+\left(x+\frac{L}{2}\right)^2}+r} - \left(x-\frac{L}{2}\right)\ln\frac{\sqrt{R^2+\left(x-\frac{L}{2}\right)^2}+R}{\sqrt{r^2+\left(x-\frac{L}{2}\right)^2}+r}\right] \quad (2.5)$$

where μ_0 is the permeability of free space ($4\pi\times10^{-7}\ Hm^{-1}$), I is the current in the wire (A), N is the total number of turns of wire in the solenoid = 440, L is the length of the solenoid = 0.1016 m, R is the coil outer radius = 0.04395 m, and r is the coil inner radius = 0.02375 m.
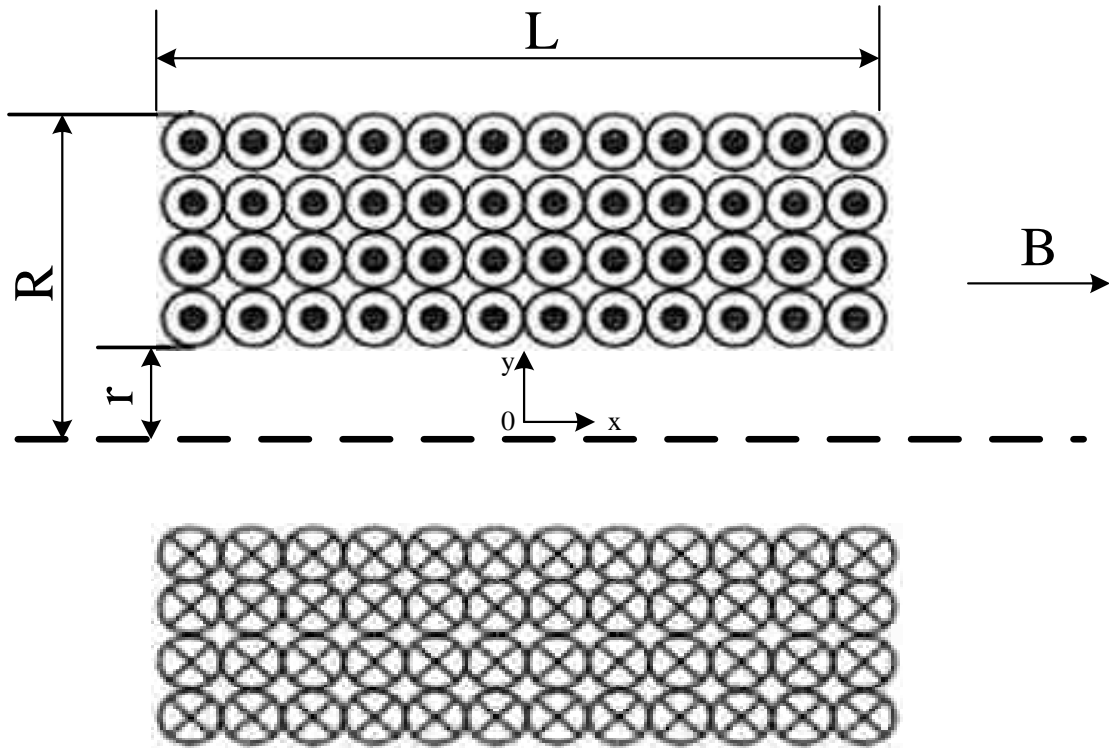
Figure 2.14. Schematic for magnetic field calculation along the axis for solenoidal coil.

Based on the parameters listed above, the magnetic flux density inside the coil along the axis for current values (280 A) is illustrated in Figure 2.15. According to the calculation results, the magnetic flux density inside the solenoid bias coil at the center has the maximum value 1.27 T. The magnetic field at both ends of the cylinder drops to 0.35 T and 0.52 T respectively.
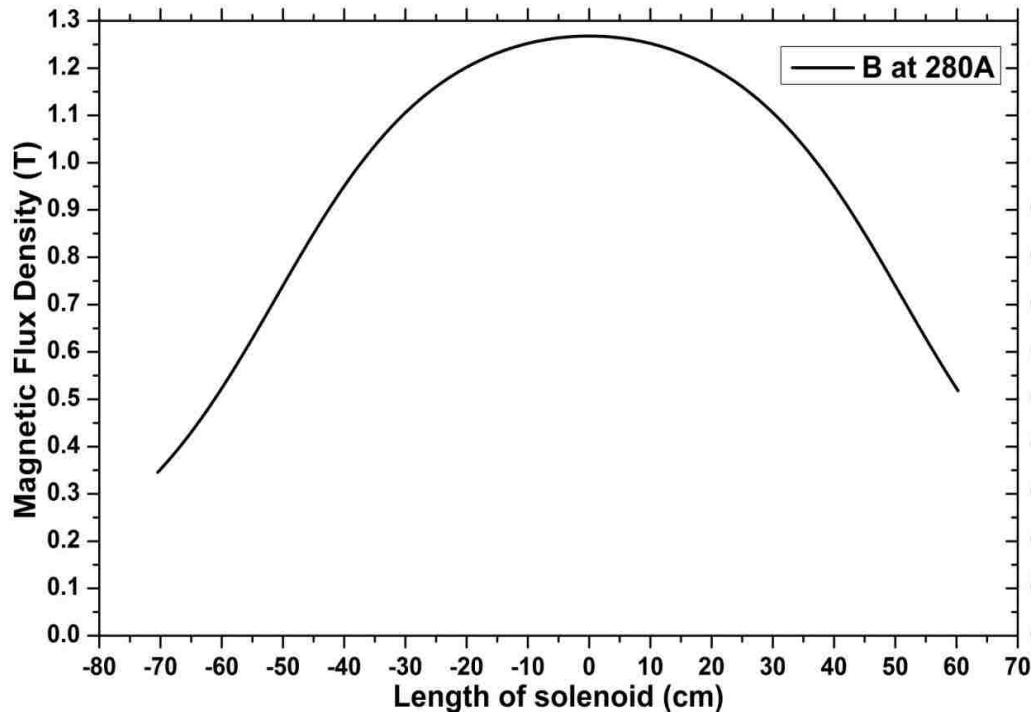
Figure 2.15. Magnetic flux density calculation along axis for discharge current 280A.

Furthermore, simulation software FEMM (Finite Element Method Magnetics) was employed to evaluate the theoretical calculation discussed above.[64] The physical dimensions of the cylinder have been measured and input into the simulation as the geometry condition. The details of dimensions are listed in Figure 2.16.

Simulation results of contours of constant magnetic flux, and density strength are plotted in Figure 2.17 for the I = 280 A case. The magnetic flux density contour both inside and outside the solenoid coil is shown. The maximum magnetic flux density is located at the center of the solenoid.

The magnetic flux density along the solenoidal coil axis was also calculated in FEMM, which indicates that the magnetic field reaches the maximum value at the center inside the cylinder and reduces with further distance from the center. To validate Equation 2.5, the calculation results, and FEM analysis results are compared and illustrated in Fig 2.18, Left.
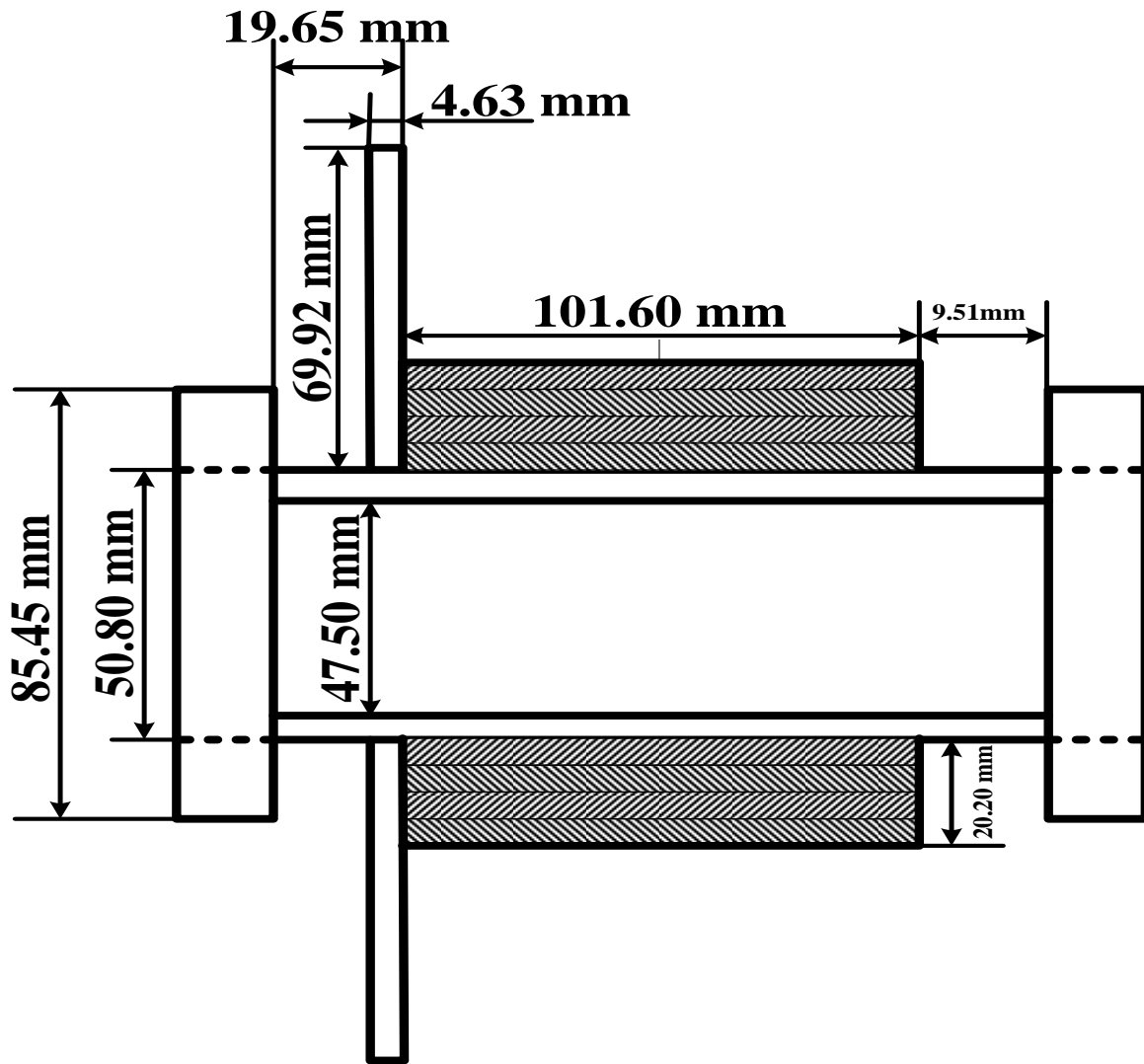
Figure 2.16. Detailed geometry and dimensions of plasma gun cylinder.

Besides the theoretical calculation and FEMM simulation, experiments have been carried out to measure the magnetic flux density along the coil axis. A DC power supply (Agilent E3631A) was employed to provide a constant 5 A DC current through the solenoidal coil. At the same time, a Gauss meter (Lakeshore 450) was utilized to measure the magnetic field along the axis. The comparison of the measured valves and FEMM simulation results is plotted in Figure 2.18, Right. As shown in Figure 2.18, the comparison yields good agreement with the theoretical calculation, FEMM simulation analysis, and measurement results. For the

44

PBEX experiment, the total length of the gun's body is 130.76 mm and the surface of the gun's cathode disk is at - 50.80 mm positioned along the axis.
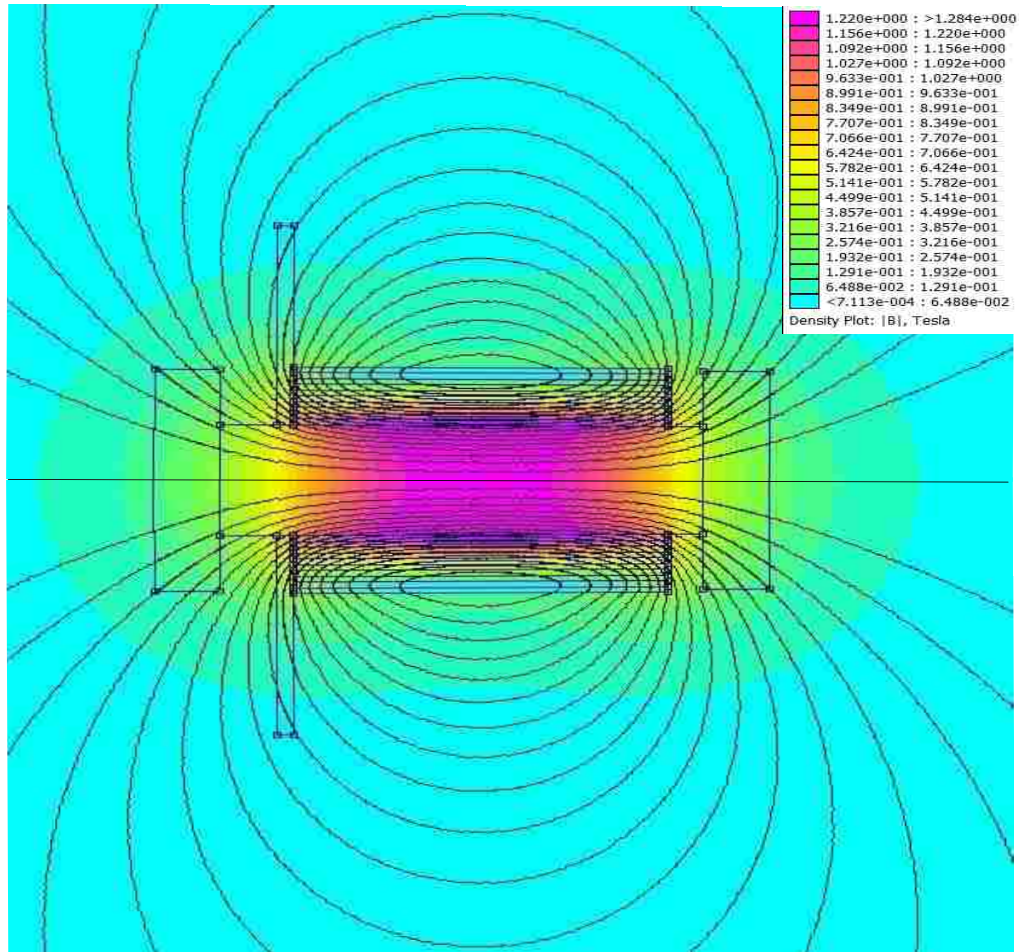
Figure 2.17. Simulation results for magnetic field contour plot and density magnitude for I=280 A case.

Based on the discussion in this section, the discharge voltage, along with the calculated inductance, can determine the discharge current through the solenoidal bias coil. The magnetic flux may then be determined by the discharge current. The details are listed in Table 2.1.
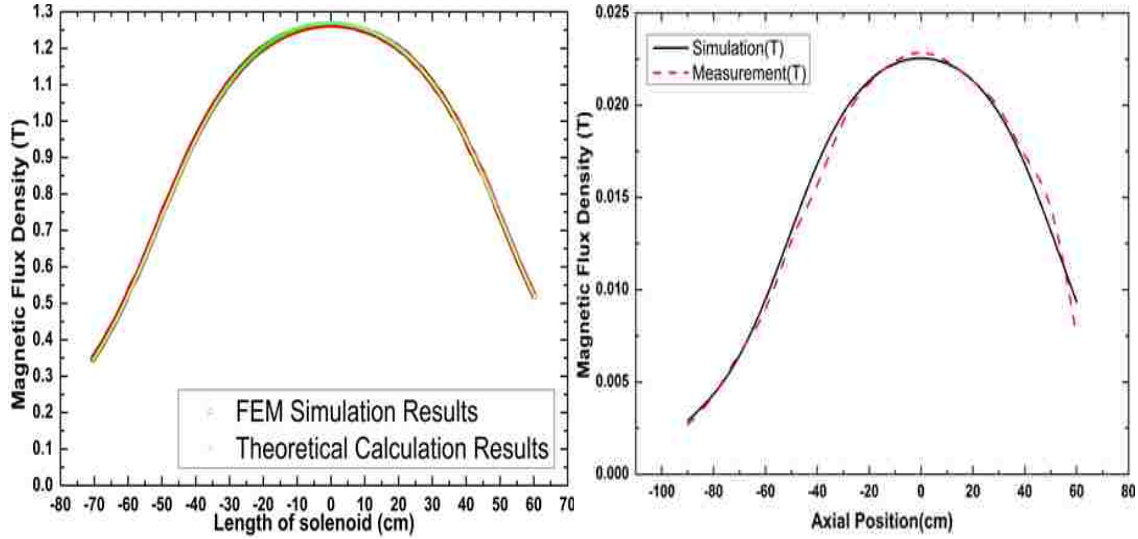
Figure 2.18. Left: the comparisons of FEMM and theoretical calculation result from Equation 2.5. Right: the comparisons of FEMM and experimental measurements.

From Table 2.1, the relation between bias flux (stuffing flux), and discharge voltage can be characterized as follows:

$$\Phi_{Bias}(mWb) = 6.1{\times}10^{-3}V_{Bias}(V) + 0.05 \tag{2.6}$$

2.2.5 Gas injection and gas valve power system

A fast gas puff system is of importance for the plasma gun experiment since Paschen breakdown, and efficient gas ionization, need a highly localized gas pressure, on the order of 100 mTorr.[44] Otherwise, a slow gas fill in the gap may cause weakly ionized cold plasma, which is inappropriate for this experiment. The fast gas valve, employed in the PBEX project, provides a transient cloud of high pressure natural argon gas localized in the gap between the inner and outer electrodes, the assembly of which is shown in Figure 2.19.[65]

46

Table 2.1. Details of discharge voltage and magnetic flux at inner electrode position.

Discharge Voltage (V)	50	100	150	200	250	300	350	400
Peak Current (A) at time t=22.9ms	71.04	143.24	210.01	283.20	352.08	412.59	481.63	531.67
Magnetic flux density (T) (at center of coil)	0.3206	0.6465	0.9478	1.2781	1.5890	1.8621	2.1737	2.3995
Magnetic Flux (mWb) (at center of coil)	0.5681	1.1456	1.6795	2.2648	2.8157	3.2997	3.8519	4.2520
Magnetic flux density (T) (at -50.80 mm)	0.1838	0.3706	0.5427	0.7319	0.9099	1.0675	1.2447	1.3756
Magnetic Flux (mWb) (at -50.80 mm)	**0.3257**	**0.6567**	**0.9616**	**1.2969**	**1.6123**	**1.8916**	**2.2056**	**2.4376**

The fast gas valve and the power system are operated as followings:

1) The pulse capacitor is charged to the pre-set voltage value via the power system.

2) The capacitor discharge, controlled by an SCR, is initiated to generate a current flowing through the thin single-turn drive coil.

3) An image current is induced in the valve piston (an adjacent aluminum disk).

4) The disk is thus repelled from the drive coil, creating a transient opening for gas to flow from the gas feed line to the annular vacuum gap between electrodes.

5) The combination of the metal spring and the high pressure gas in the gas feed line result in a large restoring force on the piston to make the valve close again.
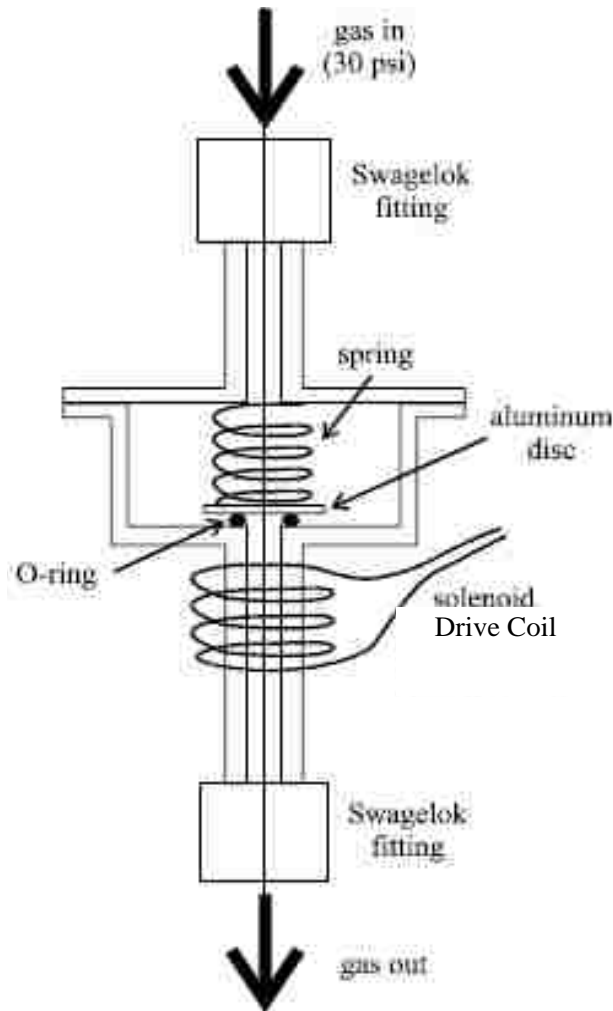
Figure 2.19. Schematic of the valve assembly: solenoidal driver coil, an aluminum disk working as valve piston, and spring used to ensure a positive seal. Picture is taken from [66].

The power system circuit schematic is shown in Figure 2.20 Top. In this circuit, R is a variable resistor with range 0 - 10 kΩ. D1, D2 and D3 are power electronic diodes. C is the pulse capacitor with a capacitance of 50 μF/1kV. An SCR is utilized as the main switch, which is controlled by the trigger control signal. A commercial, high DC voltage converter (UltroVolt Inc. model number 2C24-P60) is employed to charge the pulse capacitor. The output voltage can be varied from 0 V to 2055 V, depending on the input DC voltage. Discharge voltage

waveforms through the drive coil were recorded for different charging voltages. The results are plotted in Figure 2.20, bottom.
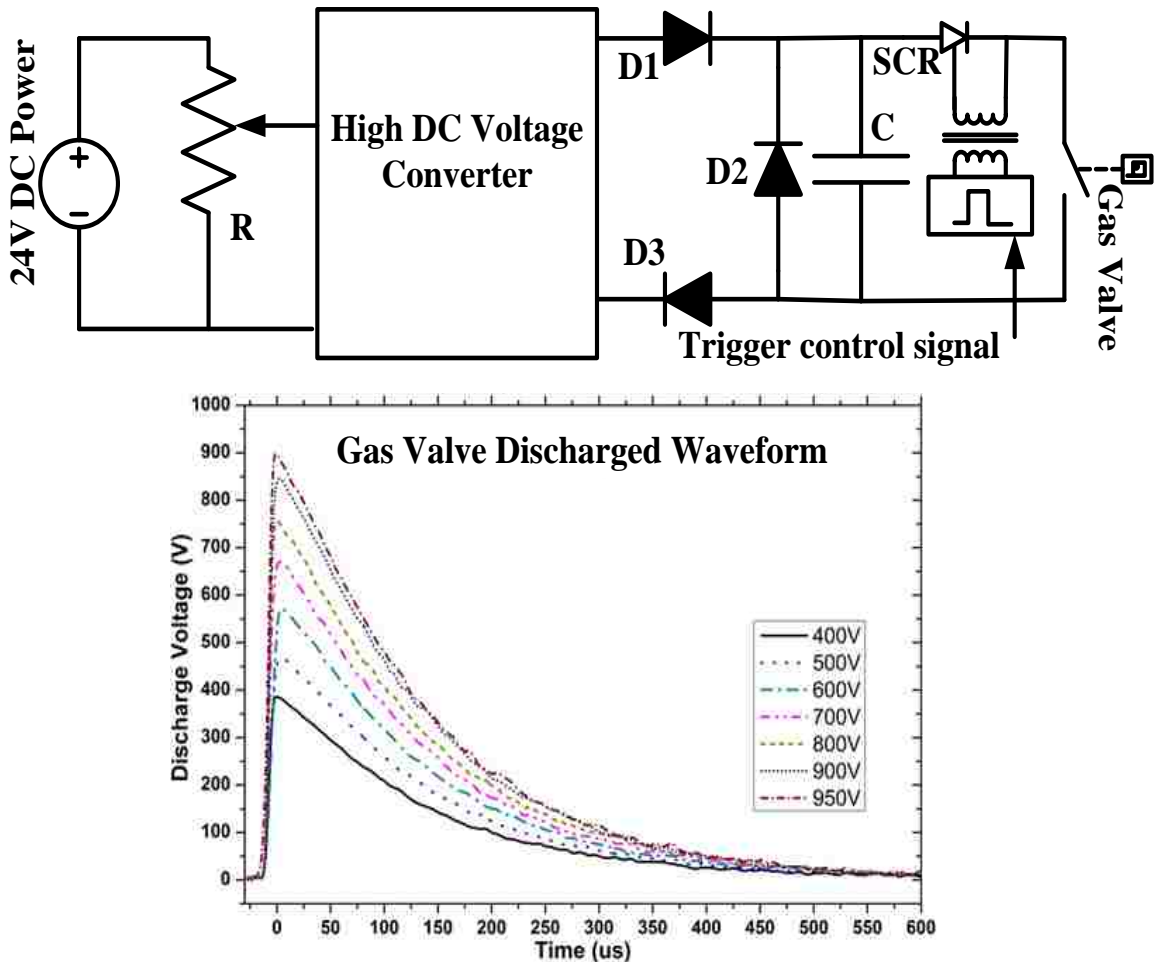
Figure 2.20. Top: Circuits schematic for gas valve pulse power system; Bottom: Voltage waveforms of the gas valve drive coil under different charge voltage.

Calibration indicates that each pulse injects 10^{20} - 10^{21} argon molecules, 6.6 - 66.4 mg in mass, into the gap depending on the operation voltage. Optimum timing of gas valve firing was found experimentally by adjusting the valve firing time to minimize the delay between main cap-bank trigger and gas breakdown.[44] A typical operating voltage is 900 V for the gas valve power system, and injects on the order of 10^{21} argon atoms.

2.3 Diagnostics

Multiple plasma diagnostics were employed in the PBEX project to study the three-dimensional (3D) dynamics of current-driven plasma jets, spheromak formation, and the general interaction between the coaxial-gun-generated plasma and background plasma. The images presented in this dissertation were taken with multiple-frame charge-coupled device (CCD) cameras. Magnetic field data was acquired with a radial array of small commercial inductor coils on a stainless steel shaft. Plasma density and temperature were measured with a double-tip Langmuir probe. Furthermore, a Pearson coil and an attenuating high voltage probe were utilized to measure the discharge current, I_{gun}, and voltage, V_{gun}. The experiment was controlled and triggered by a programmable sequencer. All the magnetic probe and gun diagnostic signals were digitized on a multiple-channel data acquisition system. The details of the diagnostics will be discussed in this section.

2.3.1 Fast CCD camera

Most of the images in this project were taken with a Hadland Ultra UHSi 12/24, as shown in Figure 2.21. The specifications for this camera are as follows:[67]

1) 12 or 24 frames per shot with 10 μs nominal between frames 12 and 13

2) 1000×860 pixels per image

3) 12 bits per pixel

4) 5 ns minimum exposure time

5) framing rate up to 200M fps

6) gigabit Ethernet (1000Mb/sec - GigE) direct to PC

The camera was placed on a tripod and positioned in front of the end-observation window as shown in Figure 2.2, D. The view of the camera is shown in Figure 2.2, B. The

camera was triggered by a trigger control signal and the typical camera operation setting for PBEX was: 12 frames with 1μs exposure time at framing rate 500k fps per plasma gun shot. The images were recorded on by a PC via Ethernet and post-pulse analyzed by utilizing the software IVV Imprint.[68]

Figure 2.21. Ultra High Speed Framing Camera: Hadland Ultra UHSi 12/24.

2.3.2 High voltage probe for discharge voltage measurement

An attenuating high-voltage probe, model No. P6015A (Ratio 1000:1), shown in Figure 2.22, was employed to measure the discharge voltage waveforms of the main cap-bank. The probe is placed across the main cap-bank and connected to the oscilloscope channel with the 1 MΩ terminal setting.

Figure 2.22. High-voltage probe P6015A for discharge voltage measurements.

Due to various plasma formations under different experimental settings, a wide range of discharge voltage waveforms were exhibited. Figure 2.23 shows four different waveforms under the same main cap-bank charge voltage but with different bias voltages: 0 V, 50 V, 120 V, and 187 V.

2.3.3 Pearson coil for discharge current measurement

A Pearson Coil (Model No. 1000), with an output ratio 5mV/A, was employed to measure the main cap-bank discharge current, I_{gun}. The coil was placed around the copper bar, which is connected to the positive electrode of the main cap-bank and to the inner electrode of the plasma gun, as indicated in Figure 2.24.

The output signal from the Pearson coil was recorded on an oscilloscope with a 1 mega ohm (MΩ) impedance setting via three attenuators in series with a total attenuation factor 2×5×5=50. The calculated and modified calibration factor for Pearson coil measurement is:

$$I_{gun} \ (kA) = 10 \times V_{measure} \ (V) \tag{2.7}$$

Typical operation with main cap-bank voltage of 8.0 kV yields a peak discharge current of $I_{gun} \sim 76.5$ kA, and gun voltage of $V_{gun} \sim 1.0$ kV, after the breakdown. Typical I_{gun} and V_{gun} traces are shown in Figure 2.25.
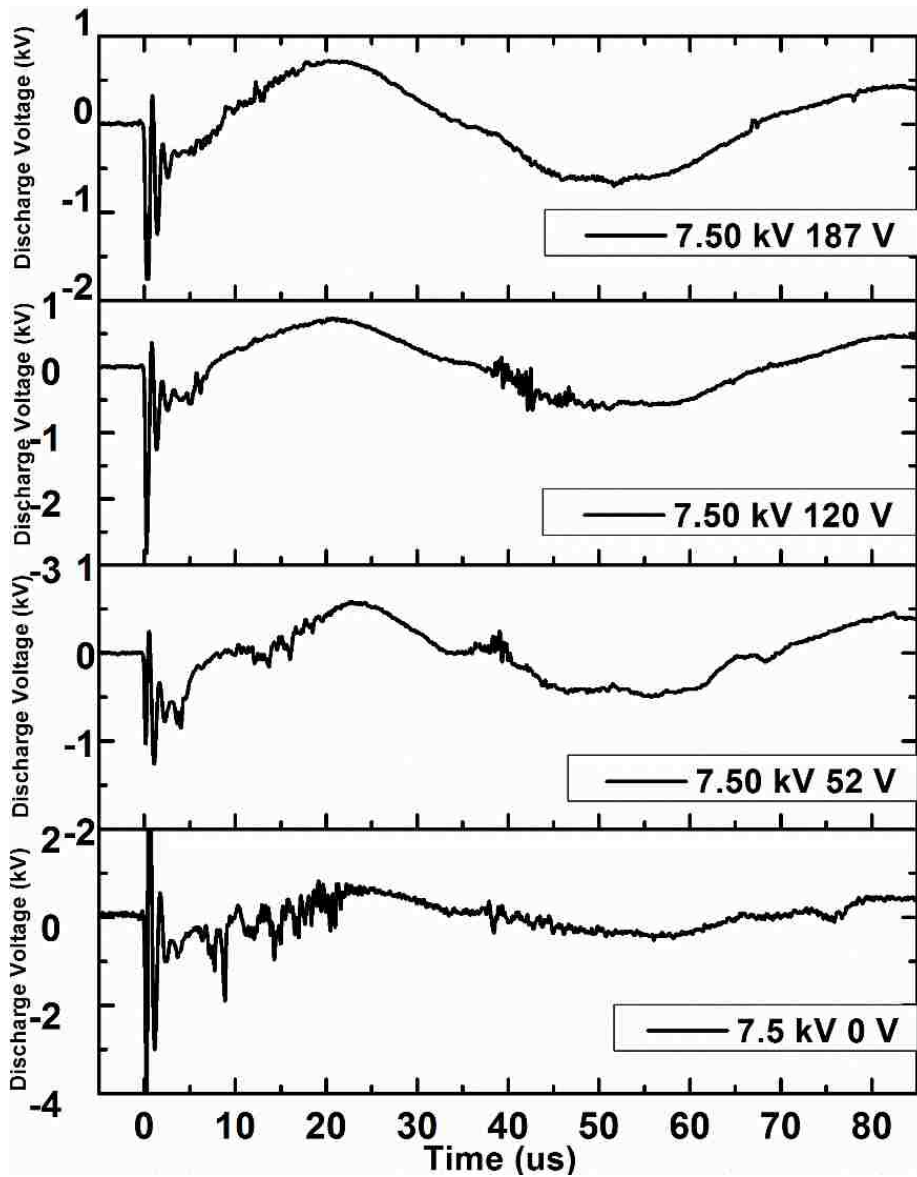
Figure 2.23. Discharge voltage waveforms under different bias voltage settings 0 V, 52 V, 120 V, and 187 V.
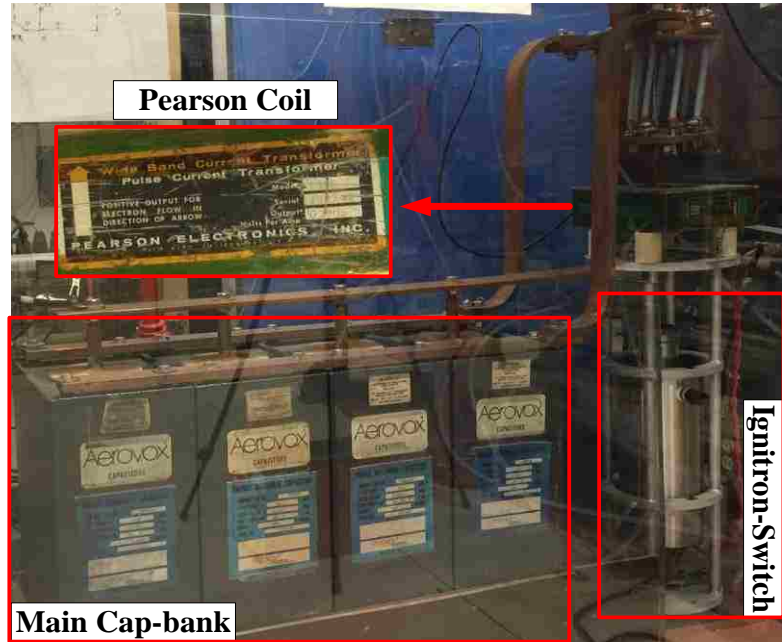
Figure 2.24. Main cap-bank construction with Pearson coil placed to measure total I_{gun}.
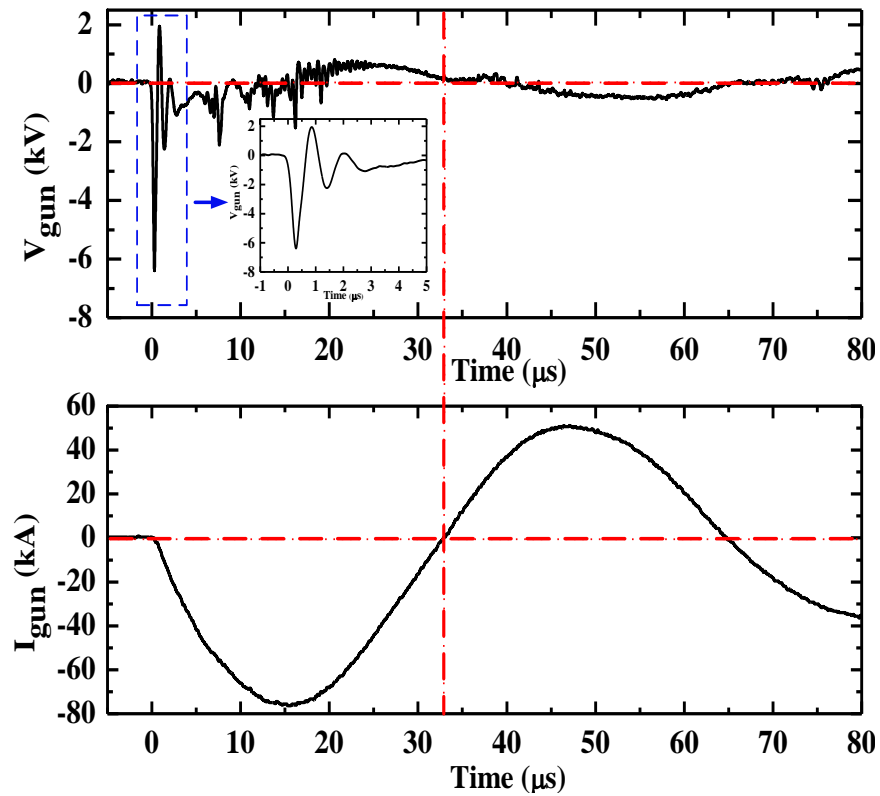
Figure 2.25. Typical I_{gun} and V_{gun} traces. Initial charge voltage is 8.0 kV. Breakdown occurs at 2 μs.

2.3.4 Langmuir probe

Langmuir probes are small conductors with known surface area that are inserted into the plasma for measuring plasma density, n, and the electron temperature, T_e, by collecting electrons, and ions, in situ.[69] Langmuir probes were employed in the PBEX project for plasma density and electron temperature measurement. Also, by placing probes at different spacial positions in the vacuum chamber, the plasma propagation velocity has been estimated for different experimental settings. The experimental set-up is shown in Figure 2.26.
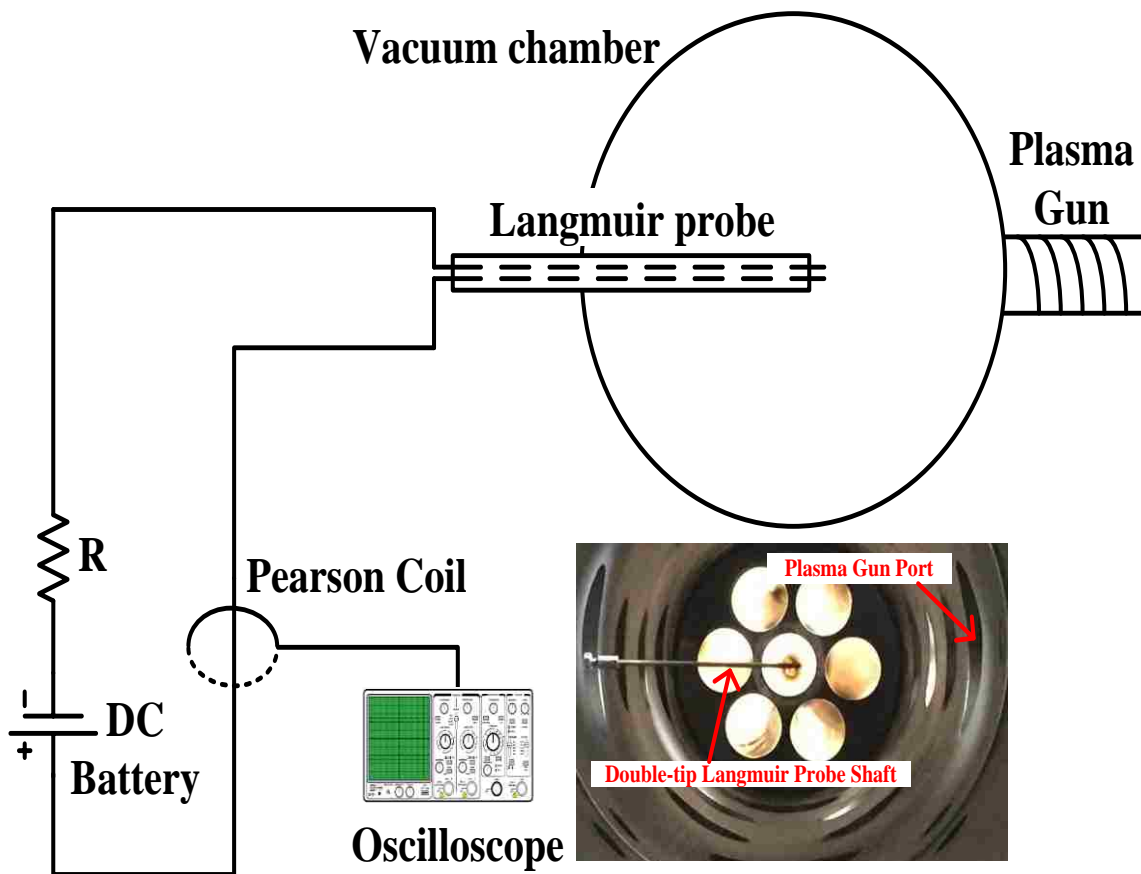
Figure 2.26. Double-tip Langmuir probe utilized for plasma density, electron temperature and propagation velocity measurements.

In the experimental set-up, the key parameters of the Pearson coil (Model No.410) are: sensitivity 0.1 V/A, output resistance 50 Ω, and maximum peak current 5000 A. The output of

the Pearson coil was connected to the oscilloscope with 1 MΩ setting. R is a variable resister, with a range from 1 Ω to 100 Ω, determined empirically to provide optimum results. A DC battery array (Exell Battery 455, 45V[70]) was employed to provide the DC bias voltage for measurement.

Typical ion saturation current, I_{sat}, and main cap-bank discharged current waveforms are exhibited in Figure 2.27.
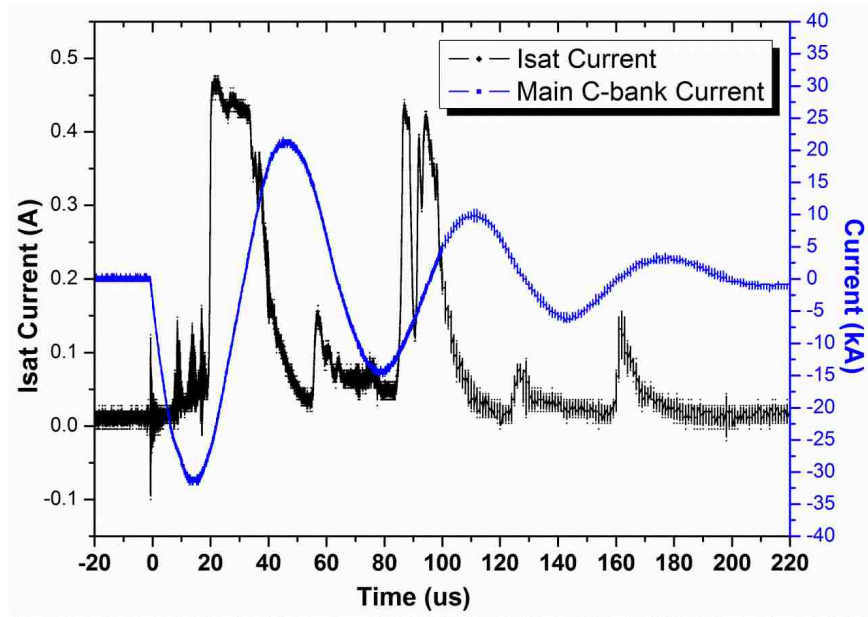
Figure 2.27. Typical measured ion saturation current I_{sat} waveform with main cap-bank discharge current I_{gun} waveform from a single shot.

Using a triple Langmuir probe, electron temperature can be measured using the following equation[71]:

$$T_e = \frac{(V_1 - V_f)}{\ln 2} \tag{2.8}$$

And electron density can be calculated from:

$$I_{sat} = 0.61en_eA\sqrt{\frac{Z_ikT_e}{M}} \rightarrow n_e = \frac{I_{sat}}{0.61eA}\sqrt{\frac{M}{Z_ikT_e}} \tag{2.9}$$

where e = electron charge, k = Boltzmann's constant, T_e = electron temperature, V_1 = positive bias voltage, V_f = floating voltage, I_{sat} = ion saturation current, Z_i = ion charge state = 1, M = ion mass, and A = probe surface area.

For the PBEX project, argon gas was employed as the working gas which has ion mass $M = 6.62 \times 10^{-26}$ kg. The probe had an area of $A = 0.082$ cm^2 (cylindrical probe tip with diameter 0.0508 cm and length 0.5 cm). The calculated electron temperature was 9.1eV and plasma electron density was 1.19×10^{20} m^{-3}. From these, the ion sound speed (given by $Cs = \sqrt{\frac{\gamma k (T_e + T_i)}{M}}$) was then calculated to be 0.803 cm/us (8.03 km/s).

2.3.5 Three-dimensional (3D) magnetic probe array

Magnetic probes (B-dot probes) are widely used as experimental diagnostics to provide quantitative information about plasma sources, especially for transient events such as plasma gun firing, laser plasma exploding, Z-pinch discharges, as well as many other nonlinear plasma phenomena such as magnetic shocks, reconnection, relaxation, etc.[72] Measuring the magnetic field in these cases can be very challenging for the following reasons: 1) the B-dot probe needs to have a sufficiently fast response time, faster than the event time scales; 2) it needs to have good robustness, and strong noise resiliency since for many events the environment is electromagnetically noisy; 3) it must be small enough that its presence does not greatly alter the plasma formation and evolution it is trying to measure; and 4) it has to be sensitive enough to pick up weak magnetic fields (a few Gauss in many cases), while also worrying about point #2. For a B-dot probe linear array, the uniformity, isolation, and alignment of each coil make the array difficult to build.[73]

The linear probe array presented here was designed for the PBEX project. Instead of winding coils manually, commercial chip inductors were employed for their precise dimensions, consistency, and ease of replacement. The linear magnetic probe array was placed in front of the plasma gun, as shown in Figure 2.28, left. The recorded signals were then analyzed to develop a complete 3D vector space plot. Contour maps of the magnetic field evolution as plasma flowed past the probe array were also constructed, as indicated in Figure 2.28, right.
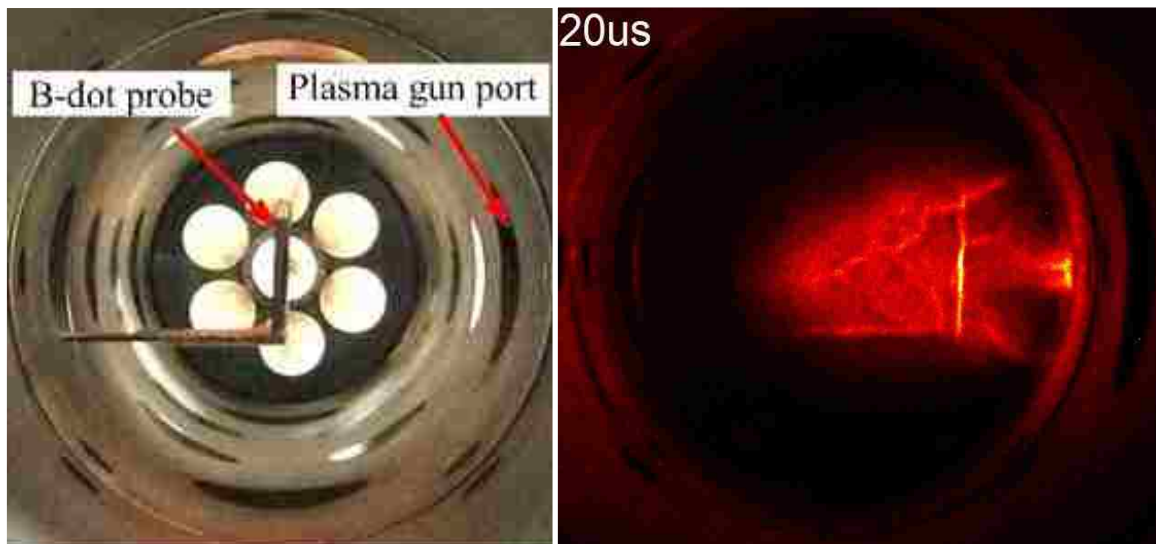
Figure 2.28. Magnetic probe (labeled B-dot probe) is placed in front of coaxial plasma gun (Left). Plasma flow (false color) past B-dot probe array (Right).

2.3.5.1 B-dot probe design and construction

Thirty-three commercial chip inductors with 66 turns each (inductance = 8.2±5% µH) were used (Coilcraft Inc. model 1008CS-822XJLB). The nominal dimensions of the chip inductors are: 2.92 mm × 2.79 mm × 2.03 mm, as shown in Figure 2.29.[74]
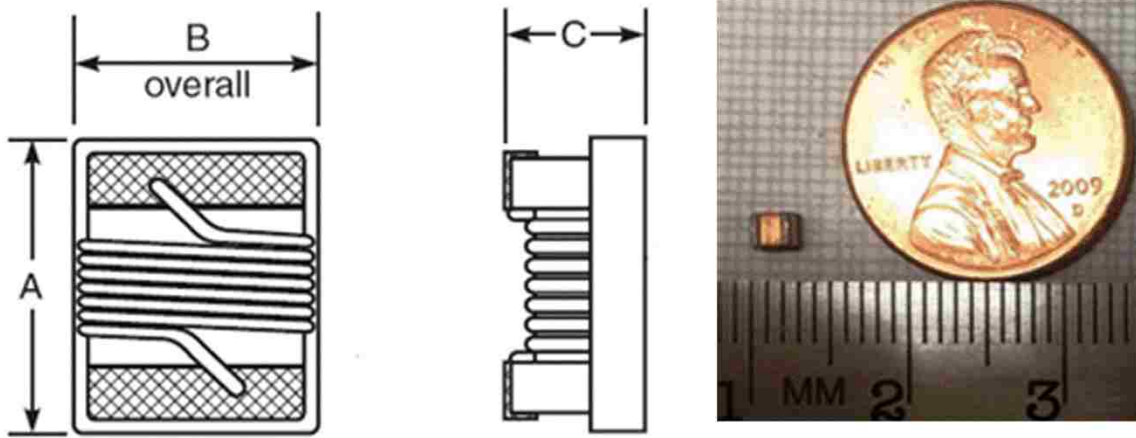
Figure 2.29. Chip inductor (1008CS-822XJLB) dimensions A: 2.92 mm, B: 2.79 mm, C: 2.03 mm, J = 5%, L= RoHS compliant silver-palladium-platinum-glass frit, B = In tape, but not machine ready.

The thirty-three inductors were grouped into 11 clusters, glued to 11 notch channels of a custom made Delrin probe holder, shown in Figure 2.30, Bottom. In each channel cell, three chip inductors are held together to measure BdotX, BdotY, and BdotZ (Cartesian coordinates), as indicated in Figure 2.30, Up. The spacing between each notch is 8.55 mm, thus the effective probe length is 108.55 mm.

Pairs of twisted magnet wires (38 AWG) were utilized to eliminate magnetic pickup noise, and soldered to the terminals of the inductors. Resistance of each individual wire strand was 617.0-681.9 ohms/1000 ft at 20 C. Overall diameters of each strand ranged from 0.0042" to 0.0047". Each twisted pair of wires was through fed he stainless steel probe shaft, and connected to a T-shape terminator's panel, then via L00 (Lemo 00 compatible) to SMA female, RG174 coaxial cable to 40MHz, 12-bit data analog digitizers system (Joerger Model TR). The soldering of the wires was done manually.
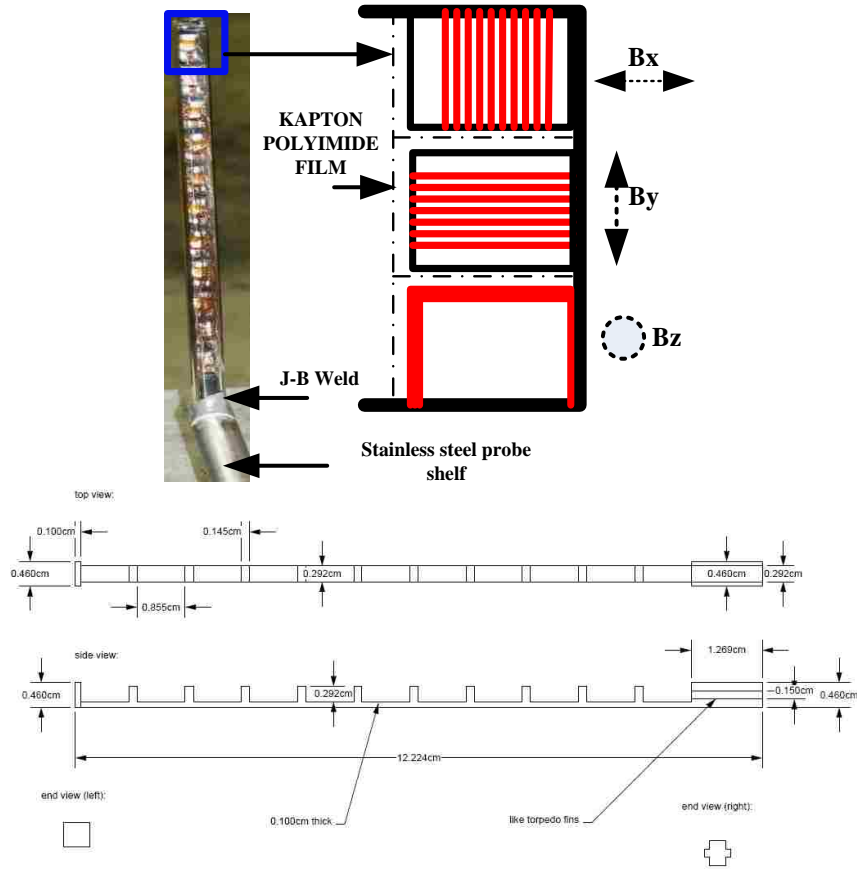
Figure 2.30. B-dot probe array design and single cluster configuration.

A razor was used to strip the insulation enamel from the wires. Kapton polyimide film was wrapped around the chip inductors to prevent electrical contact with one another. A square cross-section (5mm×5mm) quartz glass tube was used as the probe housing. A 1/2-inch diameter stainless steel shelf was used to provide mechanical support to the probe. The glass housing was glued to the tube using J-B Weld, as indicated in Figure 2.30. Furthermore, another 3/4-inch diameter stainless steel tube was employed to cover the probe's glass housing and to prevent electrostatic pickup during the plasms gun's operation, shown in Figure 2.31. The glass housing also acts as an isolation between probe wires and the stainless-steel shield tube. Finally,

another glass tube was placed over the stainless-steel tube to prevent electrical interaction with the plasma.

Figure 2.31. Stainless steel tube installation to eliminate electrostatic pick up.

2.3.5.2 B-dot probe linear array calibration

A. B-dot probe calibration principle

Using Faraday's law, the induced voltage in a closed circuit is equal to the time rate of change of the magnetic flux through the circuit as shown in Equation 2.10:

$$V = -\frac{d\Phi}{dt}$$

(2.10)

where V is the induced voltage, and ϕ is the magnetic flux through the close circuit. The magnetic flux is defined as the quantity of magnetism through a closed surface. For a plane circuit, it depends on three main factors:[75]

1) The magnitude of the magnetic field (B)

2) The closed loop area (A) of a single turn as well as the number of turns (N)

3) The orientation of the closed loop in the magnetic field (which is $\pi/2$ in this case)

The induced voltage can be expressed in above variables as $V = -\text{NA}\frac{d\text{B}}{dt}$. For practical

purposes, the values of A and N can be combined into one factor, which is referred to as the

calibration constant, **C**, in this section. Then equation 2.10 can be rewritten as

$$V = \text{C}\frac{d\text{B}}{dt} \tag{2.11}$$
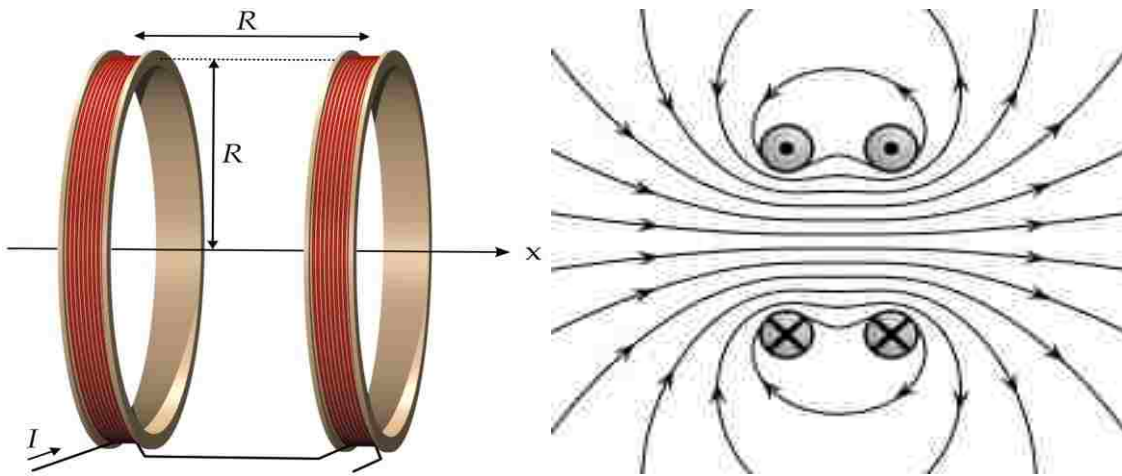
Figure 2.32. Helmholtz coil and magnetic field. Picture is taken from[76].

To obtain **C** for the chip inductors, B-dot probe calibration is necessary. A common

calibration method is to create a magnetic field source, well-known in magnitude and

orientation to calibrate the B-dot probe output signals.[77] The simplest way to generate a known

uniform magnetic field is using a Helmholtz coil because it is easy to build and has a relatively

uniform magnetic field near its center axis. It consists of two circular coils of the same radius

and number of turns which share a common axis. The distance between the two coils should

be equal to its radius as shown in Figure 2.32. When the same strength current flows in the

same direction in both coils, a uniform magnetic field is generated along the coil axis.

B. Helmholtz coil calibration

From the discussion above, to generate a uniform magnetic field along the axis, a current has to flow through the Helmholtz coil. The purpose of Helmholtz coil calibration is to set up the relation between the magnitude of the induced magnetic field versus the current flowing in the coil. The Helmholtz coil used for calibration with the dimension parameters are shown in Figure 2.33. The key parameters are: Coil 1 (W1), 23 turns; Coil 2 (W2), 20 turns; Diameter of the wire: 0.34 mm (AWG 28); Resistivity of Helmholtz coil is 2.95 Ohm and inductance is 87.58 µH measured by an LCR meter (HP 4263B).
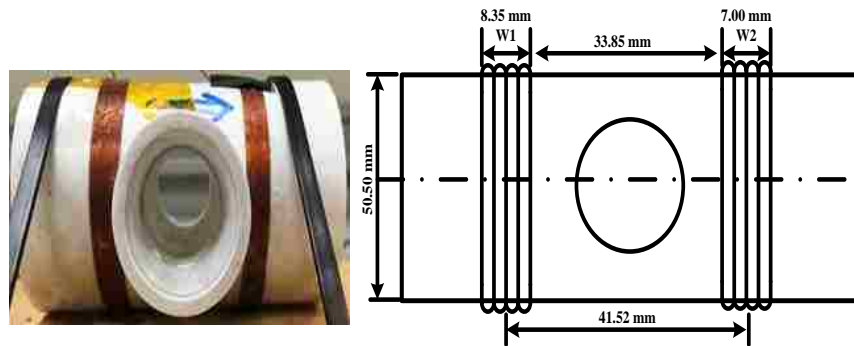
Figure 2.33. Helmholtz coil configuration and dimension parameters.

Simulation software FEMM was employed to get basic information about the magnetic distribution of the Helmholtz coil. Importing the Helmholtz coil parameters above into FEMM, the simulation results for the magnetic field distribution of the Helmholtz coil, and the magnitude of magnetic field along axis are shown in Figure 2.34. When the current, I, is 5A DC, the center magnetic field is 30 Gauss. The relation can be obtained from the simulation results using the formula below:

$$B\ (Gauss) = 6.0 \times I(A) \tag{2.12}$$
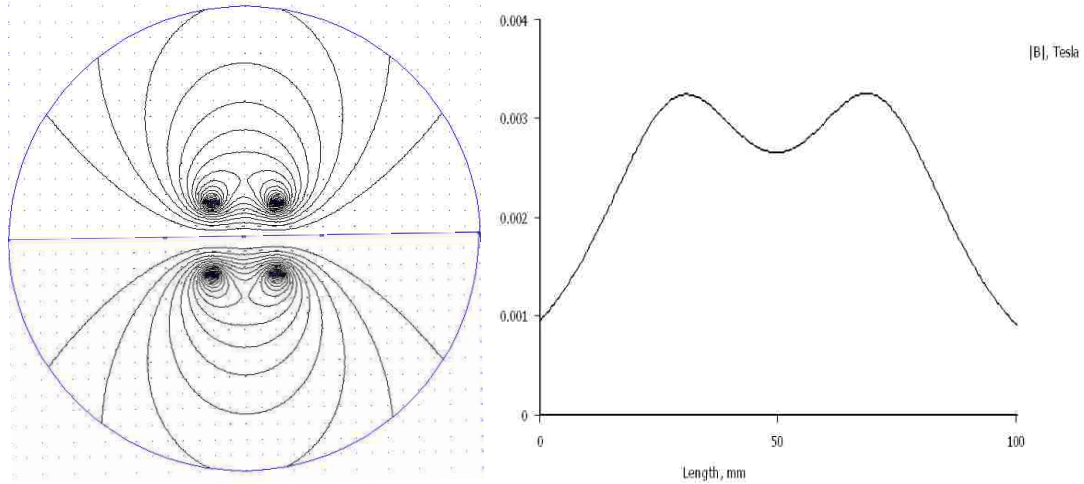
Figure 2.34. Left: the magnetic field distribution; Right: the magnitude of magnetic field along axis.

The schematic in Figure 2.35, Left, shows the Helmholtz coil calibration experimental set-up. The DC power supply provided DC voltage from 1 V up to 25 V in 1 V increments from which the current can be calculated based on Ohm's law. The current-limited resistor, R, is 25 Ω. A Gaussmeter (Lakeshore 455 DSP) was used to measure the magnitude of the induced magnetic field along the axis. Furthermore, a linear fit function from Matlab was applied to achieve the linear Eq.2.13 based on the measurements, as shown in Figure 2.35, Right. From this equation, for any current flowing through the Helmholtz coil, the magnitude of the induced magnetic field can be calculated.

$$B(Gauss) = 4.81 \times I(A) \tag{2.13}$$

C. B-dot probe calibration

As mentioned in Section 2.3.6, the B-dot probe array was used as a diagnostic for the PBEX project, in which the magnetic field oscillation frequency is typically on the order of a few hundred kilohertz. To calibrate the B-dot probe array over the frequency range of the experimental measurement, a DC to 1MHz magnetic field was generated by the Helmholtz

coil. The experiment set up is shown in Figure 2.36. The function generator (8116A Hewlett Packard) was utilized for frequency sweeps. V_R, V_{Total}, and $V_{Measure}$ are measured by an oscilloscope (Tektronix TDS 644A) with 1 MΩ setting on all channels.
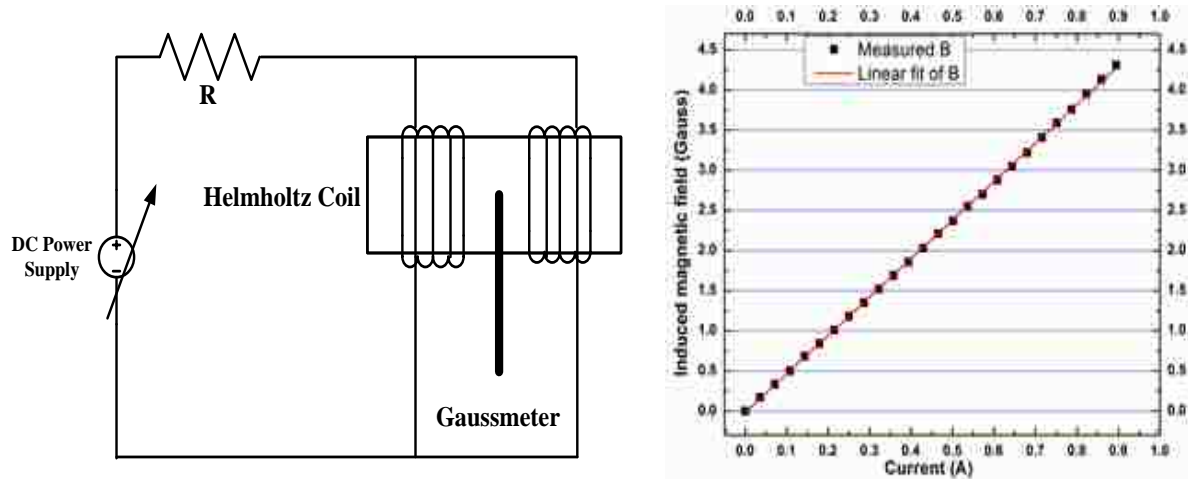
Figure 2.35. Left: Helmholtz coil calibration schematic; Right: Calibration result of Helmholtz coil.

From the circuit diagram, it is assumed that the current flowing through the Helmholtz coils follows the relation: $I=I_m\sin(\omega t)$ where I_m is the current magnitude and ω ($2\pi f$) is the angular frequency.
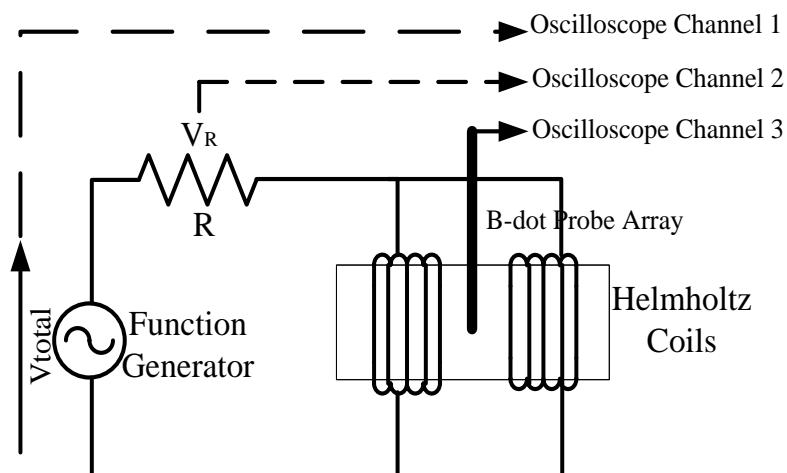
Figure 2.36. Helmholtz coil frequency sweep calibration experiment setup.

Using Eq. 2.13, the magnetic field generated by the Helmholtz coil was calculated as:

$$B = 4.81 I_m \sin(\omega t) \text{ and } |B| = 4.81 I_m \tag{2.14}$$

Combining this with Eq.2.11 yields:

$$|V_{Measure}| = \left| C \frac{dB}{dt} \right| = |4.81 C I_m \omega \cos(\omega t)| = 4.81 C I_m \omega \tag{2.15}$$

For I_m, considering the Helmholtz coil as an inductor,

$$I_m = \left| \frac{V_{HC}}{Z_{HC}} \right| = \left| \frac{V_{HC}}{\omega L_{HC}} \right| \tag{2.16}$$

From RL circuit analysis theory,

$$|V_{HC}| = \sqrt{V_{Total}^2 - \left[\frac{V_R}{R}(R + R_{HC}) \right]^2} \tag{2.17}$$

Combining Eq. 2.15, 2.16 and 2.17, the equation of the calibration factor C can be expressed as:

$$C = \frac{|V_{Measure}| L_{HC}}{4.81 \sqrt{V_{Total}^2 - \left[\frac{V_R}{R}(R + R_{HC}) \right]^2}} \tag{2.18}$$

where $V_{Measure}$ is the voltage measurement from B-dot probe (V), and V_R, and V_{Total} are indicated in Figure 2.36. As mentioned above, R_{HC} is 2.95 Ω, and L_{HC} is 87.58 μH. The magnetic field, which is numerically integrated using the calibration factor C, has units of Gauss.

Among all the 33 chip inductors, 4 chips (B_{X3}, B_{Y3}, B_{Y4} and B_{Z4}) were chosen randomly for the calibration process. The signal from the probes were recorded during the variation of the Helmholtz coil currents' magnitude and frequency:

1) For B_{X3}, the calibration shows that the relation between the measured voltage signal from the B-dot probe and the magnetic field is: $1V \propto 0.1152$ Telsa $= 1152$ Gauss.

2) For B_{Y3}, the calibration shows that the relation between the measured voltage signal from the B-dot probe and the magnetic field is: 1V∝ 0.1337 Telsa = 1337 Gauss.

3) For B_{Y4}, the calibration shows that the relation between the measured voltage signal from the B-dot probe and the magnetic field is: 1V∝ 0.1243 Telsa = 1243 Gauss.

4) For B_{Z4}, the calibration shows that the relation between the measured voltage signal from the B-dot probe and the magnetic field is: 1V∝ 0.1314 Telsa = 1314 Gauss.

The average value of the calibration constant was **1261.5** for the linear probe array. This constant was used in the numerical integration of B-dot data.

D. Post-shot numerical integration

Magnetic probe data can be obtained at a variety of azimuthal positions. Compiling data from multiple shots in order to develop a complete picture of the magnetic configuration proved unfeasible due to shot-to-shot irreproducibility.[4] Although shots with identical gun parameters generate qualitatively similar magnetic field formations, characteristics such as magnitudes and time offsets were often inconsistent. The signals from the thirty-three B-dot inductor linear probe array were recorded for each shots using three analog digitizers for the X component, Y component, and Z component respectively. The details are provided in Section 2.3.7. The sampling rate for the raw data was 40 MHz (0.025 μs), and the integration was performed numerically. The distinguishing advantage of employing fast, high bandwidth digitizers was that they significantly reduce the numerical integration error by decreasing the integration step size[78]. Also numerical integration requires no additional circuitry added to the experimental set-up. The resulting magnetic field is then determined using Eq. 2.19:

$$B(t) = C \int_{t_1}^{t_2} V_p(t) dt \tag{2.19}$$

Numerical integration can be accomplished using various techniques. Note that digitizers can add a small offset to the integration signals due to a rising or falling baseline. The method that this dissertation utilized for calculating the offset was to collect an initial sequence of data in the pre-trigger time window when the magnetic field was not present. The average voltage of this interval was the offset, which can be subtracted from the raw data before it is integrated.
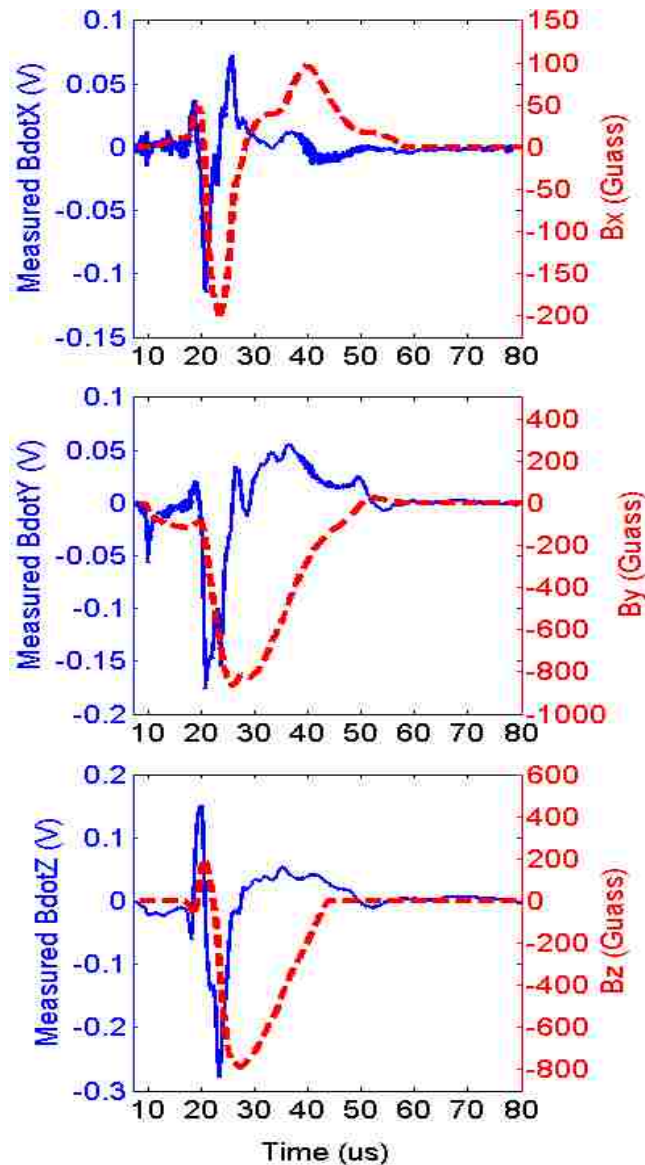
Figure 2.37. Raw and integrated data signals of the B-dot probe position at R=2cm and 10cm away from the gun port.

Figure 2.37 shows an example of the raw B-dot data (dB/dt), and integrated signal, B, at a distance of 10 cm from the plasma gun port, and a radius of 2cm from the gun axis. Using the Single Shot Propagation Inference (SSPI) method introduced by Yee and Bellan,[4, 66] it is possible to obtain approximate information on magnetic topology from one single discharge.

2.3.6 Control trigger system and data acquisition system

2.3.6.1 Control trigger system

From the discussion above, several pulse power systems (bias coil, gas valve, and main cap-bank for the coaxial gun) need to be triggered in a proper time sequence for the plasma gun operation, as well for the data acquisition system to digitize and record the probe signals. The digital delay generator (California Avionics Laboratories, INC. Model No. IO3CR) was employed to provide the multiple trigger signals for the pulse power systems.
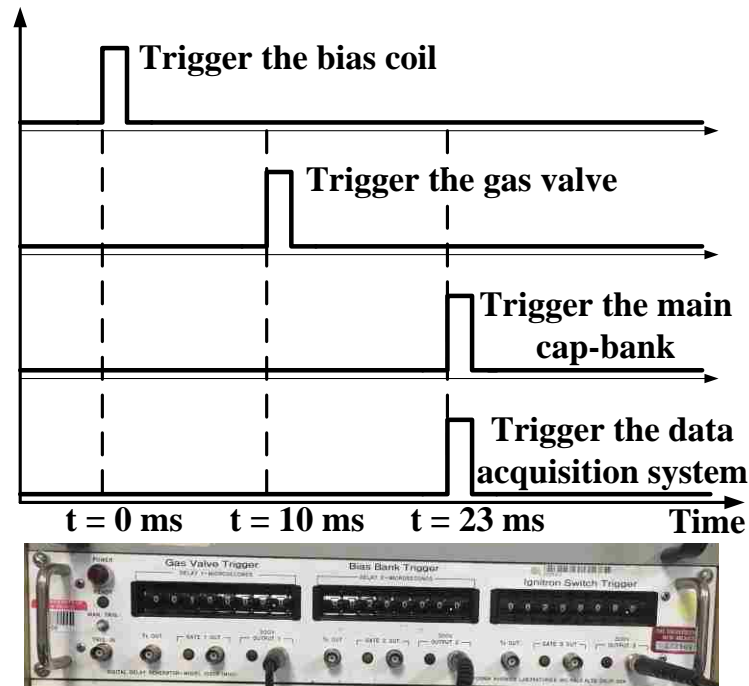
Figure 2.38. Typical trigger signal time consequence, employing digit delay generator (Model No. IO3CR).

69

A typical trigger sequence is as follows: (1) the bias coil is fired at t = 0 ms, (2) the gas valve is fired at t = 10 ms (experimentally decided, accommodating the neutral gas travel time through the gas feed line into the plasma formation region), (3) the main cap-bank ignitron-switch is trigged at t = 23 ms (considering the 23 ms rising time of the bias coil power system to reach the maximum bias flux as discussed in section 2.2.4) with gas breakdown typically occurring 2 - 3 μs later. At the same time (t = 23 ms), the digitizer data acquisition system is triggered, starting to record the probe data. The timeline is exhibited in Figure 2.38.

2.3.6.2 Data acquisition system
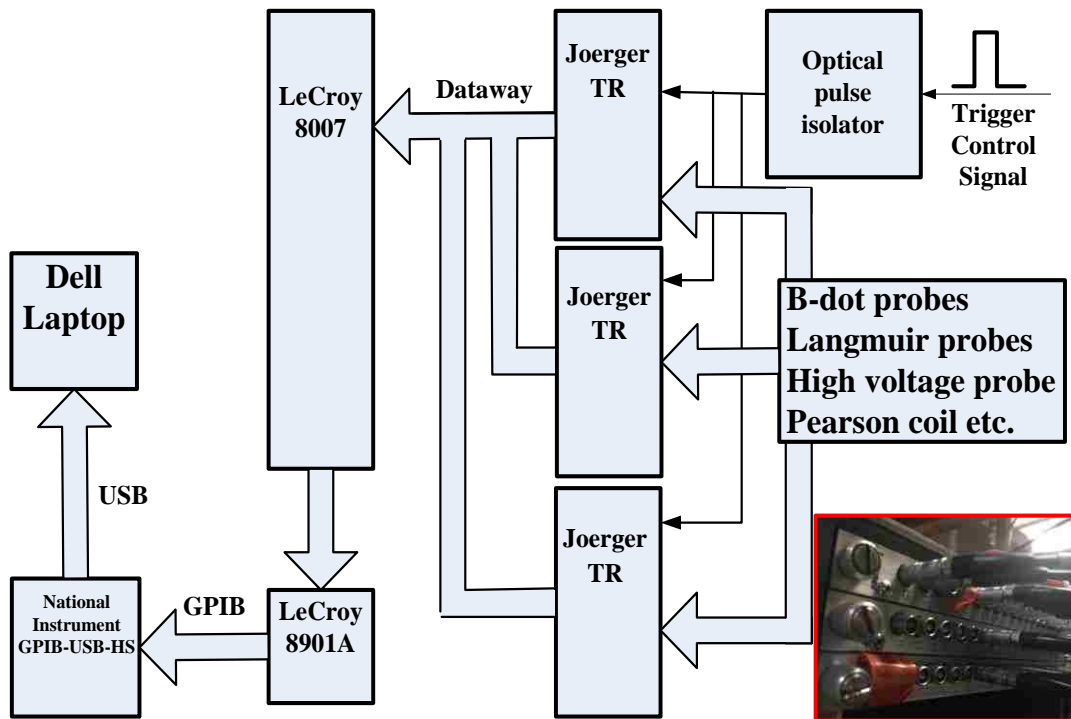
Figure 2.39. Layout of PBXE diagnostic, triggering, and data acquisition systems. Digitizer Model TR pictured at right bottom with B-dot probes connected to individual channels.

The data acquisition system is primarily made of three digitizers, which consist of 48 individual channels in total which makes it possible to record all thirty-three B-dot probe signals from one single shot, and therefore, obtain a complete magnetic field picture. The

digitizer is a Model TR from Joerger Enterprises, INC. Each analog digitizer has 16 individual channels. Each channel has a sampling rate of 40 MHz, a 12-bit resolution, 100 kΩ input impedance, 512 kB memory, and an input range of -5 V - 5 V with adjustable offset.

These digitizers communicate with a laptop computer through a CAMAC to GPIB interface (LeCroy 8901A) and a GPIB to USB interface (National Instruments GPIB-USB-HS), as shown in Figure 2.39. LeCroy 8901A provides the bidirectional GPIB (IEEE-488) communication between the laptop and the digitizers. The laptop computer, via pre-installed software (LabVIEW), can download, control, and setup commands to the digitizers, and upload data and waveforms from them.

All three digitizers, and the LeCroy 8901A interface were housed and powered by transportable mainframe (Model No. LeCroy 8007)[79] via IEEE-583 Standard Instrument Slots. All magnetic probe and gun diagnostic signals were digitized on this system.

2.4 Summary

This chapter focus was on the mechanical and electrical parts of the coaxial plasma gun. Details have been given on the design, construction, calculations, simulation, and the performance of the main cap-bank, the bias coil, the gas valve, and the diagnostics for PBEX project. This chapter's discussion has little relation to the plasma physics but the design details it covers, hopefully, can serve as a reference for prospective students who will operate the coaxial gun for the plasma physics research. As is discussed in Chapter 3 and 4, the geometry of the gun, the main cap-bank discharge current, and the bias magnetic flux induced by the bias coils are the key parameters to determine the gun's performance, and the plasma formation topology. Chapter 2 gives the detailed engineering design to show how these parameters are chosen and calculated, which makes it easy and clear to convert the directly measurable

parameters such as the main cap-bank discharge voltage, the bias discharge voltages, and the natural gas pressure in the gas feedlines into the physical parameters of the gun such as the current density, the azimuthal magnetic field strength, and the bias magnetic tension etc.

For experimental research, the hardware setup and diagnostics are the basis to make it all happen. The hardware design, construction, validation, and layout are time-consuming and sometimes "tricky" requiring experimental experiences and related knowledge.

Chapter 3 Plasma Gun Operating Regimes Classification and Performance Validation

3.1 Introduction

The coaxial plasma gun accelerates plasma into the main chamber through the Lorentz force ($\vec{J} \times \vec{B}$), associated with the gun discharge current. This force is proportional to I_{gun}^2. On the other hand, the bias magnetic field tension force, associated with the gun bias flux and proportional to Φ_{bias}^2, acts in opposition to the Lorentz force, trying to restrain the plasma from exiting the gun muzzle. The competition between these two magnetic forces determines the resulting plasma formation. If the magnetic tension of the bias field balances the magnetic pressure of the $\vec{J} \times \vec{B}$ force, a spheromak-like configuration is formed, separating from the gun muzzle by an X-point in the magnetic field configuration. However, if the bias field is insufficient, the strong $\vec{J} \times \vec{B}$ forces will launch a jet formation with a helical magnetic field structure. Conversely, if the bias magnetic field is sufficiently strong, the plasma cannot leave the gun and remains "stuffed" in the gun, which is why the bias magnetic field may also be referred to as the stuffing field or stuffing flux.

From this simple discussion, it is clear that there is a threshold ratio value of the gun discharge current, I_{gun}, and the bias flux, Φ_{bias}, for determining the coaxial gun operation regions. Experimentally, a threshold operation value, $\lambda \equiv \mu_0 \frac{I_{gun}}{\Phi_{bias}}$, has been reported.[80] Using this relationship, the coaxial plasma gun behavior can be described naturally: when λ is below the threshold value, the plasma cannot detach; when λ is close to the threshold value, a spheromak configuration is formed; and when λ is much bigger than the threshold value,

corresponding to a strong I_{gun} and a low, or zero bias flux, Φ_{bias}, the plasma takes on a jet configuration. Varies λ parameter regimes are explored in the following sections along with detailed discussions of the plasma dynamics observed, as well as theoretical models when possible.

3.1.1 Operation theoretical analysis

The simplest model assumes the toroidal magnetic field is $B_{tor} \cong \frac{\mu_0 I_{gun}}{2\pi r}$ and the poloidal magnetic field is $B_{pol} \cong \frac{\Phi_{bias}}{\pi r^2}$. The threshold λ value from these parameters when the magnetic pressure exceeds the magnetic tension is $\lambda > \frac{2}{r}$ (yielding $\lambda_{critical} = 84.21 \; m^{-1}$ for PBEX), where r is the characteristic radius of the system, such as the radius of the entrance region (the outer electrode radius for PBEX case).[4, 66]

Based on an axisymmetric spheromak in an infinite cylindrical model, the threshold value has been calculated as:[81] 1) for m = 1 symmetry, $\lambda > \frac{3.11}{r}$ (yielding $\lambda_{critical} = 130.95 \; m^{-1}$ for PBEX), where 3.11 is the first zero of the Bessel function J_0; 2) for m = 0 symmetry, $\lambda > \frac{3.83}{r}$ (yielding $\lambda_{critical} = 161.26 \; m^{-1}$ for PBEX), where 3.83 is the first zero of the Bessel function J_1.

Also based on the gun's specific physical geometry, a simple formation theory is presented as follows:[45] a thin radial current sheet is assumed to move freely axially through the annulus between the anode and the cathode as shown in Figure 3.1. Force balance on the current sheet requires that the magnetic tension of the magnetic flux be equal to the $\vec{J} \times \vec{B}$ force. Since the gun current produces the azimuthal magnetic field $B_\varphi = \mu_0 I_{gun}/2\pi r$ and $\beta \ll 1$, the pressure on the back of the sheet can be expressed as:

$$P = \frac{B_\varphi^2}{2\mu_0} = \frac{\mu_0 I_{gun}^2}{8\pi^2 r^2} \tag{3.1}$$

Then the $\vec{J} \times \vec{B}$ force can be derived by integrating this pressure over the annular region

from r_{inner} to r_{gun} as shown in Eq. 3.2:

$$F = \int_{r_{inner}}^{r_{gun}} Pr\,dr\,d\varphi = \frac{\mu_0 I_{gun}^2}{4\pi} \ln\frac{r_{gun}}{r_{inner}} \tag{3.2}$$
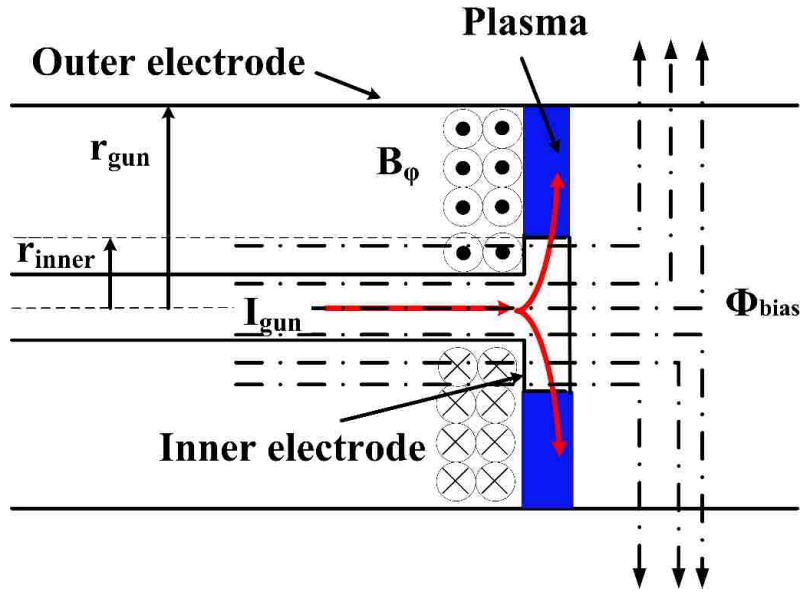
Figure 3.1. Diagram for the simple theory model analysis.

The increase of energy then can be expressed as $\delta W = F \cdot dl$. Energy is also stored in

the magnetic field. The energy per unit volume in a region containing a magnetic field B is

$W = \frac{B^2}{2\mu_0}$. It then can be shown that:

$$\delta W = \frac{B^2}{2\mu_0}\delta v = \frac{B^2}{2\mu_0} \cdot S \cdot dl = \frac{B^2}{2\mu_0}\pi r_{inner}^2 dl \tag{3.3}$$

Setting $(3.2) \cdot dl$ and (3.3) equal to one another and considering $\lambda \equiv \mu_0 \frac{I_{gun}}{\Phi_{bias}}$, and

$\Phi_{bias} = B_{bias}\pi r_{inner}^2$, one will get:

$$\lambda_{threshold} = \mu_0 \frac{I_{gun}}{\Phi_{bias}} = \frac{1}{r_{inner}} \sqrt{\frac{2}{(\ln\frac{r_{gun}}{r_{inner}})}} \tag{3.4}$$

Eq. (3.4) determines the threshold value, $\lambda_{threshold}$, according to this simple theoretical analysis. Considering the parameters (r_{inner}=1.27 cm from Figure 2.5 and r_{gun}=2.38 cm from Figure 2.16), the calculated threshold is $\lambda_{threshold}$= 140.51 m^{-1}. For the PBEX project, the measured $\lambda_{threshold}$ value is 170.37 m^{-1}, which is slightly greater than the calculated value of the gun threshold discussed above. Barners et al.[82] pointed out that for a coaxial plasma gun, the radial cross section of the plasma flow tends to form a narrow "dynamic nozzle" which accelerates the plasma flow to Alfvén speed. Considering the special compact cathode and anode's relative position in PBEX, this "nozzle" effect maybe the possible explanation for this $\lambda_{threshold}$ difference.
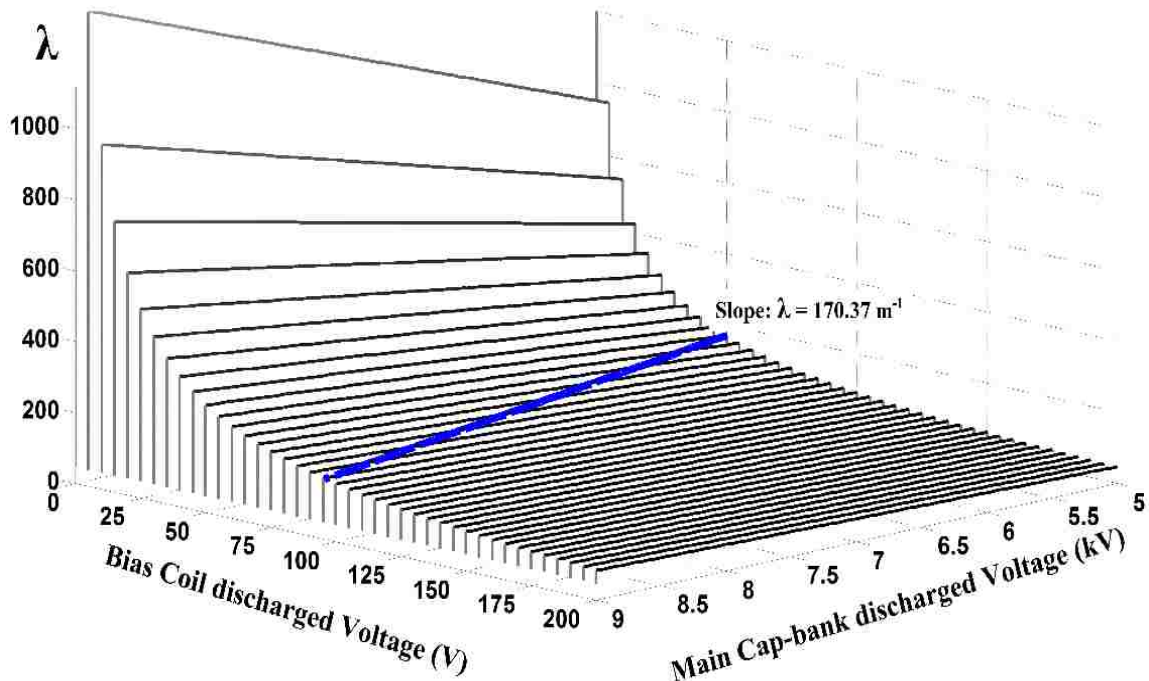
Figure 3.2. Plot of λ as a function of main cap-bank discharge voltage (kV) and bias coil discharge voltage (V).

Based on Eq.2.1 and Eq. 2.6, plotting λ as a function of main cap-bank discharge voltage (associated with $\mu_0 I_{gun}$) and bias coil discharge voltage (associated with Φ_{bias}), the threshold will be a line of slope $\lambda_{threshold}$, as shown in Figure 3.2, indicating the coaxial plasma gun can operate at a wide range of λ with various plasma formations.

These physics models, discussed above, strongly suggest that the threshold value of λ relies heavily on the particular gun's geometry, and can be determined only through a detailed experimental survey.

3.2 Camera images and movies

Diagnostic techniques using fast CCD camera imaging have become a mainstay in plasma physics research, and a very useful method for gaining spatial resolution of the plasma topology at a given time. Compared with direct probe measurements, camera images avoid the risk of perturbing the local plasma behavior since it is a passive measurement. Additionally, the camera images provide wide direct global information of the plasma morphology, structure, and properties. Thus, it is particularly simple but powerful tool for the PBEX project, specifically for investigating plasma magnetic topology.

As discussed in Chapter 2, the end-chamber window provides a generous view for camera access, allowing the coaxial gun generated plasma to be imaged as it launches from the gun port. Time sequences of pictures demonstrate qualitatively distinct plasma behavior as the coaxial plasma gun parameters per varied. Based on the images survey, plasma evolution and dynamics have been classified into four regions which will be discussed in detail in this chapter.

3.2.1 Region I: Jet plasma

In region I (as shown in Figure 3.4), there is no external bias magnetic flux applied (bias coil discharge voltage = 0). A plasma jet with a narrow front head is formed, and launched into the vacuum chamber purely by the main cap-bank discharge current, I_{gun}. In this region, indicated in Figure 3.4, a distinct narrow front head is formed at t = 16 us, followed by the jet body which starts to be kink unstable at t = 24 us. A detailed discussion of plasma characteristics and performance of this region is presented in Section 3.3.

3.2.2 Region II: Spheromaks-like plasma

In region II (as shown in Figure 3.5), a certain amount of external bias magnetic flux has been applied. At t ~13 μs, the plasma initially forms, and begins to leave the gun port following the bias magnetic field lines as indicating in Figure 3.3. At approximately t ~20 μs, plasma detaches from the gun port with a spheromak-like shape, propagating across the vacuum chamber. The leading edge (left-side) is especially bright with filamentary structures. More detailed measurements are presented in Section 3.4 to show the evidence that in region II, a spheromak-like plasma is generated by the co-axial gun.
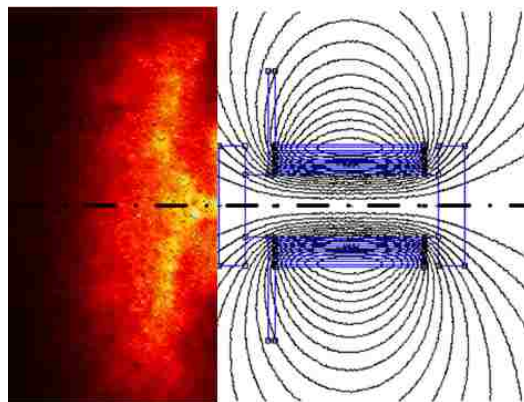
Figure 3.3. Region II initial plasma follows the bias magnetic field line: I_{gun}=76.42 kA and Φ_{bias}=0.365 mWb. (Shot No. 018042314).
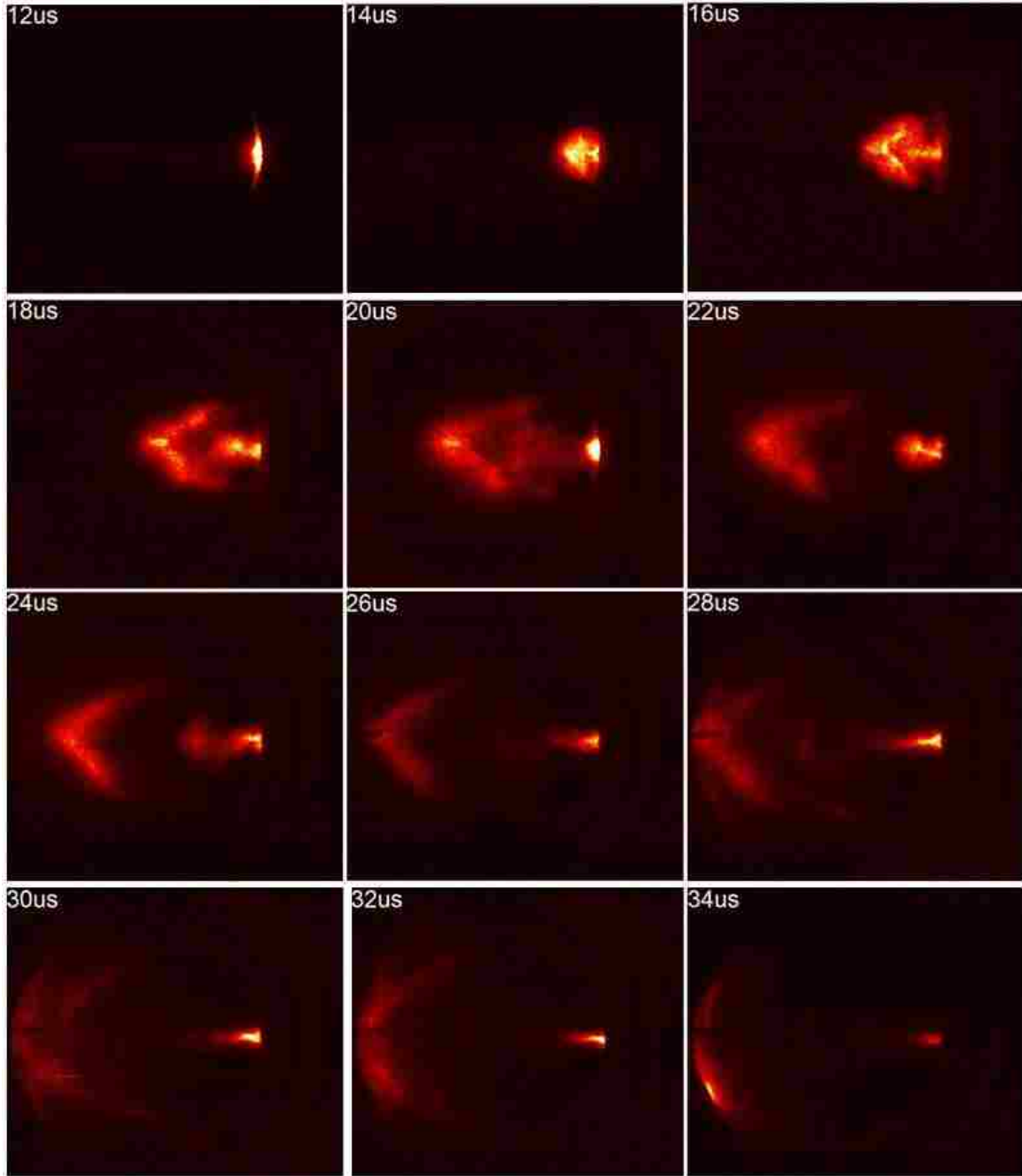
Figure 3.4. Side view image sequence for Region I with gun parameters: I_{gun}=81.14 kA and Φ_{bias}=0 mWb. (Shot No. 013042314).
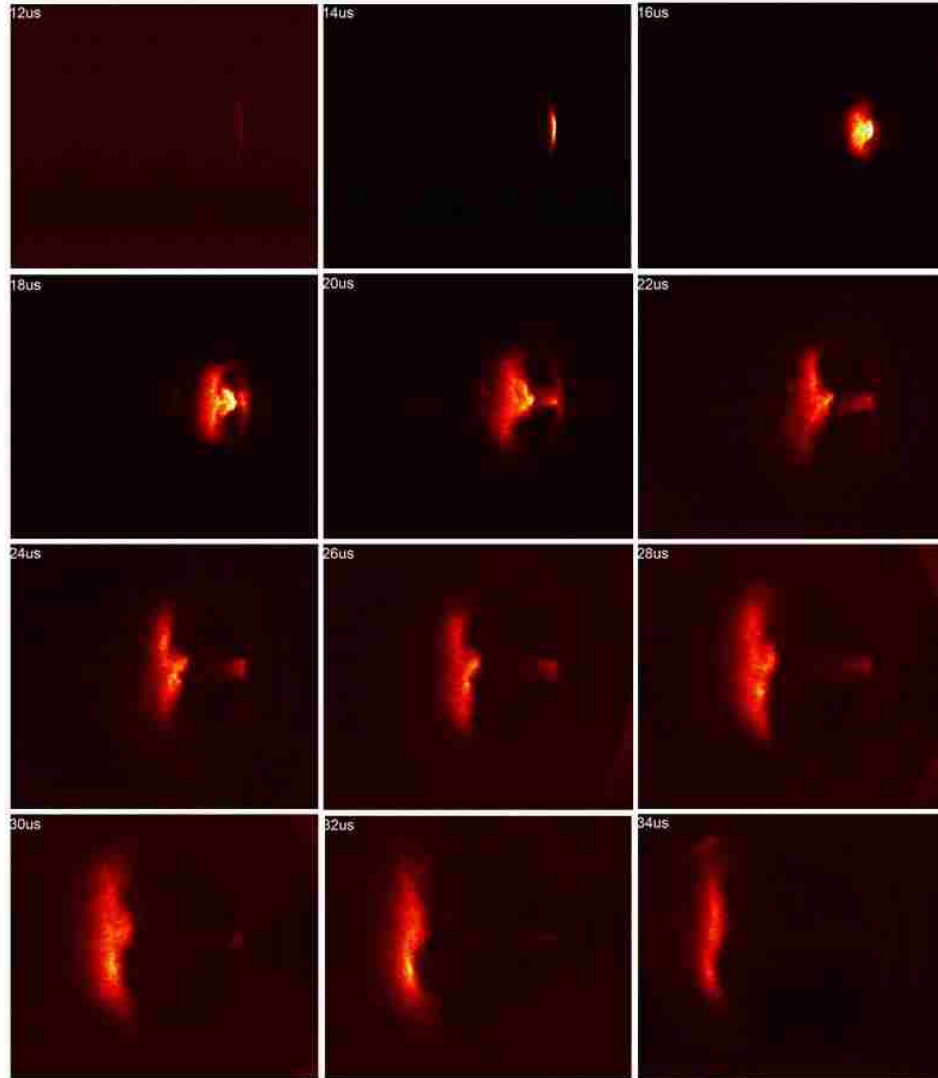
Figure 3.5. Side view image sequences for Region II with gun parameters: I_{gun}=76.42 kA and Φ_{bias}=0.365 mWb. (Shot No. 018042314).

3.2.3 Region III: Merging plasma

In this region (as shown in Figure 3.7), in sharp contrast with the other regimes, the plasma exhibits unique and interesting features of two stages. At the first stage (corresponding to I_{gun} first half-cycle), the plasma formation is similar to region II except the expansion rate is slower due to the increased magnetic tension force caused by the bias magnetic flux. Starting at around 43us, for the second stage (corresponding to I_{gun} second half-cycle), a second

plasma emerges at the gun port, propagates into vacuum chamber at the Alfvén speed, catches

the first plasma, and they merge together. This feature is illustrated by the serial images taken

from t = 41 μs to t = 61 μs in Figure 3.7.

At the same time, the Langmuir probe measurements also exhibit the plasma merge

feature for this region as shown in Figure 3.6. It clearly demonstrates that two I_{Sat} signals start

to merge at the distance z = 25 cm.
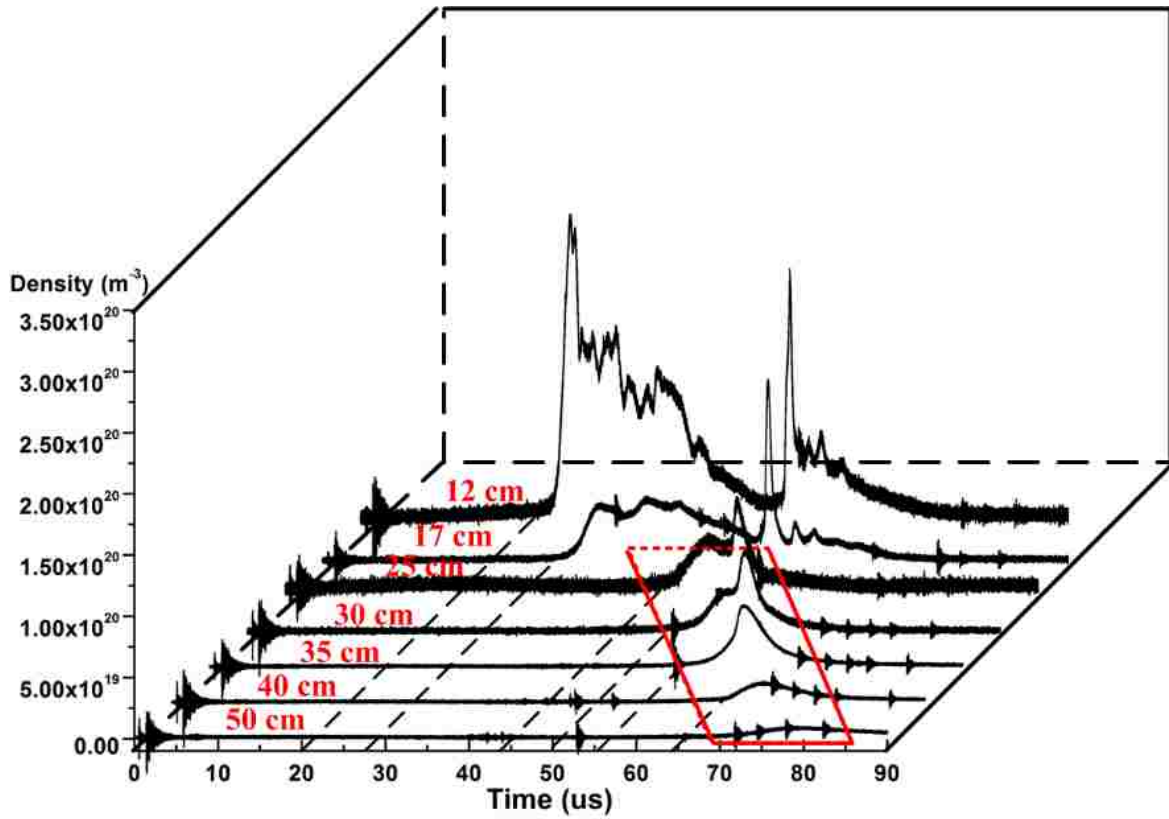
Figure 3.6. I_{Sat} density measurements at different locations along the chamber cross-section
to show the plasma merge feature for Region III.

This feature appears due to the interaction between the two discharge half-cycle of I_{gun}.

A crowbar circuit is under construction now (July,2016) to eliminate the second half-cycle.

While this feature is rich with interesting physics for further investigation, it is not within the

scope of this dissertation.
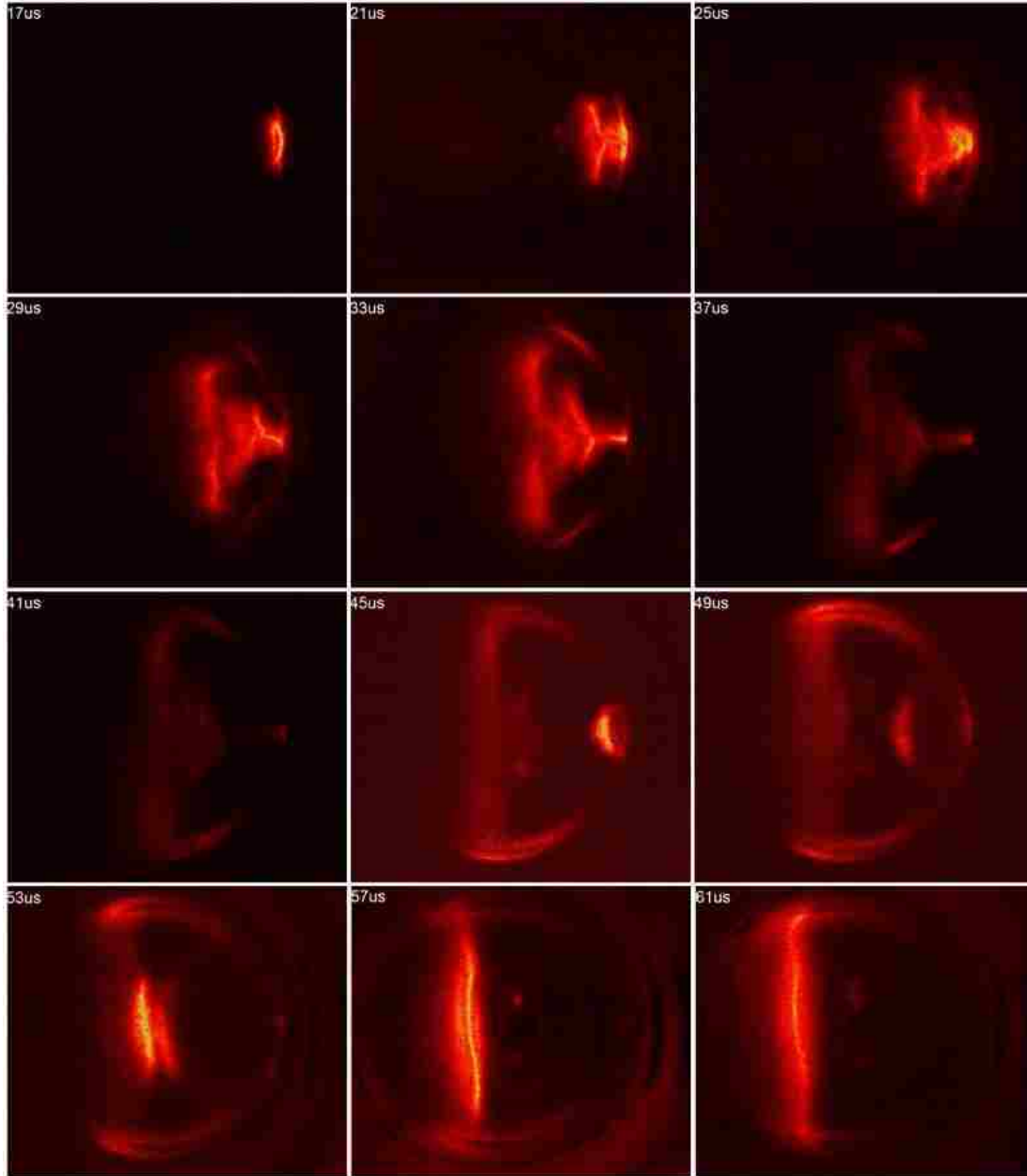
Figure 3.7. Side view image sequences for Region III with gun parameters: I_{gun}=75.48 kA and Φ_{bias}=0.802 mWb. (Shot No. 005042514).

3.2.4 Region IV: Stuffing plasma

In Region IV, plasma propagates very slowly from the gun port, barely leaves, then decays away in a short distance in the vacuum chamber, as depicted in Figure 3.8. The plasma

is confined successfully by the strong bias magnetic field flux, Φ_{bias}, also called "stuffed" in this region.
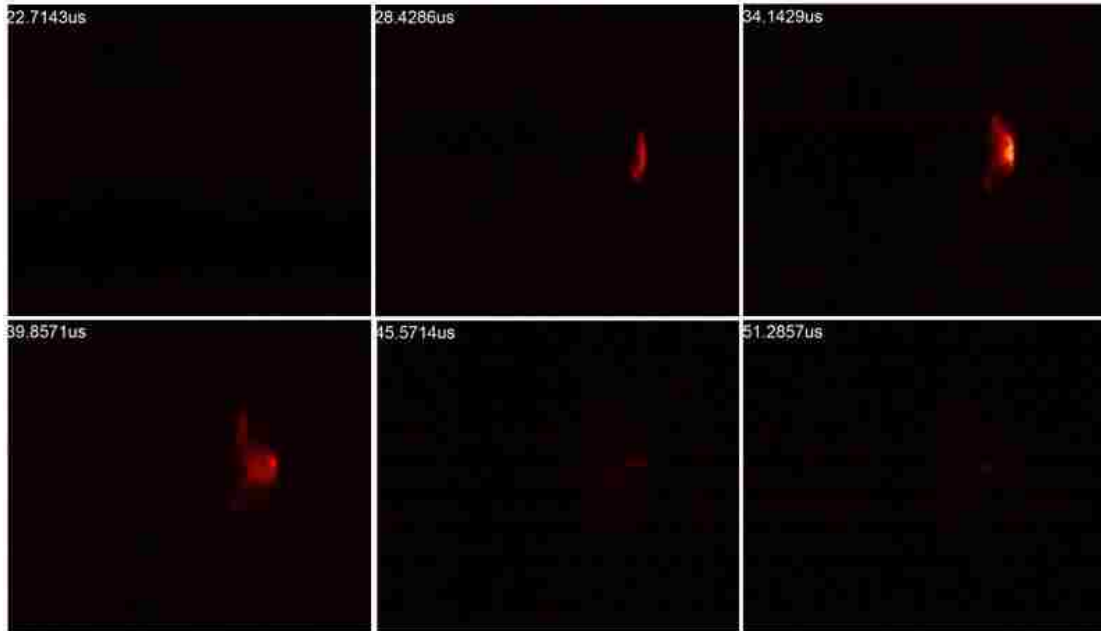
Figure 3.8. Side view image sequences for Region IV with gun parameters: I_{gun}=76.42 kA and Φ_{bias}=2.185 mWb. (Shot No. 062042314).

3.2.5 Propagation rate survey

Due to different bias magnetic field tension forces for these four regions, it is easy to predict that these cases can be distinguished by their propagation velocity. The sequences of images from Figure 3.4, Figure 3.5, Figure 3.7, and Figure 3.8 are used to estimate the propagation speed for these four regions. The data is plotted in Figure 3.9 with linear fits applied.

As Figure 3.9 indicates, the linear fit plots show that the propagation speed varies with bias magnetic flux, from 0.5 cm/us of Region IV to 3.6 cm/us of Region I. These results agree with the physics expected i.e., plasma motion is heavily restricted by magnetic tension forces provided by the applied bias magnetic field. Two key notes need to be addressed here: 1) for

all four regions, after the plasma leaves the gun port, it propagates at a roughly constant velocity which is easy to predict in the vacuum case. 2) for Region III, the velocity is estimated from the image data before the second plasma catches the first one.
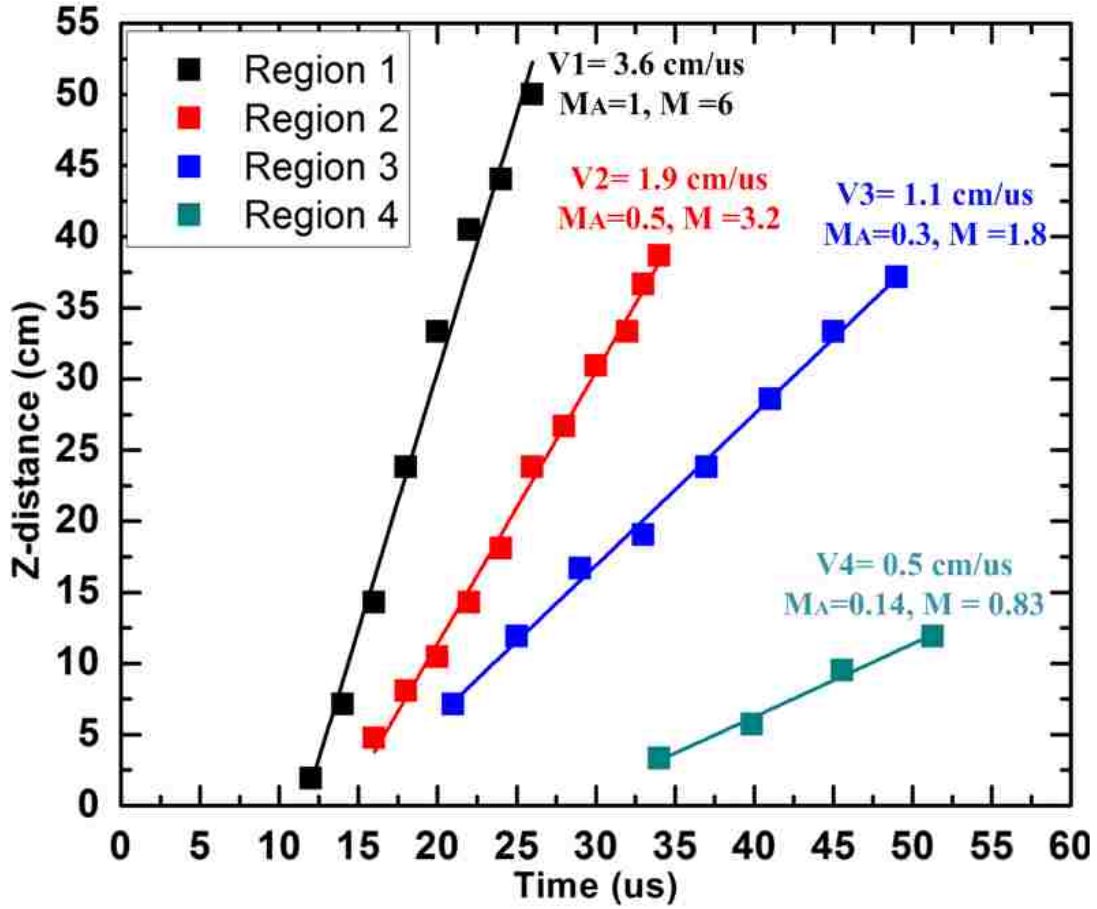
Figure 3.9. Plasma propagation velocity of the four regions, obtained from the sequences images data taken from CCD camera.

3.2.6 Plasma gun operation survey with λ_{gun} values

As discussed above, the key parameter, which governs the plasma gun's performance and generated-plasma formation, is $\lambda_{gun} = \mu_0 \frac{I_{gun}}{\Phi_{bias}}$, the ratio of the plasma gun discharged current to the bias magnetic flux. The images exhibited in this section directly show how the gun-generated-plasma formation is affected by the λ_{gun} settings. Numerous experiments have

been carried out, employing the high speed camera, to survey plasma formations associated with sweeping the gun current, I_{gun}, and the bias magnetic flux, Φ_{bias}, settings. The results are shown in Figure 3.10 with boundaries λ_{gun} values imposed. Each point stands for a series of 12 images obtained at a certain combined setting of I_{gun} and Φ_{bias}.
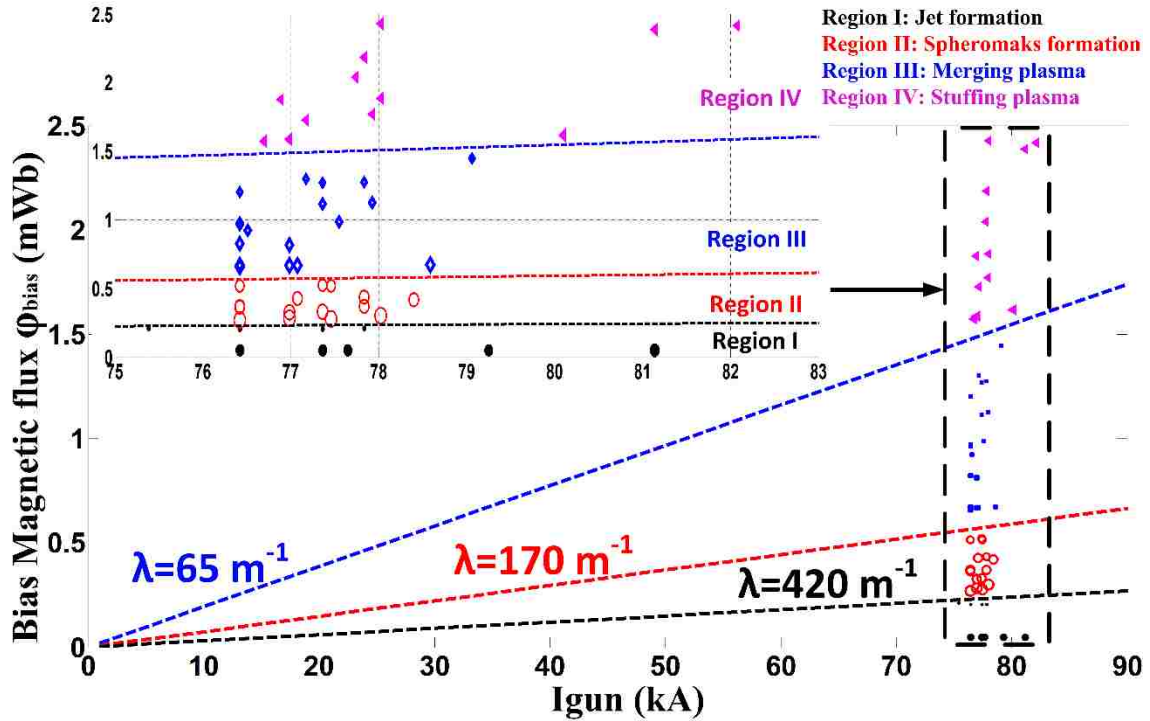
Figure 3.10. Region classification survey from I_{gun} and Φ_{bias} setting scans. Boundary λ_{gun} values are indicated respectively as 65 m^{-1}, 170 m^{-1}, and 420 m^{-1}.

3.3 Regime I: plasma jet formation and propagation into vacuum

MHD plasma jets exist in various systems in a wide range of physical dimensions, from laboratory experimental jets to astrophysical objects. In astrophysics, energetic, highly collimated, and relativistic jets are usually observed from active galactic nuclei (AGNs)-scale jets to stellar-scale jets. Figure 3.11 shows some typical examples: M87 AGN, radio galaxy 3C31 (NGC 383), and HH47 proto-stellar jet, respectively. Highly polarized synchrotron radiation is observed from both AGN jets and stellar jets. This suggests that jets have a strongly

organized magnetic field, which plays a crucial role in generating, collimating, accelerating, and propagating both AGN jets and stellar jets. The C31 jet and several other AGNs jets reveal a global m =1 kink-like instability,[83] shown in Figure 3.11 Pic B, implying a strong current along the jet propagation direction (defined as the z axis), or equivalently, a strong toroidal magnetic field around the jet. All these facts suggest the existence of a z-pinch-like mechanism, squeezing the plasma jet against the pressure gradient at the jet center region.
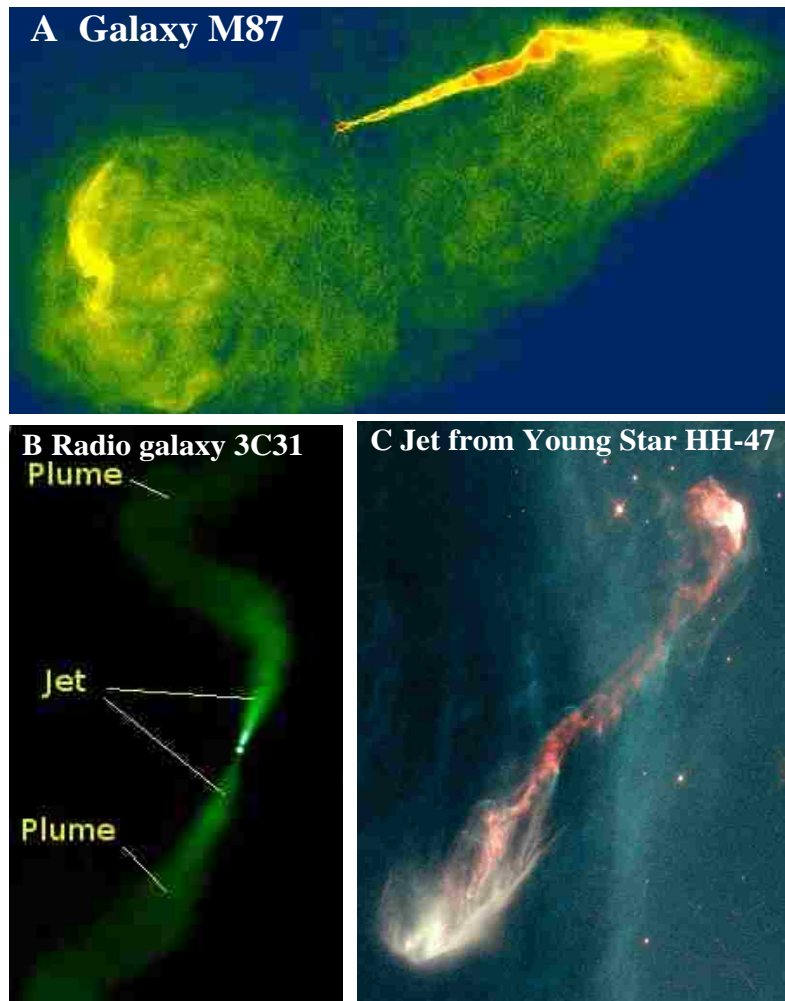
Figure 3.11. A: Radio image of the galaxy M87, taken with the Very Large Array (VLA) radio telescope.[84] Credit: National Radio Astronomy Observatory/National Science Foundation. B: False color image of radio galaxy 3C31 and its jet in 1.4 GHz radial band by VLA.[85] Credit: R. A. Laing, A. H. Bridle et al., NRAO. C: The view of a three trillion mile-long jet called HH-47.[86] Credit: J. Morse/STScI, and NASA/ESA.

Although observation, model analysis, and numerical simulation are all necessary approaches to investigate astrophysical jets, there is a natural limitation to these methods as discussed in Chapter 1. The laboratory experiments can fill the research gap of investigating the key physical processes in nonlinear systems, especially when the magnetic field is evolved. Caltech [29, 47, 87] has employed pulse power facilities, as shown in Chapter 1, to experimentally simulate these astrophysical jets. The experimental results provide a clear guide and strong motivation to analyze the PBEX data. In this section, the plasma jet's initial acceleration, jet-head velocity property, global helical magnetic field structure, and m=1 kink instability will be discussed in details. In this section, no bias flux is applied, or, equivalently, there is no initial external poloidal magnetic field.

3.3.1 Initial stage of plasma jet formation

To characterize a particular coaxial plasma gun, the initial stage heavily depends on the physical design parameters, such as: the capacitor bank characteristics, inner and outer electrodes radius ratio, electrode topological geometry, working gas employed, whether the gun is operated with bias flux (staffing flux) or not, etc[88].

A cylindrical system is utilized for analysis, illustrated in Figure 3.12. The origin is at the center of cathode, and the z axis is the plasma gun axis along the plasma flow direction, φ is the azimuthal direction about the axis, and r is the distance from the axis. At the same time, the φ direction is the toroidal direction and r, z directions are called poloidal direction. Flux coordinates will be used in this chapter when necessary.
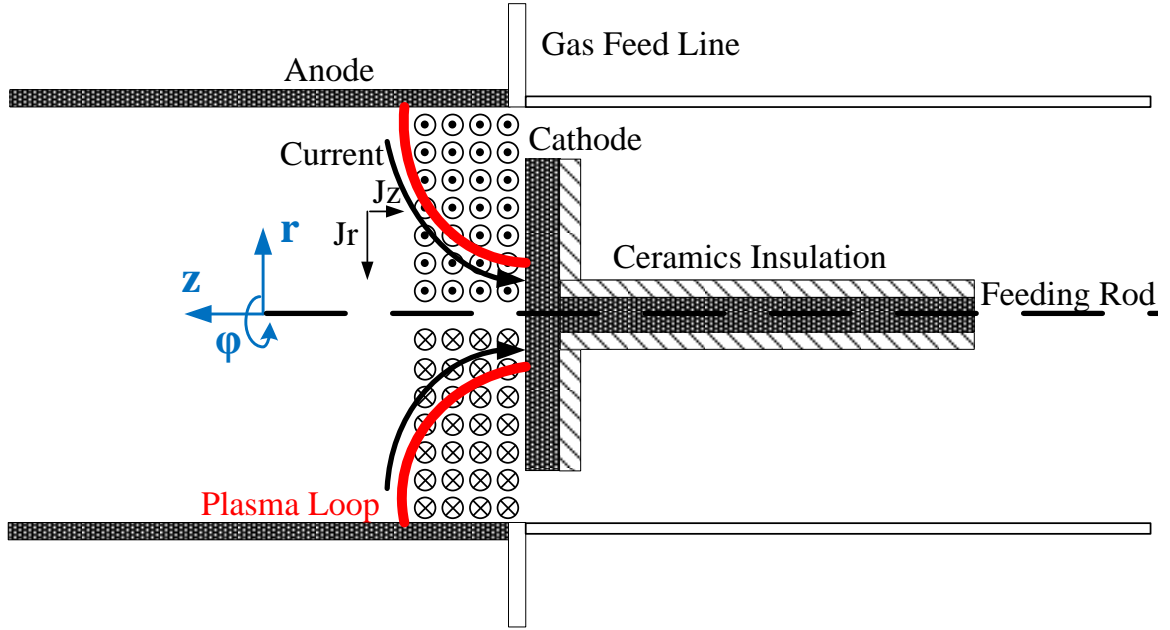
Figure 3.12. Discharge current (J_r and J_z) and azimuthal magnetic field configuration (B_φ) with a cylindrical coordinate applied during initial stage (Step 1).

In the initial stage, the ignitron-switched main cap-bank applies a large voltage (5.5 kV - 9.0 kV) across the electrode gap. Due to the nature of the ignitron, this happens very quickly. According to Paschen breakdown criteria,[89] the high voltage breaks down the neutral argon gas, ionizes the gas into a plasma, and subsequently drives a current through the resulting plasma, creating an initial azimuthal magnetic field (B_φ) as shown in Figure 3.12. The initial current and magnetic field geometry can be viewed from another aspect: Figure 3.13 exhibits the simulation results of the initial stage, from which it is easy to get the topological distribution of the radial current J_r and the azimuthal magnetic field B_φ.
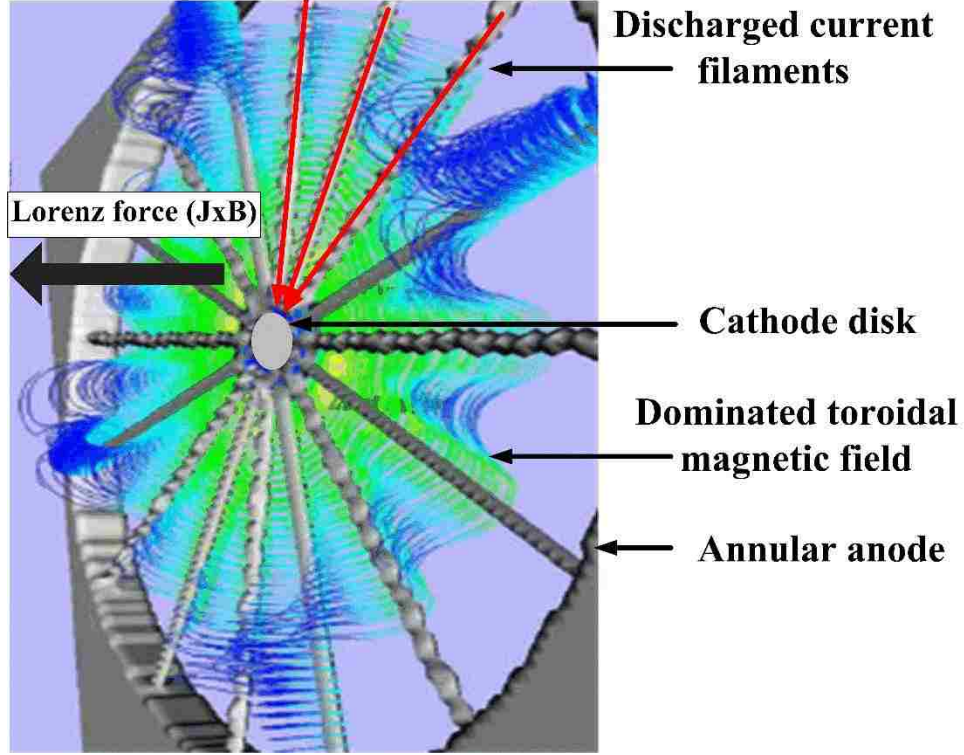
Figure 3.13. Radial discharge current filaments (grey color) connecting inner and outer electrodes. The dominant magnetic field is toroidal (colored) and global Lorenz force (J×B) is along z axis. Picture is taken from [90].

Now we consider the plasma dynamics, namely the Lorentz force: $F \equiv \vec{J} \times \vec{B} = (J_r + J_z) \times B_\varphi = J_r \times B_\varphi + J_z \times B_\varphi = J_r B_\varphi \hat{z} + J_z B_\varphi (-\hat{r})$. The force can be decomposed into z and r components as follows:

$$F_z = J_r B_\varphi \hat{z} \text{ and } F_r = -J_z B_\varphi \hat{r} \tag{3.5}$$

The minus sign of F_r means the direction is radially towards the center, which is the pinch force. The z component is the force that produces the axial expansion of the plasma. Applying Ampere's law, the toroidal magnetic field B_φ can be obtained as below:

$$B_\varphi(r) = \frac{\mu_0 J_z}{2\pi r} \hat{\varphi} \tag{3.6}$$

where J_z is the discharge current density in the z direction, and r is the radius.

89
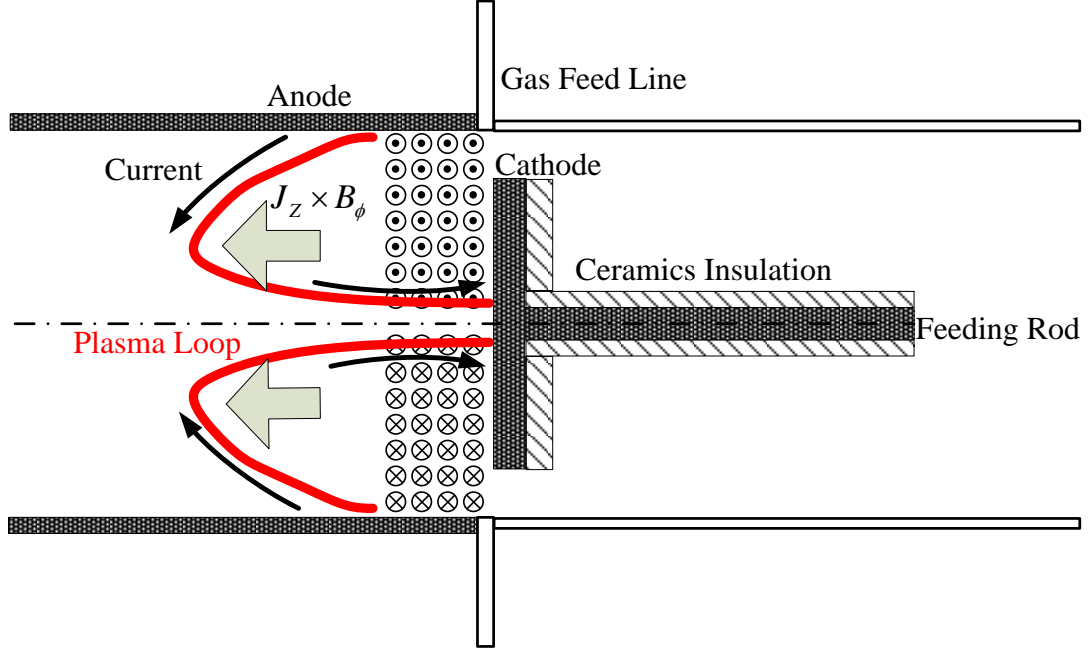
Figure 3.14. Current elongates along z-axis due to Lorentz force ($J_r \times B_\varphi$) force (Step 2).

Substituting (3.6) into (3.5), the radial and azimuthal force components can be expressed as:

$$F_z = \frac{\mu_0 J_z J_r}{2\pi r}\hat{z} \text{ and } F_r = -\frac{\mu_0 J_z J_z}{2\pi r}\hat{r} \tag{3.7}$$

In the initial stage when $J_r \gg J_z$, an axial symmetric current sheet is formed, mostly in the r direction, as shown in Figure 3.12 and Figure 3.13. As a result, the force applied to the plasma along the axial direction is much stronger compared to the pinch force, so that the plasma gets elongated and accelerated in the axial direction. From Eq. 3.7, it is clear that the Lorentz force falls radially as $\frac{1}{r}$. Thus a differential axial acceleration of the plasma, and a radial spread of plasma velocity are predicted, as depicted in Figure 3.14.

3.3.2 Acceleration stage: snow plow model

For the PBEX project, the current rise time (tens of microseconds) is longer than the typical Alfvén time (several microseconds) of the system. The Alfvén wave propagation effects

90

can therefore be neglected. The discharge current thus can be treated as in an analog circuit without radiation effects and retarded time.[91]

Outer Electrode

Plasma Element

V_z dr

r

Inner Electrode

Axis

z
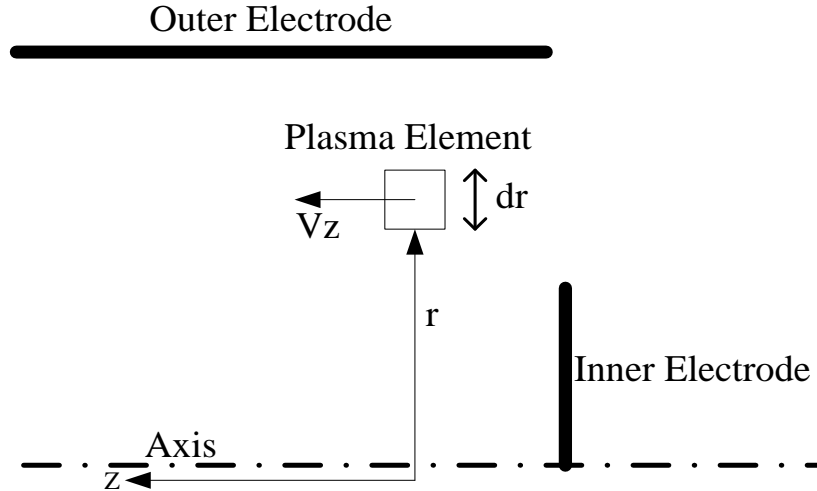
Figure 3.15. Illustration of a plasma element in the current sheet from the snow plow model.

A simple snow plow model has been set up,[92] as shown in Figure 3.15. The z-component of the Lorentz force, F_z, acts uniformly on a thin disk of plasma coincident with the current sheet. As the sheet moves forward in the axial direction, it sweeps the pre-exiting natural argon gas, adds to itself all of the gas mass over the cylindrical electrodes region, and leaves vacuum behind it.

Assuming the discharge current is $I = I_0 \sin(\omega t)$, where I_0 is the amplitude of the first half period, the plasma jet is accelerated and propagates into the vacuum chamber. Since $L_{circuit} \gg L_{gun}$, and $\frac{dL_{gun}}{dz}$ is very small, it is reasonable to assume ω as a constant for the theoretical model calculation.

Under these conditions, the momentum equation from MHD theory becomes:

$$F_z = J_r \times B_\varphi = \frac{B_\varphi^2}{2\mu_0} = \frac{dV_z}{dt} \int_0^z \rho_1 dz + \rho_1 V_z^2 \tag{3.8}$$

where B_φ is the toroidal magnetic field immediately behind the current sheet, μ_0 is the vacuum permeability, V_z is the current sheet velocity along axial direction, z is the axial position, and ρ_1 is the neutral argon gas mass ahead of the current sheet.

Considering the total mass $d(\rho_1 V_z) = 2\pi r z n_e dr dV_z$, from the snow plow model, where n_e is plasma density, using (3.6) and (3.8), the following relation can be derived:

$$\frac{d}{dt}\left(\frac{d(z^2)}{2dt}\right) = \frac{\mu_0 I_0^2 \sin^2 \omega t}{4\pi^2 r^2 n_e} \tag{3.9}$$

Eq. 3.9 is then solved by integrating on both sides twice over t, using the mathematic integration of $\int \sin^2(\omega t) = \frac{1}{\omega}\left(\frac{\omega t}{2} - \frac{\sin(2\omega t)}{4}\right) = \frac{\omega t - \sin(\omega t)\cos(\omega t)}{2\omega}$. The solution for z is then obtained:

$$z = \sqrt{\frac{\mu_0 I_0^2}{8\pi^2 r^2 n_e \omega^2}(\omega^2 t^2 - \sin^2(\omega t))} \tag{3.10}$$

The plasma front surface evolution with time is plotted in Figure 3.16 top, which shows the plasma is elongated due to the $J_r \times B_\varphi$ force, and a distinct conical jet head is formed due to the radial spread of the axial Lorentz force. After the jet head leaves the gun muzzle, it keeps the conical shape and propagates with a roughly constant radial velocity profile in the main vacuum chamber.

Note with respect to Eq. 3.10: this analysis only considers the $J_r \times B_\varphi$ force along the z direction. Plasma rotation is neglected, and no electron, or ion, temperature gradient is included. Electrode material ablation and plasma-wall interaction are neglected as well. The plasma front-head surface plot is in very good agreement with experimental data which is shown in Figure 3.16 Bottom.
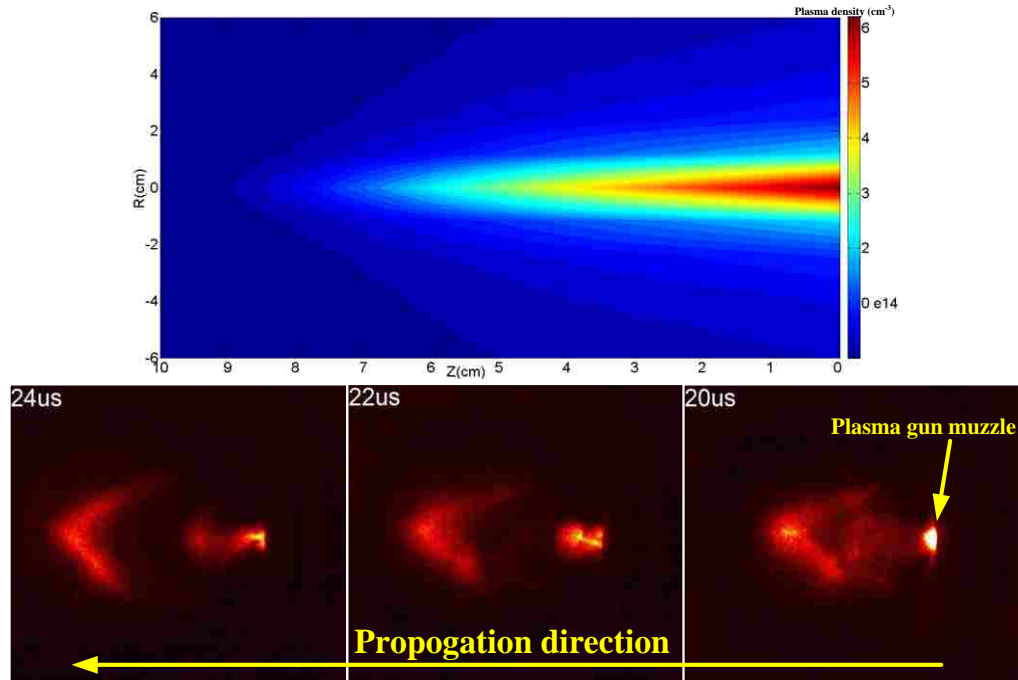
Figure 3.16. Top: snow plow model simulation of plasma acceleration at the initial stage due to $J_r \times B_\varphi$ force; Bottom: Fast camera images (false color) of argon plasma jet propagating across the vacuum chamber with a distinct jet head (Shot No. 013042314, 8.50kV main cap-bank voltage without bias voltage).
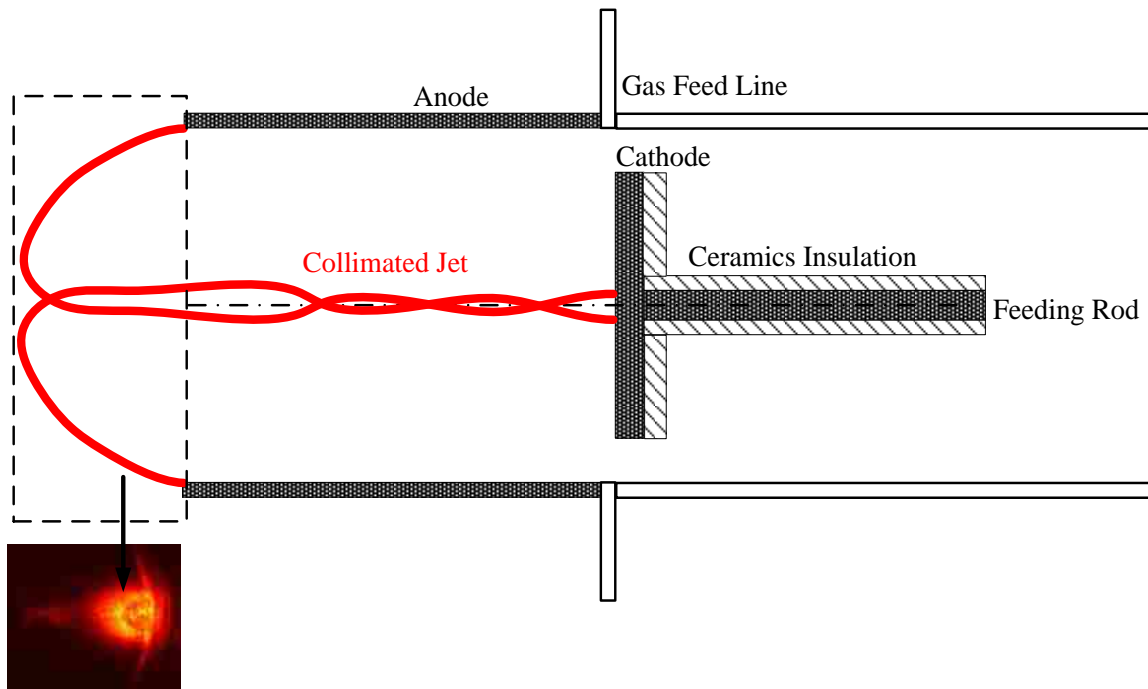
Figure 3.17. Collimated plasma jet formation (Step 3).

With the plasma length increasing along the z axis, as discussed above, the J_z component increases as well, continuously applying a non-uniform radial pinch force to the plasma. The pinch force squeezes the plasma in the central region (small r), and elongates the plasma axially even further to form a collimated and straight jet, as shown in Figure 3.17.

3.3.3 Plasma jet velocity characterization

Section 3.3.1 and section 3.3.2 have discussed the process of plasma jet initialization, propagation, and collimation in detail using MHD analysis. Based on the above discussion, Spruit has categorized the magnetized plasma jet acceleration process into three distinct regions: input power region, magnetic energy ($\frac{B_\phi^2}{\mu_0}$) dominant region, and kinetic energy ($n_e V_z^2$) dominant region.[93]

For PBEX jets, in the near-electrode region, with the increase of discharge current, the induced azimuthal magnetic field, B_φ, increases, and the magnetic energy dominates. Subsequently the Lorentz force ($J \times B$) starts to accelerate the plasma along the z-axis, resulting in an increase of jet propagation velocity. This mechanism converts magnetic energy into kinetic energy. At the jet head location, the poloidal current (J_z) turns back, and forms a closed current loop. This results in a dramatic decrease in the total + z poloidal current due to the cancelation of the forward and return currents, and causes the kinetic energy to dominate in the jet head region.

According to the discussion above, and assuming the magnetic pressure balances the plasma thermal pressure, Kumar and Bellan have proposed a simple axisymmetric model to investigate the plasma jet dynamic flow along the axial direction.[87] The model set up a

Bernoulli-like relation between the toroidal magnetic energy, and the kinetic energy of plasma jet.

$$\frac{\partial}{\partial z}\left[n_e v_z^2 + \frac{B_{\varphi,a}^2}{\mu_0}\left(1 - \frac{r^2}{2a^2}\right)\right] = 0 \tag{3.11}$$

where a is the plasma jet radius, n_e is plasma density, and $B_{\varphi,a}$ is the toroidal field at the jet boundary ($B_{\varphi,a} = \frac{\mu_0 I}{2\pi a}$).

Evaluating Eq. 3.11 at $r = 0$, gives a Bernoulli-like equation:

$$n_e v_z^2 + \frac{B_{\varphi,a}^2}{\mu_0} = n_e v_z^2 + \frac{\mu_0 I^2}{4\pi^2 a^2} = Const. \tag{3.12}$$

Furthermore, evaluating Eq. 3.12 at the jet base ($z \sim 0$), the z-axial velocity is approximately zero and the magnetic energy, $\frac{B_{\varphi,a}^2}{\mu_0}$, dominates. At the plasma jet head where $B_{\varphi,a} \approx 0$, the kinetic energy dominates. This is consistent with the theory analysis above. Evaluating equation 3.12 at the jet head yields:[94]

$$v_z\big|_{jet\ head} \cong \frac{I}{2\pi a}\sqrt{\frac{\mu_0}{n_e}} \propto \frac{I}{\sqrt{n_e}} \tag{3.13}$$

Eq. 3.13 clearly shows that the axial velocity of the MHD driven plasma jet is linearly related to the discharge current, I, and inversely related to the square root of the jet density, n_e. This relation has been discussed, and analyzed, by other research groups.[87, 95-98]

This jet property has also been investigated in the PBEX project. Two methods have been employed to measure the spatial jet-head velocity across the main vacuum chamber. One method uses a series of image data, with known time interval, to estimate the propagation velocity by measuring the plasma jet head's spatial position. The other method employs a double-tip Langmuir probe at different space positions in the vacuum chamber as shown in

Figure 3.18, Top. A group of typical ion saturation current traces from Langmuir probe measurements at different space locations is shown in Figure 3.18, Bottom. The sharp rise time makes it possible to estimate the average velocity of the plasma as $V_{jet} = \frac{\text{Distance}}{\text{Time of delay}}$
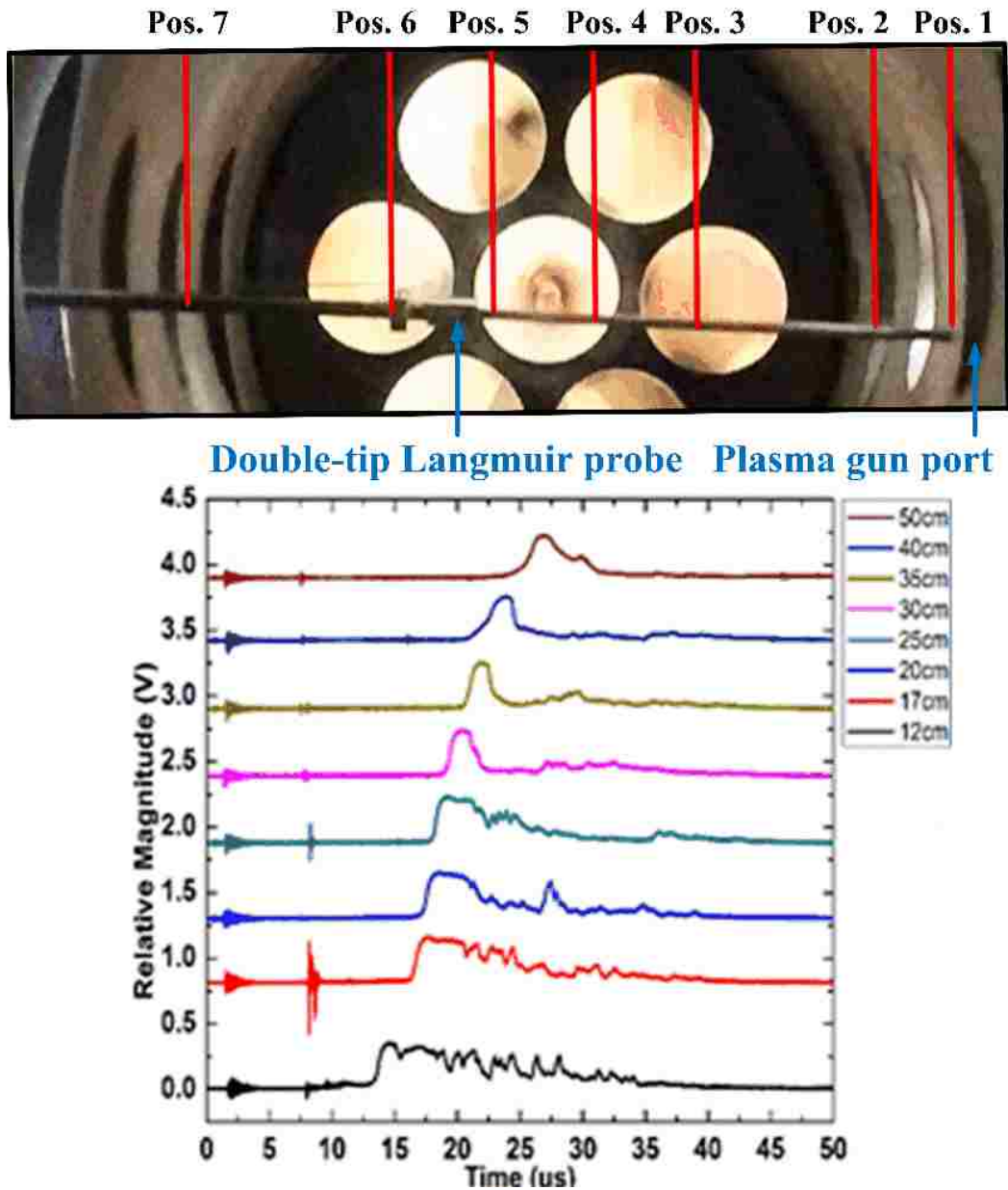
Figure 3.18. Top: a double-tip Langmuir probe placing at 7 different spatial positions in the vacuum chamber for plasma density measurement and propagation speed estimation. Bottom: typical ion saturation current signals at different spatial locations to estimate the average plasma jet propagation velocity.
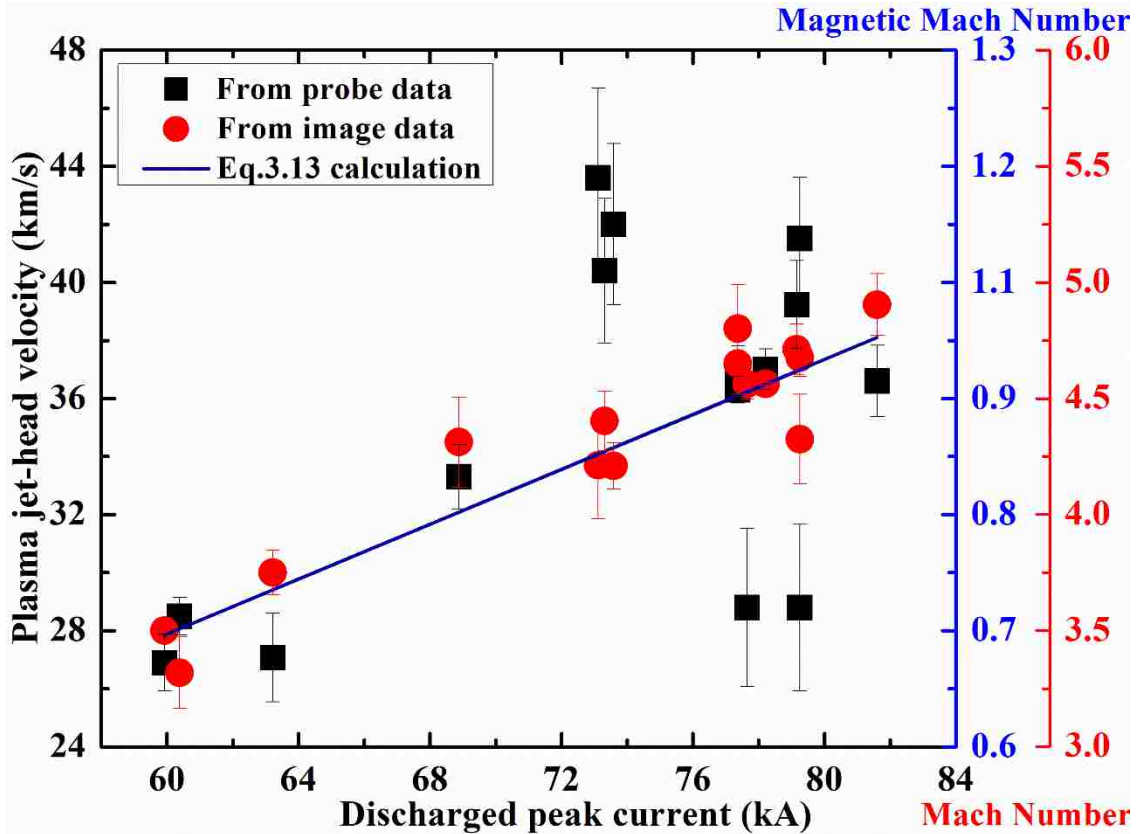
Figure 3.19. Plasma jet velocity as a function of discharged current peak.

PBEX experimental results are shown in Figure 3.19. The red dots are calculated from CCD camera image data, and the black squares are from Langmuir probe signals at various spatial positions in the main vacuum chamber. The error bars are determined from the standard deviation. The error bars for Langmuir probe data are larger due to some experimental factors: Langmuir probe droop off axis, shot-to-shot variations, etc.

At the same time, substituting the experimentally measured results ($n_e = 4{\times}10^{20}\ m^{-3}$, $a \sim 2.5\ cm$, $I_z \sim 55 - 85\ kA$) into Eq. 3.13, the calculated result is also plotted in Figure 3.19, which is consistent with the measured results.

From an unstrict qualitative analysis, Eq. 3.13 can be interpreted as follows: assuming the total injected toroidal magnetic field energy works on the plasma and accelerates the plasma

jet into the main vacuum chamber, and considering the conservation of total energy, it can be shown that $B_\varphi^2 \sim n_e v_z^2$. Hence $v_z \sim \dfrac{B_\varphi}{\sqrt{n_e}} \sim \dfrac{I_z}{\sqrt{n_e}}$.[96, 97]

3.3.4 Global magnetic field configuration

With the development of the plasma jet, considering the "frozen-in" property of ideal MHD theory, the initial dominant toroidal magnetic field (B_φ) is "frozen-in", dragged by the plasma jet, and converted into poloidal magnetic field (B_z and B_r). Consequently, the global magnetic field (the composition of B_φ, B_z and B_r) will show a helical-like spatial structure. Figure 3.20 indicates the global helical magnetic configuration with the projected shadow plots at both poloidal and toroidal planes. The illustrated poloidal and toroidal magnetic field structures from Figure 3.20 are easy and straightforward to understand, but are also a powerful tool to validate the measured magnetic field data.
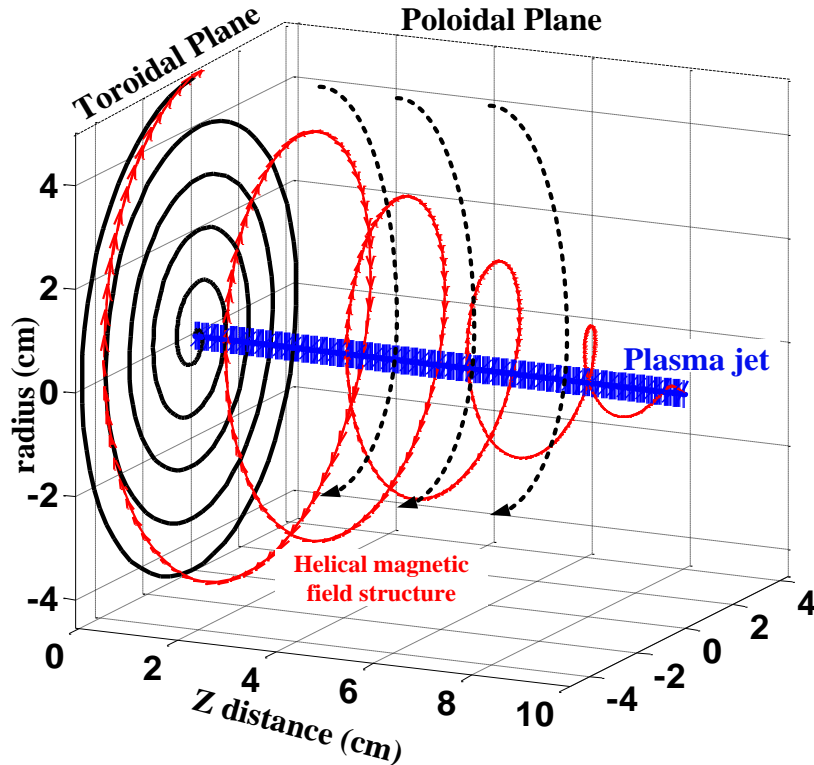
Figure 3.20. Illustration of helical magnetic configuration for plasma jet.

Typical magnetic field vector data, along with magnetic field streamline plots (data from Shot No.011073015) in the poloidal and toroidal planes, are shown in Figure 3.21. It is clear that the plots at both poloidal and toroidal planes are consistent with the illustrations from Figure 3.20. This is strong evidence that there is a global helical magnetic field configuration associated with the plasma jet propagation. Note that for the data plotted in Figure 3.21, the B-dot probe array is placed in the main vacuum chamber at the position which is 10 cm away from the gun port, as shown in Figure 2.28. For this particular shot (Shot No.011073015), the B-dot probe has detected both upstream and downstream magnetic field signals shown in both planes. The reason for this is because the jet is experiencing a radial variation simultaneously with its axial propagation. This radial variation is possibly caused by the $m = 1$ kink instability which will be discussed in the next section.

The helical magnetic field configuration has been identified in astrophysical jets from observational evidence of polarized synchrotron Faraday rotation across the jets,[99] and from theoretical model simulations.[100] The similar helical magnetic field structure identified in PBEX project supports the possibility of employing laboratory experiments to simulate the astrophysical phenomena.
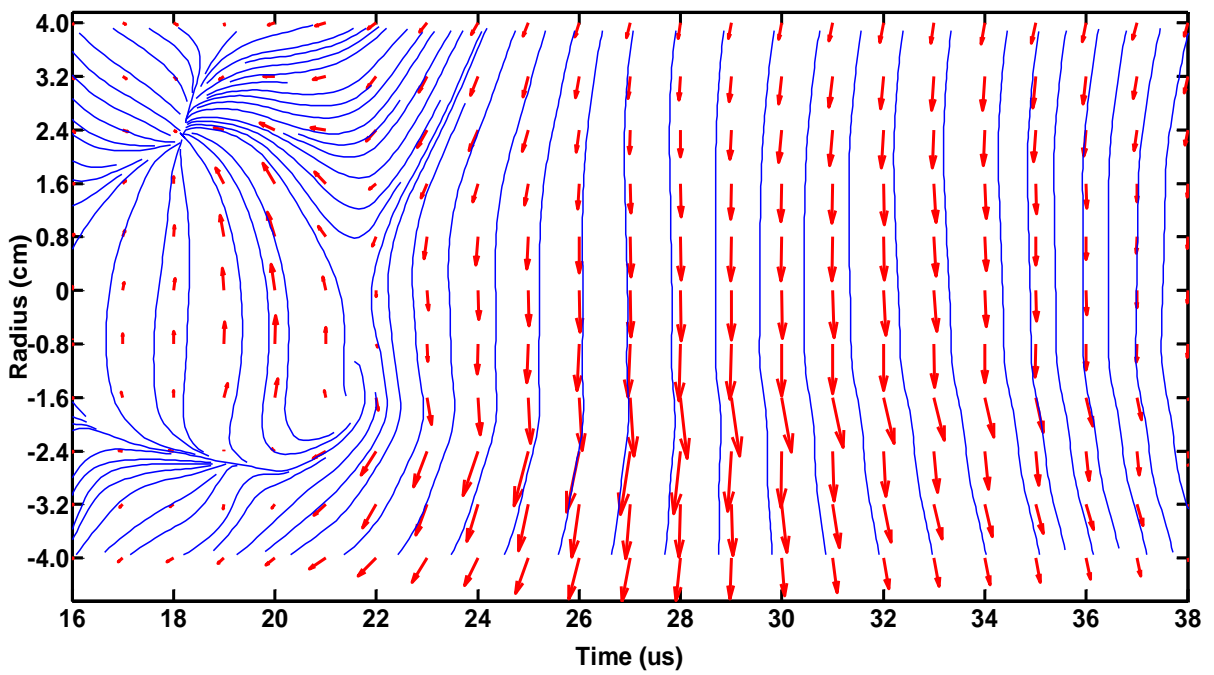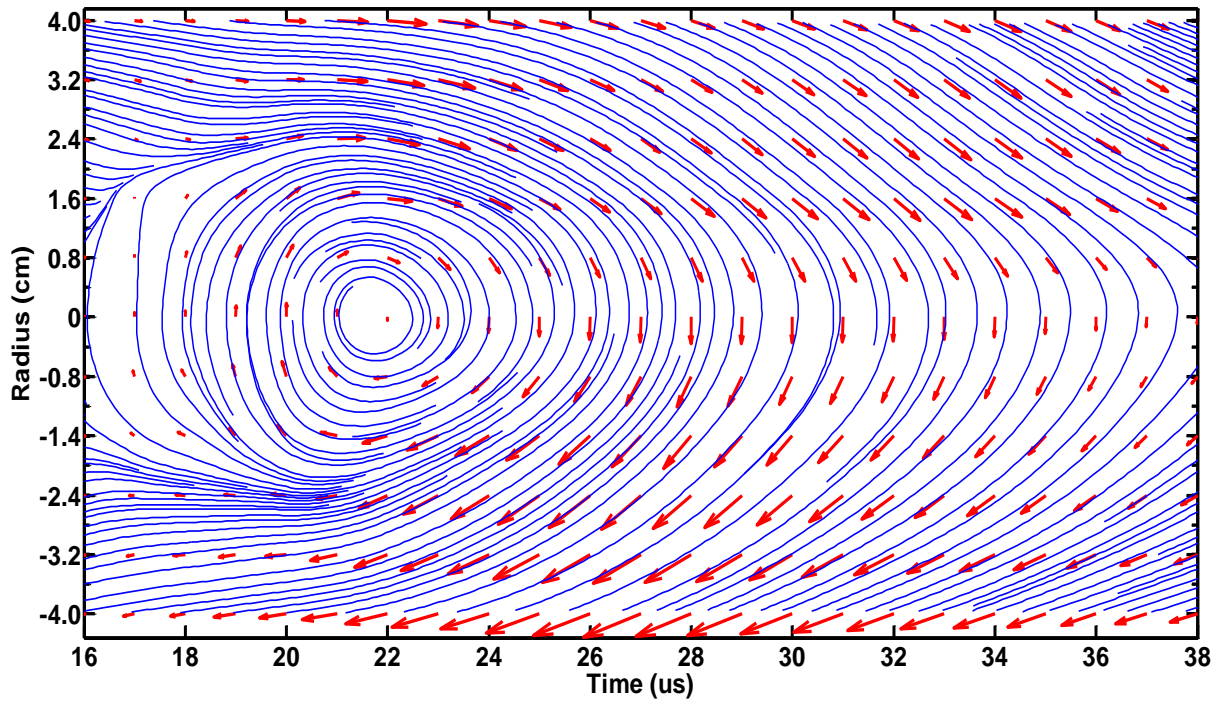
Figure 3.21. Top: magnetic field vector and streamline plots in the toroidal plane. Bottom: magnetic field vector and streamline plots in the poloidal plane.

3.3.5 Current-driven (CD) m = 1 kink instability

Consider an initially homogeneous cylindrical plasma column (radius a), as shown in Figure 3.22. Consider, also, an induced radial perturbation, which causes the field lines to be curved. Inside the kinked plasma column, the magnetic pressure, $(\frac{B_\varphi^2}{2\mu_0})$, becomes stronger, while outside of the kinked plasma column, magnetic pressure becomes weaker. As a result, the initial perturbation grows along the radial direction and the plasma jet body undergoes instability.
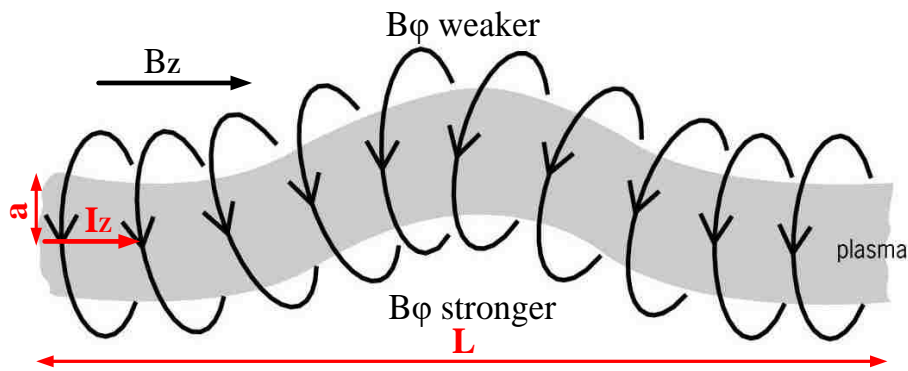
Figure 3.22. Kink instability m=1 mode.

3.3.5.1 Kruskal-Shafranov condition

Kruskal and Shafranov apply the ideal MHD equations to a cylindrical plasma column with a helical magnetic field configuration (B_φ and B_z). Assuming only a skin current exists, without going through too much detail, the solution of the linearized MHD equations, with appropriate boundary conditions, leads to the following dispersion relation:

$$\rho\omega^2 = -\frac{B_{\varphi,a}^2}{\mu_0 a^2} + \frac{k_z^2 B_z^2}{\mu_0} + \frac{[k_z B_z + (m/a)B_{\varphi,a}]^2}{\mu_0} \tag{3.14}$$

where ρ is the plasma density, k_z is the axial wave number, and $k_z a = m$.

It can be shown that only a perturbation with m = 1 can be unstable. Therefore:

$$\omega^2 = \left(\frac{2k_z^2 B_z^2}{\mu_0 \rho}\right)\left(1 + \frac{B_{\varphi,a}}{k_z a B_z}\right) \tag{3.15}$$

In addition, the plasma boundary is unstable for $k_z < 0$ and $|k_z a| < B_{\varphi,a}/B_z$. Then the minimum perturbation wavelength can be defined as:

$$\lambda_z = 2\pi a \frac{B_z}{B_{\varphi a}} \tag{3.16}$$

In practice, the wavelength is usually limited by the plasma column length, l. In accordance with Eq. 3.16, the instability criterion, which is also called the Kruskal-Shafranov criterion, is:

$$q(a) \equiv \frac{2\pi a B_z}{l B_{\varphi}} \tag{3.17}$$

where a and l are the radius and length of the plasma column, respectively. $q(a)$ is the safety factor taken from the concept in Tokamaks. When $q(a)$ drops below the $q(a)=1$ threshold, current-driven kink instabilities can develop in the plasma column.

Considering $B_{\varphi}(a) = \frac{\mu_0 I_z}{2\pi a}$, Eq. 3.17 can be rewritten as:

$$I_z = \frac{(2\pi a)^2 B_z}{\mu_0 L} \tag{3.18}$$

where I_z is the plasma current. Equivalently to $q(a) < 1$, when the plasma current exceeds the condition $\left(\frac{(2\pi a)^2 B_z}{\mu_0 L}\right)$, a linearly unstable helical kink is obtained.[101]

3.3.5.2 Kink instability of plasma jet

For certain discharge currents in the PBEX experiment, a collimated jet forms along the z direction. Due to imperfect laboratory conditions, the plasma obtains enough non-axisymmetric initial perturbations that cause the plasma to develop a helical instability with

toroidal mode number, m = 1, as shown in Figure 3.23. This observed kink instability has been verified to be consistent with the ideal MHD kink instability discussed above by two independent experimental measurements described below.
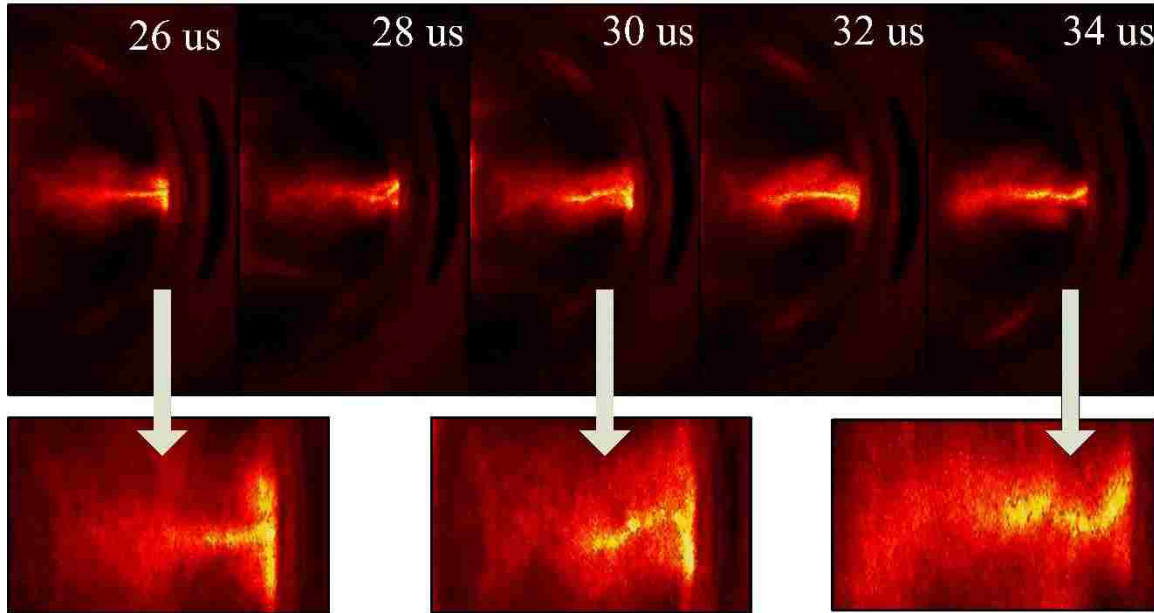
Figure 3.23. Plasma jet in which the central column becomes helical and a kink instability grows (Shot No. 001050714). 2.0 μs interframe time.

First, based on Eq. 3.17, the consistency with the Kruskal-Shafranov criterion is checked with the direct magnetic probe measurements from a single shot. For a given a and L, radial profiles of B_Z and B_φ yield safety factor $|q|$ profiles as a function of time, as shown in Figure 3.24. These profiles indicate that the current-driven kink instability starts to develop at a certain time. Initially $|q|$ is greater than 1 because l is small. Then, with the increase of l, according Eq. 3.17, $|q|$ starts to drop in the central region of the plasma jet. When $|q|$ drops below 1, the helical kink instability is observed, which is consistent with a current-driven MHD kink.
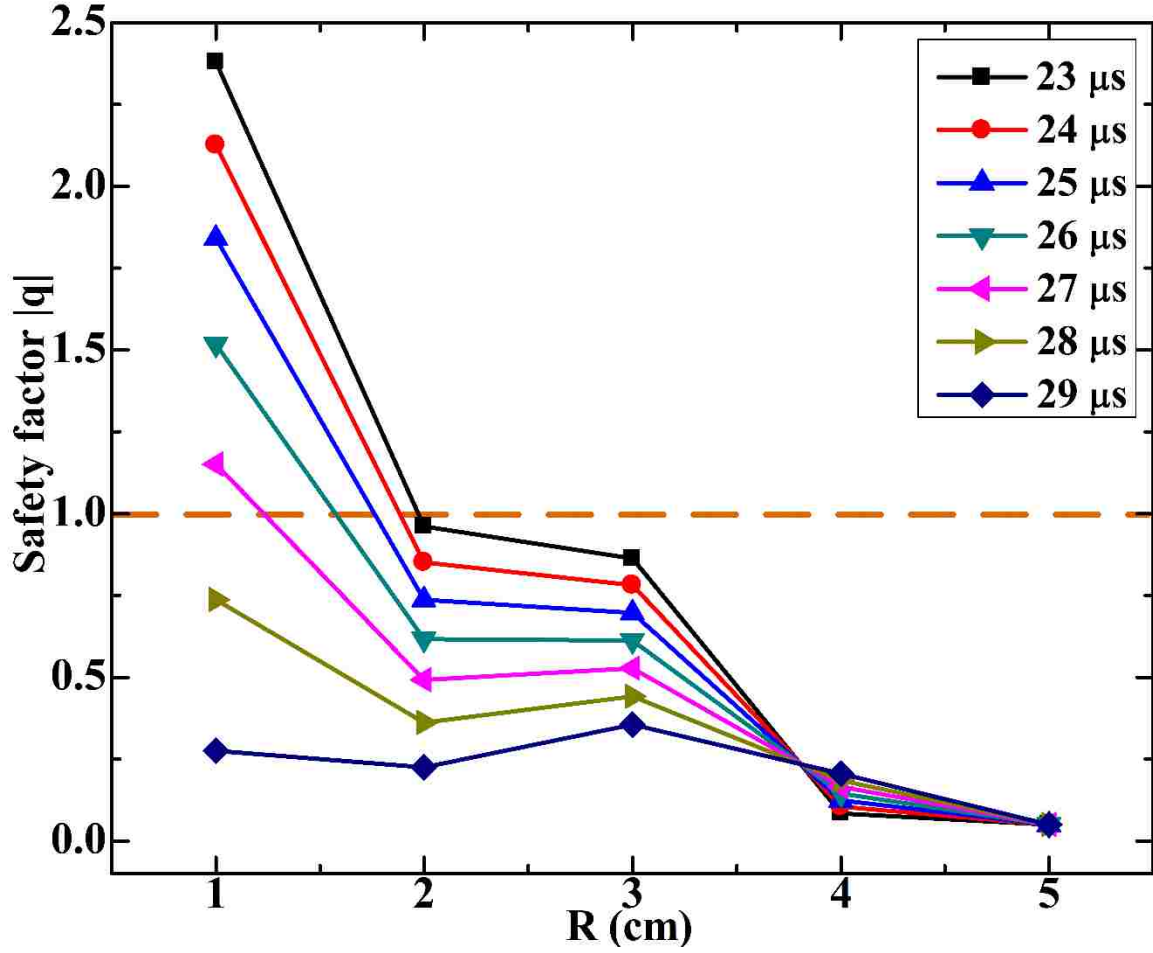
Figure 3.24. Radial profile of safety factor q (Shot No.001050714). Kink instability has developed when $|q|$ near axis drops below unity.

Secondly, we can use the PBEX experimental parameters to re-express the Kruskal-Shafranov criterion. Although B_Z is not actually constant as a function of radius, φ_{gun} can be approximately written as $\varphi_{gun} \approx \pi a^2 B_Z(a)$. Also if we assume that the entire discharge current, I_z, is flowing through the jet body column in the radius, a, then $B_\varphi(a) = \frac{\mu_0 I_z}{2\pi a}$. The Kruskal-Shafranov criterion for kink instability (Eq. 3.17) can be re-expressed as:[29]

$$\lambda_{gun} = \frac{\mu_0 I_z}{\varphi_{gun}} > \frac{4\pi}{l} \tag{3.19}$$
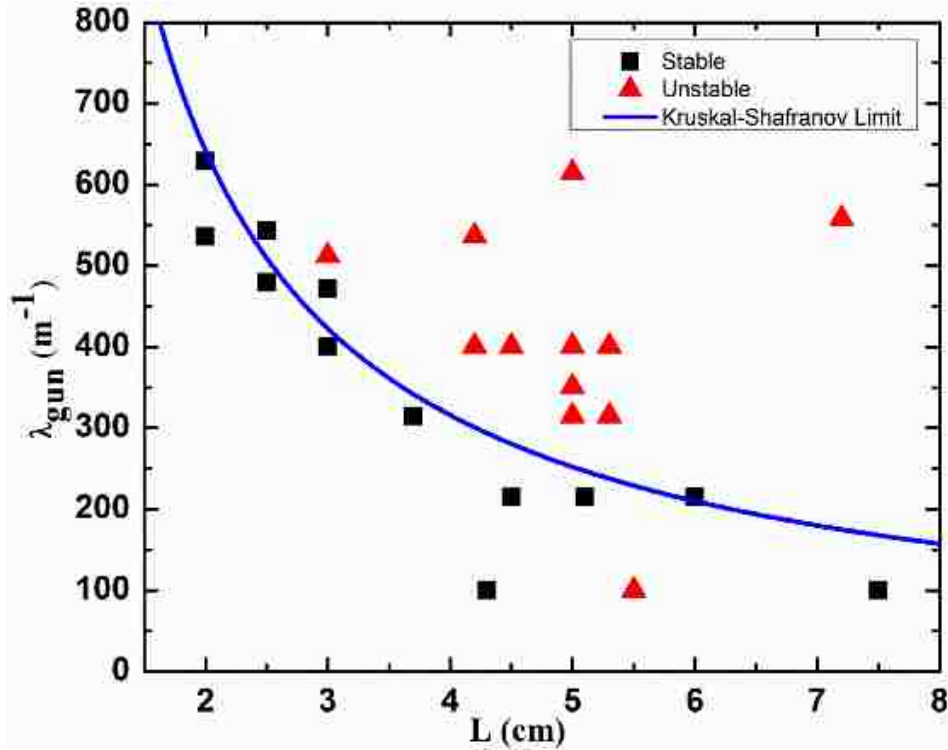
Figure 3.25. Plot of λ_{gun} versus plasma jet column length l. The stability boundary is in the good agreement with Kruskal-Shafranov criterion.

Thus, the experimentally observed kink instability can be compared to the Kruskal-Shafranov condition by knowing λ_{gun} and l for a particular shot in which a plasma column forms and a kink develops. Figure 3.25 shows the experimental results to compare with Eq. 3.19. The data points are taken from different shots, (No. 013042314, No. 043050714, No. 044050714, No. 012050914, No. 013050914 and No. 022050914 respectively), and different time-point within these shots (before and after kink instability occurs). The plot shows consistency with the Kruskal-Shafranov criterion for MHD kink instability.
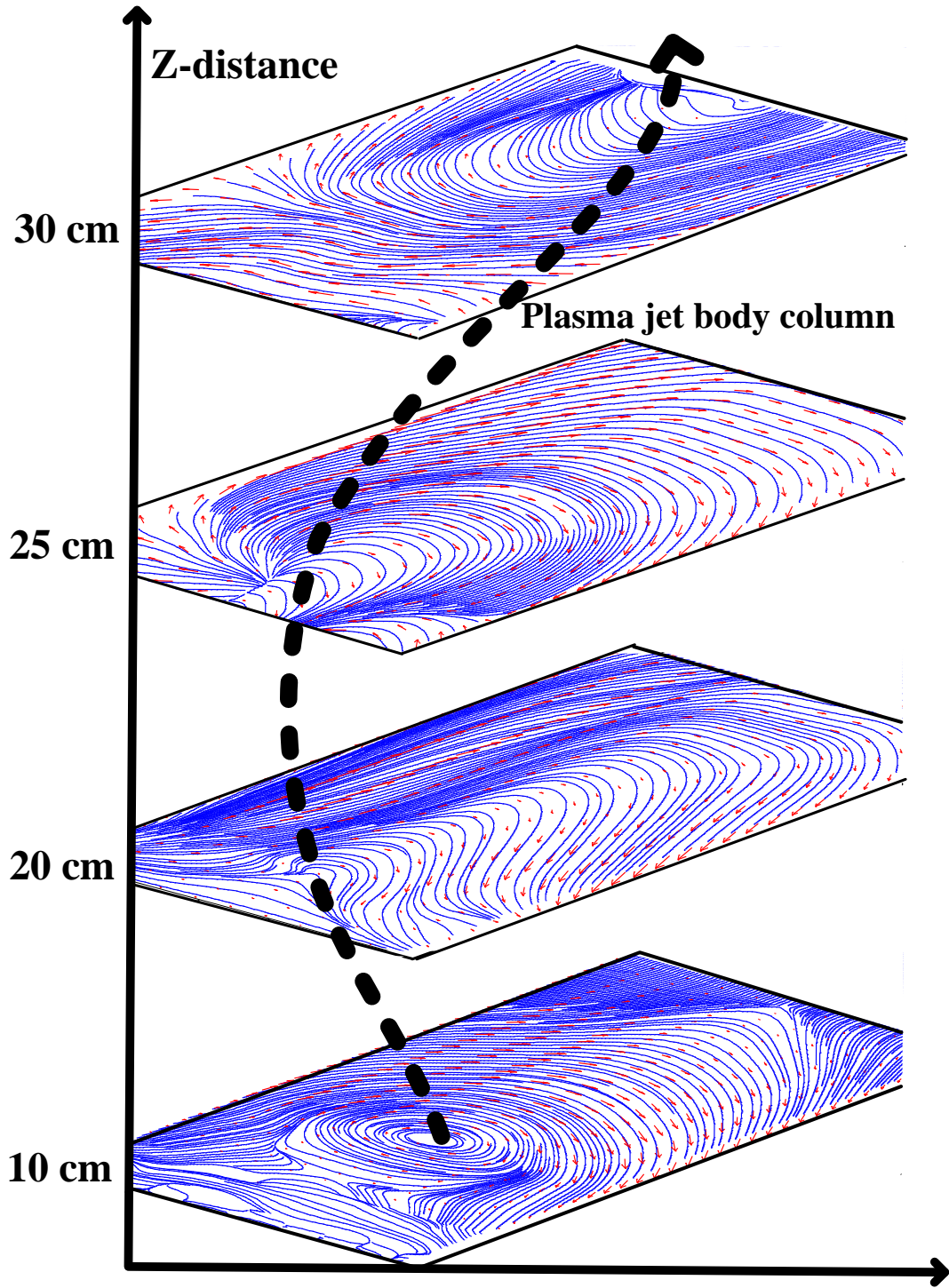
Figure 3.26. Multiple position toroidal magnetic field vector with streamline plots to indicate the kink instability.

Last but not least, magnetic data analysis similar to that in Section 3.3.4 has been carried out to validate the kink instability. Toroidal magnetic field vector plots with streamline at multiple axial positions are shown in Figure 3.26. From the plot, it is straightforward to see the underlying kink instability of the plasma jet column. Note that the toroidal magnetic field vector plots at multiple positions are taken from different shots. Some shot-to-shot variations exists, but this plot still carries some information about the global magnetic field configuration and indicates the existence of a kink instability.

3.3.5.3 Relevance to astrophysical jets and solar physics

High resolution very-long-baseline interferometry (VLBI) observations show that many AGNs, and quasar jets, display wiggles, or kinks, on sub-parsec to parsec scales.[102, 103] Based on both theoretical analyses and observational phenomena, MHD instabilities have long been suggested as a possible mechanism for the observed wiggled, or kinked, structures. Furthermore, coronal mass ejections[104] (CMEs) in our solar systems have been linked to various heliospheric structures including eruptive prominences,[105] magnetic clouds, and ejections from coronal arcades.[106] The twisted magnetic flux ropes model is a popular one to describe these structures' magnetic topology. Multiple observations,[107] theoretical calculations,[108] and numerical analyses[109] have suggested that the kink instability may lead to the eruption of coronal magnetic flux ropes.

Due to observational limitations, detailed magnetic field information in these crucial areas is still lacking. Laboratory experiments provide *in situ* measurements to contribute to better understandings of astrophysical jets, and solar-relevant kink phenomena.

3.4 Regime II: spheromak-like plasma bubble formation and characterization

3.4.1 Introduction

As discussed in Section 3.1, operating the plasma gun with $\lambda > \lambda_{threshold}$, a spheromak-like plasma is formed. The steady state is characterized by:

$$\nabla P = J \times B \tag{3.20}$$

This expression (the general form of the Grad Shafranov Equation) shows the force balance between magnetic force and the kinetic pressure gradient. For the coaxial plasma gun case, $\beta \sim 0.1$, so that $\nabla P \approx 0$ in Eq. 3.20 and the equilibrium equation reduces to:

$$\nabla \times B = \lambda B \tag{3.21}$$

Eq. 3.21 simply states the force free state, which means the Lorentz force, $J \times B$, term vanishes in the MHD equation of motion. This property of plasma's tendency to be in a force-free equilibrium state agrees very well with astrophysical observations.[4]

3.4.1.1 Taylor relaxation theoretical analysis

Taylor expanding on the results above, suggests that magnetic reconnection processes may be the dominant mechanism of converting magnetic energy while the magnetic helicity is preserved.[110] The converted magnetic energy naturally approaches the minimum energy state, which is referred to as the Taylor state. This process of magnetic energy decaying through magnetic reconnection into the Taylor state is referred to as the Taylor relaxation process. The biggest advantage of the Taylor approach is that there is no required knowledge about the plasma's initial condition to fully determine its final state. In the laboratory plasma, a Taylor state configuration is called a spheromak, which is discussed in detail in this section.
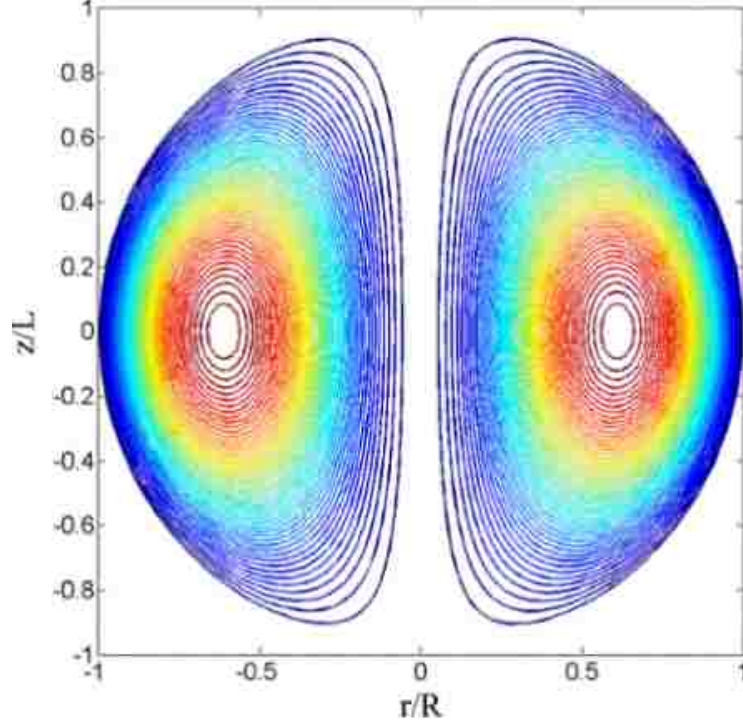
Figure 3.27. Spheromak poloidal flux surface structure.

Taking the curl of Eq. 3.21 gives the vector Helmholtz equation:

$$\nabla^2 \vec{\boldsymbol{B}} + \lambda^2 \vec{\boldsymbol{B}} = 0 \tag{3.22}$$

From Eq. 3.22, it is clearly shown that λ is an eigenvalue solution and λ^{-1} is related to the characteristic dimensions of the system.[69] Assuming λ is a constant (which constrains a force free state), the equations' general solutions for cylindrical coordinates are listed below:[45]

$$B_r = B_0 \frac{k_z}{k_r} J_1(k_r r)\cos(k_z z)$$

$$B_\varphi = B_0 \frac{\lambda}{k_r} J_1(k_r r)\sin(k_z z)$$

$$B_z = B_0 J_0(k_r r)\sin(k_z z) \tag{3.23}$$

where B_0 is an arbitrary constant, $k_z = \frac{m\pi}{L}$, $k_r = \frac{x_n}{R}$, x_n are roots of the Bessel function J_1, $\lambda = \sqrt{k_z^2 + k_r^2}$, R is the radius and L is the length of the cylinder. The lowest energy state will be the m = n = 1 state. The surface of constant poloidal magnetic flux is shown in Figure 3.27.

3.4.1.2 Spheromak formation by coaxial gun

The coaxial plasma gun operation sequence to launch a spheromak bubble is summarized in this section. There are five steps:

1) The bias flux power system discharges to generate the poloidal magnetic field, as shown in Figure 3.28. This magnetic field is also called the stuffing magnetic field. As discussed in detail in Chapter 2, the time scale of the pulse (~ms) is much greater than the gun-generated plasma lifetime (~μs). Therefore it is reasonable to treat the bias magnetic field as a quasi-static DC field.

2) The gas valve power system discharges, causing the high-speed valve to then puff a cloud of neutral gas (argon for PBEX project) into the annular gap between the inner and outer electrodes, shown in Figure 3.29.

3) The ignitron-switched main cap-bank discharges. According to Paschen's law, the applied high voltage across the electrode gap ionizes the neutral gas into plasma, and drives ~kA level discharge current through it. At the same time, the current creates a toroidal magnetic field "frozen" into the plasma. This step is illustrated in Figure 3.30.
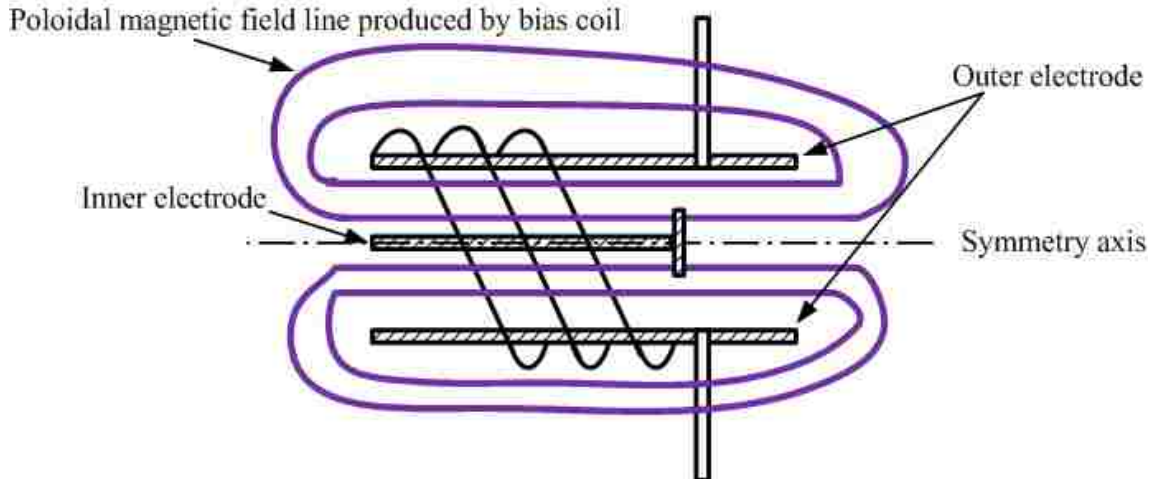
Figure 3.28. Spheromak formation sequence (Step 1).
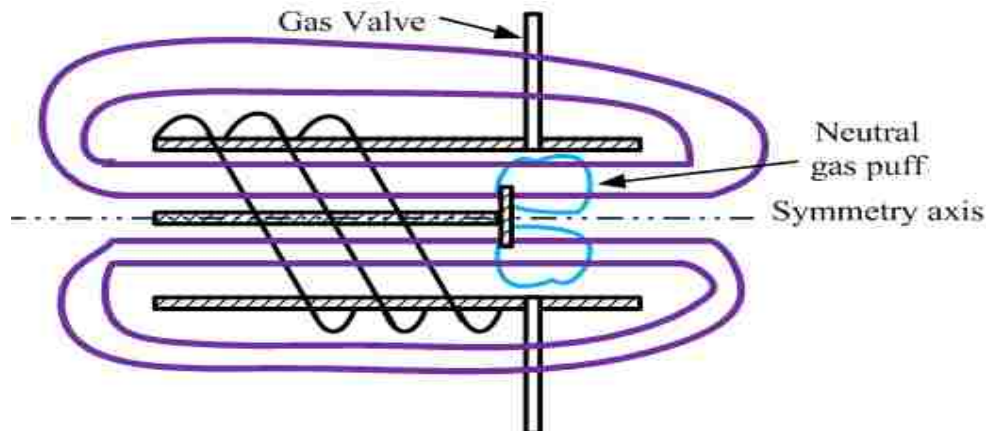
Figure 3.29. Spheromak formation sequence (Step 2).

4) The $\vec{J} \times \vec{B}_{toroidal}$ force acts on the plasma expelling it out of the gun port muzzle against the bias magnetic flux tension. As a result, the bias magnetic flux is extended with this plasma motion. Furthermore, this poloidal magnetic field stretching process consumes kinetic energy from the plasma and converts it into magnetic energy. This process is shown in Figure 3.31.
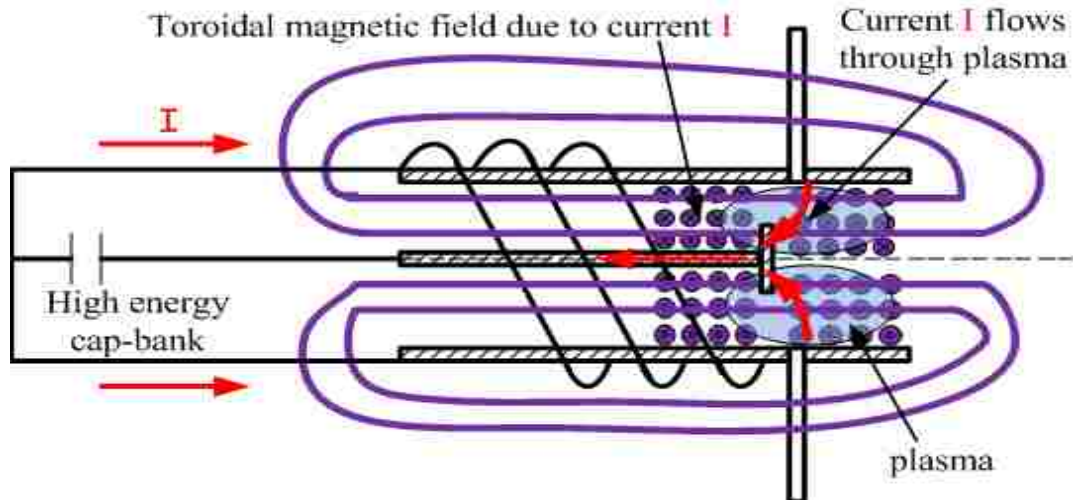
Figure 3.30. Spheromak formation sequence (Step 3).
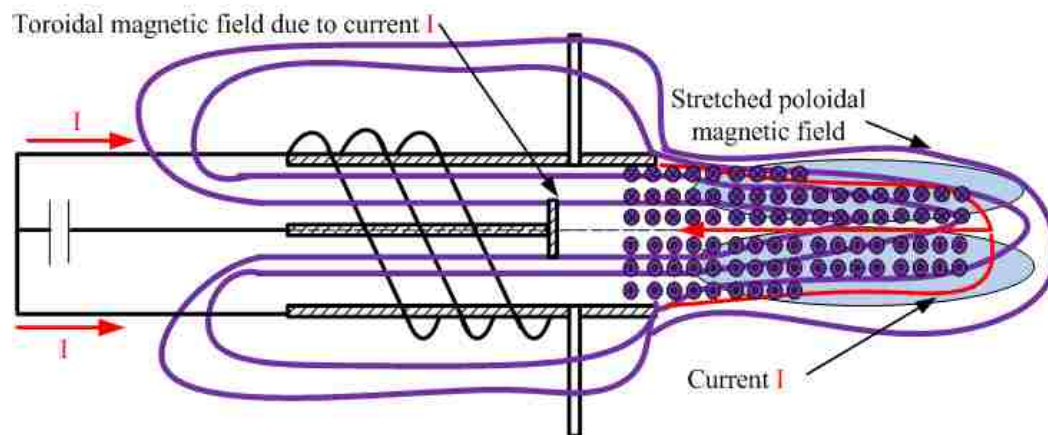
Figure 3.31. Spheromak formation sequence (Step 4).

5) If the $\vec{J} \times \vec{B}_{toroidal}$ force is strong enough to overcome the magnetic tension force provided by the bias poloidal magnetic field, the poloidal magnetic field is efficiently stretched, broken, and reconnected as shown in Figure 3.32. At the same time, a spheromak with self-closed poloidal and toroidal magnetic field structure is formed and launched into the vacuum chamber. The formation process is then complete.

112
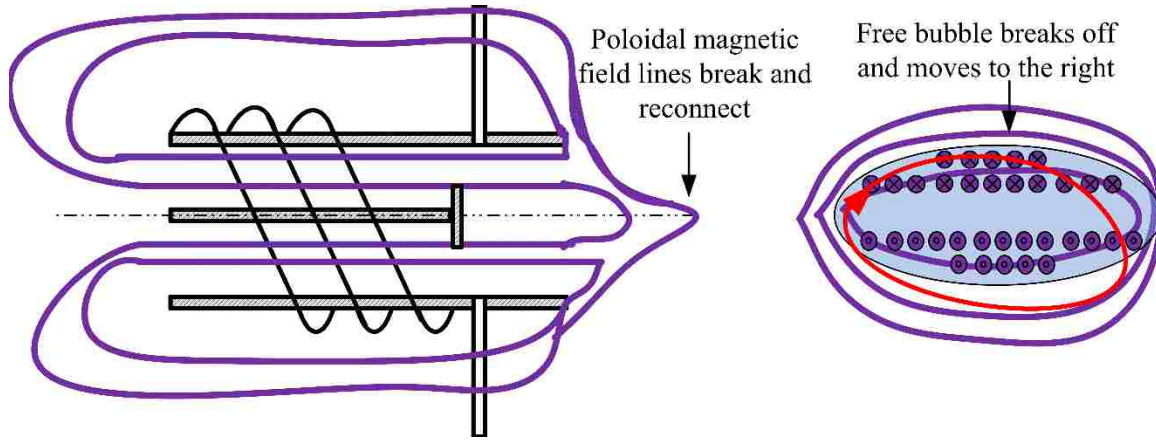
Figure 3.32. Spheromak formation sequence (Step 5).

3.4.2 Experimental data

3.4.2.1 Current and voltage characteristics

The main cap-bank discharge current and voltage waveforms with the coaxial plasma gun operated in Regime II are displayed in Figure 3.33. The operation settings are I_{gun}= 71.7 kA and Φ_{bias} = 0.36 mWb. As shown in Figure 3.33, the ignitron-switched cap-bank discharges at t = 1.1 μs and neutral gas is ionized into plasma at 0.6 μs afterwards with the discharge voltage dropping dramatically. The plasma can be treated as an inductive load so that the circuit behaves as an underdamped oscillator. The discharge current reaches its peak at t = 14.9 μs and reverses polarity at t = 32.3 μs. Since the helicity injection rate is proportional to the voltage across the electrodes,[66] the helicity injection process ends when the discharge voltage reverses its polarity at t = 16.1 μs. This is approximately when the spheromak should be detached from the gun port muzzle. This prediction is confirmed with image data taken by CCD camera as shown in Figure 3.34. The voltage spikes, detected in the voltage signal during the time when helicity injection ends (boxed in Figure 3.33), also suggests a magnetic reconnection process during spheromak formation.[111]

113
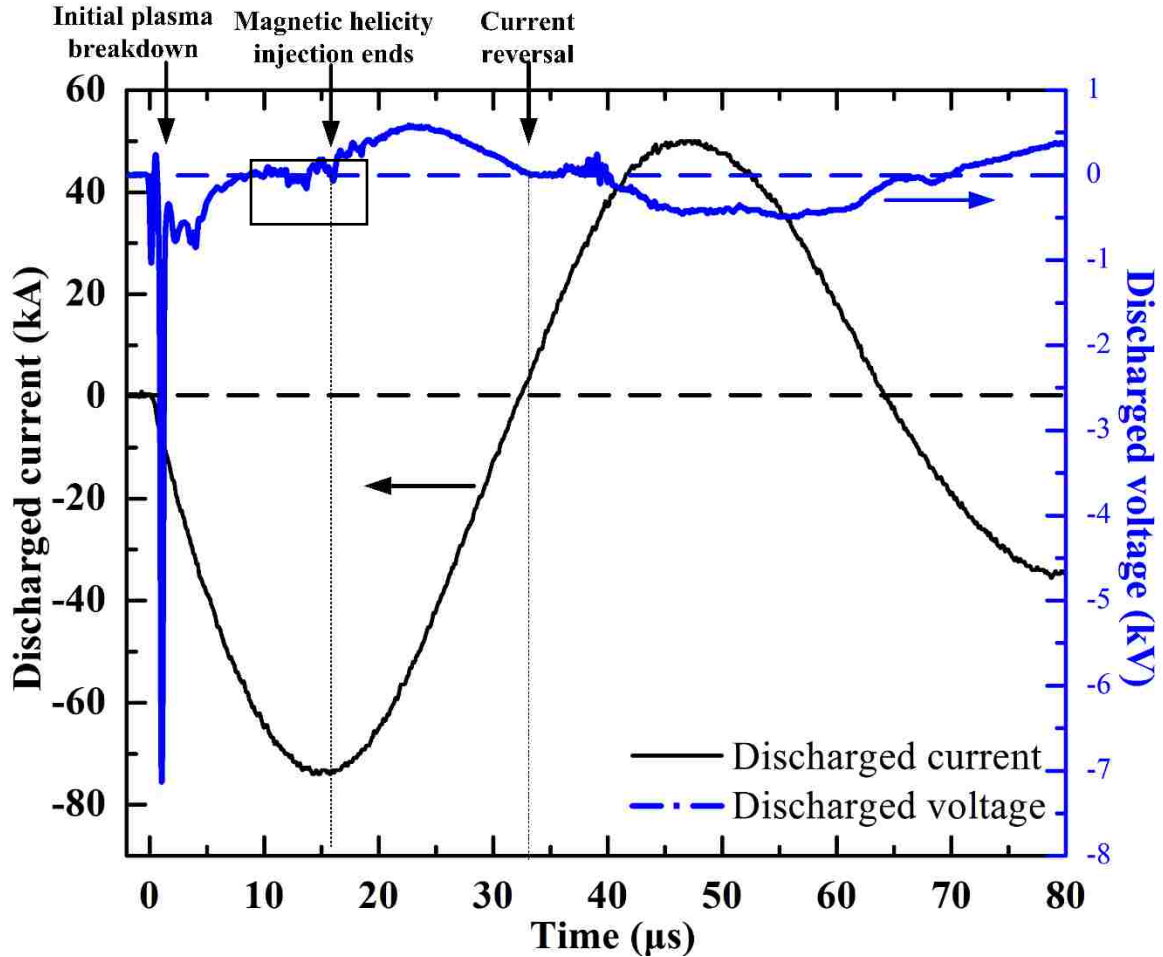
Figure 3.33. Typical coaxial gun discharge current and voltage signals for region II operation. (I_{gun}= 71.7 kA and Φ_{bias}= 0.36 mWb).

3.4.2.2 CCD camera images

Figure 3.34 shows typical camera data with a series of images to illustrate the plasma evolution. These images are taken from the end-view window. The coaxial gun is located at the right edge and launches plasma towards the left. The L-shape magnetic B-dot probe is visible in these images.

As discussed in section 3.2, plasma formed under these settings is classified as being in Region II, and exhibits distinct spheromak-like behavior compared to other regions. For this particular shot (I_{gun}= 71.7 kA and Φ_{bias}= 0.36 mWb), as shown in Figure 3.34, beginning at
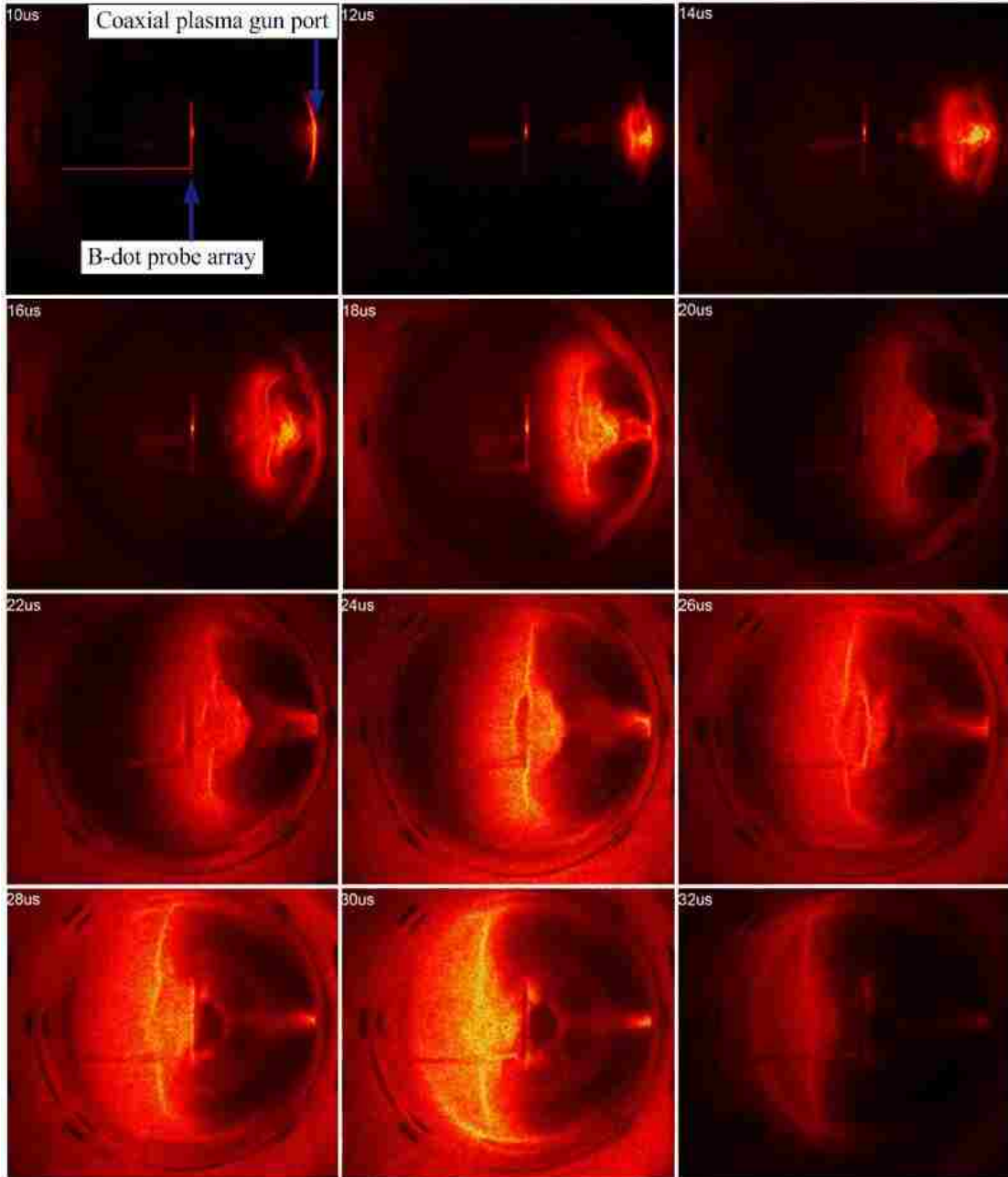
Figure 3.34. Image sequence of plasma evolution with coaxial gun operated at typical settings in region II. (I_{gun}=39.11 kA and Φ_{bias}=0.62 mWb, Shot No. 014050914).

t = 10 μs, plasma appears at the gun muzzle and follows the bias magnetic field lines. Around t = 16 μs, plasma detaches from the gun port and expands continuously into the vacuum chamber. At t = 18 μs, the front (leftmost) leading edge becomes brighter compared to the remaining plasma. This brighter region continues to gradually expand and propagate to the left.

Note that significant irreproducibility has been found in the images data due to multiple factors, such as asymmetric initial breakdown, imperfect electrode condition, and complex asymmetric boundary conditions. Nevertheless, in all these images data for Region II settings, a clear bright leading (left most) edge is visibly detected.

These images obtained from a CCD camera give good insight to the plasma dynamics present in the device and provide evidence of spheromak-like bubble formation. However, it is not clear from these images whether a characteristic close-surface toroidal flux is in fact formed during this process. In order to exam the magnetic structure of the plasma, the magnetic probe array is employed.

3.4.2.3 Magnetic signals measured by magnetic probe array

A sample of magnetic data obtained using the probe array is shown in Figure 3.35, Figure 3.36, and Figure 3.37 for a single shot taken under the typical gun operation settings for Region II. For these data, the probe is placed at $z = 25$ cm away from the gun port in the $\varphi = 0$ poloidal plane. As indicated from the image data (shot No.137080515), most of the magnetic activity takes place between $t = 14$ µs and $t = 40$ µs.

Note that a secondary magnetic signal is detected during the period of time $t = 50$ µs ~70 µs due to the secondary plasma launched into the vacuum chamber by the second half-cycle discharge of the main cap-bank current. Upon future completion of a crowbar circuit[112], this secondary signal should be adequately removed.

Bz (Gauss)
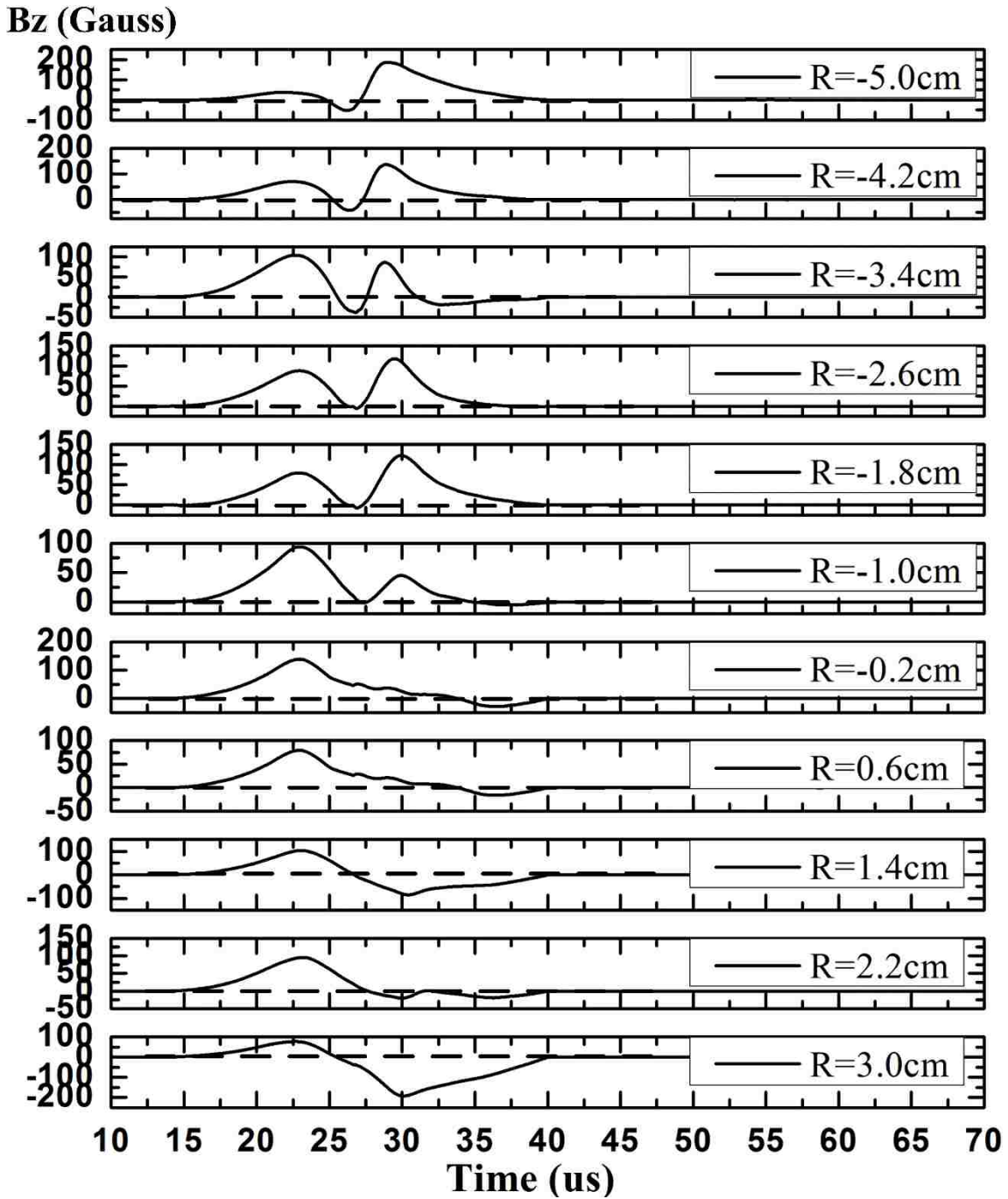
Figure 3.35. Typical B_z magnetic data with coaxial plasma gun operation settings in region II. (I_{gun}=79.25 kA and Φ_{bias}=0.39 mWb, Shot No. 137080515).

117
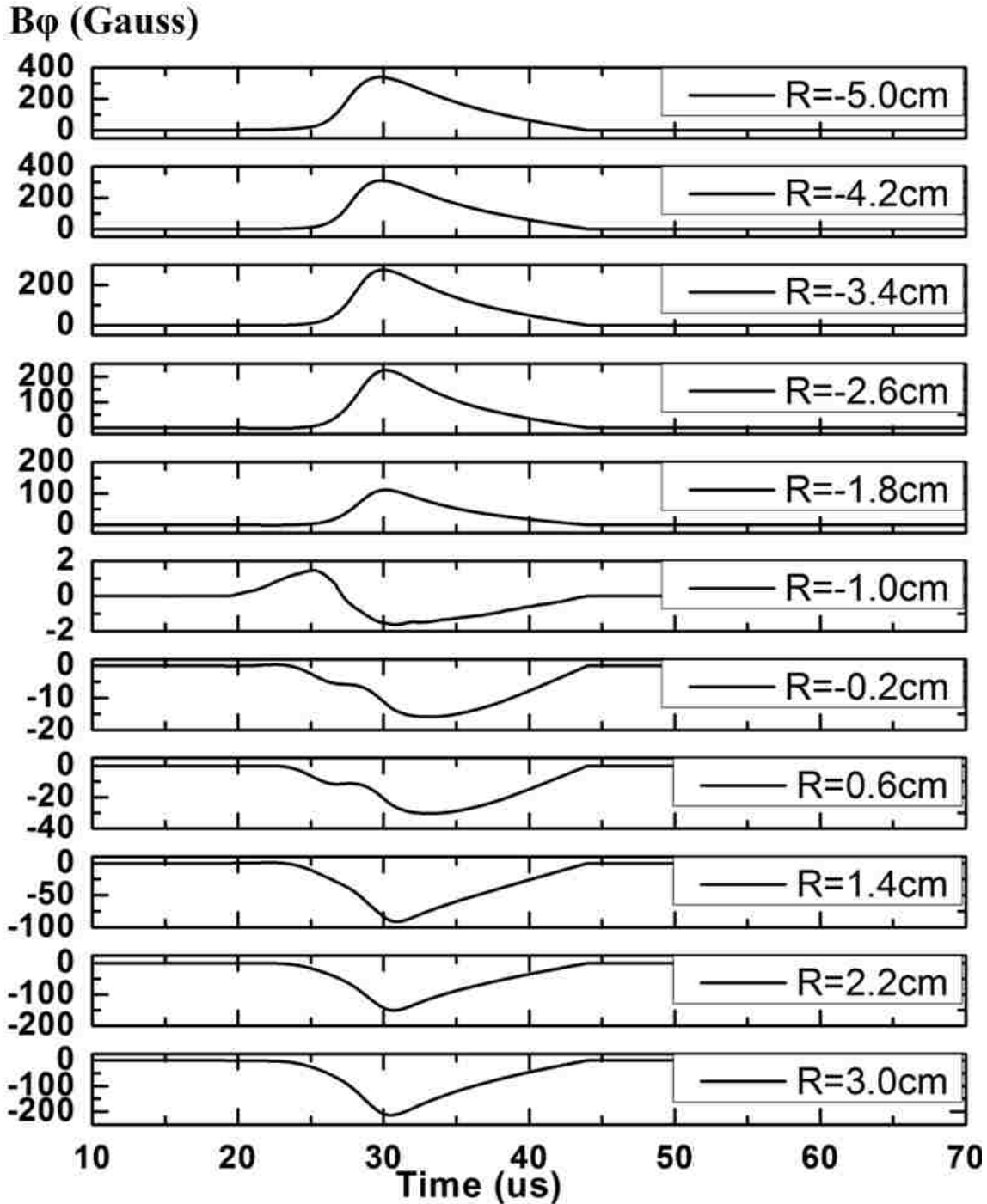
Figure 3.36. Typical B_φ magnetic data with coaxial plasma gun operation settings in region II. (I_{gun}=79.25 kA and Φ_{bias}=0.39 mWb, Shot No. 137080515).

For the PBEX project, magnetic probe data are obtained at multiple positions in the vacuum chamber. Unfortunately, there is shot-to-shot irreproducibility, which complicates
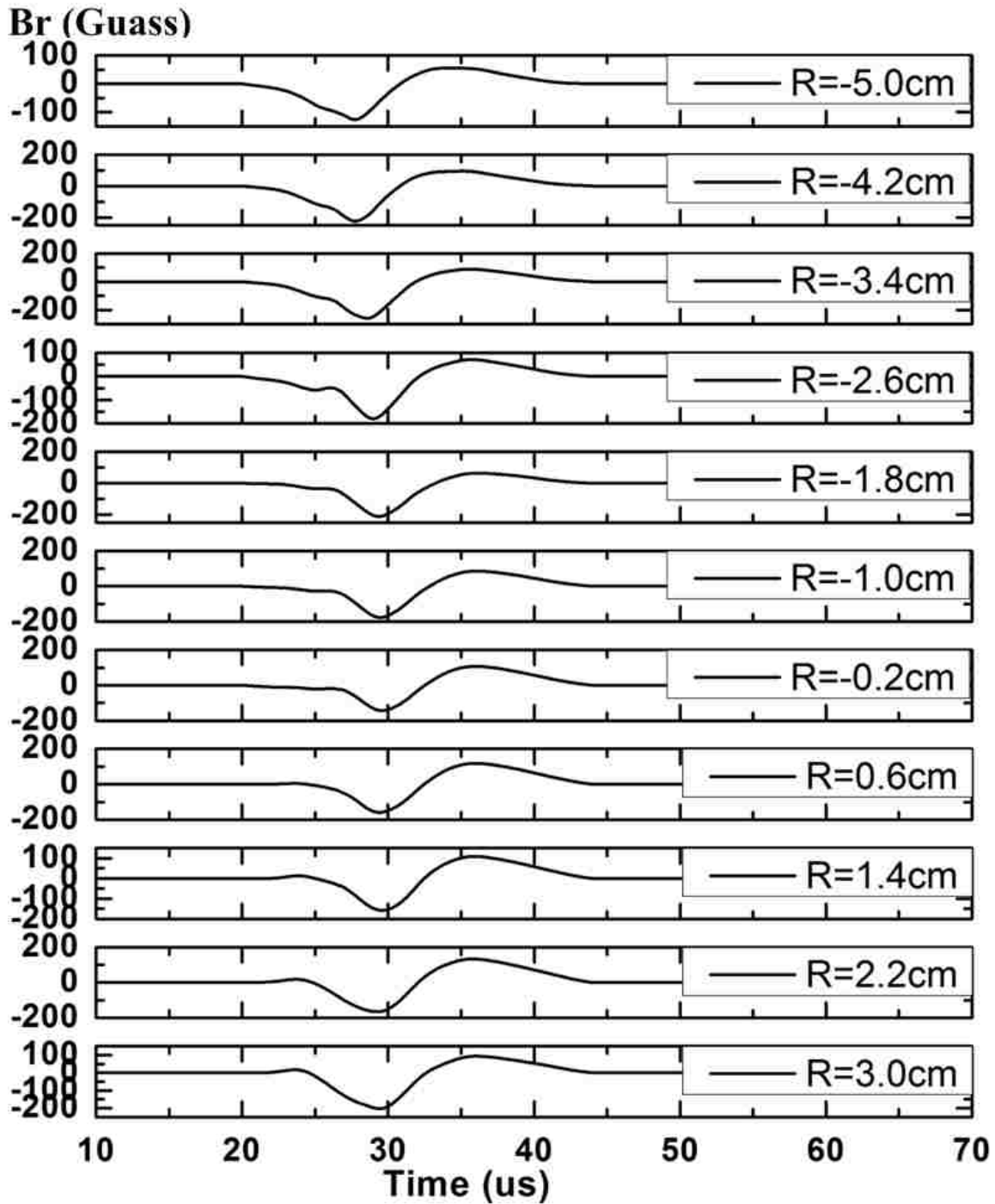
Figure 3.37. Typical B_r magnetic data with coaxial plasma gun operation settings in region II. (I_{gun}=79.25 kA and Φ_{bias}=0.39 mWb, Shot No. 137080515).

the analysis and interpretation. Although the plasma behavior is qualitatively similar under the

same gun operation settings for Region II, for quantitative magnetic field structure analysis,

the magnetic signal magnitudes and time delays (offset) have significant variation. This is problematic when analyzing the plasma's characteristic poloidal and toroidal magnetic field profiles at different radii, and makes identification of spheromak-like plasma formation difficult.

3.4.3 Spheromak-like bubble formation verification

In this section, several methods are employed to examine and verify spheromak-like plasma bubble formation in Region II, including a plasma propagation conjecture, and fitting poloidal and toroidal magnetic profiles to Bessel functions. Furthermore, λ time evolution in the vacuum chamber will be presented in the next section.

3.4.3.1 Plasma propagation conjecture

A similar method as was applied to the analysis of the magnetic field data for the jet case was employed to validate the measured magnetic field data for the spheromak case. The principle of this method is schematically exhibited in Figure 3.38, Top, with the gun-generated plasma propagating from right to left through the B-dot probe array. If the spheromak-like configuration is formed successfully and passes through the B-dot probe array, the B_r, B_Z, and B_φ signals detected by the probe array should be of a form illustrated in Figure 3.38, Bottom.

During this period of plasma passing time, B_Φ is typically unipolar, with upper-half positive and lower-half negative. B_Z is positive near the axis and negative further away from the axis. At the same time, B_r oscillates $1 \sim 2$ cycles. These characteristic magnetic field signals are consistent with the typical magnetic field data shown in Figure 3.35, Figure 3.36, and Figure 3.37 for shot No. 137080515 with the probe position at $z = 25$cm and $\varphi = 0$ poloidal plane. It is clear that B_r signals show bipolar oscillated waveforms as predicted. For B_φ signals,

the upper part signals are unipolar negative and the lower part are unipolar positive. For B_Z, the theoretical prediction also agrees with the measured results very well, which is illustrated in more detail in the next section when theoretical Bessel functions are used to fit the measured data.
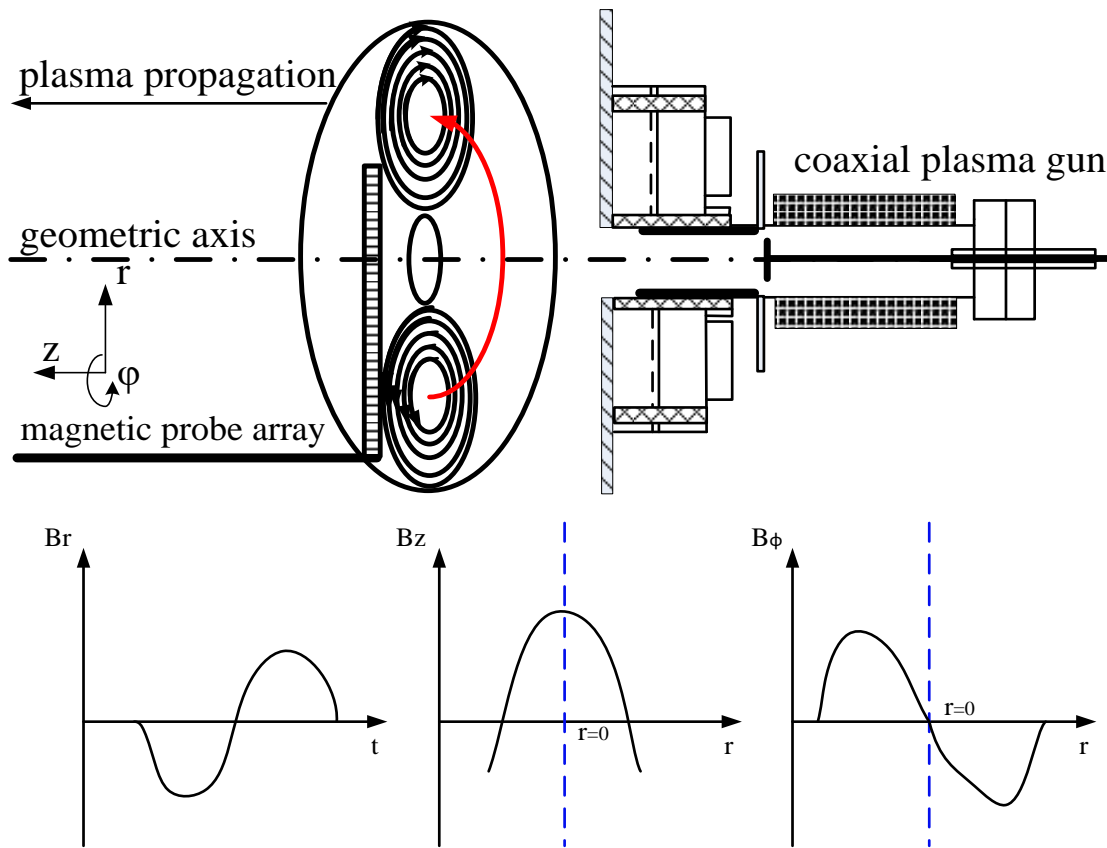
Figure 3.38. Sketch of spheromak plasma with typical magnetic field waveform.

Figure 3.39 shows the spatial magnetic field configuration from an example shot (No. 137080515). The toroidal magnetic field is plotted as a contour map on the top and the poloidal magnetic field's vector plot, with B-field streamlines, is shown at the bottom. It is important to note that the B-dot probe array is placed at $Z = 25$cm in space for this particular shot. Data with increased Z means early in time and vice versa.
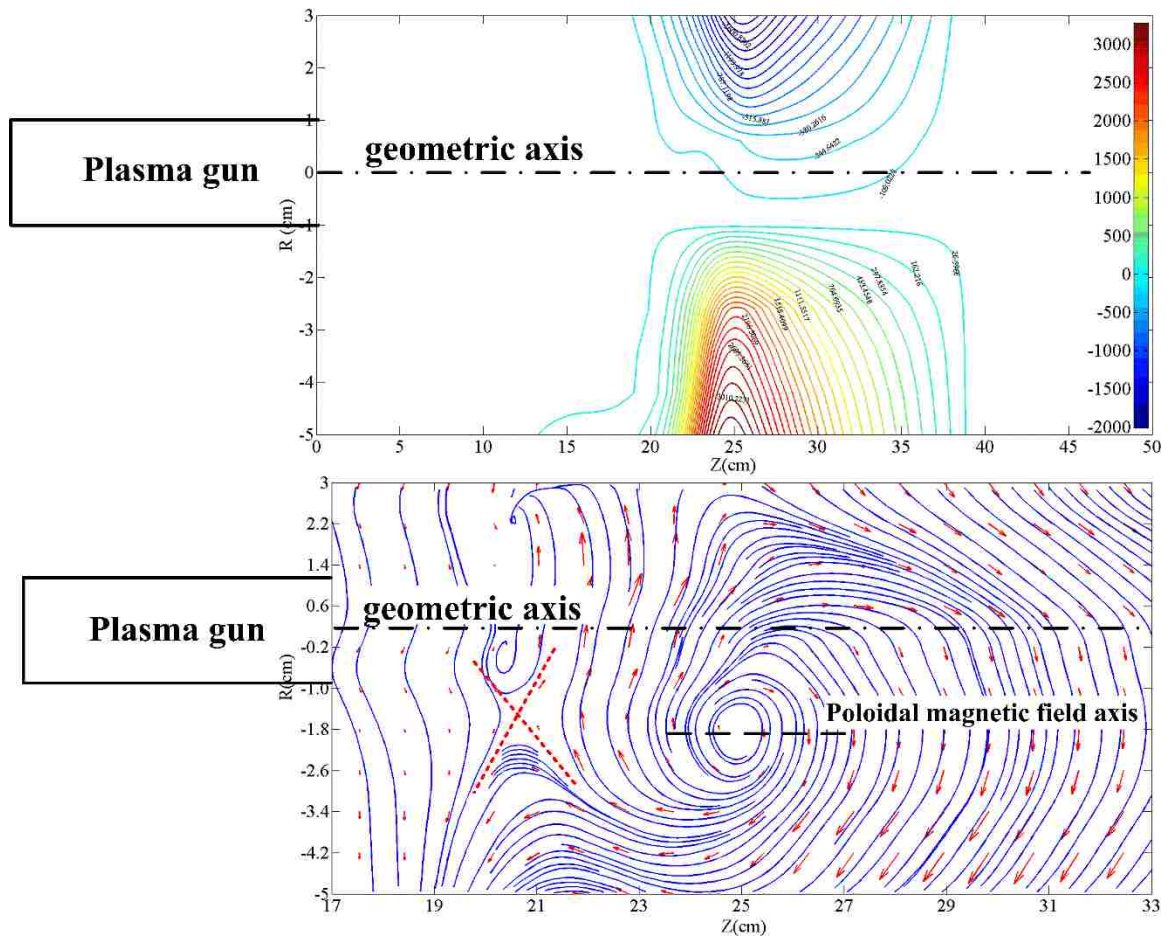
Figure 3.39. Top: contour plot of toroidal magnetic field symmetric around the geometric axis with inverse direction on each side. Bottom: vector plot of poloidal magnetic field with streamline lines.

Comparing the measurements with the theoretical analysis, the spheromak-like configuration is very clear. The vortex-like closed poloidal magnetic field lines with the polarized peak in toroidal magnetic field are consistent with the spheromak magnetic field topology. Specifically, the measurement plot shows that the toroidal magnetic field is roughly symmetric around the geometric axis with opposite direction for up and down sides (colored blue and red respectively in Figure 3.39). For the poloidal magnetic field configuration, the magnetic field axis is off the geometric axis and trailing behind the spheromak; a clear X-point indicates that magnetic reconnection happens during the plasma evolution.

3.4.3.2 A theoretical Bessel-function model fit

As discussed in Chapter 1 and Section 3.4.1, Taylor relaxation theory leads to the particular Taylor state force-free equilibrium which is characterized by $J = \lambda B$, with λ as a constant, independent of space position.[113] This theoretical analyses provides two ways to examine experimental data: 1) fitting measured magnetic field data to a Bessel function model; 2) calculating spatial λ to examine whether it is a constant during the time evolution. In this section, the measured magnetic field data will be fit to Bessel function model and spatial λ calculation will be validated in the next section.

Figure 3.40 shows the results of fitting a Bessel function of Eq. 3.23 to the radial profile of B_φ, and B_Z, at t = 25 μs as illustrated in Figure 3.39. These force-free eigenmode fits are a good match to the experimental data, and lend support to verify the spheromak-like formation in Region II. The errors are mainly introduced from: 1) the fact that the experimental boundary condition is not quite the same as that used in Eq.3.23's derivation where a cylinder boundary condition with closed ends is assumed. 2) The B-dot probe array perturbs the measurements, especially at the probe edges.

Furthermore, from the numerical fit of the Bessel function and Eq. 3.23, both k_z and k_r can be determined. Then $\lambda = \sqrt{k_z^2 + k_r^2}$ is calculated as 162.8 m^{-1} which is very close to the practical value of $\lambda_{threshold}$= 170.37 m^{-1} (Section 3.1).
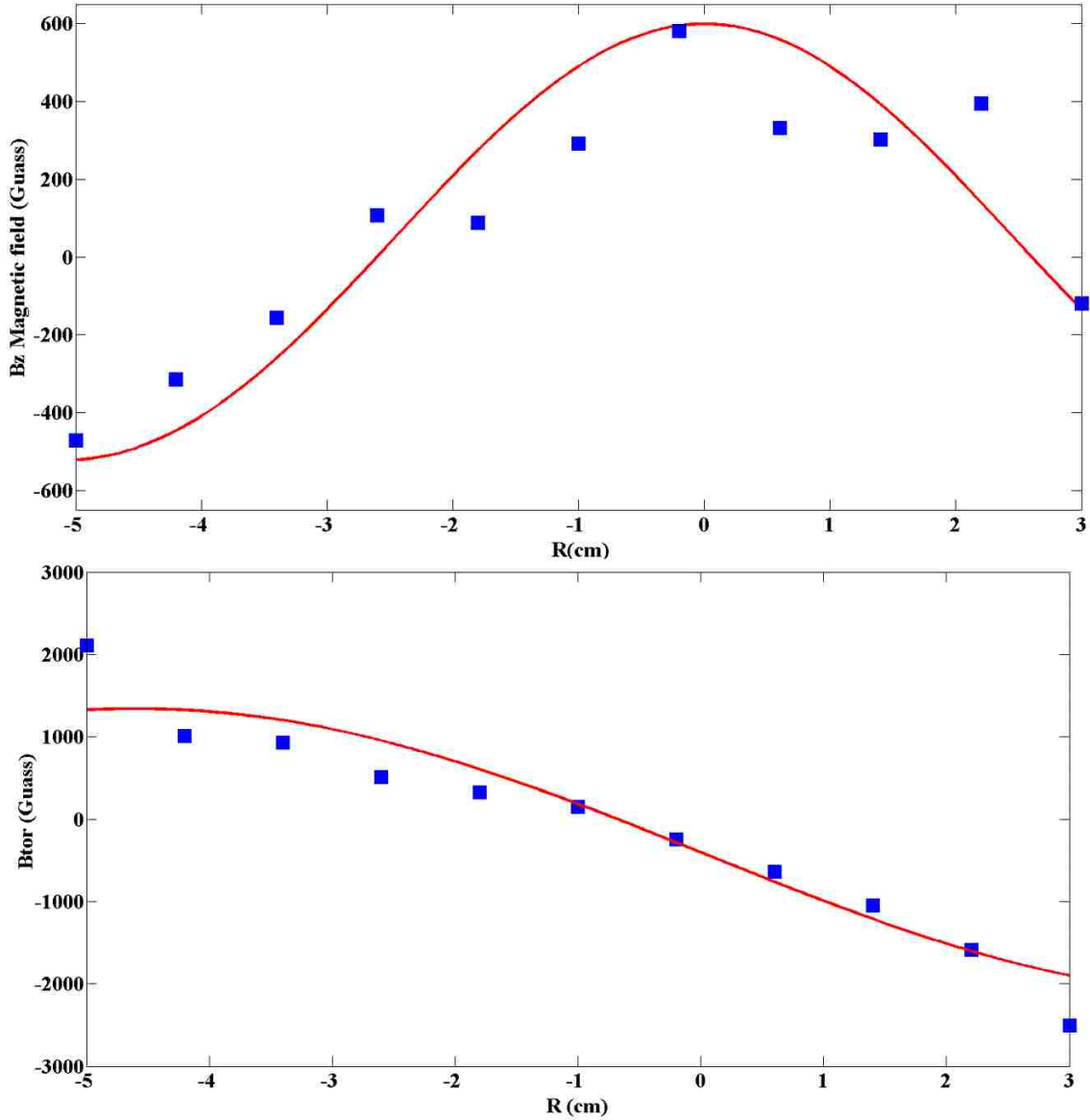
Figure 3.40. Experimental B_Z and B_φ magnetic field radial profile in the $\varphi = 0$ poloidal plane with theoretical Bessel-function fit.

3.4.4 Taylor relaxation characterization

For the coaxial plasma gun operation, a poloidal discharged current is driven through the plasma to generate a toroidal magnetic flux. The induced toroidal magnetic flux is injected into the system along with the linked pre-exit poloidal magnetic flux which is generated by the bias coil. As discussed above, the plasma then experiences Taylor-relaxation into an

equilibrium state. The original toroidal magnetic flux is usually much greater than the pre-exit poloidal magnetic flux. It is assumed that the relaxation process is a possible mechanism to convert the toroidal flux into poloidal flux.[56] A number of experiments have reported on this flux conversion associated with the relaxation process in spheromak devices.[4, 56, 114, 115] In this section, PBEX data is presented to demonstrate the magnetic flux conversion during the relaxation process.

3.4.4.1 Poloidal magnetic flux calculation

The poloidal flux, $\psi_{pol}(r, z)$, is the flux through the circle with its center at r = 0 lying in the geometric axis at axial position z.[116]

$$\psi_{pol}(r, z) = \int_0^R 2\pi r \cdot B_z(r, z) dr \tag{3.24}$$

with the boundary conditions (considering $\nabla \cdot B = 0$):

$$\psi_{pol}(r = 0, z) = 0 \ and \ \psi_{pol}(r = R, z) = 0 \tag{3.25}$$

The integral given in Eq. 3.24 is very straightforward and is calculated by employing the measured magnetic field data from Shot No. 137080515 and converting the time dependence into z-direction distance dependence (the propagation speed of 1.8 cm/us is estimated during the calculation).

The calculated result of the estimated poloidal flux is shown in Figure 3.41. An interesting note is that for this particular shot, $\psi_{pol}(r = R)$ naturally vanishes without any artificial constant added during the calculation, which means $\psi_{pol}(r = R)$ can be treated as $\psi_{pol}(r \sim \infty)$. This also shows that $\psi_{pol}(r = 0)$ does not go to zero, which is expected since that there is an offset between the axis of symmetry of the device and the geometric axis. This asymmetry demonstrates again that plasma formation is sensitive to the initial conditions of

plasma gun discharge. This shot-to-shot variation is a potential issue for experimental measurements.
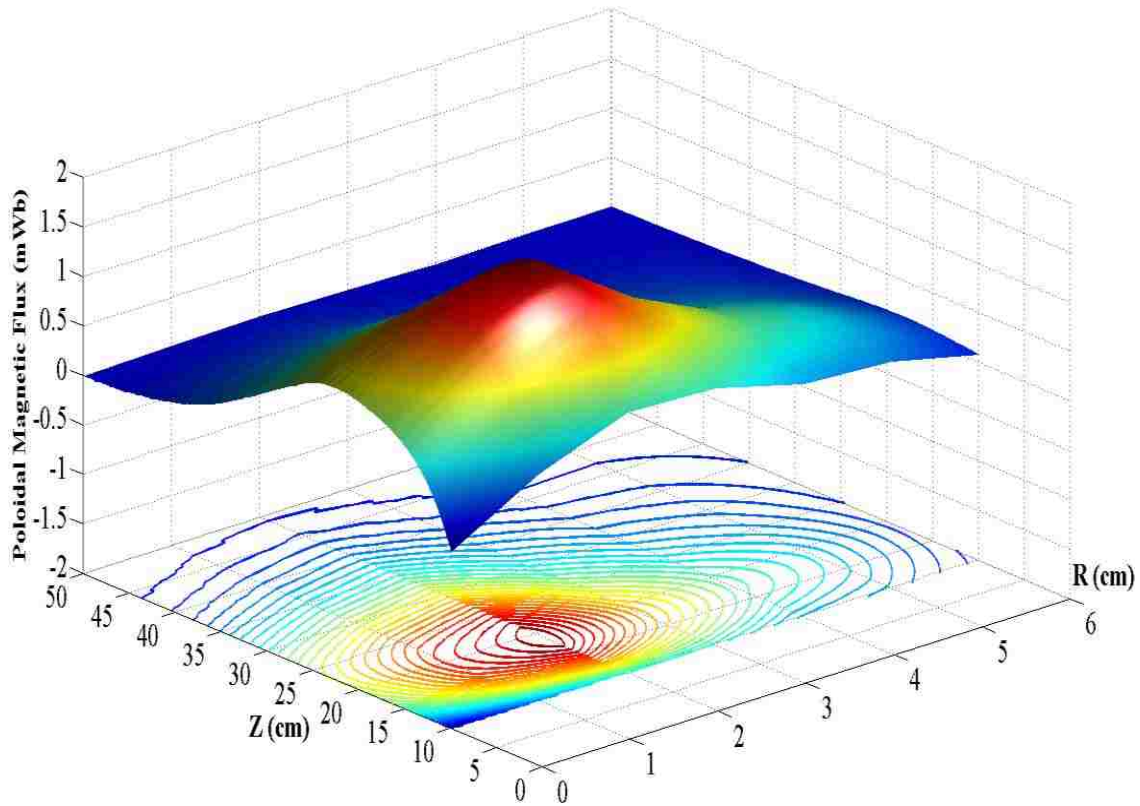
Figure 3.41. Calculated poloidal magnetic flux surface.

The location of the maximum poloidal magnetic flux is located on the spheromak magnetic axis as indicated in Figure 3.39, and Figure 3.41. For this particular shot, the magnitude of poloidal magnetic flux is 1.5 mWb, which is roughly triple the applied external bias magnetic flux (0.62 mWb). This dramatic increase in poloidal magnetic flux is beyond measurements, and calculations, uncertainties, and provides strong evidence that Taylor relaxation is occurring.

In addition to the fixed probe position signal analysis, various positions of B-dot probe data have been employed to examine the spheromak-like formation time evolution and spatial distribution. The peak poloidal flux at different positions across the vacuum chamber has been

calculated from multiple shots (Shot No.031073015, No.033073015, No.031080515, No.032080815, No.136080515, No.137080515, No.138080515, No.033081315, No.034081315, No.032081915, No.033081915, No.032082415, No.033082415 and No.034082415). The results are plotted in Figure 3.42, with the mean value of the maximum poloidal flux shown with black squares, and the standard deviation of the calculations as error bars.
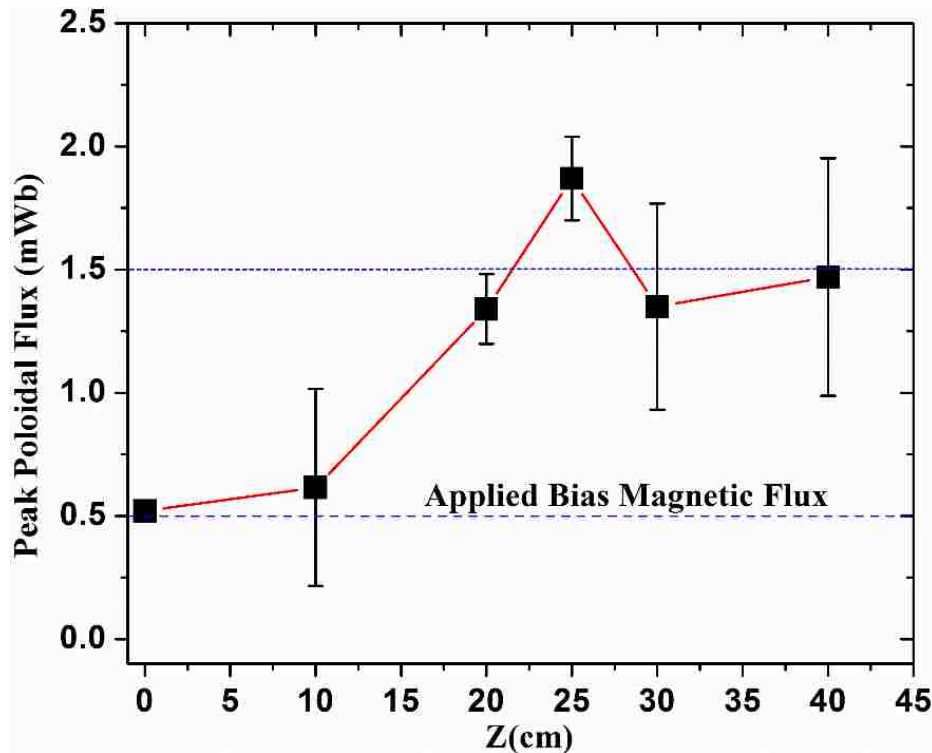
Figure 3.42. Measured peak value of poloidal flux at various probe position.

Figure 3.42 indicates that the peak value increases from 0.52mWb up to 1.5 mWb in the region $0 < z < 25$cm along with the position where the reconnection X point is detected as shown in Figure 3.39. The rise of poloidal magnetic flux happens simultaneously with the magnetic reconnection and spheromak detachment process. When the detachment completes, the poloidal flux remains roughly a constant with the spheromak propagating across the vacuum chamber.

3.4.4.2 Toroidal magnetic flux calculation

The net toroidal flux carried within the spheromak can be defined as:[66]

$$\Phi_{tor} = \int_0^{z_{max}} dz \int_0^R dr \cdot B_\varphi \tag{3.26}$$

Due to the fact that the B-dot probe has limited length and axial range (z direction), it is impossible to measure and calculate the toroidal magnetic flux over the whole region. A practical method, Full Width at Half Max (FWHM), is employed to estimate the toroidal magnetic flux. FWHM has been a useful and powerful method, and is widely used in plasma data analysis.[117-119]

For this method, the integration area is defined as the area where the absolute value of the toroidal magnetic flux is greater than half of the peak value. This solution is indicated in Figure 3.43. Similarly, as shown in Figure 3.39, the upper plot is the toroidal contour plot with the integration area marked. The lower plot is the poloidal vector plot for the same shot (No.033081315). The classic poloidal vortex structure followed by a magnetic X-point covers the qualitatively equivalent area. However, the FWHM area is leading the vortex in space as shown in the experimental data in Figure 3.43.

The calculated results using the measured magnetic field data from multiple shots are shown in Figure 3.44. Once again, the mean value of the maximum poloidal flux is indicated as black square, and the standard deviation of the calculations is used as the error bar. The toroidal flux drops from 8.5 mWb to 5.0 mWb at the position z = 20cm, while the poloidal flux increases approximately at the same location as shown in Figure 3.42. These results agree with flux conversion, which is a typical characteristic of the relaxation process.
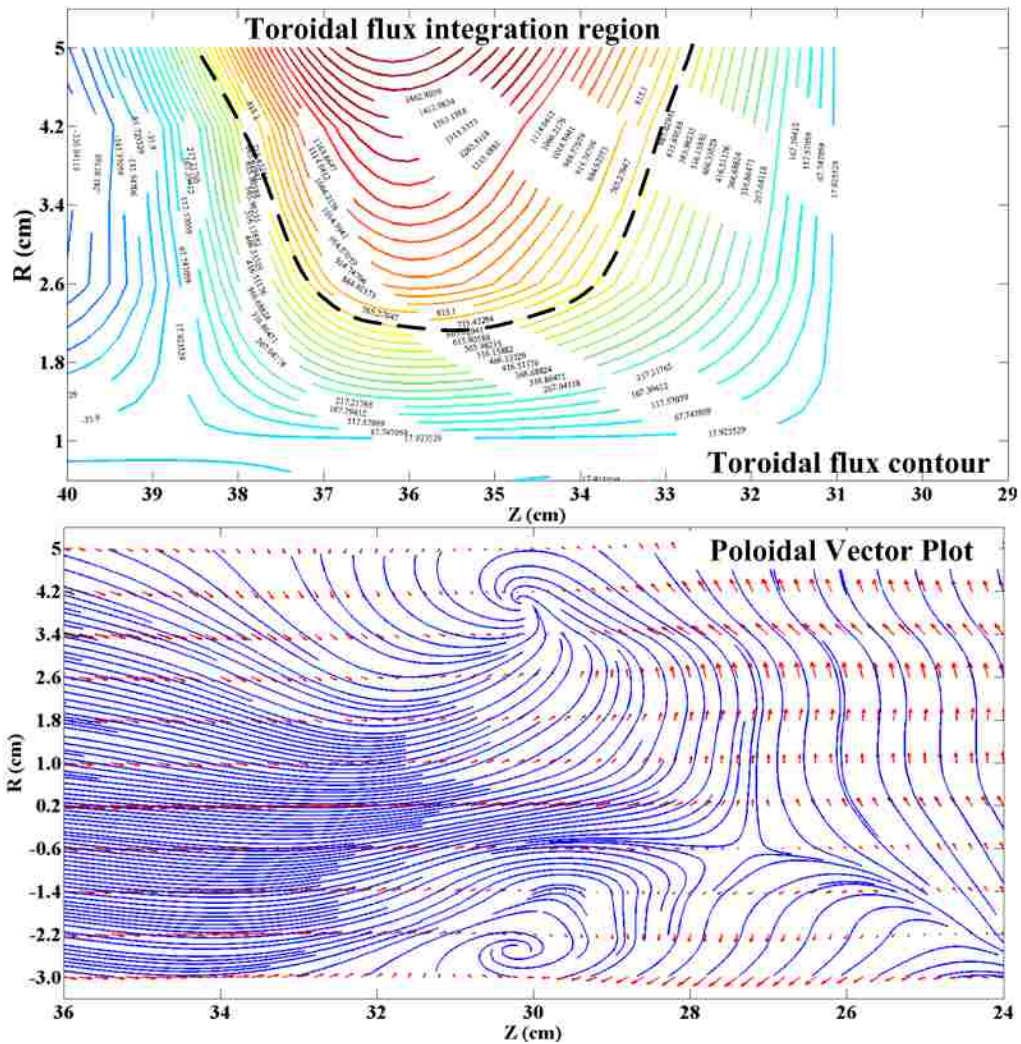
Figure 3.43. Illustration of FWHM method used to integrate toroidal magnetic flux.
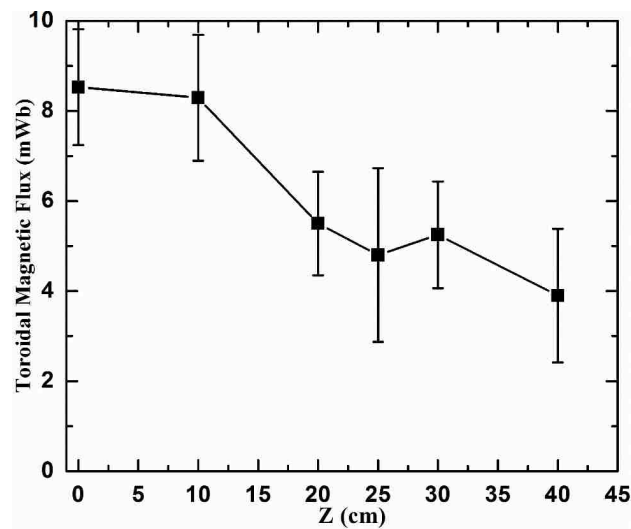
Figure 3.44. Calculated toroidal magnetic flux (employing FWHM) at various probe position.

An important feature to note here is that for the PBEX project, the ratio (poloidal flux to toroidal flux) of 1:3 is observed in the spheromak-like plasma during the space region 20 cm $< z < 35$cm.

3.4.5 Spatial variation and time evolution of λ

3.4.5.1 Dynamic λ calculation

Taylor relaxation theory predicts a spatially constant λ to achieve a force-free state.[110] For such an equilibrium, the plasma is in the lowest energy state for a given injection helicity. As discussed above, the plasma's λ is the key parameter to characterize plasma dynamic evolution. It indicates the direction of injected helicity flow, whether or not a spheromak-like plasma is formed successfully, and the ratio between the magnetic energy and the total helicity of the system.[69]

In this section, the λ dynamics during the plasma lifetime is calculated and analyzed to examine the Taylor relaxation process. Assuming a near force-free state, the dynamic λ can be quantitatively determined by:[120]

$$\lambda = \frac{\mu_0 J_\varphi}{B_\varphi} \qquad (3.27)$$

for B_φ, the measured data can be used for the calculation directly. And for J_φ, the detailed method is presented below.

3.4.5.2 Current density J_φ calculation

The toroidal current density, J_φ, can be calculated in cylindrical coordinates as follows:

$$J_\varphi = \frac{1}{\mu_0}(\nabla \times \vec{B})_\varphi = \frac{1}{\mu_0}\left(\frac{\partial B_r}{\partial z} - \frac{\partial B_z}{\partial r}\right) \qquad (3.28)$$

This equation requires spatial differentiation operations which are particularly sensitive to the input data.[121] So, once again, it is important to calculate and analyze the magnetic field data from one single shot due to the reproducibility issues mentioned previously. The terms $\frac{\partial B_r}{\partial z}$ and $\frac{\partial B_z}{\partial r}$ can be evaluated in a poloidal plane employing the method discussed above from a single plasma discharge.
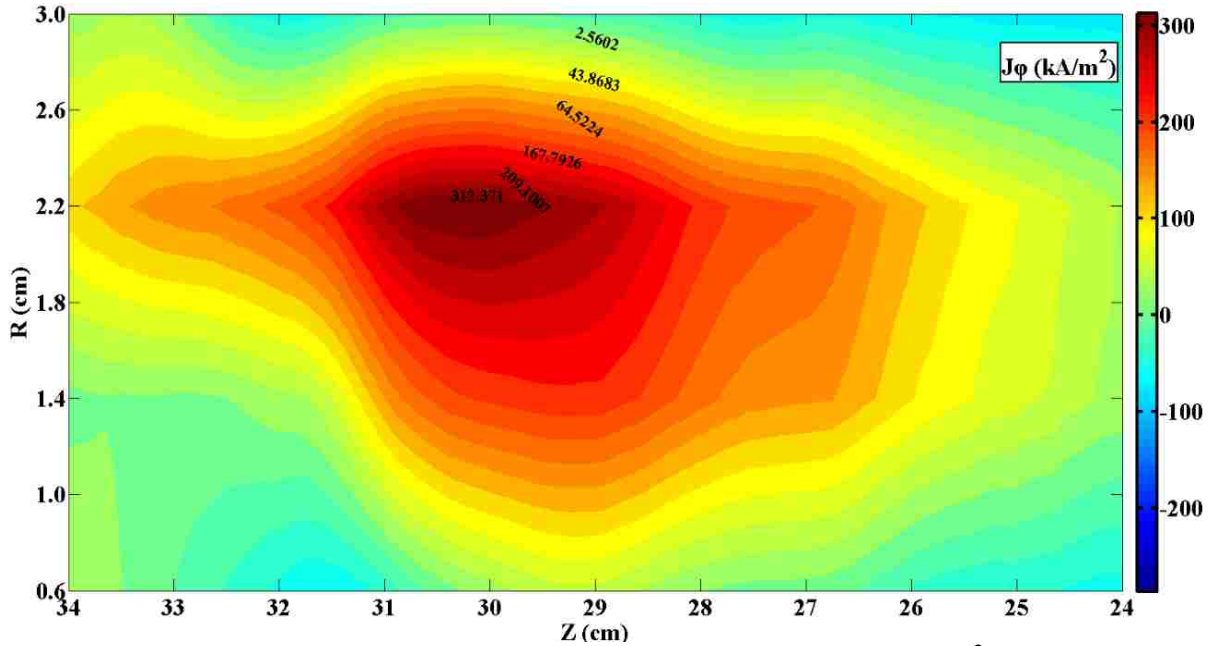
Figure 3.45. Contour plot of calculated toroidal current density J_φ (kA/m^2) in the poloidal plane.

Figure 3.45 shows the contour plot of the calculated J_φ in the poloidal plane. The magnetic field data was obtained with the probe positon at z = 30 cm and φ = 0. It is noted here that the J_φ contour plot is similar to the B_φ contour which is again strong evidence for a force-free state.

Once the J_φ value is determined, λ can be quantitatively determined by Eq. 3.27. The contour plot of the calculated λ is shown in Figure 3.46. Combined with Figure 3.45, these two plots show the analysis process for λ calculation. It is noted here that as $\left|B_\varphi\right| \to 0$, the value of

λ increases without bound, and loses any realistic physical meaning. For this reason, during the calculation, $|B_\varphi|$ at any position where the value is less than 5% of the peak value is forced to zero. At these locations, J_φ typically has a smaller value as well. As a result, this assumption does not affect the calculation results dramatically.[4]
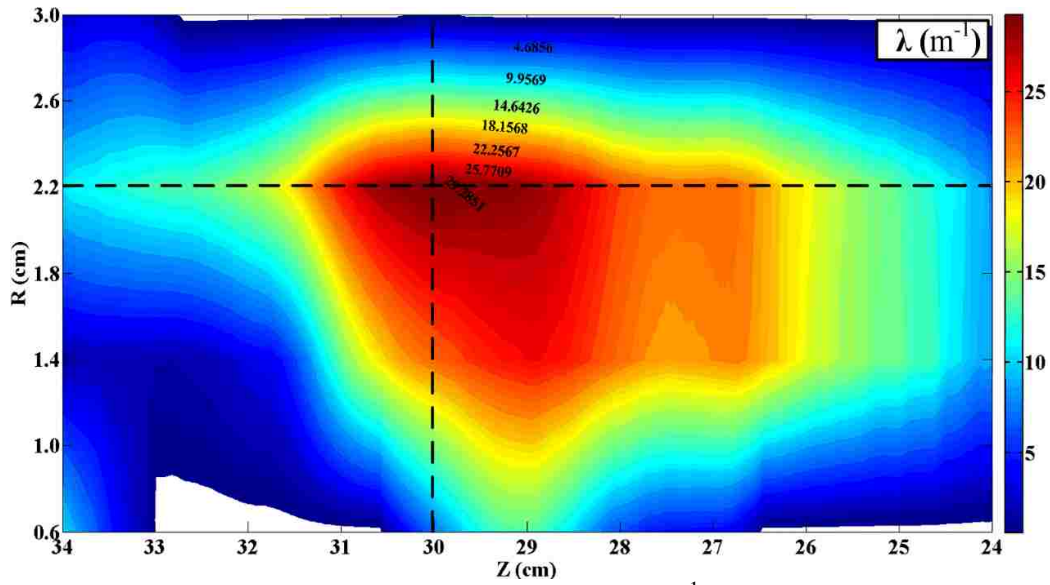
Figure 3.46. Contour plot of calculated λ (m^{-1}) in poloidal plane.

3.4.5.3 λ spatial evolution

The two dashed lines in Figure 3.46 indicate the location of the data to show the spatial characteristics of λ. The radial and axial profiles are plotted in Figure 3.47 with the probe position at z = 30 cm, $\varphi = 0$, and central r = 2.2 cm respectively. The radial profile of λ (the lower one) shows a centrally peaked profile, where the axial profile exhibits a relaxing spheromak plasma. This kind of λ profile is also observed, and reported, by other similar spheromak experiments.[4, 114]
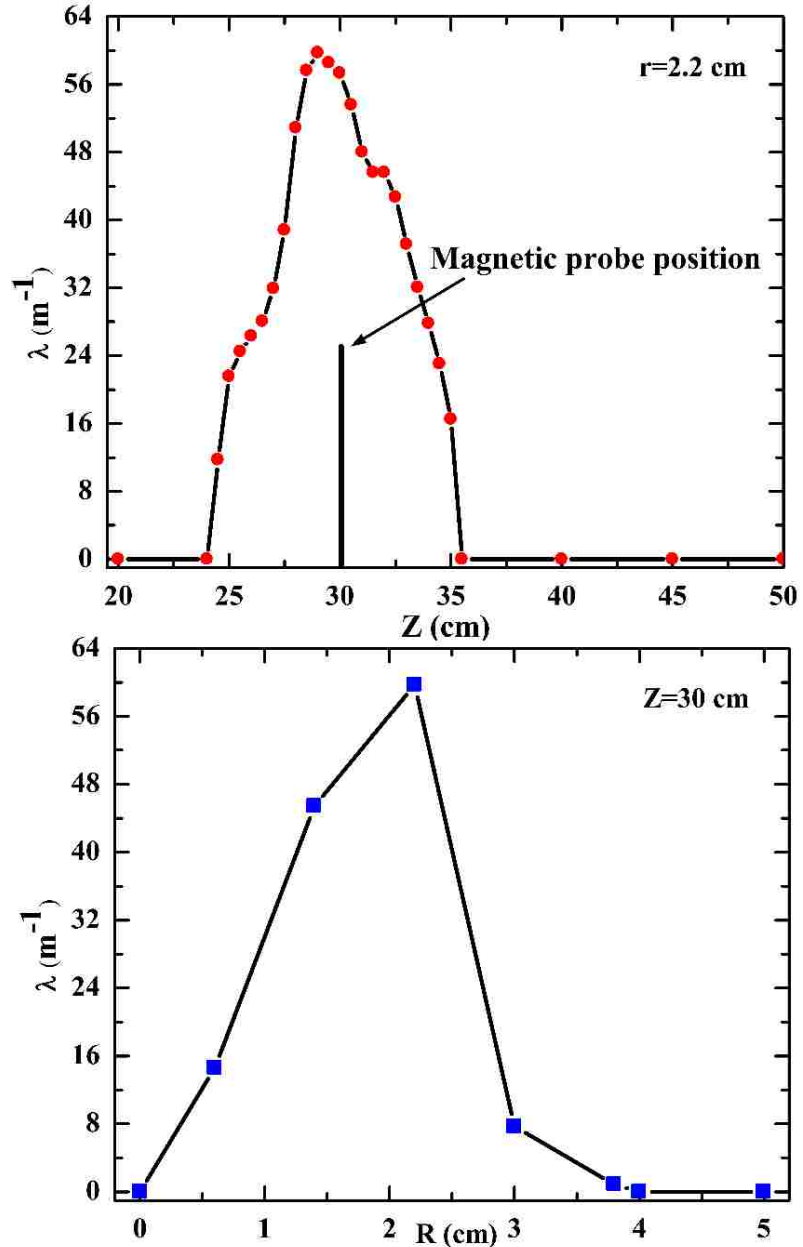
Figure 3.47. Axial and radial profile of λ at Z = 30 cm and r = 2.2 cm, respectively.

3.4.5.4 λ time evolution

As discussed in detail in Section 3.4.4.1, a similar method used to analyze the time evolution of the poloidal magnetic flux was employed to infer the λ time evolution process by calculating peak λ values at several spacial locations across the vacuum chamber. The result is plotted in Figure 3.48.
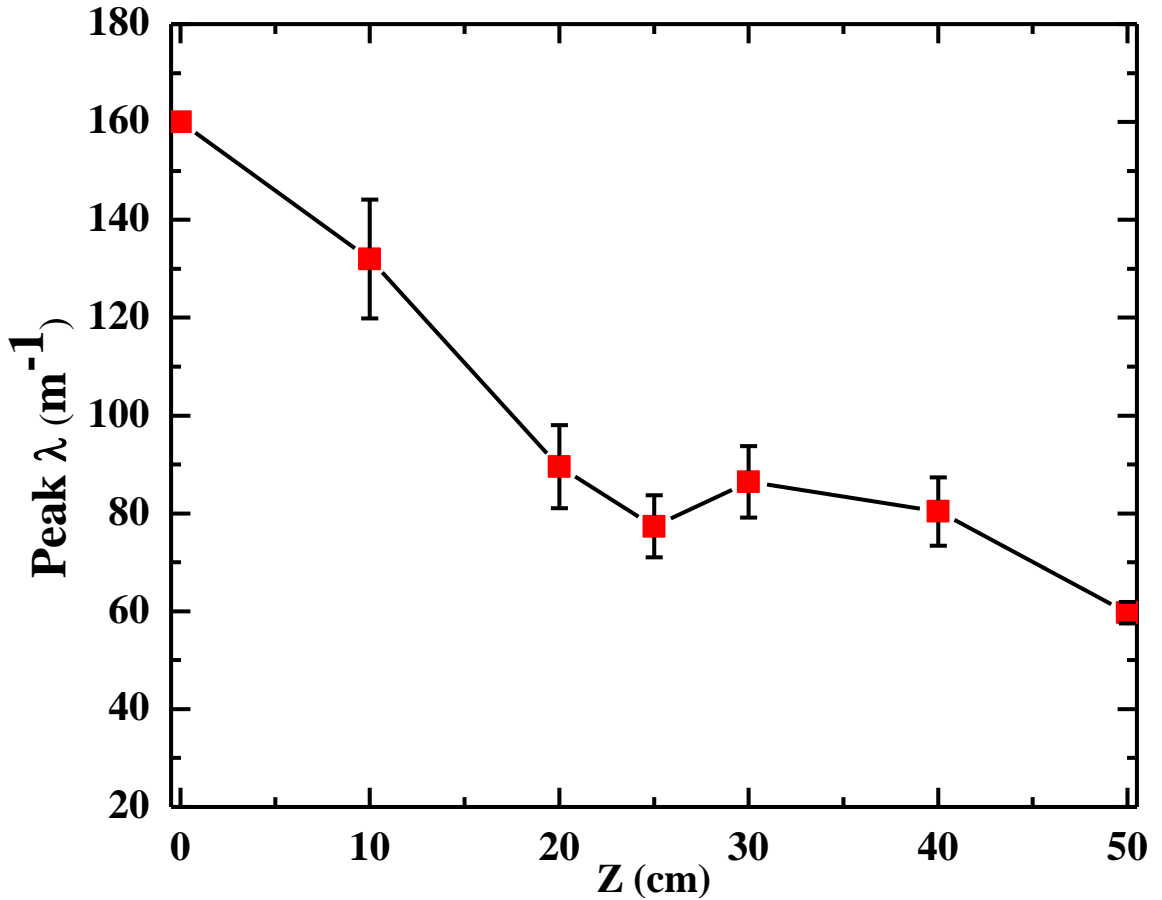
Figure 3.48. Peak λ values along z-axial in the vacuum chamber.

The plot in Figure 3.48 indicates that the λ drops quickly after the plasma leaves the gun port muzzle. The original value, $\lambda_{gun} = \frac{\mu_0 I_{gun}}{\Phi_{bias}} = 159.3$ m^{-1}, drops to $\lambda = 79.7$ m^{-1}. Throughout the central area in the vacuum chamber (20 cm < z < 35cm), a roughly constant λ value is achieved, indicating the occurrence of Taylor relaxation process under the assumption of no, or small, expansion of the plasma in this space region.

3.5 Summary

For the coaxial plasma gun operation, during the initial breakdown, a plasma forms in a radially symmetric arrangement. The breakdown path is determined by the gas density according to Paschen's law. An ~ 80 kA peak current flows from the anode to the cathode

creating an induced toroidal magnetic field. The self-generated Lorenz force expels the plasma out of the gun muzzle. At the same time, if there is a bias magnetic field applied to the plasma, the magnetic tension force will try to pull the plasma back into the gun muzzle. The practical parameter, $\lambda = \frac{\mu_0 I_{gun}}{\varphi_{bias}}$, dictates the plasma formation generated by the gun. A high-speed camera was employed to survey the plasma topology, and evolution, under different plasma gun settings. Based on image data, four operation regions have been identified.

In region I, a current-driven plasma jet was formed and launched into the main vacuum chamber. A snowplow model was set up to simulate the jet head performance which is consistent with the image obtained. Furthermore, a Bernoulli-like relation was set-up to characterize the property of the plasma jet-head velocity. Based on magnetic field measurements from a 3D B-dot probe array, a global helical magnetic structure was determined. For PBEX's experimental apparatus, this was a right-handed helix.

The current-driven plasma jet was susceptible to current-drive instabilities. The plasma column exhibited the current-driven ideal MHD kink instability consistent with the Kruskal-Shafranov criterion. The criterion can be expressed in terms of the PBEX experimental parameters. When the plasma length satisfies Eq. 3.19, the plasma column begins to kink. The formerly straight column becomes helical. This is also observed in the toroidal magnetic field vector plots at multiple axial positions.

In Region II, neutral argon gas was puffed into the electrode region where it is ionized by the high voltage ($6\,\text{kV} - 10\,\text{kV}$) applied between the cathode and anode. After the ionization, a large discharged current flows along the inner electrode (generating an azimuthal magnetic field B_φ), through the plasma, and into the outer electrode. The plasma was pushed forward by

the $J \times B_\varphi$ force against the applied bias magnetic tension. The plasma carried the magnetic field lines with it due to the "frozen-in" condition. Magnetic field lines reconnect behind the plasma, forming a donut-shaped spheromak. This spheromak-like plasma formation was verified from the measured experimental data. Both poloidal and toroidal magnetic fields show a closed-surface magnetic flux structure followed by a clear x-point, which indicates a magnetic reconnection process when the spheromak detaches from the gun muzzle.

Based on the assumption that the plasma is in a force-free state (dramatic changes in the magnetic field are omitted), and propagates at a constant velocity with a small expansion during the measurement, the magnetic topology in the system length range is investigated from one single shot. Fitting the radial profile of the magnetic field data into a Bessel-function model provides a direct method to verify the Taylor-relaxed state. The results indicate that a Taylor relaxation process occurs simultaneously with the spheromak formation. The results of the poloidal flux and the toroidal flux calculation show the magnetic flux conversion process along with the Taylor relaxation process.

At the same time, the spatial and temporal profiles of λ are calculated. A radial profile of λ shows a peak near the magnetic axis, and decreases away from the axis. The time evolution shows a roughly constant λ which indicates the plasma is in a force-free state.

In Region III, a second plasma was formed due to ringing of the discharged current. A merging of these two plasmas was observed. A crowbar circuit is under construction to eliminate the second plasma. In Region IV, due to the strong bias magnetic field, plasma barely leaves the gun muzzle. Detailed study of regions Region III and IV is outside the scope of this thesis.

Chapter 4 Launching Plasma into a Background Magnetized Plasma/Background Magnetic Field

4.1 Introduction

Although interstellar space is very empty and the stars are very far apart, the space between the stars still contains a very diffuse medium of gas and dust which is called the interstellar medium (ISM).[122] The chemical compositions of the ISM is neutral hydrogen gas (HI), molecular gas (mostly H2), ionized gas (HII), and dust grains.[123] The interstellar medium contains about of 5-10 billion solar masses worth of gas and dust.[124] One piece of strong evidence for this is that the ionized hydrogen (in the plasma state) can be detected during the process of fluorescence, glowing with a pinkish red color as shown in Figure 4.1. As a result, the astro-jet and bubble radio lobes propagate into the ISM rather than into vacuum.

Figure 4.1. Red light from H emission in the Triffid Nebula. Image Credit: R Jay Gabany.[125]

For the PBEX project, in order to be more accurate and closer to the astrophysical situation, the background magnetized plasma generated by the HelCat (Helicon-Cathode) linear device was employed to simulate the ISM effects in the astrophysical environment.
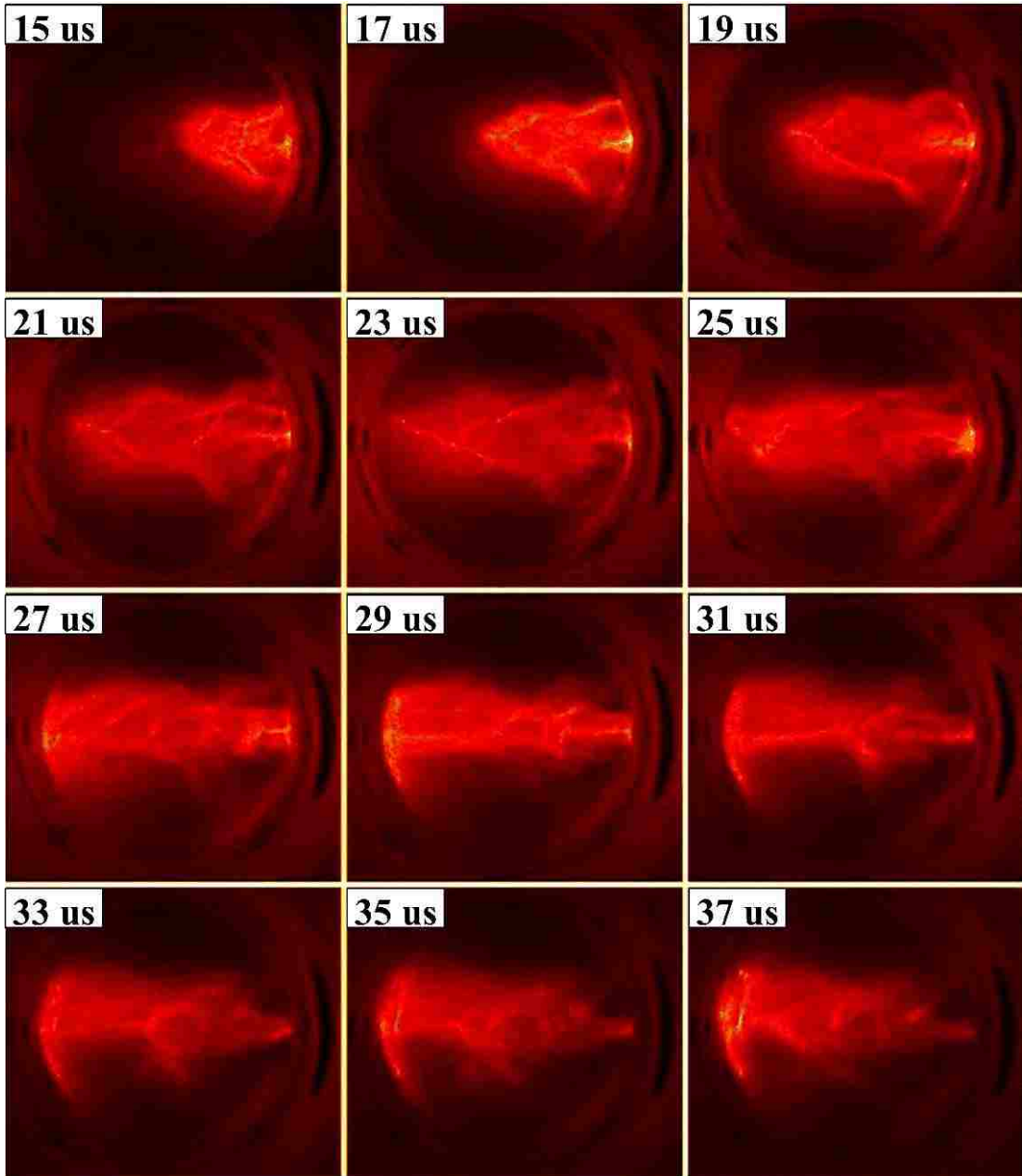
Figure 4.2. Plasma jet is launched into the background magnetized plasma (Shot No. 007050114).

As discussed in Chapter 3, the plasma generated by HelCat has a lower density and lower temperature than the coaxial-gun-generated plasma. The experimental setup, which aims at launching plasma into a background magnetic field/plasma, is innovative and brings new results and insights into plasma-gun-related experimental research.
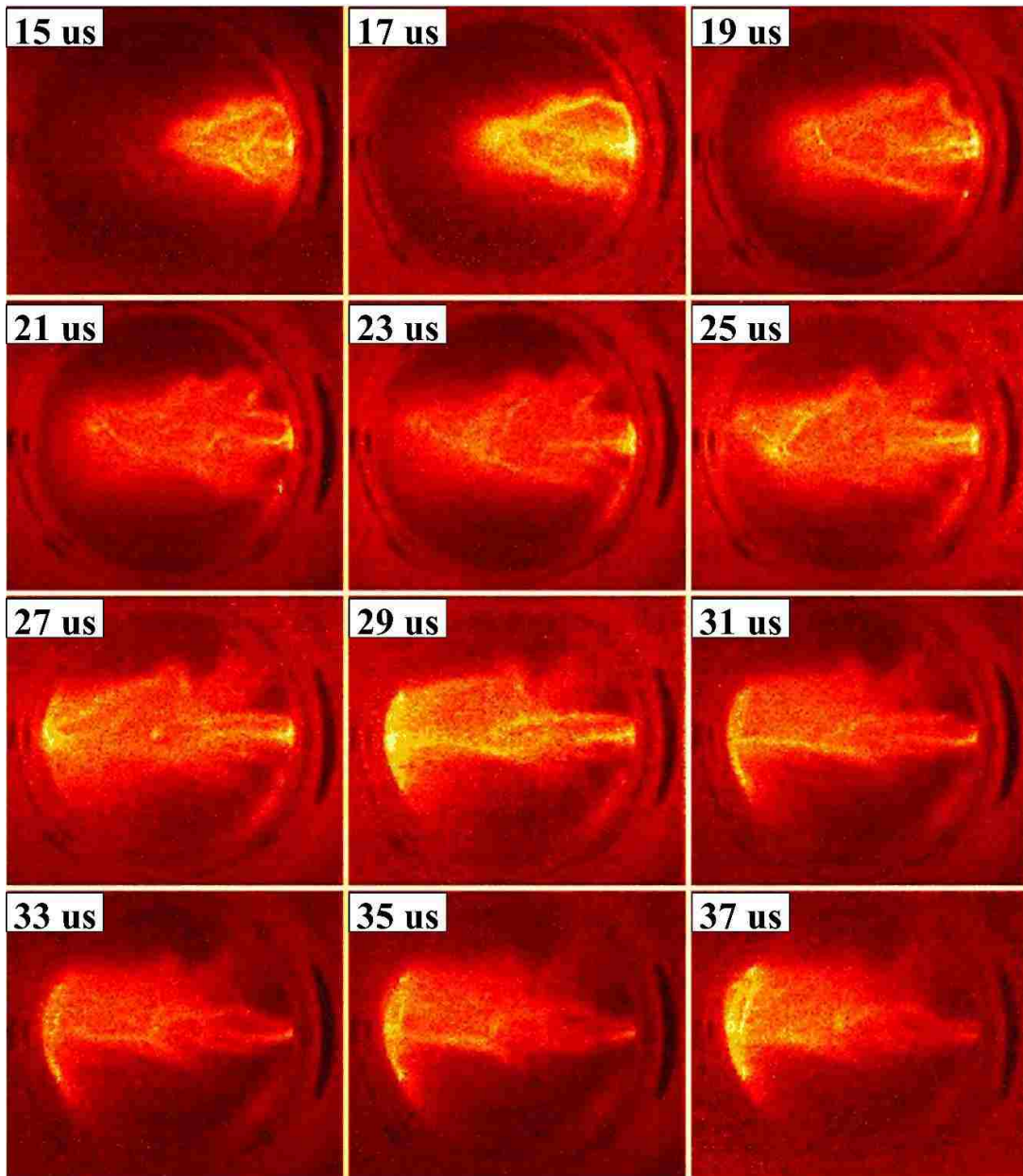
Figure 4.3. Plasma jet is launched into the background magnetized field (Shot No.008050114).

Figure 4.2, and Figure 4.3, highlight the similarities between launching the coaxial-gun-generated plasma into a background magnetized plasma, and a background magnetic field without plasma. Both figures show the image data taken with the same discharge current absent any bias magnetic flux. As discussed in Chapter 2, for these experimental settings, both launched plasmas are in the same region: Regime I i.e. plasma jet formation.

Figure 4.2 shows the plasma jet's evolution, after the plasma jet leaves the gun muzzle, with a background magnetized plasma, and Figure 4.3 shows the jet's development with a background magnetic field, but no plasma. From these image data, there is no evident difference between these two cases. Magnetic field measurements lend further support for this conclusion. This similarity is reasonable since for the background plasma, $\beta_{background} \ll 1$, which means that the magnetic pressure dominates over the plasma kinetic pressure, and the background magnetic field plays the key role for the interaction between the background magnetized plasma and the gun-generated plasma. As a result, in this Chapter's discussion, without loss of generality, all the data results presented here are for the case where the coaxial gun launches different plasma formations into a background magnetic field without plasma.

4.2 Plasma jet propagating into the background magnetic field

For operation Regime I, where the coaxial gun generated plasma jet propagates into the main vacuum chamber with a background magnetic field of 500 Gauss, a more stabilized jet body column (with longer column length and longer life-time) is observed from the image data compared with the jet launched into the vacuum as shown in Figure 3.23. In this section, the experimental data from the CCD camera and the B-dot probe array are presented to show the stabilized plasma jet formation. Theoretical and computational efforts are underway.

4.2.1 Experimental data

4.2.1.1 CCD camera images

The image data in Figure 4.3 show the case where a plasma jet is generated and launched into the main vacuum chamber with a background magnetic field of 500 Gauss.
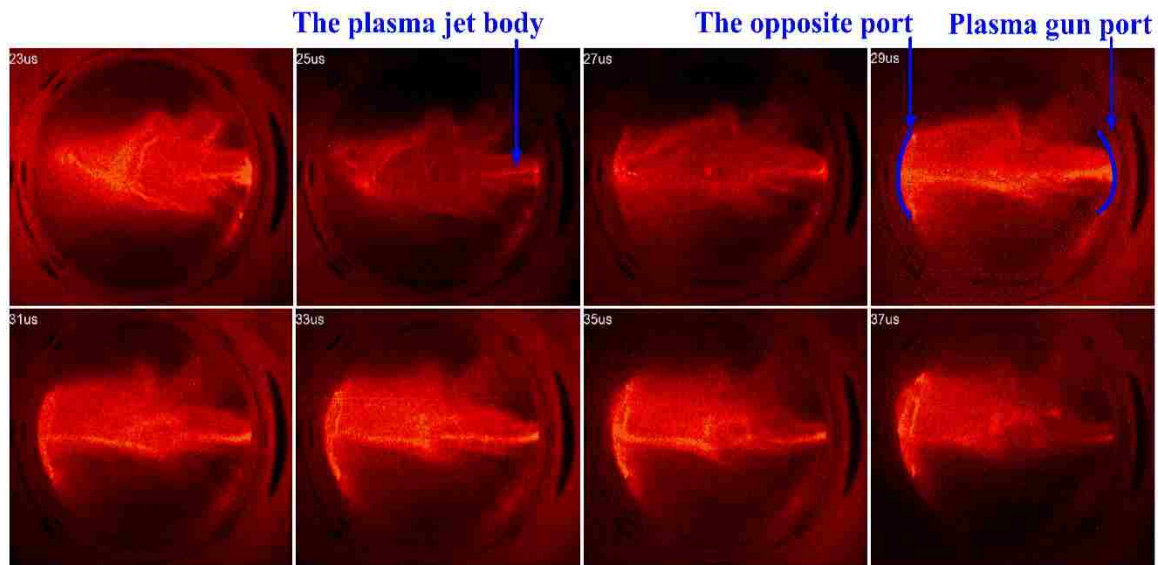
Figure 4.4. A more stabilized plasma jet column is observed (Shot No.008050114).

From the image data, a jet with a parabolically shaped advancing front is formed at t = 15 μs. At t = 29 μs, the visible jet body length reaches the full length (50 cm) across the vacuum chamber from the gun muzzle to the opposite port as marked in Figure 4.4. The jet body with a full length lasts from approximately t = 29 μs to t= 37 μs, when the plasma jet starts to dissipate. Note that the plasma jet can possibly last even longer in time, considering t = 37 μs is the time point when the main cap-bank discharged current, I_{gun}, reverses direction as shown in Figure 3.33.

4.2.1.2 Poloidal and toroidal magnetic field measurement

For the plasma jet launched into a background magnetic field, the poloidal and toroidal magnetic fields were measured with the B-dot probe array. The poloidal magnetic field radial

profile is plotted, and compared to the plasma jet launched into vacuum in Figure 4.5. Also, for the radial profile of the toroidal magnetic field, the result, along with the comparison to vacuum, is plotted in Figure 4.6. For both Figure 4.5 and Figure 4.6, the magnetic field data were obtained with the probe positon at z = 20 cm and φ = 0 in the poloidal plane. (Shot No. 003112315 for the plasma jet into the 500 G background magnetic field case, and shot No. 009080515 for the vacuum case)

As shown in Figure 4.5 and Figure 4.6, both the poloidal and toroidal magnetic fields dramatically increase when the plasma jet prorogates into the background magnetic field. The increase in magnitude is because the magnetic tension force of the background magnetic field works on the jet body, like an external pinch force, to compact the jet body, making it denser and more collimated. As a result, the magnetic flux density, B, and the current density, J_z, are increased leading to an increased measurement of both the poloidal and toroidal magnetic fields.

Furthermore, from Figure 4.6, it is evident that for the plasma jet propagating into vacuum, in the B-dot probe measurement range, the locations of the peak toroidal magnetic field are at $r = \pm4$ cm, while for the jet launched into the background magnetic field, the locations are at $r = \pm1.5$ cm. This reduction in radius is strong evidence for the pinch effect caused by the background magnetic tension force.
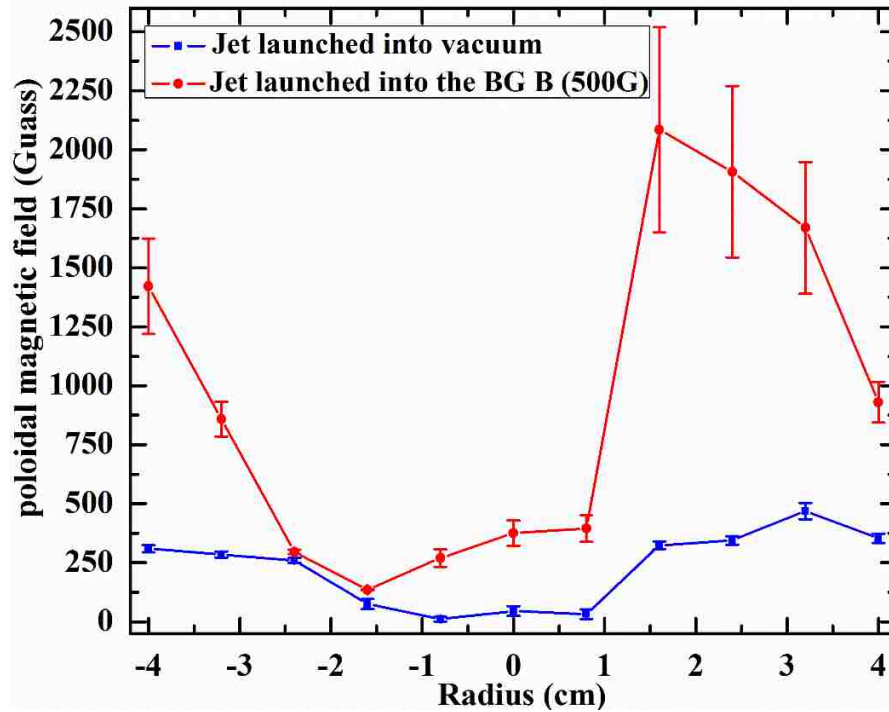
Figure 4.5. The radial profile of the poloidal magnetic field for both the plasma jet into vacuum and into the background magnetic field cases.
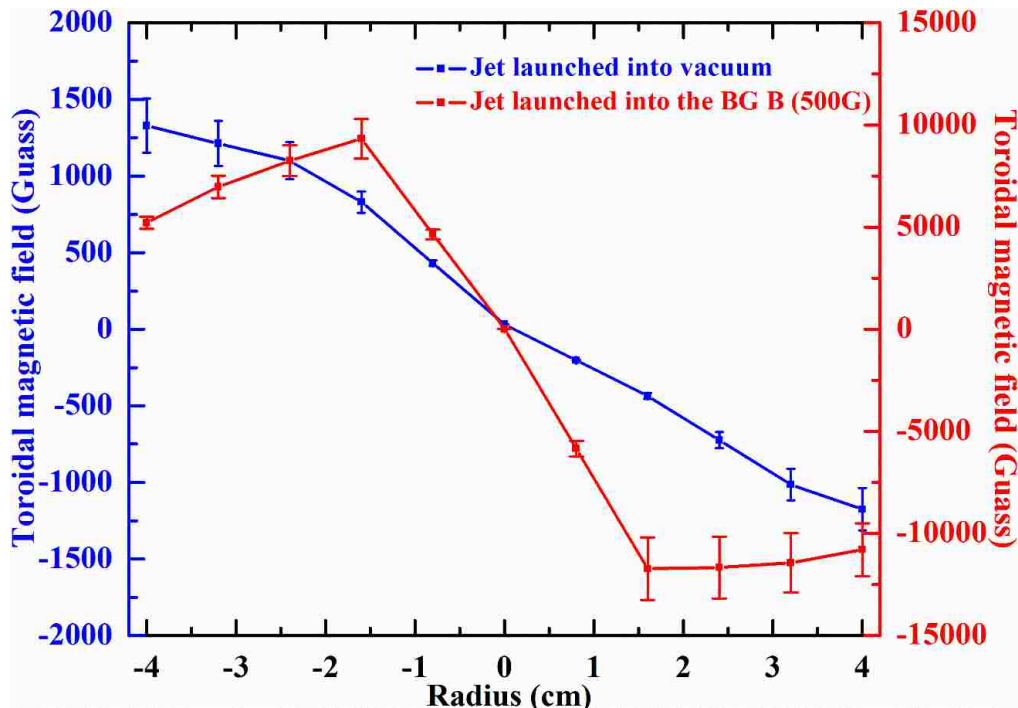
Figure 4.6. The radial profile of the toroidal magnetic field for both the plasma jet into vacuum and into the background magnetic field cases.

4.2.2 Plasma jet stabilization analysis

As discussed in section 4.2.1, a more stabilized plasma jet is observed when launched into a perpendicular background magnetic field (500 G in strength). The conclusion of a "more stabilized" jet is sustained by two straightforward results: 1). The absolute length of the jet is 50 cm, which is much longer than the 10 cm length observed for the vacuum case as shown in Figure 3.23; 2) the life-time is ~ 3 t_{Alfven} ($t_{Alfven} \equiv \frac{l}{V_{Alfven}}$) which is prolonged compared to the vacuum case in which the plasma jet has the life-time ~ 1 t_{Alfven}. Comparing the experimental settings for these two cases, the only difference is the added background magnetic field in the main vacuum chamber. Apparently the background magnetic field plays an important role in the jet stabilization process. In the following sections, the theoretical analysis will be presented in detail.

4.2.2.1 Safety factor analysis

As discussed in Chapter 3, for an m=1 kink instability, the Kruskal-Shafranov criterion gives the safety factor $q(a) \equiv \frac{2\pi a B_z}{l B_\varphi}$ (Eq. 3.17), where a and l are the radius and length of the plasma column respectively. From Eq. 3.17, it can be shown that increased poloidal magnetic field (or the so-called axial magnetic field) contributes to the stabilization of the kink-mode instability. The toroidal magnetic field, on the other hand, has the opposite effect. Also, considering the jet into the background magnetic field case, the length of the plasma, l, increases and the radius of the plasma, a, narrows, both of which have a negative influence on the jet stabilization. Taking all of these factors into consideration, the time-evolution of the

safety factor, $|q|$, at multiple radial positions is plotted in Figure 4.7 from the data of Shot No. 003112315 with the probe positon at z = 20 cm and $\varphi = 0$.
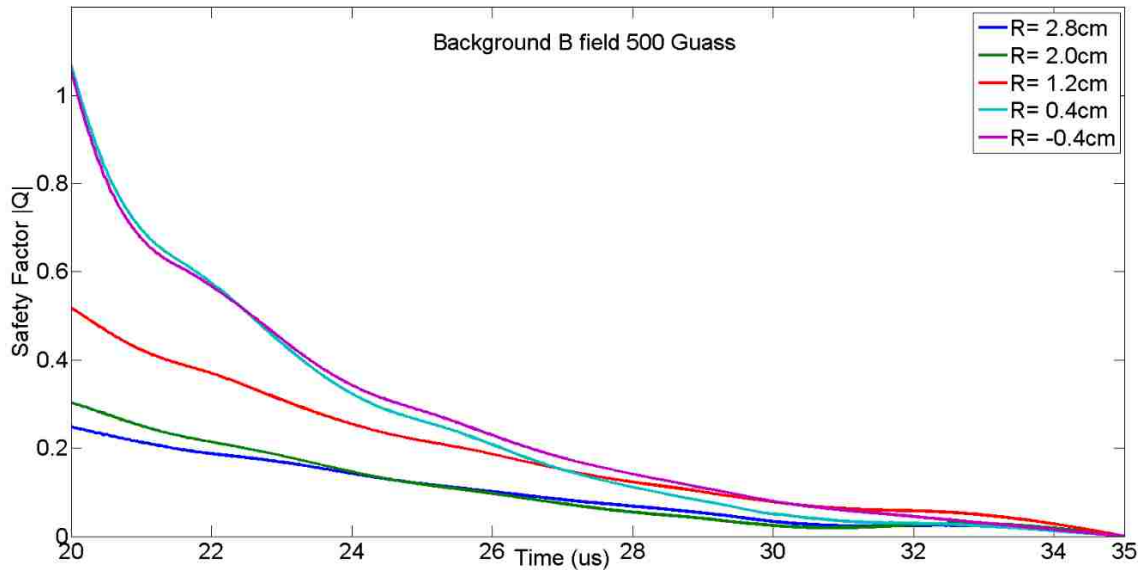
Figure 4.7. The time evolution plot of the safety factor's radius profile.

As shown in Figure 4.7, the "localized" safety factors, where the B-dot probe is placed, are below unity. Based on the Kruskal-Shafranov criterion, the plasma jet should experience the kink mode instability which will deform and break the jet column. However, the image data shown in Figure 4.4 indicates a globally more stable plasma jet column. As S.A. Colgate et. al[126] proposes, the current-driven instability may be separated into "internal" short-wavelength modes close to the neighborhood of the central column, and very long wavelength "external" modes corresponding to the entire jet.[126] Furthermore, these localized instability modes referred as "internal kinks" do not destroy the collimation of the jet.

4.2.2.2 The modified snowplow model

For the coaxial-gun-generated plasma jet to successfully cross the vacuum chamber and reach the opposite port, the plasma jet must have a high enough kinetic energy density that

it can penetrate the background magnetic field, and continue to propagate. This requirement may be stated as $\frac{\rho_{jet} V_{jet}^2}{2} \geq \frac{B_{background}^2}{2\mu_0}$, where ρ_{jet} is the plasma jet mass density, V_{jet} is the plasma jet velocity, and $B_{background}$ is the background magnetic field strength. Based on the PBEX parameters, substituting $n \sim 10^{20} \ m^{-3}$, $M_{Argon} = 6.62 \times 10^{-26} \ kg$, and $V_{jet} = 2.7 \sim 3.7 \times 10^4 \ m/s$ into $\frac{\rho_{jet} V_{jet}^2}{2}$, one gets $P_{jet} = 2413$ - 4531.4 Pascal (Pa). For $\frac{B_{background}^2}{2\mu_0}$, using $B_{background} = 500$ Gauss (0.05 Telsa), one gets $P_B = 995$ Pa. As a result, $P_{jet} \sim 4P_B$ which means the plasma jet can propagate into the background magnetic field.

Following this, we calculate the magnetic diffusivity:

$$\eta \equiv \frac{1}{\mu_0 \sigma_0} \tag{4.1}$$

where μ_0 is the permeability of free space ($4\pi \times 10^{-7} \ Hm^{-1}$) and σ_0 is the electrical conductivity.

For the electrical conductivity σ_0 calculation:

$$\sigma_0 \equiv \frac{n_e e^2}{m_e \nu_c} \tag{4.2}$$

where n_e is the electron density ($10^{20} \ m^{-3}$ for PBEX), e is the electron charge ($1.6 \times 10^{-19} \ C$), m_e is the electron mass ($9.1 \times 10^{-31} \ kg$), ν_c is the collision frequency.

For the collision frequency ν_c, the practical formula $4.80 \times 10^{-8} Z^4 \mu^{-\frac{1}{2}} n_i \ln\Lambda \ T_e^{-\frac{3}{2}}$ is used for the calculation where Z=1, $\mu = 40$, $n_i \sim 10^{14} cm^{-3}$, $T_e = 10 \ eV$ and $\ln\Lambda = 6.8$. The electron collision rate ν_e is $1.6 \times 10^5 \ s^{-1}$. Substituting ν_e into Eq. 4.2, one can get that the electrical conductivity σ_0 is $1.7 \times 10^7 \ S/m$. Then from Eq. 4.1, the magnetic diffusivity η is 21.4 m²/s.[127]

Furthermore, the magnetic Reynolds number, $R_M \equiv \frac{V \cdot l}{\eta}$, where V is a typical velocity scale of the flow ($3.5 \times 10^4 m/s$) and l is a typical length scale of the flow (0.3 m), can be calculated $\rightarrow R_M \sim 10^2 \gg 1$. Since $R_M \gg 1$, the magnetic diffusion is relatively unimportant on the length scale l. The background magnetic field lines are then advected with the plasma jet propagation, as indicated in Figure 4.8.
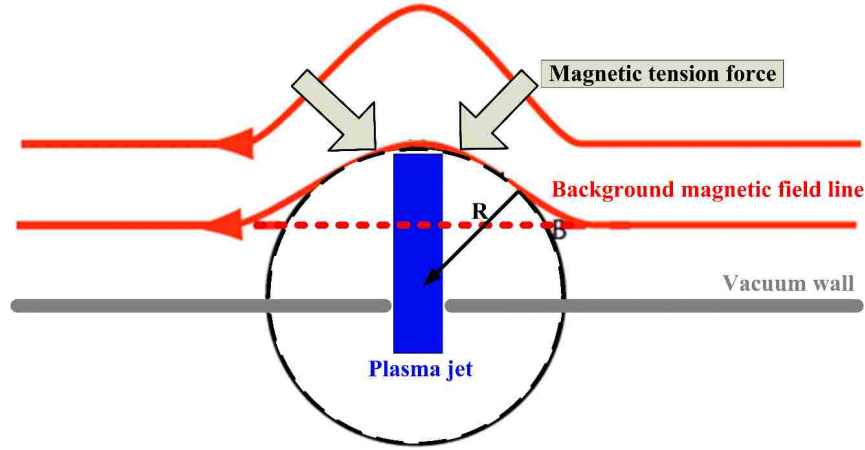
Figure 4.8. The plasma jet propagates into the background magnetic field.

The advected background magnetic field line is curved with the movement of the plasma jet. As discussed in Chapter 1, the curved magnetic field will induce a magnetic tension force to act on the plasma jet as:

$$F_{tension} \equiv \frac{B_{background}^2}{\mu_0} \frac{\hat{R}}{R} \tag{4.3}$$

where $\hat{R}$ is the unit vector pointing from the magnetic field line to the center of curvature, and R is the radius of curvature of the field line shown in Figure 4.8.

The plasma jet now experiences two forces: the $\vec{J} \times \vec{B}$ force which is from the main cap-bank discharged current, and the magnetic tension force which comes from the curved background magnetic field.
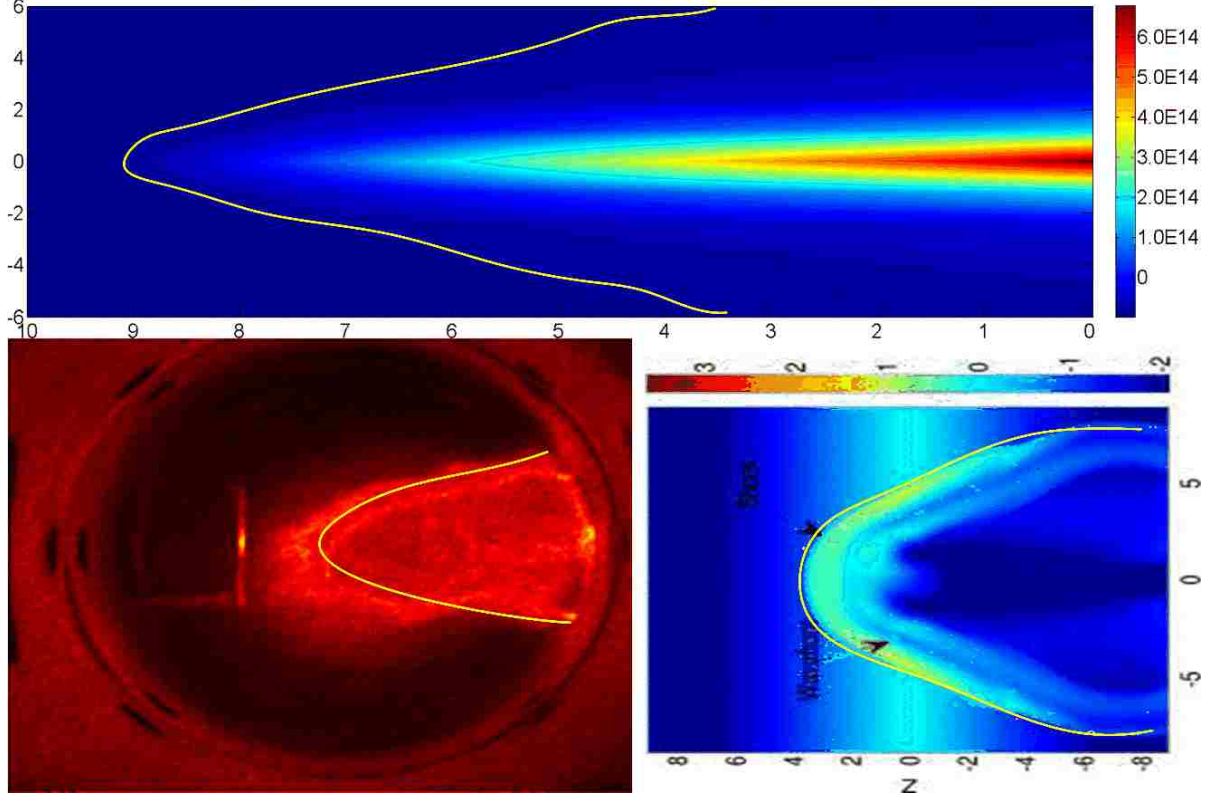
Figure 4.9. Top: the simulation results from the modified snowplow model with the jet front head marked. Bottom left: the image data shows the jet-head formation. Bottom right: The simulation results of CosmoMHD code from Los Alamos National Laboratory (LANL). The picture is taken from [128].

Based on the snow plow model discussed in Section 3.3.2, a modified model is presented here by adding the magnetic tension force term. Then, the radial profile of the plasma propagation distance, z, for a certain time, t, can be expressed as:

$$z = \sqrt{\frac{\mu_0 I_0^2}{8\pi^2 r^2 n_e \omega^2}(\omega^2 t^2 - \sin^2(\omega t))} - \frac{1}{\sqrt{\mu_0 n_e}}\frac{B_{background}}{r}t \quad (4.4)$$

The simulation result is plotted in Figure 4.9, Top. At the same time, the image data taken from CCD camera data is shown in Figure 4.9, Bottom left, and the simulation results using a cosmological magnetohydrodynamics code (CosmoMHD)[128] is exhibited in Figure 4.9, Bottom right. All these results indicate that the plasma jet is pushed back by the background

148

magnetic tension force. Instead of a typical conic-shaped jet head which is observed in the jet into vacuum case, the edge of the jet-head for this case is more backward. These results provide the evidence for an axial sheared flow which contributes to the global jet stabilization process.

4.2.2.3 Linearization of the MHD equations

The stabilizing effect of a sheared axial flow on the m = 1 kink instability has been investigated experimentally with the Zap Flow Z-pinch experiment,[53] as well as theoretically and computationally.[53, 129]

For the kink instability, due to its natural asymmetry property, it is not suitable to analyze the stability by analytical methods which are used for the m = 0 sausage case. As a result, numerical methods must be used, i.e. 3D nonlinear methods, or the linearization of the ideal MHD equations.[130] A seed initial perturbation is introduced to the linearized equations. After several growth times, the solution to the linear development converges to the fastest growing mode, and the real and imaginary parts of the frequency, ω, are obtained.[131]

The plasma jet equilibrium can be expressed by the MHD force balance equation:

$$\nabla P + \rho\left(\vec{V} \cdot \nabla\right)\vec{V} = \vec{J} \times \vec{B} \tag{4.5}$$

where P is the plasma pressure, ρ is the mass density, $\vec{V}$ is the plasma jet velocity, $\vec{J}$ is the current density, and $\vec{B}$ is the magnetic field.

For the PBEX project, assuming the gradients are only radial, a constant initial axial magnetic field, B_Z, is applied, and the plasma jet only propagates in the z-direction, Eq. 4.5 can be simplified to:

$$\frac{B_\theta}{\mu_0 r} \frac{d(rB_\theta)}{dr} + \frac{dP}{dr} = 0 \tag{4.6}$$
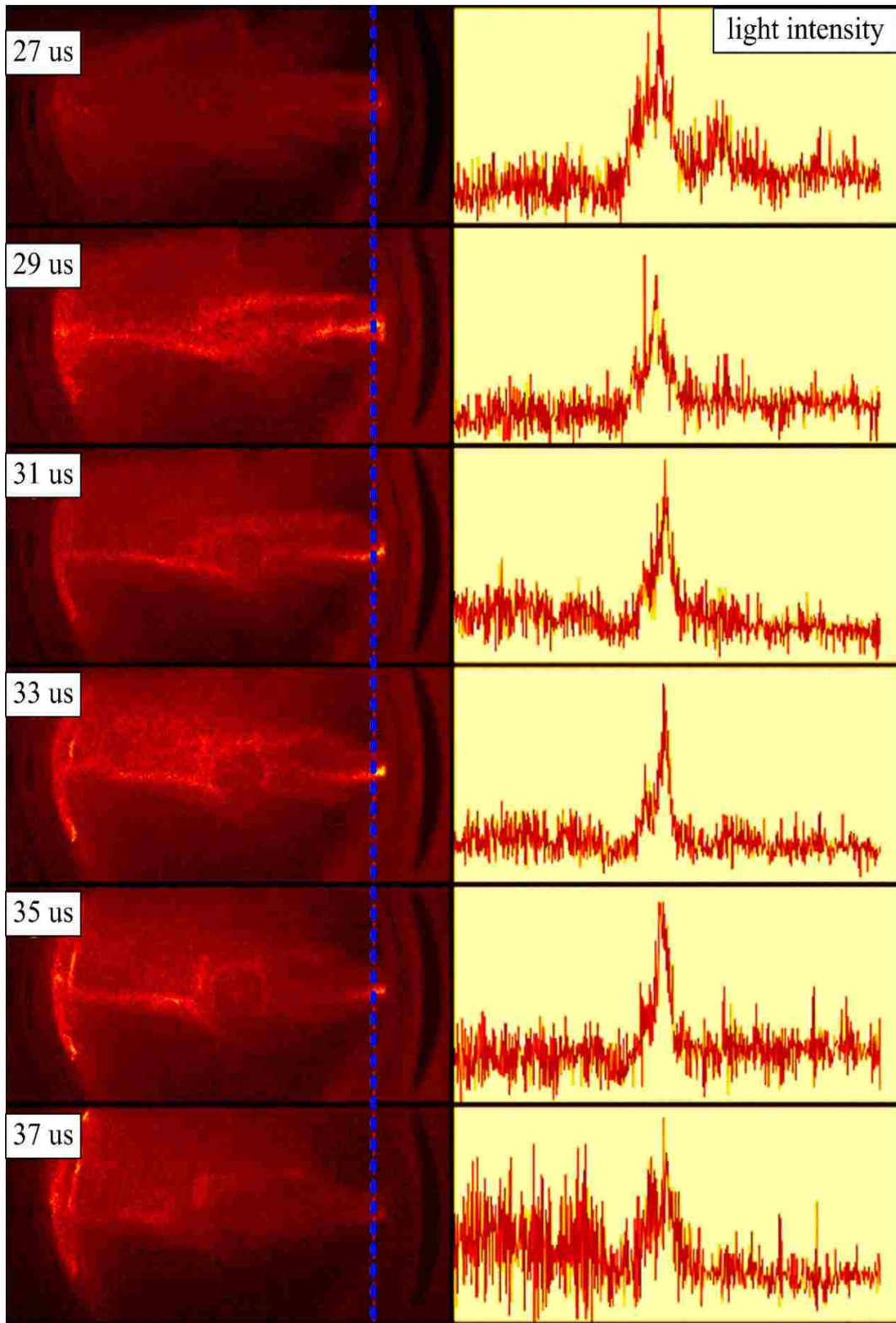
Figure 4.10. Right: the line-out plasma intensity measurement on the dotted line from the left image data (Shot No.008050114).

There are two unknown terms, P and B_θ, in Eq. 4.6. The plasma pressure term, P, can be estimated from the image data. Assuming the plasma intensity and the plasma density are directly related,[132] for $T_i = T_e = Const$, the plasma pressure is also positively correlated with the plasma density. As a result, the radial profile of the initial plasma pressure follows the plasma intensity from the image data as plotted in Figure 4.10.

For constant electron drift velocity across the jet, with $T_i = T_e$, the Bennett equilibrium profile for the pressure, P, is of the form:

$$P_0 = \frac{1}{\left(1+\frac{r^2}{a^2}\right)^2} \tag{4.7}$$

where r is the radius, and a is a practical factor which sets the radius of the jet pressure profile.

Eq.4.7 satisfies the general radial force balance equation Eq. 4.6, and was employed to fit the plasma intensity profile shown in Figure 4.10. The result is shown in Figure 4.11. This result indicates that the Bennett equilibrium profile fits the initial plasma pressure data well. As a result, it is a good and reasonable assumption. We can substitute Eq. 4.7, with a = 0.048, which is determined by the fitting result shown in Figure 4.11, into Eq. 4.6, to obtain the magnetic field, B_θ, profile as:

$$B_{0\theta} = \sqrt{2}\frac{\frac{r}{a}}{1+\left(\frac{r}{a}\right)^2} \tag{4.8}$$

Based on Eq. 4.7 and Eq. 4.8, the initial profiles of P and B_θ are established to satisfy the general radial force equilibrium equation Eq. 4.6. The radial profile of the plasma pressure and the toroidal magnetic field are plotted in Figure 4.12, where the plasma pressure profile is taken from the Bennet pressure fitting result, as shown in Figure 4.11, and the toroidal magnetic field profile is calculated from Eq. 4.8.
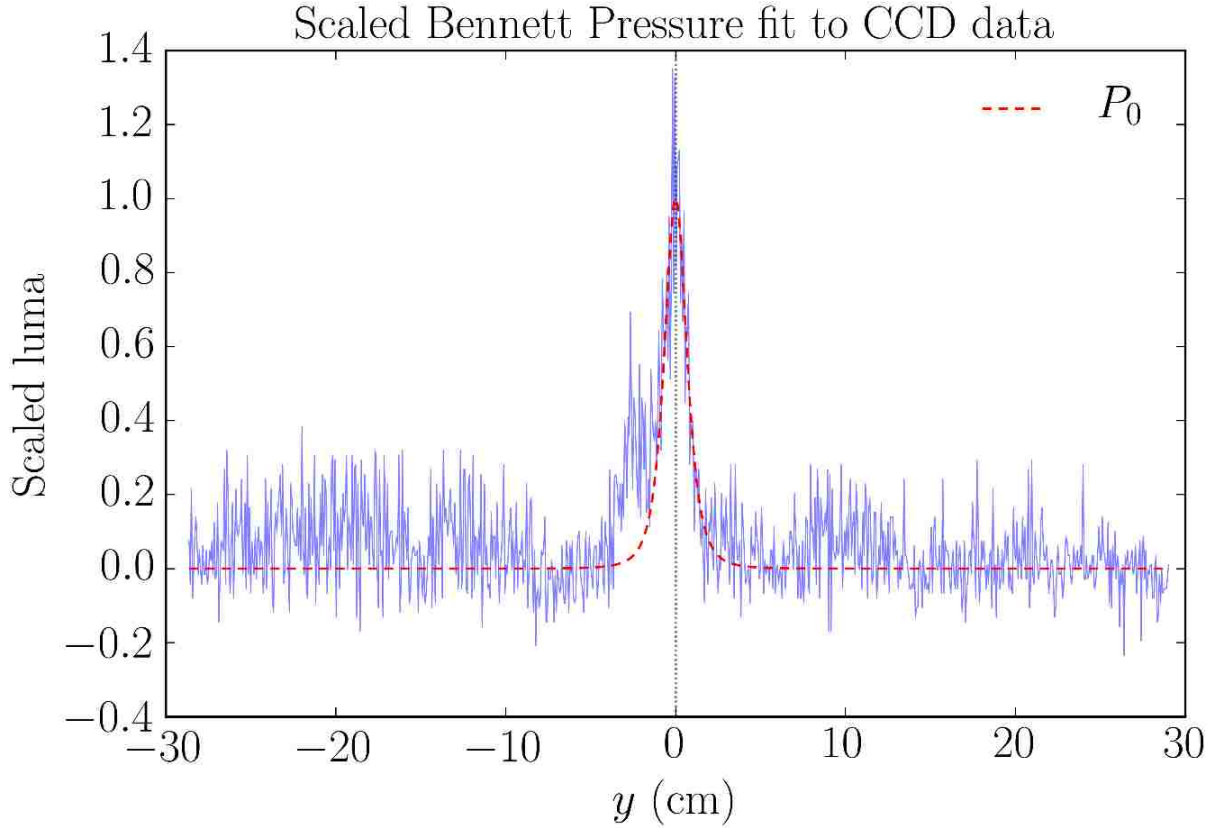
Figure 4.11. Bennett pressure fit to the image data. Credit to: Dr. Dustin Fisher.

Considering the measured toroidal magnetic field radial profile as shown in Figure 4.6, the calculated results have a similar profile to that of the measured data. The experimental data show good consistency with the initial conditions of the model. Without the tedious calculations, based on this initial condition, the linearization of the MHD equations has shown that a sheared axial flow can stabilize the kink mode of the plasma jet and the required amount of the flow shear is given by:

$$\frac{dV_z}{dr} \geq 0.1 k V_A \tag{4.9}$$

where k is the axial wave number, and V_A is the Alfvén velocity. The results from the PBEX project with the plasma jet propagating into the background magnetic field were employed to examine this result.
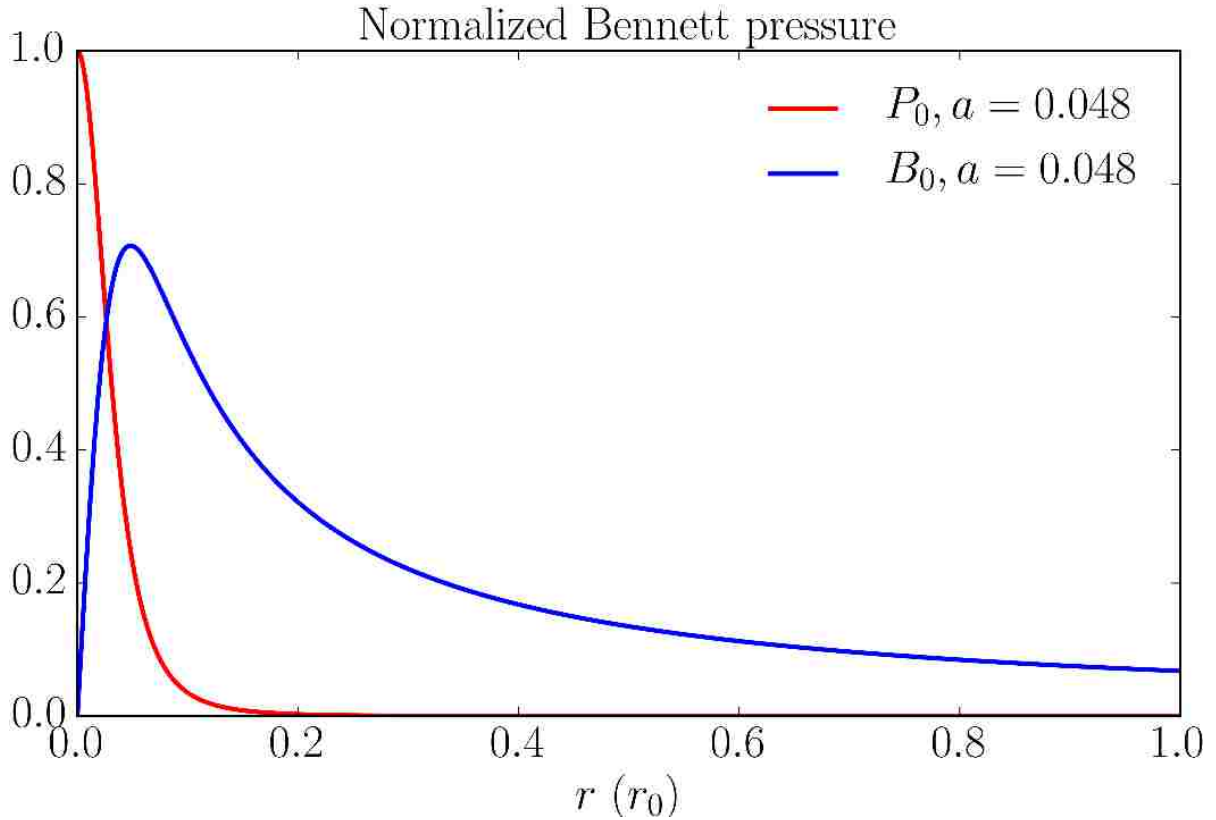
Figure 4.12. The normalized radius profile of the plasma pressure and the toroidal magnetic field with the initial Bennet pressure equilibrium.

4.2.3 Discussion of results

The radial profile of the plasma velocity was calculated based on the time delay between the initial rises of the toroidal magnetic field measured by the magnetic probe array which was placed at various positions in the main chamber at 10 cm intervals.

The results are plotted in Figure 4.13. From these plots, it is clearly shown that after the plasma jet is initially formed at the plasma gun muzzle, the jet head propagates at roughly the same velocity. Then the background magnetic tension force starts to work on the body column, causing the velocity to drop radially along with the axial propagation, and an axial sheared flow is formed.
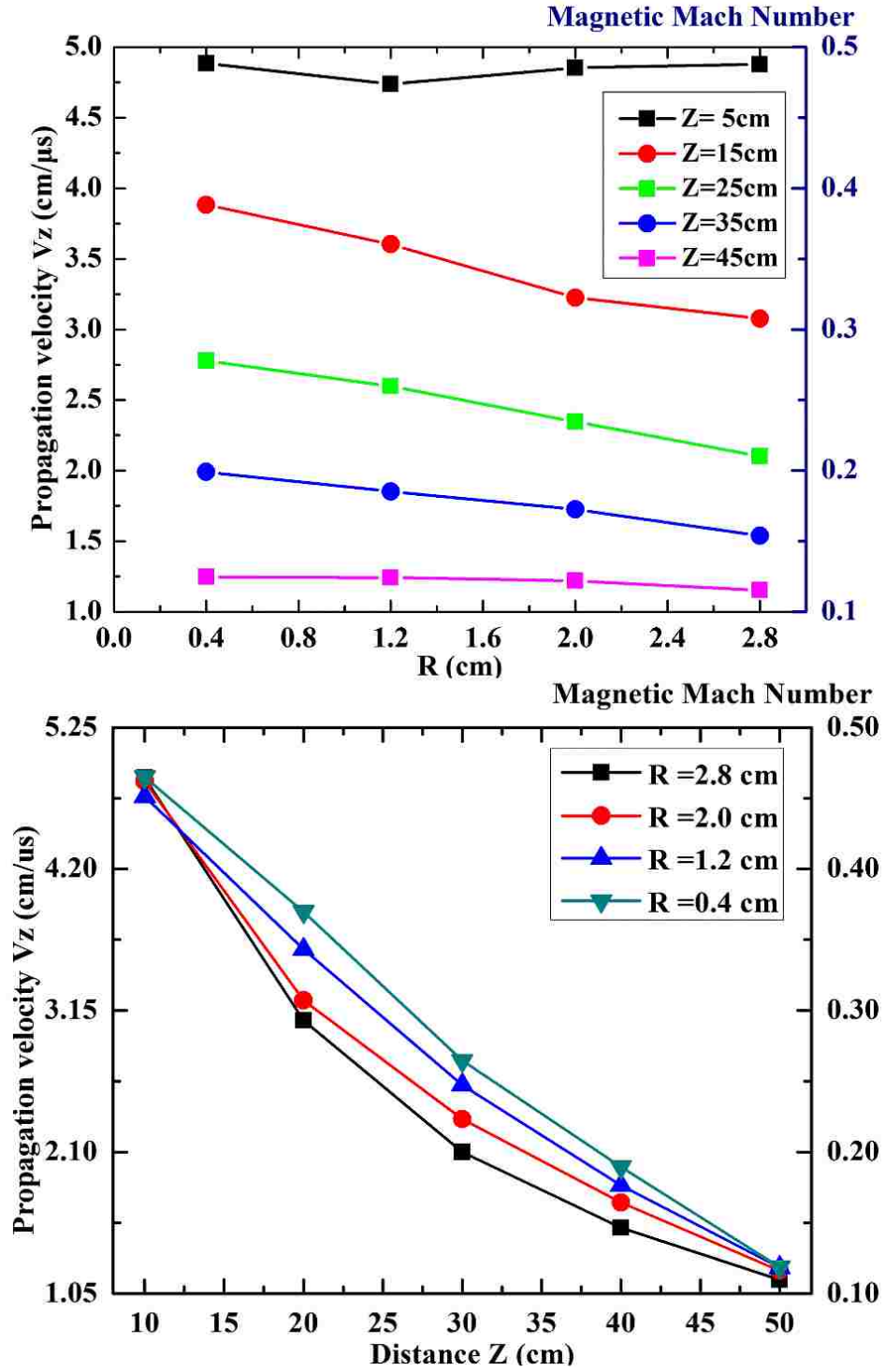
Figure 4.13. The radius profile of the plasma jet axial velocity at various space positions.

Throughout the main part of the chamber (z =15 cm to 35 cm), there is a strong axial sheared flow, as shown in Figure 4.13. The background magnetic field's relative position to the plasma jet changes from its originally perpendicular orientation (z = 0 cm) to one that is curved (z =15 cm ~35 cm), and finally to an orientation parallel with the jet (z =50 cm). As a result, the calculated axial velocity at different radii are back to uniform again when the plasma jet reaches the opposite port (z = 50 cm).
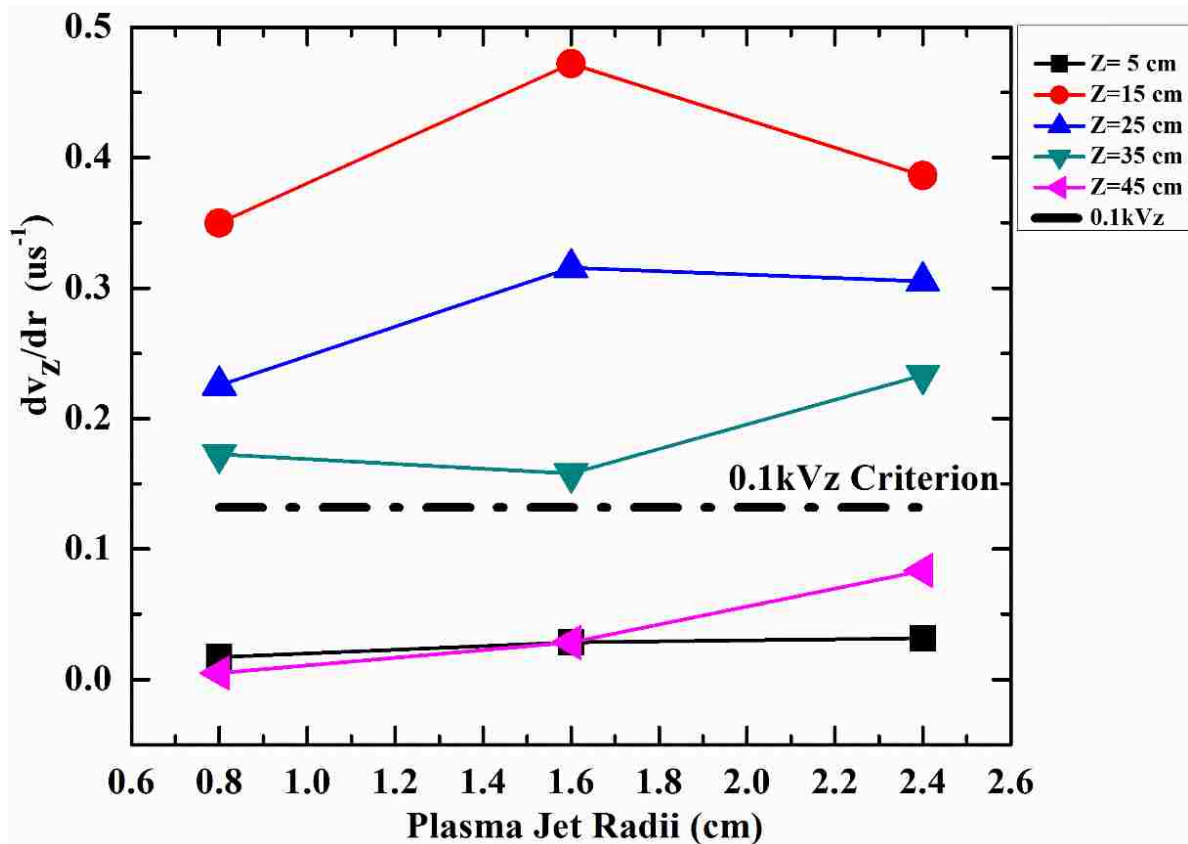
Figure 4.14. The spatial velocity shear is calculated. A positive velocity shear is measured.

After the radial velocity profile was obtained at different positions in the vacuum chamber, the axial sheared flow was determined and the result is plotted in Figure 4.14. As shown in this plot, for the main region of the chamber (z = 15 cm to 35 cm), the magnitude of the axial shear is above the threshold line, from Eq. 4.9, indicated by a horizontal line. The

results from the PBEX experiment are consistent with the theoretical analysis of the axial sheared flow stabilization of Eq. 4.9. The plasma jet, which is generated by the co-axial plasma gun, initially acts as a snowplow. Then after the plasma jet leaves the gun muzzle, the background magnetic tension force starts working on the jet body, and a stable jet is observed form the image data. The evolution of the axial velocity profile shows a velocity shear, which is above the theoretical threshold, $0.1kV_A$, and is measured throughout the main part of the chamber.

4.3 Spheromak-like plasma propagating into the background magnetic field

For operation Regime II, the coaxial-gun-generated spheromak propagates into the main chamber with the background magnetic field (500 Gauss). The self-organized spheromak is deformed due to the background magnetic tension force. Furthermore, a suspected magnetic Rayleigh–Taylor instability is observed from the image data. In this section, the experimental data from CCD camera and the B-dot probe array are presented to show the deformation of the spheromak's magnetic field configurations. The growth rate of Rayleigh–Taylor instability is also calculated based on the image data.

4.3.1 Experimental data

4.3.1.1 CCD camera images

The image data in Figure 4.15 shows the case where a spheromak plasma is generated and launched into the main vacuum chamber with a background magnetic field (500 Gauss).
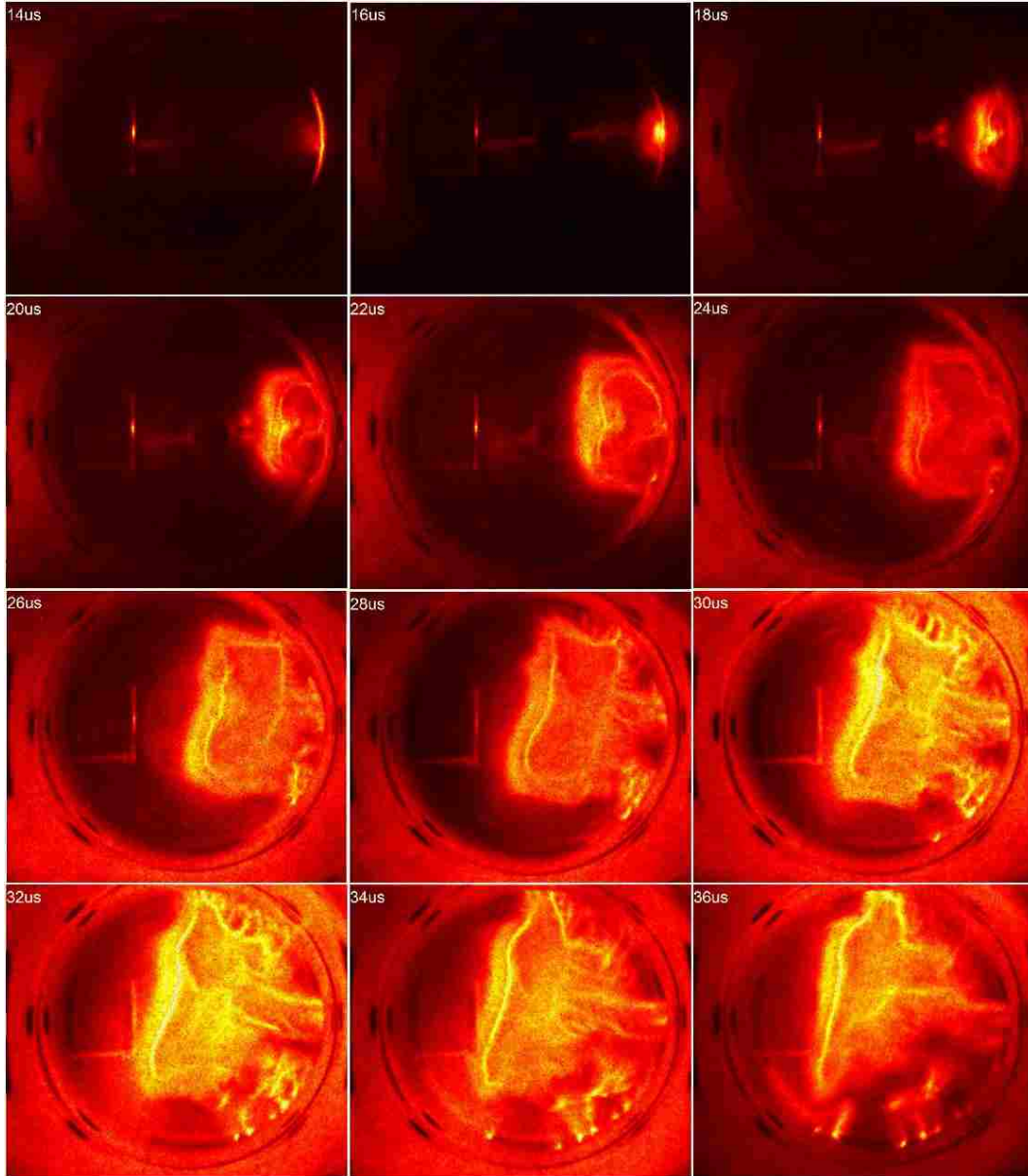
Figure 4.15. The spheromak propagates into the 500 Gauss background magnetic field. (Shot No.034050914).

From the image data, at the first stage, similar to the vacuum case, the gun-generated plasma follows the bias magnetic field line, then a typically symmetric spheromak shape is formed around t = 20 μs. Then at t = 22 μs, the spheromak starts to propagate into the chamber with a perpendicular 500 Gauss background magnetic field. The plasma does not travel strictly

157

along the z-axis as it does in the vacuum case in Figure 3.34. Instead, the plasma veers off axis and upward. The typical self-closed spheromak configuration does not hold anymore. Furthermore, on the upper side, the magnetic Rayleigh–Taylor (RT) instability develops from t = 26 μs. During the time period from t = 28 μs to t = 32 μs, the typical RT "fingers" are observed at the interface between the plasma and the background magnetic field.
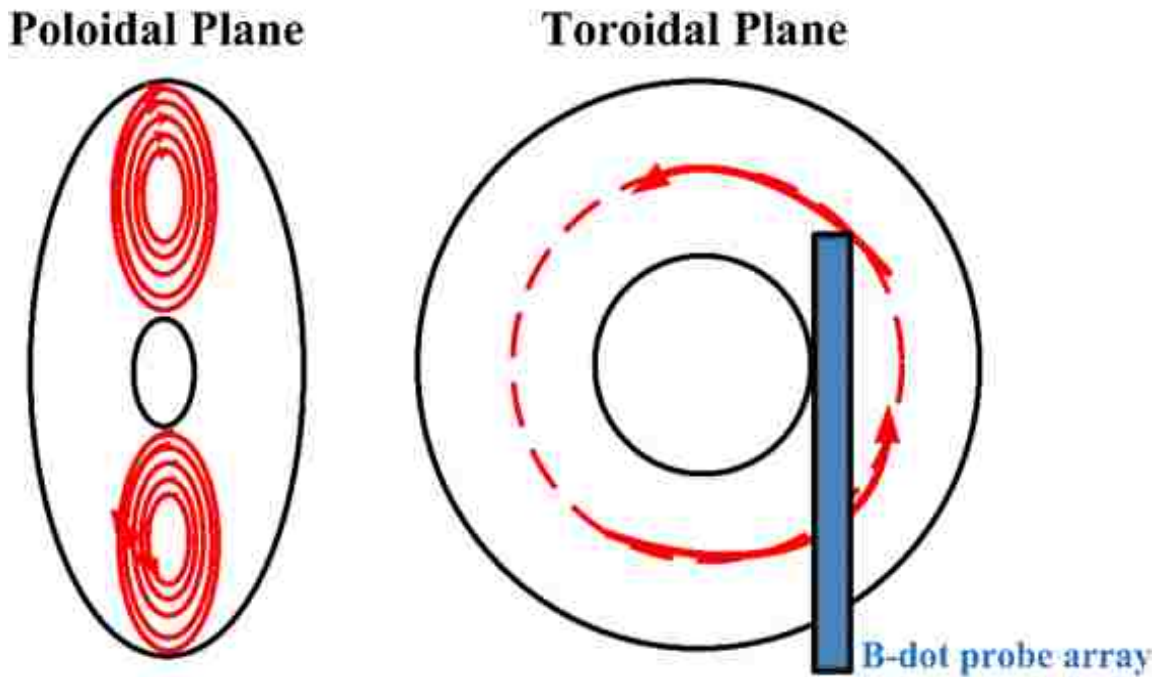
Figure 4.16. Typical poloidal and toroidal magnetic field configurations of a spheromak.

4.3.1.2 Poloidal and toroidal magnetic field measurement

For this case, the poloidal and toroidal magnetic field at various spatial positions are measured by the B-dot probe array. As discussed in Chapter 3, for the spheromak-like plasma, the typically self-closed poloidal and toroidal magnetic field configurations are shown in Figure 4.16.
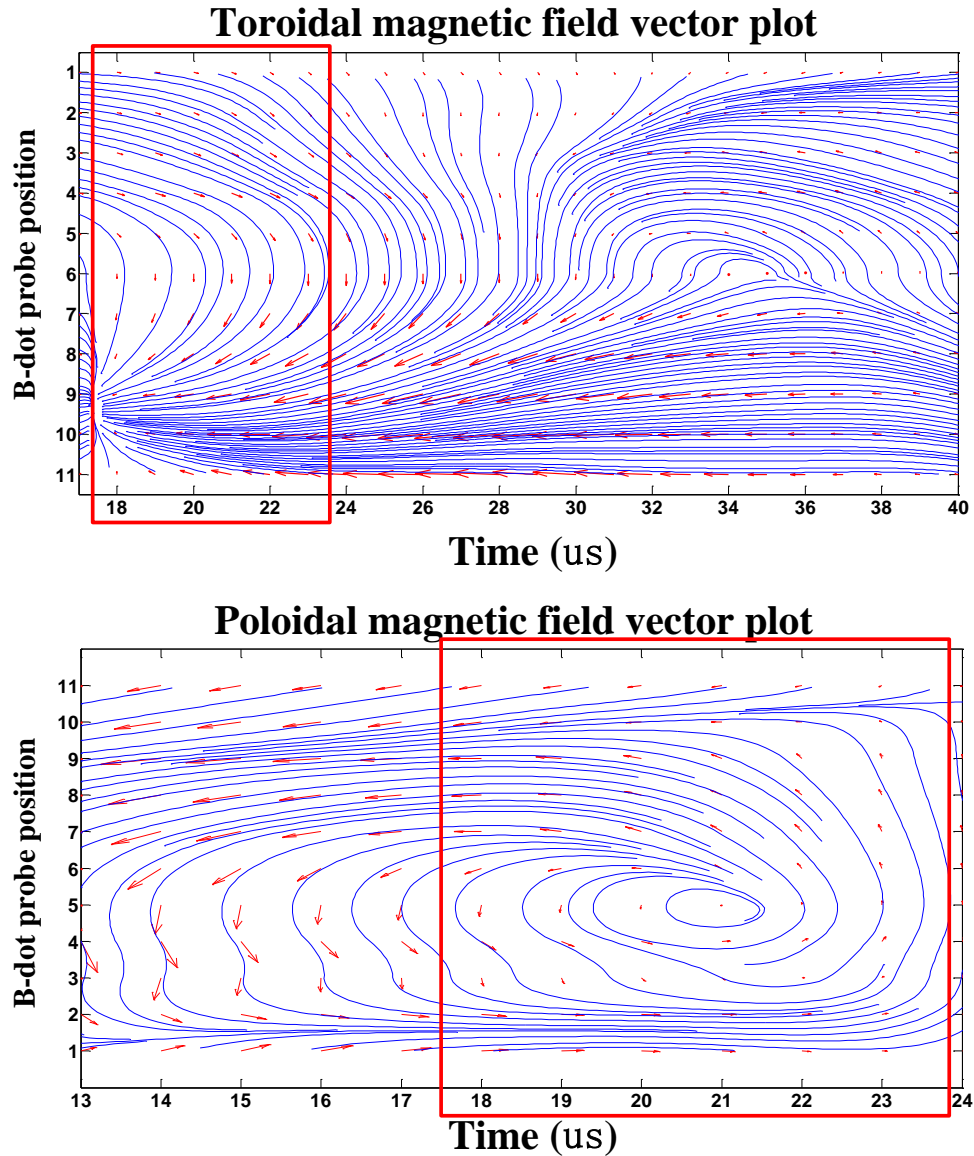
Figure 4.17. The toroidal and poloidal magnetic field vector plots with the streamlines. The B-dot probe is placed at the edge of the gun muzzle. Shot No.009112215.

Figure 4.17 shows the poloidal and toroidal magnetic field vector plots along with their streamlines. These plots are obtained from the measured magnetic field data from the B-dot probe array. For the particular shot, the B-dot probe array is placed right at the edge of the gun's muzzle where the typical spheromak configuration has been generated by the coaxial plasma gun under the operation settings for Regime II. However, the background magnetic

field has little effect on the plasma bubble. As shown in Figure 4.17, both the toroidal and the poloidal magnetic field vector plots are consistent with the characteristic magnetic configuration of a spheromak, indicated in Figure 4.16, during the time period from t = 18 μs to t = 23 μs. This time frame is marked in the red rectangle which also agrees with the image data shown in Figure 4.15.

Toroidal magnetic field vector plot

Poloidal magnetic field vector plot
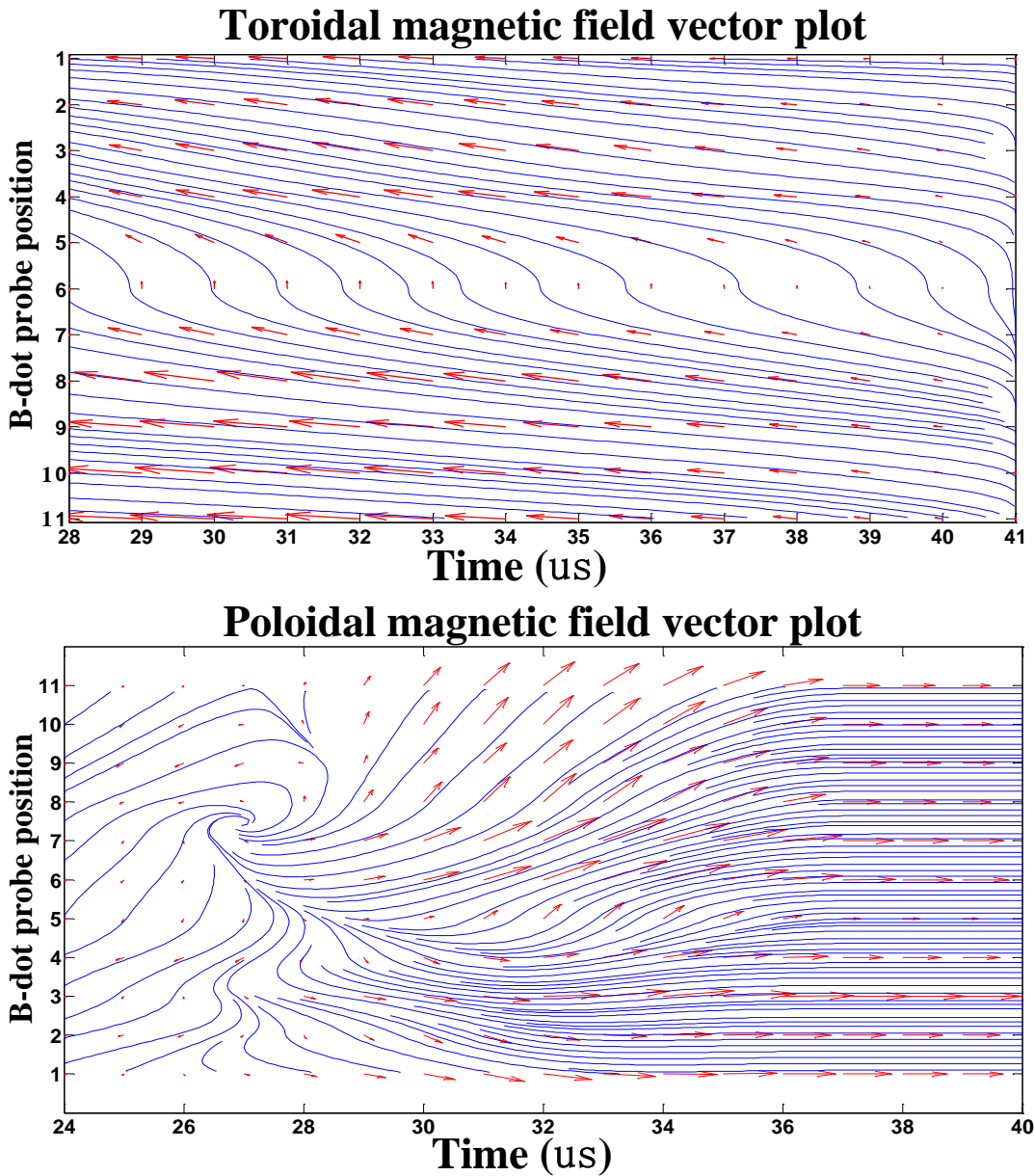
Figure 4.18. The toroidal and poloidal magnetic field vector plots with the streamlines. The B-dot probe is placed 20 cm away from the gun muzzle in the main chamber. Shot No.009112315.

160

A note addressed here is that for the toroidal magnetic field vector plot, the upper part of the probe array (position 1 to position 5) shows the changing of the toroidal magnetic field direction from left-to-right to right-to-left (the transient time is around t = 28 μs) while the lower part of the array (position 6 to position 11) keeps the right-to-left direction all the time.

This result indicates that later in time, with the spheromak propagating into the background magnetic field, the background magnetic field starts to affect the plasma, deforming the spheromak's internal self-closed magnetic field configuration. Figure 4.18 shows the measured poloidal and toroidal magnetic field vector plot results along with their streamlines in which the B-dot probe array is placed 20 cm away from the gun muzzle. Figure 4.18 clearly shows that the self-closed toroidal and poloidal magnetic field configurations do not hold any more. At this location, the toroidal magnetic field is pointing in the right-to-left direction which matches the toroidal vector plot results of the same time frame in Figure 4.17. The poloidal vector plot in Figure 4.18 also shows that the self-closed poloidal magnetic field structure is broken and eventually points in one direction.

4.3.2 Discussion of results

A simple physical picture is presented in Figure 4.19. Based on the 2D image data, the upper and lower parts of the spheromak's leading edge experience Lorentz force in roughly opposite directions due to the background magnetic field, and the discharged current, as indicated in Figure 4.19. These two unbalanced, and asymmetric, $J \times B$ forces cause the plasma's leading edge to drift upwards.
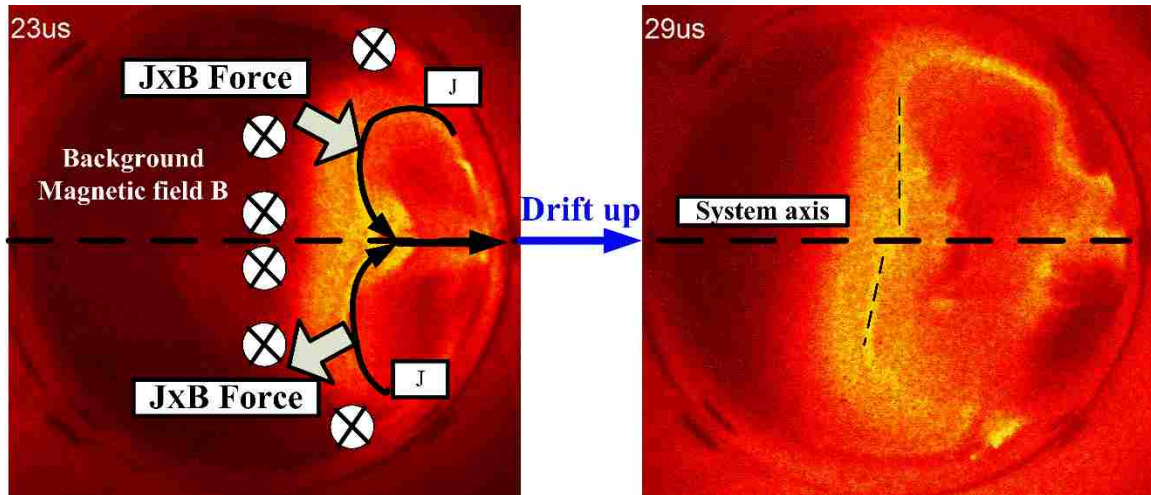
Figure 4.19. The plasma leading edge experiences the asymmetric $J \times B$ force.

Furthermore, if we take the plasma bubble's toroidal magnetic field in account. The configurations of both $B_{background}$ and $B_{toroidal}$ are shown in Figure 4.20. Clearly, at the interface between the plasma and the background magnetic fields, for the upper part, these two magnetic field are antiparallel to each other and vice versa for the lower part.

As detailed in Chapter 1, the formation and evolution of the Rayleigh-Taylor instability in a magnetized plasma heavily depends on the geometry of the magnetic field relative to the interface (between the plasma and the background magnetic field for the PBEX project). In the case of a magnetic field perpendicular to the surface, the magnetic Rayleigh-Taylor instability will reduce to the unmagnetized fluid case. The magnetic field has no effect for large wavelength disturbances. In the case of the magnetic field parallel to the interface, the magnetic Rayleigh-Taylor instability will simply interchange the magnetic field lines between the interface if $\vec{k} \cdot \vec{B} = 0$ (the disturbance is perpendicular to the magnetic field). If $\vec{k} \cdot \vec{B} \neq 0$, the disturbance is at an oblique angle with respect to the magnetic field and the magnetic tension force stabilizes the Rayleigh-Taylor instability.
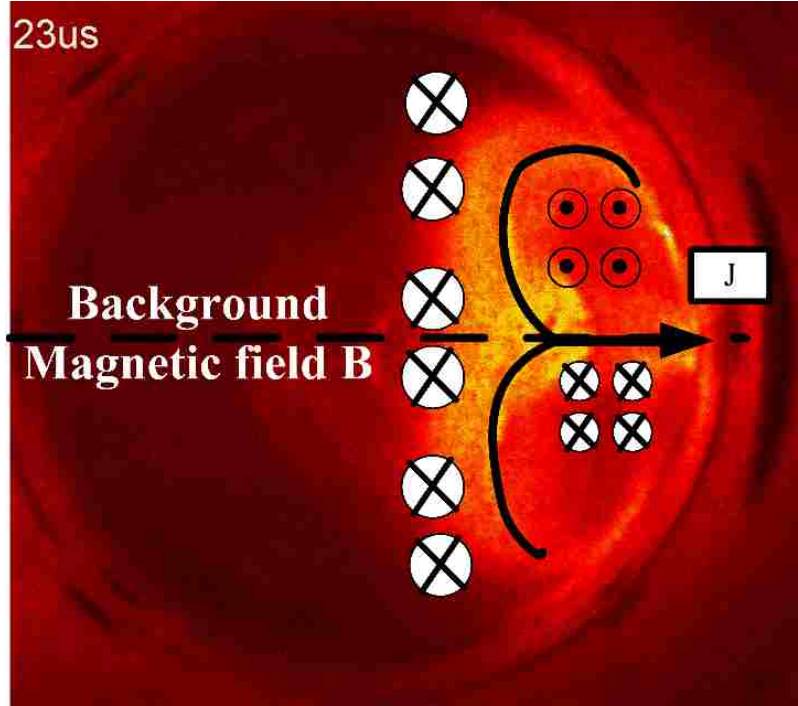
Figure 4.20. The cartoon picture shows the background magnetic field and the spheromak's toroidal magnetic field configurations.

The growth rate of the two-dimensional (2D) magnetic Rayleigh-Taylor instability is expressed below:[36]

$$\gamma^2 = a\vec{k} - \frac{(\vec{k}\cdot\vec{B})^2}{\mu_0\rho_{plasma}} \tag{4.10}$$

where $\vec{B}$ is the unperturbed magnetic field vector, a is the acceleration, $\vec{k}$ is the perturbation wave-vector, and ρ_{plasma} is the plasma density.

Eq.4.10 indicates that the term, $\vec{k}\cdot\vec{B}$, contributes to the stabilization, and suppresses the instability growth rate as discussed above. For the upper part of the plasma, the $B_{background}$ and $B_{toroidal}$ are antiparallel at the interface as shown in Figure 4.20. Consequently, the stabilization term, $\vec{k}\cdot\vec{B}$, is reduced and the Rayleigh-Taylor instability is more likely to happen at the upper side rather than the lower side.

163
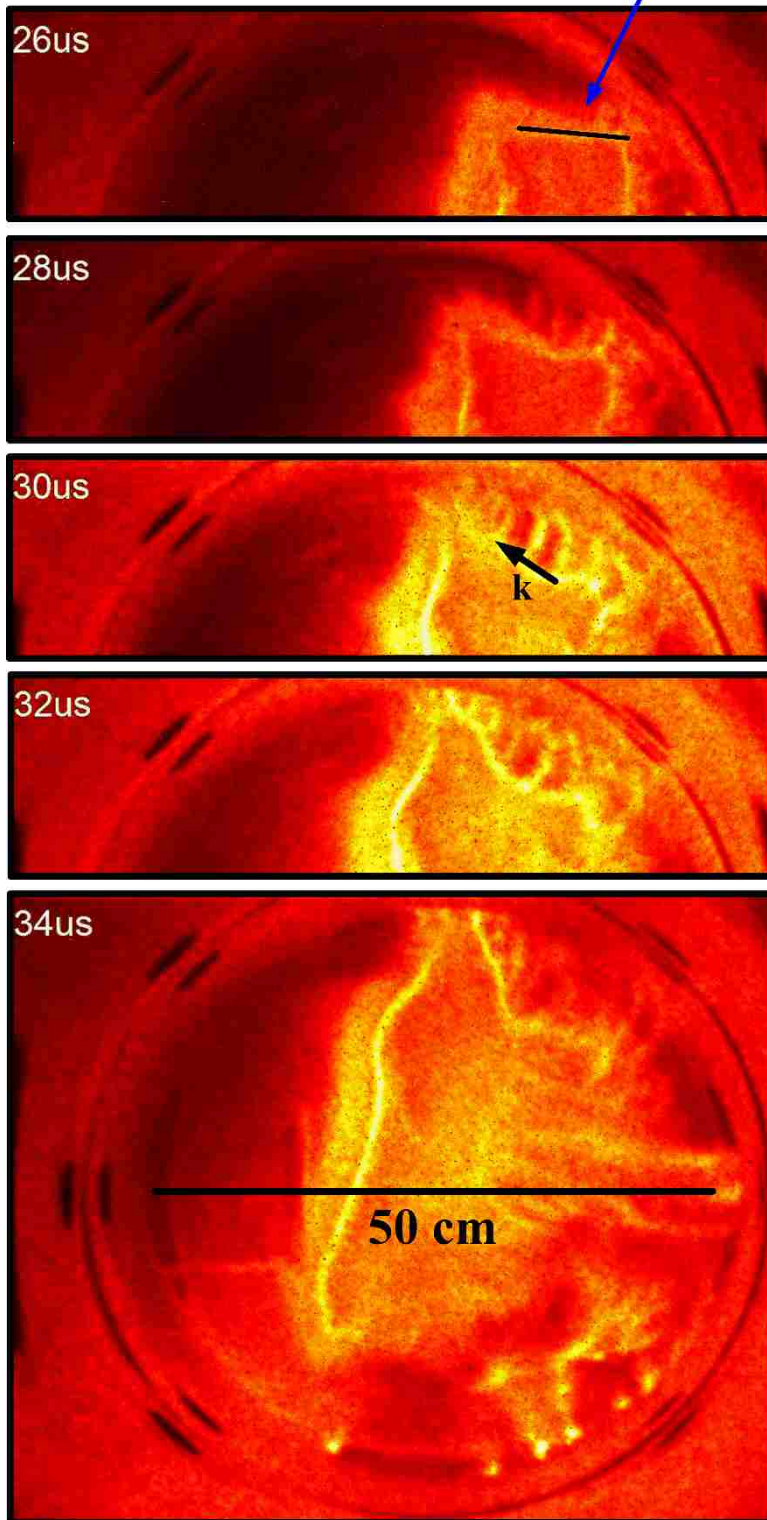
Figure 4.21. The magnetic Rayleigh-Taylor instability growth rate calculation based on the image data. (Shot No.034050914).

The Rayleigh-Taylor instability growth rate can be estimated directly from the image data. Based on the image data shown in Figure 4.21, the fine structure amplitude's time-evolution gives an observed growth rate $\gamma_{RT} \approx \mathbf{1.43} \times \mathbf{10^6}\ \boldsymbol{s^{-1}}$

Also from the images, the measured transverse acceleration of the filament is: $a \approx$ 1.78×10^{10} m/s^2. The axial wavenumber, k, is 503 m^{-1}. Then the calculated growth rate is: $\gamma_{RT-c} = \sqrt{a \cdot k} = \mathbf{3.0} \times \mathbf{10^6}\ \boldsymbol{s^{-1}}$. Both calculations are in good agreements with each other.

The agreement between the calculated and observed growth rates, along with the observed location, and spatial periodicity of the "finger" structures are all consistent with the Rayleigh-Taylor instability.[35] These results confirm that the finger structures are the Rayleigh-Taylor instability, and the growth rate is in the order of $\sim 10^6\ s^{-1}$ for the PBEX project.

4.4 Summary

In this chapter, the gun-generated plasma jet, and spheromak-like plasma, propagating into a background magnetized plasma, and a background magnetic field, were discussed in detail. Both the CCD camera data, and B-dot probe data show that there is no obvious difference between the gun-generated plasma travelling into a background magnetized plasma, and into a background magnetic field. The remainder of this chapter focused on the plasma's evolution for propagating into the background magnetic field.

Plasma jets propagating into background magnetic field were found to be more stabilized as compared to propagation in vacuum. The calculated magnetic Reynold's number indicates that the background magnetic field is advected with the plasma flow. The bending magnetic field lines create a magnetic tension force that acts on the jet body, pinching the jet body column even further, and causing a significant radial shear in the axial flow. The measured poloidal and toroidal magnetic field data confirms the pinch effects. Furthermore,

the linearization of MHD equations shows that if the axial sheared flow is greater than the criterion, $0.1kV_A$, it can suppress, or reduce the m =1 kink instability, making the jet more stable. The measured axial sheared flow data are consistent with the theoretical analysis.

Significant differences are also found in the case of spheromak plasmas propagating into background magnetic field as compare with vacuum. When spheromaks propagate into a background magnetic field, non-uniform expansion is observed, and a magnetic Rayleigh-Taylor (MRT) instability is observed at the upper side in the image data. A simple physical picture is proposed to describe how the background magnetic field affects the spheromak. The observed non-uniform plasma expansion (up-down non-uniformity) is due to different $\vec{J} \times \vec{B}$ forces. The measured poloidal and toroidal magnetic field data show that the plasma does not hold the typical self-closed magnetic configuration under the influence of a background magnetic field. On the upper side, the opposite directions of the background and the toroidal magnetic field reduce the stabilization term $(\vec{k} \cdot \vec{B})$ which makes it easier for the MRT to happen at this side. The growth rate is calculated from the image data, and the results indicate that the MRT growth rate is in the order of $10^6 \ s^{-1}$ for the PBEX project.

Chapter 5 Summary and Future Work

This thesis reports on three main results from the PBX project carried out on the Helicon-Cathode (HelCat) linear plasma device at the University of New Mexico (UNM).

The first section describes the experimental apparatus. Details have been presented in Chapter 2 for the design, construction, simulation, debugging, characterization, and calibration of the gun's performance. A long-term issue for the PBEX project has been that references on similar experiments have little information about their experimental set-ups. Hopefully Chapter 2 can serve as the reference for prospective students who will continue the PBEX project. The co-axial plasma gun is now working routinely. The hardware and diagnostics have been fully developed.

Next, the gun's performance has been classified into four regimes, similar to Yee, Hsu, and Bellan's results,[44] based on CCD camera image data. For Regime I and Regime II, which are the most interesting regimes, Chapter 3 gives detailed analysis of experimental data, mainly magnetic field data obtained from the B-dot probe array. These experiments on gun operating regimes match well with similar experiments carried out on other devices. The experiments discussed in the Chapter 3 are verification experiments to examine the gun's performance, validate the model's prediction, and support theories about the plasma jets and spheromaks. Details were presented on how to analyze the large amounts of spatial data, visualize the 3D magnetic field configurations, make spatial vector plots etc.

Thirdly, this dissertation reports the results of two sets of new plasma experiments performed within the PBEX project. The two distinct topics, regardless of the different variations, are united in one theme: the effects of the perpendicular magnetic field on the evolution of the various magnetized plasma formations.

167

For the plasma jet propagating into the background magnetic field, a global stabilization of a jet column is observed. Although the localized B-dot probe measurements indicate an internal kink instability is present, it does not deform the global jet column. Linearization of the ideal MHD equations shows that if the axial sheared flow is greater than $0.1kV_A$, axial sheared flow contributes to the stabilization process. For this case, the tension force from the background magnetic field causes the axial sheared flow. The measured spatial evolution of the axial velocity profile shows a significant velocity shear which meets the stabilization criterion.

For the case of a spheromak-like plasma propagating into a background magnetic field, both the image data and magnetic field data show that the typical self-closed magnetic field configuration of the spheromak is deformed and no longer maintains its original shape due to the asymmetric Lorentz force from the background magnetic field. Furthermore, at the upper side of the plasma's leading edge, a magnetic Rayleigh-Taylor instability is observed from the image data. The growth rate is calculated to confirm the observed finger structure is consistent with the magnetic Rayleigh-Taylor instability.

For the future work, a more suitable MHD theory is being developed for the axial sheared flow stabilization for the PBEX project. At the same time, the 3D Bats-R-US code[133] is employed to model the actual experiment with the proper boundaries. Furthermore, new diagnostics such as multiple channel spectroscopic array will contribute to the detail measurements of the plasma parameters' radial profile.

References

1   F Chen Francis, 'Introduction to Plasma Physics and Controlled Fusion', *Plasma Physics* (1984).

2   Rainer Beck, 'Galactic Magnetic Fields', *Scholarpedia,* 2 (2007), 2411.

3   Thaisa Storchi-Bergmann, Jack A Baldwin, and Andrew S Wilson, 'Double-Peaked Broad Line Emission from the Liner Nucleus of Ngc 1097', *The astrophysical journal. Chicago. Vol. 410, no. 1, pt. 2 (June 1993), p. L11-L14* (1993).

4   J Yee, and PM Bellan, 'Taylor Relaxation and Λ Decay of Unbounded, Freely Expanding Spheromaks', *Physics of Plasmas (1994-present),* 7 (2000), 3625-40.

5   MR Brown, AD Bailey III, and PM Bellan, 'Characterization of a Spheromak Plasma Gun: The Effect of Refractory Electrode Coatings', *Journal of applied physics,* 69 (1991), 6302-12.

6   Lyman Spitzer, *Physics of Fully Ionized Gases* (Courier Corporation, 2013).

7   Xiaoyue Guan, Hui Li, and Shengtai Li, 'Relativistic Mhd Simulations of Poynting Flux-Driven Jets', *The Astrophysical Journal,* 781 (2014), 48.

8   Robert S Cohen, Lyman Spitzer Jr, and Paul McR Routly, 'The Electrical Conductivity of an Ionized Gas', *Physical Review,* 80 (1950), 230.

9   Lyman Spitzer Jr, and Richard Härm, 'Transport Phenomena in a Completely Ionized Gas', *Physical Review,* 89 (1953), 977.

10   Douglas C Giancoli, *Physics for Scientists and Engineers with Modern Physics*. Vol. 2 (Pearson Education, 2008).

11   Russell M Kulsrud, *Plasma Physics for Astrophysics*. Vol. 77 (Princeton University Press Princeton, 2005).

12   Johan Peter Goedbloed, and Stefaan Poedts, *Principles of Magnetohydrodynamics: With Applications to Laboratory and Astrophysical Plasmas* (Cambridge university press, 2004).

13   Johan P Goedbloed, Rony Keppens, and Stefaan Poedts, *Advanced Magnetohydrodynamics: With Applications to Laboratory and Astrophysical Plasmas* (Cambridge University Press, 2010).

14   E Infeld, 'Magnetic Reconnection: Mhd Theory and Applications, by Er Priest and Tg Forbes. Cambridge University Press, 2000. 600+ Xii Pages. Isbn 0 521 481 79 1.£ 50,

$85', (Cambridge Univ Press, 2001).

15 Paul M Bellan, *Fundamentals of Plasma Physics* (Cambridge University Press, 2008).

16 JBj Taylor, 'Relaxation and Magnetic Reconnection in Plasmas', *Reviews of Modern Physics,* 58 (1986), 741.

17 Lodewijk Woltjer, 'A Theorem on Force-Free Magnetic Fields', *Proceedings of the National Academy of Sciences,* 44 (1958), 489-91.

18 Arnie Heller, 'Experiment Mimics Nature's Way with Plasmas'.

19 Reinhard Mundt, 'Jets from Young Stars', in *Radiation Hydrodynamics in Stars and Compact Objects* (Springer, 1986), pp. 7-9.

20 Bo Reipurth, and John Bally, 'Herbig-Haro Flows: Probes of Early Stellar Evolution', *Annual Review of Astronomy and Astrophysics,* 39 (2001), 403-55.

21 DA Schwartz, HL Marshall, JEJ Lovell, BG Piner, SJ Tingay, M Birkinshaw, G Chartas, M Elvis, ED Feigelson, and KK Ghosh, 'Chandra Discovery of a 100 Kiloparsec X-Ray Jet in Pks 0637–752', *The Astrophysical Journal Letters,* 540 (2000), L69.

22 Ralph E Pudritz, 'Jets from Accretion Discs', *Philosophical Transactions of the Royal Society of London A: Mathematical, Physical and Engineering Sciences,* 358 (2000), 741-58.

23 RD Blandford, and MJ Rees, 'A 'Twin-Exhaust'model for Double Radio Sources', *Monthly Notices of the Royal Astronomical Society,* 169 (1974), 395-415.

24 Attilio Ferrari, 'Modeling Extragalactic Jets', *Annual Review of Astronomy and Astrophysics,* 36 (1998), 539-98.

25 Richard VE Lovelace, GV Ustyugova, and AV Koldoba, 'Magnetohydrodynamic Origin of Jets from Accretion Disks', *arXiv preprint astro-ph/9901256* (1999).

26 A Königl, and Arnab Rai Choudhuri, 'Force-Free Equilibria of Magnetized Jets', *The Astrophysical Journal,* 289 (1985), 173-87.

27 GV Ustyugova, RVE Lovelace, MM Romanova, H Li, and SA Colgate, 'Poynting Jets from Accretion Disks: Magnetohydrodynamic Simulations', *The Astrophysical Journal Letters,* 541 (2000), L21.

28 XZ Tang, 'Self-Organization of Radio Lobe Magnetic Fields by Driven Relaxation', *The Astrophysical Journal,* 679 (2008), 1000.

29   Scott C Hsu, and Paul M Bellan, 'A Laboratory Plasma Experiment for Studying Magnetic Dynamics of Accretion Discs and Jets', *Monthly Notices of the Royal Astronomical Society,* 334 (2002), 257-61.

30   Andrea Ciardi, Sergey V Lebedev, Adam Frank, Francisco Suzuki-Vidal, Gareth N Hall, Simon N Bland, Adam Harvey-Thompson, Eric G Blackman, and Max Camenzind, 'Episodic Magnetic Bubbles and Jets: Astrophysical Implications from Laboratory Experiments', *The Astrophysical Journal Letters,* 691 (2009), L147.

31   David H Sharp, 'An Overview of Rayleigh-Taylor Instability', *Physica D: Nonlinear Phenomena,* 12 (1984), 3-18.

32   M Kruskal, and M Schwarzschild, 'Some Instabilities of a Completely Ionized Plasma', in *Proceedings of the Royal Society of London A: Mathematical, Physical and Engineering Sciences* (The Royal Society, 1954), pp. 348-60.

33   FL Curzon, A Folkierski, R Latham, and JA Nation, 'Experiments on the Growth Rate of Surface Instabilities in a Linear Pinched Discharge', in *Proceedings of the Royal Society of London A: Mathematical, Physical and Engineering Sciences* (The Royal Society, 1960), pp. 386-401.

34   MG Haines, 'A Review of the Dense Z-Pinch', *Plasma Physics and Controlled Fusion,* 53 (2011), 093001.

35   Subrahmanyan Chandrasekhar, *Hydrodynamic and Hydrodynamic Stability* (OUP, 1961).

36   EG Harris, 'Rayleigh‑Taylor Instabilities of a Collapsing Cylindrical Shell in a Magnetic Field', *Physics of Fluids (1958-1988),* 5 (1962), 1057-62.

37   Andrew Hillier, Thomas Berger, Hiroaki Isobe, and Kazunari Shibata, 'Numerical Simulations of the Magnetic Rayleigh-Taylor Instability in the Kippenhahn-Schlüter Prominence Model. I. Formation of Upflows', *The Astrophysical Journal,* 746 (2012), 120.

38   J Jeff Hester, 'The Crab Nebula: An Astrophysical Chimera', *Annu. rev. Astron. astrophys.,* 46 (2008), 127-55.

39   Thomas E Berger, Gregory Slater, Neal Hurlburt, Richard Shine, Theodore Tarbell, Bruce W Lites, Takenori J Okamoto, Kiyoshi Ichimoto, Yukio Katsukawa, and Tetsuya Magara, 'Quiescent Prominence Dynamics Observed with the Hinode Solar Optical Telescope. I. Turbulent Upflow Plumes', *The Astrophysical Journal,* 716 (2010), 1288.

40   DD Ryutov, RP Drake, and BA Remington, 'Criteria for Scaled Laboratory Simulations of Astrophysical Mhd Phenomena', *The Astrophysical Journal Supplement Series,* 127

(2000), 465.

41   Auna Louise Moser, 'Dynamics of Magnetically Driven Plasma Jets: An Instability of an Instability, Gas Cloud Impacts, Shocks, and Other Deformations' (Citeseer, 2012).

42   Hantao Ji, Riccardo Betti, Troy Carter, Paul Drake, Cary Forest, Jeremy Goodman, Thomas Intrator, Philipp Kronberg, Hui Li, and Edison Liang, 'Roles, Current Status, Opportunities, Future Trends, and Funding Issues for Laboratory Plasma Astrophysics', *submitted to Study Group on Facilities, Funding and Program* (2009).

43   Division of Laboratory Astrophysics Division, 'Division of Laboratory Astrophysics Division'.

44   SC Hsu, and PM Bellan, 'On the Jets, Kinks, and Spheromaks Formed by a Planar Magnetized Coaxial Gun', *Physics of Plasmas (1994-present),* 12 (2005), 032103.

45   Michael R Brown, 'Scaling Studies of Spheromak Formation and Equilibrium', *Physics of Plasmas,* 5 (1998), 1027.

46   F Suzuki-Vidal, M Bocchi, SV Lebedev, J Skidmore, G Swadling, G Burdiak, AJ Harvey-Thompson, P de Grouchy, SN Bland, and GN Hall, 'Jet-Ambient Interaction of a Supersonic, Radiatively-Cooled Jet in Laboratory Experiments', *EAS Publications Series,* 58 (2012), 127-31.

47   Scott C Hsu, and Paul M Bellan, 'Experimental Identification of the Kink Instability as a Poloidal Flux Amplification Mechanism for Coaxial Gun Spheromak Formation', *Physical review letters,* 90 (2003), 215002.

48   Kil-Byoung Chai, and Paul M Bellan, 'Extreme Ultra-Violet Movie Camera for Imaging Microsecond Time Scale Magnetic Reconnection', *Review of Scientific Instruments,* 84 (2013), 123504.

49   Gunsu S Yun, and Paul M Bellan, 'Plasma Tubes Becoming Collimated as a Result of Magnetohydrodynamic Pumping', *Physics of Plasmas (1994-present),* 17 (2010), 062108.

50   The Swarthmore Spheromak Experiment (SSX), 'Http://Plasma.Physics.Swarthmore.Edu/Ssx/Index.Html'.

51   MR Brown, David A Schaffner, and PJ Weck, 'Magnetohydrodynamic Turbulence: Observation and Experimenta)', *Physics of Plasmas (1994-present),* 22 (2015), 055601.

52   Yue Zhang, Alan G Lynn, Scott C Hsu, M Gilmore, and C Watts, 'Design of a Compact Coaxial Magnetized Plasma Gun for Magnetic Bubble Expansion Experiments', in *Pulsed Power Conference, 2009. PPC'09. IEEE* (IEEE, 2009), pp. 233-38.

53   U Shumlak, BA Nelson, RP Golingo, SL Jackson, EA Crawford, and DJ Den Hartog, 'Sheared Flow Stabilization Experiments in the Zap Flow Z Pinch', *Physics of Plasmas (1994-present),* 10 (2003), 1683-90.

54   H Alfvén, L Lindberg, and P Mitlid, 'Experiments with Plasma Rings', *J. Nuclear Energy, Pt. C. Plasma Phys.-Accelerators-Thermonuclear Research,* 1 (1960).

55   L Lindberg, E Witalis, and CT Jacobsen, 'Experiments with Plasma Rings', *Nature,* 185 (1960), 452-53.

56   L Lindberg, and C Jacobsen, 'On the Amplification of the Poloidal Magnetic Flux in a Plasma', *The Astrophysical Journal,* 133 (1961), 1043.

57   John Marshall, 'Performance of a Hydromagnetic Plasma Gun', *Physics of Fluids (US),* 3 (1960).

58   M Gilmore, AG Lynn, TR Desjardins, Y Zhang, C Watts, SC Hsu, S Betts, R Kelly, and E Schamiloglu, 'The Helcat Basic Plasma Science Device', *Journal of Plasma Physics,* 81 (2015), 345810104.

59   Alan G Lynn, Mark Gilmore, Christopher Watts, Janis Herrea, Ralph Kelly, Steve Will, Shuangwei Xie, Lincan Yan, and Yue Zhang, 'The Helcat Dual-Source Plasma Device', *Review of Scientific Instruments,* 80 (2009), 103501.

60   TR Desjardins, and M Gilmore, 'Dynamics of Flows, Fluctuations, and Global Instability under Electrode Biasing in a Linear Plasma Device', *Physics of Plasmas (1994-present),* 23 (2016), 055710.

61   Model   No.   GL-37207A, 'Http://www.Relltubes.Com/Filebase/En/Src/Datasheets/Nl2888a-Feb2013.Pdf'.

62   David W Knight, and Devon Ottery St Mary, 'Solenoid Inductance Calculation', *Режим доступу: http://www. g3ynh. info/zdocs/magnetics/Solenoids. pdf* (2013).

63   A Mosallanejad, and A Shoulaie, 'Investigation and Calculation of Magnetic Field in Tubular Linear Reluctance Motor Using Fem', *Advances in Electrical and Computer Engineering,* 10 (2010), 43-48.

64   Finite Element Method Magnetics, 'Http://www.Femm.Info/Wiki/Homepage'.

65   JC Thomas, DQ Hwang, RD Horton, JH Rogers, and R Raman, 'A Simple Fast Pulse Gas Valve Using a Dynamic Pressure Differential as the Primary Closing Mechanism', *Review of scientific instruments,* 64 (1993), 1410-13.

66   Jimmy Yee, 'Experimental Investigations in Spheromaks: Injection into a Tokamak and

Formation in an Unbounded Environment' (California Institute of Technology, 2000).

67   Ultra UHSi 12/24 Manuel, (http://www.nacinc.com/datasheets/UltraUHSi-12-24.pdf).

68   IVV Imprint, 'Http://www.Invisiblevision.Com/Products/Ultra-High-Speed-Framing/'.

69   Paul M Bellan, *Spheromaks: A Practical Application of Magnetohydrodynamic Dynamos and Plasma Self-Organization* (World Scientific, 2000).

70   Exell Battery 455 45V, 'Http://www.Exellbattery.Com/Exell-Battery-455-Neda-201-Alkaline/'.

71   Muhammad Yasin Naz, Abdul Ghaffar, NU Rehman, S Naseer, and Muhammad Zakaullah, 'Double and Triple Langmuir Probes Measurements in Inductively Coupled Nitrogen Plasma', *Progress In Electromagnetics Research,* 114 (2011), 113-28.

72   ET Everson, P Pribyl, CG Constantin, A Zylstra, D Schaeffer, NL Kugland, and C Niemann, 'Design, Construction, and Calibration of a Three-Axis, High-Frequency Magnetic Probe (B-Dot Probe) as a Diagnostic for Exploding Plasmas', *Review of Scientific Instruments,* 80 (2009), 113505.

73   CA Romero-Talamás, PM Bellan, and SC Hsu, 'Multielement Magnetic Probe Using Commercial Chip Inductors', *Review of scientific instruments,* 75 (2004), 2664-67.

74   Coilcraft Inc. model 1008CS-822XJLB, 'Http://www.Coilcraft.Com/1008cs.Cfm'.

75   Lucas A Morton, 'Calibration of a Magnetic Field Probe as a Diagnostic for Laser-Produced Plasma' (University of California, Los Angeles, 2010).

76   Helmholtz coil, 'Https://En.Wikipedia.Org/Wiki/Helmholtz_Coil'.

77   Ryan A Pahl, Joshua L Rovey, and David J Pommerenke, 'Calibration of Magnetic Field Probes at Relevant Magnitudes', in *Pulsed Power Conference (PPC), 2013 19th IEEE* (IEEE, 2013), pp. 1-6.

78   Kurt A Polzin, and Carrie S Hill, 'Standard Practices for Usage of Inductive Magnetic Field Probes with Application to Electric Propulsion Testing', (2013).

79   LeCroy 8007, 'Http://Teledynelecroy.Com/Lrs/Dsheets/8007.Htm'.

80   Cris W Barnes, JC Fernandez, I Henins, HW Hoida, TR Jarboe, SO Knox, GJ Marklin, and KF McKenna, 'Experimental Determination of the Conservation of Magnetic Helicity from the Balance between Source and Spheromak', *Physics of Fluids (1958-1988),* 29 (1986), 3415-32.

81   Michael J Schaffer, 'Exponential Taylor States in Circular Cylinders', *Physics of Fluids*

(1958-1988), 30 (1987), 160-63.

82   Cris W Barnes, TR Jarboe, GJ Marklin, SO Knox, and I Henins, 'The Impedance and Energy Efficiency of a Coaxial Magnetized Plasma Source Used for Spheromak Formation and Sustainment', *Physics of Fluids B: Plasma Physics (1989-1993),* 2 (1990), 1871-88.

83   Philip Hardee, 'Agn Jets: From Largest to Smallest Angular Scales', in *Journal of Physics: Conference Series* (IOP Publishing, 2008), p. 012052.

84   Close-up Look at a Jet near a Black Hole in Galaxy M87 (Ground-Based View), 'Https://www.Spacetelescope.Org/Images/Opo9943b/'.

85   3C31   VLA   20cm   intensity   gradients, 'Http://www.Cv.Nrao.Edu/~Abridle/3c31sobl.Htm'.

86   Jet from Young Star (HH-47), 'Https://www.Spacetelescope.Org/Images/Opo9524g/'.

87   Deepak Kumar, and Paul M Bellan, 'Nonequilibrium Alfvénic Plasma Jets Associated with Spheromak Formation', *Physical review letters,* 103 (2009), 105003.

88   SF Schaer, 'Coaxial Plasma Gun in the High Density Regime and Injection into a Helical Field', *ACTA PHYSICA POLONICA SERIES A,* 88 (1995), S-77.

89   Frank Llewellyn-Jones, *Ionization and Breakdown in Gases*. Vol. 33 (Methuen, 1957).

90   A Ciardi, SV Lebedev, A Frank, EG Blackman, DJ Ampleford, CA Jennings, JP Chittenden, T Lery, SN Bland, and SC Bott, '3d Mhd Simulations of Laboratory Plasma Jets', *Astrophysics and Space Science,* 307 (2007), 17-22.

91   P. M. Bellan, 'Why Current-Carrying Magnetic Flux Tubes Gobble up Plasma and Become Thin as a Result', *Physics of Plasmas,* 10 (2003), 1999-2008.

92   Marek Rabiński, and Krzysztof Zdunek, 'Snow Plow Model of Ipd Discharge', *Vacuum,* 70 (2003), 303-06.

93   HC Spruit, 'Theory of Magnetically Powered Jets', in *The Jet Paradigm* (Springer, 2010), pp. 233-63.

94   Xiang Zhai, 'Experimental, Numerical and Analytical Studies of the Mhd-Driven Plasma Jet, Instabilities and Waves' (California Institute of Technology, 2015).

95   Dmitri A Uzdensky, and Andrew I MacFadyen, 'Magnetar-Driven Magnetic Tower as a Model for Gamma-Ray Bursts and Asymmetric Supernovae', *arXiv preprint astro-ph/0609047* (2006).

96   D Lynden-Bell, 'Magnetic Collimation by Accretion Discs of Quasars and Stars', *Monthly Notices of the Royal Astronomical Society,* 279 (1996), 389-401.

97   Donald Lynden-Bell, 'On Why Discs Generate Magnetic Towers and Collimate Jets', *Monthly Notices of the Royal Astronomical Society,* 341 (2003), 1360-72.

98   CT Chang, 'Shock Wave Phenomena in Coaxial Plasma Guns', *Physics of Fluids (1958-1988),* 4 (1961), 1085-96.

99   Sol N Molina, Iván Agudo, José L Gómez, Thomas P Krichbaum, Iván Martí-Vidal, and Alan L Roy, 'Evidence of Internal Rotation and a Helical Magnetic Field in the Jet of the Quasar Nrao 150', *Astronomy & Astrophysics,* 566 (2014), A26.

100   Avery E Broderick, and Jonathan C McKinney, 'Parsec-Scale Faraday Rotation Measures from General Relativistic Magnetohydrodynamic Simulations of Active Galactic Nucleus Jets', *The Astrophysical Journal,* 725 (2010), 750.

101   M. Kruskal, and J. L. Tuck, 'The Instability of a Pinched Fluid with a Longitudinal Magnetic Field', *Proceedings of the Royal Society of London A: Mathematical, Physical and Engineering Sciences,* 245 (1958), 222-37.

102   TP Krichbaum, A Witzel, RS Booth, AJ Kus, BO Ronnang, A Witzel, DA Graham, IIK Pauliny-Toth, A Quirrenbach, and CA Hummel, '43 Ghz-Vlbi Observations of 3c273 after a Flux Density Outburst in 1988', *Astronomy and Astrophysics,* 237 (1990), 3-11.

103   AP Lobanov, and JA Zensus, 'A Cosmic Double Helix in the Archetypical Quasar 3c273', *Science,* 294 (2001), 128-31.

104   Nancy Crooker, Jo Ann Joselyn, and Joan Feynman, 'Coronal Mass Ejections', *Washington DC American Geophysical Union Geophysical Monograph Series,* 99 (1997).

105   James Chen, 'Theory of Prominence Eruption and Propagation: Interplanetary Consequences', *Journal of Geophysical Research: Space Physics,* 101 (1996), 27499-519.

106   Spiro K Antiochos, Peter J MacNeice, Daniel S Spicer, and James A Klimchuk, 'The Dynamic Formation of Prominence Condensations', *The Astrophysical Journal,* 512 (1999), 985.

107   DM Rust, and A Kumar, 'Evidence for Helically Kinked Magnetic Flux Ropes in Solar Eruptions', *The Astrophysical Journal Letters,* 464 (1996), L199.

108   Philip A Isenberg, and Terry G Forbes, 'A Three-Dimensional Line-Tied Magnetic Field Model for Solar Eruptions', *The Astrophysical Journal,* 670 (2007), 1453.

109   T Török, and B Kliem, 'Confined and Ejective Eruptions of Kink-Unstable Flux Ropes', *The Astrophysical Journal Letters,* 630 (2005), L97.

110   J Brian Taylor, 'Relaxation of Toroidal Plasma and Generation of Reverse Magnetic Fields', *Physical Review Letters,* 33 (1974), 1139.

111   E Bickford Hooper, Thomas Andrew Kopriva, Barry I Cohen, David N Hill, Harry S McLean, Reginald D Wood, Simon Woodruff, and Carl R Sovinec, 'Magnetic Reconnection During Flux Conversion in a Driven Spheromak', *Physics of Plasmas (1994-present),* 12 (2005), 092503.

112   Paul Horowitz, Winfield Hill, and Thomas C Hayes, *The Art of Electronics*. Vol. 2 (Cambridge university press Cambridge, 1989).

113   WC Turner, GC Goldenbaum, EHA Granneman, JH Hammer, CW Hartman, DS Prono, and J Taska, 'Investigations of the Magnetic Structure and the Decay of a Plasma-Gun-Generated Compact Torus', *Physics of Fluids (1958-1988),* 26 (1983), 1965-86.

114   SO Knox, Cris W Barnes, GJ Marklin, TR Jarboe, I Henins, H Wr Hoida, and BL Wright, 'Observations of Spheromak Equilibria Which Differ from the Minimum-Energy State and Have Internal Kink Distortions', *Physical review letters,* 56 (1986), 842.

115   M Nagata, T Kanki, T Masuda, S Naito, H Tatsumi, and T Uyama, 'Relaxation Oscillations and Toroidal-Current Regeneration in a Helicity-Driven Spheromak', *Physical review letters,* 71 (1993), 4342.

116   Allen H Boozer, 'Physics of Magnetically Confined Plasmas', *Reviews of modern physics,* 76 (2005), 1071.

117   Juan C Jiménez-Muñoz, and José A Sobrino, 'A Generalized Single-Channel Method for Retrieving Land Surface Temperature from Remote Sensing Data', *Journal of Geophysical Research: Atmospheres,* 108 (2003).

118   Michael S Barnes, John C Forster, and John H Keller, 'Ion Kinetics in Low-Pressure, Electropositive, Rf Glow Discharge Sheaths', *Plasma Science, IEEE Transactions on,* 19 (1991), 240-44.

119   Chao Zhang, and Tie Jun Cui, 'Negative Reflections of Electromagnetic Waves in a Strong Chiral Medium', *Applied Physics Letters,* 91 (2007), 194101.

120   Alexei A Pevtsov, Richard C Canfield, and Thomas R Metcalf, 'Patterns of Helicity in Solar Active Regions', *The Astrophysical Journal,* 425 (1994), L117-L19.

121   Kendall E Atkinson, *An Introduction to Numerical Analysis* (John Wiley & Sons, 2008).

122   Christopher Watts, Yue Zhang, Alan Lynn, Ward Manchester, and C Nick Arge, 'Laboratory-Generated Coronal Mass Ejections', *Proceedings of the International Astronomical Union,* 6 (2010), 36-39.

123   CS Beals, 'On the Interpretation of Interstellar Lines', *Monthly Notices of the Royal Astronomical Society,* 96 (1936), 661.

124   Katia M Ferriere, 'The Interstellar Environment of Our Galaxy', *Reviews of Modern Physics,* 73 (2001), 1031.

125   George H Herbig, 'Emission-Line Stars in the Vicinity of Messier 8, Messier 20, and Simeis 188', *The Astrophysical Journal,* 125 (1957), 654.

126   Stirling A Colgate, T Kenneth Fowler, Hui Li, E Bickford Hooper, Joseph McClenaghan, and Zhihong Lin, 'Quasi-Static Model of Magnetically Collimated Jets and Radio Lobes. Ii. Jet Structure and Stability', *The Astrophysical Journal,* 813 (2015), 136.

127   Wolfgang Baumjohann, and Rudolf A Treumann, *Basic Space Plasma Physics* (World Scientific, 1997).

128   Shengtai Li, Hui Li, and Renyue Cen, 'Cosmomhd: A Cosmological Magnetohydrodynamics Code', *The Astrophysical Journal Supplement Series,* 174 (2008), 1.

129   TD Arber, and DF Howell, 'The Effect of Sheared Axial Flow on the Linear Stability of the Z-Pinch', *Physics of Plasmas (1994-present),* 3 (1996), 554-60.

130   U Shumlak, and CW Hartman, 'Sheared Flow Stabilization of the M= 1 Kink Mode in Z Pinches', *Physical review letters,* 75 (1995), 3285.

131   VI Sotnikov, I Paraschiv, V Makhin, BS Bauer, JN Leboeuf, and JM Dawson, 'Linear Analysis of Sheared Flow Stabilization of Global Magnetohydrodynamic Instabilities Based on the Hall Fluid Model', *Physics of Plasmas (1994-present),* 9 (2002), 913-22.

132   Nicole S Love, and Chandrika Kamath, 'Image Analysis for the Identification of Coherent Structures in Plasma', in *Optical Engineering+ Applications* (International Society for Optics and Photonics, 2007), pp. 66960D-60D-12.

133   Gabor Toth, Ovsei Volberg, Aaron J Ridley, Tamas I Gombosi, Darren L De Zeeuw, Kenneth C Hansen, David R Chesney, Quentin F Stout, Kenneth G Powell, and Kevin J Kane, 'A Physics-Based Software Framework for Sun-Earth Connection Modeling', *Multiscale Coupling of Sun-Earth Processes, edited by: Liu, ATY, Kamide, Y., and Consolini, G* (2005), 383-97.